

**SURFACE MODIFIED SUPERPARAMAGNETIC  
NANOPARTICLES FOR FUNCTIONAL BIOMEDICAL  
APPLICATIONS**

**Ansar E B**

**Ph.D. THESIS  
2016**



**SREE CHITRA TIRUNAL INSTITUTE FOR MEDICAL  
SCIENCES AND TECHNOLOGY  
THIRUVANANTHAPURAM**

**INDIA**

**2016**

## DECLARATION

I, Ansar E B, hereby certify that I had personally carried out the work depicted in the thesis entitled, “*Surface Modified Superparamagnetic Nanoparticles for Functional Biomedical Applications*”, except where due acknowledgment has been made in the text. No part of the thesis has been submitted for the award of any other degree or diploma prior to this date.

Ansar E B

Reg.No: PhD/2011/03

Trivandrum

12-08-2016

# SREE CHITRA TIRUNAL INSTITUTE FOR MEDICAL SCIENCES & TECHNOLOGY

Thiruvananthapuram – 695011, INDIA

(An Institute of National Importance under Govt. of India)

Phone: (91)0471-2520271 Fax: (91)0471-2341814

Email: varma@sctimst.ac.in Web site – www.sctimst.ac.in



## CERTIFICATE

This is to certify that **Mr. Ansar E B**, in the Bioceramics laboratory of this institute has fulfilled the requirements prescribed for the Ph. D. degree of the Sree Chitra Tirunal Institute for Medical Sciences and Technology, Thiruvananthapuram. The thesis entitled, “*Surface Modified Superparamagnetic Nanoparticles for Functional Biomedical Applications*” was carried out under my direct supervision. No part of the thesis was submitted for the award of any degree or diploma prior to this date.

Dr. P.R. Harikrishna Varma  
(Research Supervisor)

Trivandrum  
12-08-2016

Office Seal

**The thesis entitled**  
**Surface Modified Superparamagnetic Nanoparticles for Functional**  
**Biomedical Applications**

Submitted by

**Ansar E B**

for the degree of  
**Doctor of Philosophy**  
Of

**SREE CHITRA TIRUNAL INSTITUTE**  
**FOR MEDICAL SCIENCES AND TECHNOLOGY,**  
**THIRUVANANTHAPURAM - 695011**

is evaluated and approved by

.....  
Dr. P.R. Harikrishna Varma  
(Research Supervisor)

.....  
Examiner

**DEDICATED TO  
MY FAMILY & TEACHERS**

## **ACKNOWLEDGMENT**

*I take this opportunity to express immeasurable gratitude to many people for their support during the PhD work which made this thesis possible.*

*First of all, I would like to express my heartfelt gratitude and respect to my supervisor Dr. P.R. Harikrishna Varma, scientist-F, BCL, SCTIMST is beyond description. Dr. Harikrishna Varma has offered constant support, strong encouragement and motivation throughout the course of this study. I thank him for the systematic guidance, and for lighting the path of my budding research career via preparation of this thesis.*

*The Director, SCTIMST and The Head, BMT Wing is greatly acknowledged for the facilities provided throughout the doctoral programme. I am very much indebted to The Dean, The Registrar and The Deputy Registrar for all the academic assistance in this venture.*

*I thank the members of my doctoral advisory committee, Dr. K. Sreenivasan, scientist G, Polymer Analysis Lab, Dr. Mohanan P. V, scientist F, Toxicology division and Dr. R. S. Jayasree, Scientist E, Biophotonics and Imaging Laboratory or their timely suggestions, support and critical comments.*

*I thank Department of science and technology, Govt. Of India for the fellowship provided during the doctoral programme and Department of biotechnology Govt. of India for funding for the international conferences which I attended in China.*

*This work was completed only because of the help and support given by Dr. Manoj Komath, Mr. Vijayan S, Dr. Sureshbabu S, and Mr. Nishad KV. I also thank them for the training given in material synthesis, analysis by XRD, FTIR, ICP, SEM etc. during the work. I am grateful to Mr. Sreekanth PJ, Dr. Padmaja P, Dr. Rajesh P, Ms Nimmy Mohan, Ms. Sandhya, for all the support during my work.*

*It is great pleasure for me to thank to Dr. Annie John, Dr. Francis BF, and all members of TEM for their help and support in cell culture studies. My sincere thank to Dr. Jayasree and Dr. Shaiju S Nazeer of BPL Lab for help, support and conducting the MRI analysis. I thank Dr. Lissy K. Krishnan and Mr. Ranjith Katha of TRU Lab for Hemolysis studies and FACS analysis. I thank to Dr. Sabareeswaran and all members of Histopathology Lab and Dr. TV Kumary, Dr. Anil Kumar P. R and all members of Tissue culture Lab for various aspects of cell study. I thank to Dr. C. Radhakumary of Polymer analysis Lab and Mr. Willi Paul of Central Analytical Facility for help thermal analysis and DLS studies.*

*I am very much indebted to Dr. Anil Sukumaran of King Saud University, Prof. Yokogawa of Osaka City University and Dr. Wilfried Wunderlich of Tokai University for providing various aspects of experimental study, instrumental facilities and for fruitful discussions. I gratefully acknowledge the support and help given by my friends, staff and students of BMT wing of SCTIMST.*

*I have no words to express gratitude to my family members who provided the most precious support. I am indebted to my parents, wife, brothers and sister for their endless support, encouragement, love and prayers.*

**Ansar E B**

## TABLE OF CONTENTS

DECLARATION OF AUTHORSHIP .....	ii
CERTIFICATE BY THE RESEARCH GUIDE .....	iii
APPROVAL OF THESIS .....	iv
ACKNOWLEDGMENTS .....	vi
TABLE OF CONTENTS .....	vii
LIST OF FIGURES .....	xiv
LIST OF TABLES .....	xxi
ABBREVIATION .....	xxii
SYNOPSIS .....	xxiii
Chapter 1 .....	1
INTRODUCTION .....	1
1.1 Nanotechnology .....	1
1.2 Nanoparticles .....	2
1.3 Importance of Nanoparticles in the Biomedical Field .....	4
1.4 Magnetism and Superparamagnetic Nanoparticles .....	6
1.5 Potential Application of Superparamagnetic Nanoparticles in the Biomedical Field....	7
1.5.1 Targeted Cell Therapy .....	7
1.5.2 Diagnostic Tool- Magnetic Resonance Imaging (MRI) Contrast Agent .....	8
1.5.3 Therapeutic Agent – Magnetic Hyperthermia Cancer Treatment .....	9
1.6 Limitation of the Current Approaches .....	9
Hypothesis .....	12
Objectives of the Study .....	12
Chapter 2 .....	14
LITERATURE REVIEW .....	14
2. 1 Superparamagnetism and Superparamagnetic Iron Oxide Nanoparticles [SPION]....	14
2.2 Different Method of SPION Synthesis and Importance of Co-precipitation .....	15
2.3 Versatile Applications of SPION and Importance in Potential Biomedical Field .....	16
2.3.1 Targeted Delivery and Therapy .....	16
2.3.1.1 Three Dimensional Cell Culturing and Magnetic Microspheres .....	18

2.3.2 MRI Contrast Agent.....	20
2.3.2.1 Magnetic Resonance Imaging .....	20
2.3.2.2 Magnetic Resonance Imaging- Importance of Contrast Agent.....	21
2.3.2.3 Spinel Crystal Structure and its Modification .....	22
2.3.2.4 Synthesis of Spinel Ferrite .....	23
2.3.3 Hyperthermia Cancer Therapy – Importance of Magnetic Field .....	23
2.3.3.1 Temperature Sensitivity of Cancer Cells .....	24
2.3.3.2 Hyperthermia Heating Mechanism of Magnetic Nanoparticles.....	25
2.3.4 Theranostic Application of Magnetic Nanoparticles .....	27
2.4 Problems Associated with Bare SPION Particles in Biomedical Applications .....	27
2.4.1 Importance of Surface Modification .....	29
2.4.2 Inorganic Molecules Used as Surface Coating Agent – Hydroxyapatite Crystals	30
2.4.3 Surface modification – Trisodium citrate (TC) Molecules .....	32
Chapter 3.....	34
MATERIALS AND METHODS.....	34
3.1 Developemtn of Superparamagnetic Iron Oxide Embedded Hydroxyapatite Nanocomposite .....	34
3.1.1 Materials .....	34
3.1.2 Synthesis of Nano Iron Oxide Embedded Hydroxyapatite Composites (HAIO)..	34
3.1.3 Physicochemical Characterizations HAIOs and SPION.....	35
3.1.3.1 High Resolution Ttransmission Electron Microscopy (HRTEM) and Energy Dispersive X-ray Spectra (EDS).....	35
3.1.3.2 Environmental Scanning Electron Microscopy (ESEM) and Energy Dispersive X-ray Spectra (EDS).....	36
3.1.3.3 X-ray Diffraction Analysis (XRD).....	36
3.1.3.4 Dynamic Light Scattering (DLS) and Zeta Potential Measurements.....	36
3.1.3.5 Fourier Transform Infrared Spectra (FTIR).....	37
3.1.3.6 Vibrating Sample Magnetometry (VSM).....	37
3.1.4 Biological Evaluation of HAIOs.....	37
3.1.4.1 In vitro Biocompatibility- cell Culture.....	37
3.1.4.2 Cell viability MTT Assay .....	38
3.1.4.3 Cell viability Alamar blue Assay .....	38
3.1.4.4 In vitro Hemocompatibility.....	39

3.1.4.5 Cellular Uptake: Prussian blue Staining and Flow Cytometry Evaluations...	40
3.2 HAI050 Assisted Cell Separation, Manipulation and Culturing using External Magnetic field for Introducing Targeted Cell Delivery and Therapy .....	40
3.2.1 Cell separation .....	40
3.2.2 Morphological Study: Cell Separation.....	41
3.2.2 Cell Culture of Magnetically Separated Cells.....	41
3.2.2.1 Cytoskeleton, Morphology Evaluations by Confocal Laser Scanning Microscopy (cLSM).....	41
3.2.3 HAI050 Aided Three Dimensional Cell Culture.....	42
3.2.3.1 Morphological Evaluation-ESEM Technique.....	42
3.2.3.2 DAPI Nuclear Staining and Phase Contrast Imaging.....	43
3.2.4 Magnetic Microsphere Synthesis .....	43
3.2.5 Physicochemical Characterizations.....	44
3.2.5.1 ESEM and EDS Analysis.....	44
3.2.5.2 XRD and FTIR Analysis.....	44
3.2.6 Biological Characterizations .....	44
3.2.6.1 Cell Culture.....	44
3.2.6.2 Cytotoxicity - Alamar Blue Assay and Light Microscopic Technique.....	44
3.2.6.3 Hemolysis and RBC Morphology Analysis.....	45
3.2.7 Three Dimensional Cell Culture using Magnetic Microsphere .....	46
3.2.7.1 ESEM Analysis.....	46
3.2.7.2 Live- Dead Staining and DAPI Nuclear Staining Evaluation .....	46
3.3 Theranostic Efficiency Evaluation of HAI050 (Hyperthermia Therapy and MRI Contrast Agent).....	47
3.3.1 Magnetic Hyperthermia Evaluation of HAI050 and SLP Calculation.....	47
3.3.2 HAI050 <i>in vitro</i> Hyperthermia Evaluation.....	48
3.3.2.1 Quantitative Estimation of Dead Cell Population – FACS Analysis .....	48
3.3.2.2 Quantitative Estimation of Cell Death Mechanism - FACS Analysis .....	49
3.3.2.3 Hyperthermia Treated Cells Morphology Evaluation – ESEM Technique ...	49
3.3.3 Magnetic Resonance Imaging Contrast Efficiency of HAI050.....	49
3.3.3.1 In vitro MRI Analysis .....	50
3.4 Improve the Theranostic Efficiency of Superparamagnetic Nanoparticles Through Crystal Modification .....	51

3.4.1 Development of Manganese Substituted SPION (MnIO) Nanocrystal <i>via</i> an Aqueous Co-precipitation .....	51
3.4.1.1 Materials: .....	51
3.4.1.2 Synthesis of MnIO .....	51
3.4.1.3 Development of Various Concentration of Mn <sup>2+</sup> Substituted SPION.....	52
3.4.1.4 Physicochemical Characterizations of MnIOs .....	52
3.4.1.4.1 TEM and HRTEM analysis.....	52
3.4.1.4.2 Powder X-ray Diffraction .....	53
3.4.1.4.3 Fourier Transform Infrared Spectra (FTIR) .....	53
3.4.1.4.4 Thermogravimetric Analysis.....	53
3.4.1.4.4 Inductively Coupled plasma-Optical Emission Spectroscopy .....	53
3.4.1.4.5 ESEM and EDS spectrum .....	54
3.4.1.4.5 Magnetic Property Measurement of MnIOs .....	54
3.4.1.4 Biological Evaluations of MnIOs.....	54
3.4.1.4.1 Cell Culture .....	54
3.4.1.4.2 Cytotoxicity - Alamar Blue Assay and Light Microscopy.....	54
3.4.1.4.3 Hemolysis Assay.....	55
3.4.1.4.4 Clotting Time .....	55
3.4.1.4.5 RBC Aggregation.....	56
3.4.1.4.6 WBC Aggregation.....	56
3.4.1.4.7 Platelet Aggregation.....	56
3.4.1.4.8 Cell Uptake .....	57
3.4.1.5 MnIOs Contrast Effect in Magnetic Resonance Imaging .....	57
3.4.2 Development of Surface Modified Manganese Substituted SPION .....	58
3.4.2.1 Materials .....	58
3.4.2.2 Synthesis of Surface Modified MnIO Nanoparticles (MnIOTCs) .....	58
3.4.2.3 Physicochemical Characterizations.....	59
3.4.2.3.1 Dynamic Light Scattering .....	59
3.4.2.3.2 X-ray Diffraction Technique.....	59
3.4.2.3.3 Thermogravimetric Analysis.....	59
3.4.2.3.4 Transmission Electron Microscopic Analysis.....	59
3.4.2.3.5 Fourier Transform Infrared Spectra .....	60
3.4.2.3.6 Vibrating Sample Magnetometry analysis .....	60

3.4.2.4 Biological Evaluations .....	60
3.4.2.4.1 Cell Culture .....	60
3.4.2.4.2 Cytoskeleton Evaluation .....	60
3.4.2.4.3 Cytotoxicity- Alamar blue Assay and Light Microscopic Technique.....	61
3.4.2.4.4 Cell Uptake .....	61
3.4.2.4.5 Blood Compatibility Studies .....	61
3.4.2.5 Contrast Efficiency in MRI.....	62
3.4.2.6 Hyperthermia Studies.....	62
3.4.2.7 Hyperthermia – Cell Death Evaluation .....	62
3.4.2.7.1 Hyperthermia Cell Death – FACS Analysis .....	63
3.4.2.7.2 Hyperthermia Cell Death – ESEM Analysis.....	63
Chapter 4.....	64
RESULTS .....	64
4.1 Development of SPION Embedded HA Nanocomposites (HAIO) .....	64
4.1.1 Synthesis of HAIO and Physicochemical Characterizations .....	64
4.1.2 Biological Evaluation of HAIOs .....	72
4.2 HAIO50 Assisted Cell Separation, Manipulation and Culturing Using External Magnetic Field for Introducing Targeted Cell Delivery .....	78
4.2.1 HAIO50 Aided Cell Separation Experiment.....	78
4.2.2 Structure and Morphology Evaluation of Magnetically Separated Cells.....	81
4.2.3 Magnetically Separated Cells were Cultured under <i>In vitro</i> Condition .....	83
4.3 HAIO50 Conjugated HeLa Cells were Magnetically Levitated and used for Three Dimensional [3D] Culturing .....	84
4.3.1 Synthesis of HAIO Embedded Polycaprolactone Magnetic Microspheres [HAIO PCL] and Physicochemical Characterization.....	86
4.3.1.1 Biological Evaluation and 3D culture of HAIO PCL .....	89
4.4 Theranostic Efficiency Evaluation of HAIO50 (Hyperthermia Therapy and MRI Contrast Agent).....	92
4.4.1 Hyperthermia Therapeutic Evaluation of HAIO50.....	92
4.4.1.1 Hyperthermia Therapeutic Evaluation of HAIO50 under In vitro Condition	94
4.4.2 MRI Contrast Efficiency Evaluation of HAIO50 Particles.....	97
4.5 Improve the Theranostic Efficiency of Superparamagnetic Nanoparticles Through Crystal Modification .....	100

4.5.1 Development of Manganese Substituted SPION (MnIO) Nanocrystal <i>via</i> an Aqueous Co-precipitation .....	100
4.5.1.1 Physicochemical Characterization of MnIOs.....	101
4.5.1.2 Biological Evaluations of MnIOs.....	109
4.5.1.3 Magnetic measurement and relaxivity calculation of MnIOs .....	114
4.5.2 Surface Modified Manganese Ferrite (MnIOTCs) Nanoparticle for MRI Contrast Efficiency and Hyperthermia Theranostic Evolutions.....	115
4.5.2.1 Physicochemical Characterizations of MnIOTCs .....	116
4.5.2.2 Biological Ealuations of MnIOTCs .....	120
4.5.2.3 Theranostic Evaluation of MnIOTCs.....	123
Chapter 5.....	130
DISCUSSION.....	130
5.1. Development of Stable Superparamgnetic Nanocomposite (HAIO) Particles <i>via</i> an Aqueous Co-precipitation Method.....	131
5.1.1 Physicochemical Characterizations of Developed HAIOs.....	132
5.1.2 Biocompatibility Evaluations of HAIOs.....	134
5.2 HAIO50 Assisted Cell Separation, Manipulation and Culturing using External Magnetic Field for Introducing Targeted Cell Delivery .....	135
5.2.1 HAIO50 Nanocomposites Cells Separation using External Magnetic Field and Characterizations.....	136
5.2.2 Magnetically Separated Cells Morphological Analysis and <i>in vitro</i> Culturing ..	137
5.2.3 Three Dimensional Cell Culture using Magnetic Levitation Technique .....	138
5.2.4 Magnetic Microsphere Development and 3D Cell Culturing .....	139
5.3 Assessment of Contrast Enhancement in MR imaging and Hyperthermia Therapeutic Efficiency of HAIO50 Particles in an <i>In vitro</i> Condition .....	140
5.3.1Hyperthermia Therapeutic Efficiency.....	140
5.3.2 Contrast Enhancement in Magnetic Resonance Imaging.....	144
5.4 Development of Manganese ion Substituted Magnetic Property Modified Superparamagnetic Nanocrystal (MnIO) <i>via</i> an Aqueous Co-precipitation Method.....	146
5.4.1 Synthesis and Characterization of MnIO .....	146
5.4.2 Evaluation of Contrast Efficiency in Magnetic Resonance Imaging .....	151
5.5 Evaluation of Contrast Enhancement in MRI imaging and Hyperthermia Therapeutic Efficacy [theranostic] of MnIO Particles in an <i>In vitro</i> Condition .....	155
5.5.1 Synthesis of Stable MnIOs using Trisodium Citrate Surface Modification.....	155

5.5.2 Theranostic Evaluation of MnIO75TC .....	158
Chapter 6.....	162
SUMMARY .....	162
Conclusion .....	168
Future Directions .....	170
REFERENCES .....	171
List of Publications .....	196
Selected Conference Presentations .....	1977
Curriculum vitae .....	199

## LIST OF FIGURES

<b>Figure 1A:</b> X-ray diffraction (XRD) pattern of (a) HA, (b) SPION and (c) HAI0; [-HA PDF = 00-009-0432, - SPION PDF = 01-071-6336] .....	65
<b>Figure 1B:</b> XRD pattern of a) HAI010 b) HAI030 c) HAI070 d) HAI090; [- HA PDF= 00-009- 0432, - SPION PDF= 01-071-6336] .....	65
<b>Figure 2:</b> Transmission Electron Micrographs of various weight percentage of SPION embedded HA samples (a) HAI010, (b) HAI020, (c) HAI030, (d) HAI040, (e) HAI050 and (f) Higher magnification of HAI050.....	66
<b>Figure 3:</b> Scanning Electron Micrographs of HAI0s a) HAI010 b) HAI020 c) HAI030 d) HAI040 and e) HAI050.....	67
<b>Figure 4:</b> Energy Dispersive Spectra (EDS) of (a) HAI010, (b) HAI020, (c) HAI030 (d) HAI040 and (e) HAI050 from TEM grid.....	68
<b>Figure 5:</b> Energy Dispersive Spectra (EDS) of a) HAI010 b) HAI020 c) HAI030 d) HAI040 and e) HAI050 from SEM stub.....	68
<b>Figure 6A:</b> Fourier Transform Infra red Spectra of a) SPION b) HA & c) HAI050...69	
<b>Figure 6B:</b> Fourier Transform Infra red Spectra (FTIR) of various weight percentages of HAI0s a) HAI010 b) HAI030 c) HAI070 and d) HAI090.....	70
<b>Figure 7:</b> Field-dependent magnetization curves (M-H) at 300K for magnetic composite with compositions of a)HAI010 b)HAI030 c) HAI050 d)HAI070 e)HAI090 f)SPION and g) HA .....	71
<b>Figure 8:</b> (a) hydrodynamic size and (b) zeta potential value of HAI050 particles..	72
<b>Figure 9:</b> MTT test of HeLa cells treated with 0.75mg/ml & 1.5mg/ml of SPION and HAI0s.....	72

<b>Figure 10:</b> Cell Activity at 24hrs contact with HAI050 various concentration evaluation via Alamar Blue assay.....	73
<b>Figure 11:</b> Phase contrast light micrographs of HeLa cells incubated with 120µg of HAI050 - a) Control and b) stained with Prussian Blue.....	74
<b>Figure 12A:</b> FSC vs SSC plots of Flow Cytometric measurement of granularity change in HeLa cells; A, B & C are represents 120µg, 240 µg & 480 µg of HAI050 in contact with 10 <sup>6</sup> cells and (i), (ii), (iii) & (iv) indicated analysis at time points - 0,5, 10 .....	75
<b>Figure 12B:</b> FSC vs SSC plots of Flow Cytometric measurement of granularity change in HeLa cells; A control, B & C are represents 30µg & 60µg of HAI050 in contact with 10 <sup>6</sup> cells and (i), (ii), (iii) & (iv) indicated analysis at time points - 0,5, 10 .....	76
<b>Figure 13:</b> Visible Light (A- i, iii, v) & UV (B - ii, iii, vi) Illumination of Acridine Orange (AO) stained HeLa cells incubated with HAI050 for 15min and separated with an external magnet (MT) placed in the vicinity between 4 <sup>th</sup> and 5 <sup>th</sup> tubes [0.3T]: M=H.....	79
<b>Figure 14:</b> The Acridine Orange (AO) pre-stained HeLa cells were incubated with various concentrations of HAI050 for 15min and magnetically separated. Supernatant collected and the corresponding pellets were re-dispersed in PBS buffer.....	81
<b>Figure 15:</b> Giemsa Stained HeLa cells: (a) cells alone indicated by clear blue spheres (b) Magnetically separated HAI050 pellet containing cells identical to (a); and (c) HAI050 alone.....	82
<b>Figure 16:</b> Scanning Electron Micrographs: (a) Cells alone and (b) Magnetically Separated HAI050 Cell pellet. The corresponding energy dispersive spectra are in inset.....	83
<b>Figure 17:</b> Confocal Laser Scanning Micrographs of magnetically separated HAI050 Cell pellet in culture for 24 hrs (i) in DIC mode (ii) DAPI (nuclei) stained	

cells (iii) Rhodamine Phalloidin stained Actin and (iv) merged image of (ii) & (iii).....	84
<b>Figure 18:</b> (a) Low and [(b), (c)] high magnification of ESEM images of three dimensionally cultured HeLa cells sheet on 72h.....	85
<b>Figure 19:</b> Cell sheet construct ruction after 72h 3D culturing (a) DAPI nuclear staining (b) phases contrast light microscopic image .....	86
<b>Figure 20:</b> SEM images of polycaprolactone microsphere (a) PCL 5 (b) PCL 7.5 (c) PCL10 .....	87
<b>Figure 21:</b> (a) & (b) are Low and high magnification SEM images of HAIO PCL magnetic microsphere.....	87
<b>Figure 22:</b> XRD measurement of magnetic microspheres (a) PCL (b) HAPCL (c) HAIOPCL.....	88
<b>Figure 23:</b> FTIR measurement of magnetic microspheres (a) PCL (b)HAIOPCL ...	88
<b>Figure 24:</b> Cell Activity at 24hrs contact with HAIO PCL various size range having 2mg/ml concentration evaluation via Alamar Blue assay.....	89
<b>Figure 25:</b> Scanning Electron Micrographs: (a) RBC cells alone and (b) 1mg/ml of 250- 350 $\mu\text{m}$ size HAIO PCL exposed RBC cells.....	90
<b>Figure 26:</b> Scanning Electron Micrographs: (a) HAIO PCL microsphere (b) HeLa cell seeded over HAIO PCL microsphere and cultured under 3D model condition.....	91
<b>Figure 27:</b> Fluorescence microscopic images of cells over microspheres (a) Live-dead analysis using Acridine orange ethidium bromide (b) DAPI nuclear staining...91	91
<b>Figure 28:</b> Heat profile of 5mg of samples (a) HAIO50 and (b) SPION for different currents.....	92

<b>Figure 29:</b> Time versus temperature graphs for various suspensions having different concentrations of samples (a) 5mg/ml, (b) 10mg/ml of HAIO50 and (c) 5mg/ml, (d) 10mg/ml of SPIONs.....	93
<b>Figure 30:</b> Normal dot-plots obtained from FACS data showing HeLa cells distribution (Propidium iodide staining) after hyperthermia analysis. (A) Control sample [Hela cell + HAIO particles without AMF application] (B) test sample [Hela cells + HAIO particle.....	95
<b>Figure 31:</b> Typical dot plot obtained from FACS data showing HeLa cells distribution Annexin V/ Propidium Iodide (PI) staining (A) HAIO+ HeLa cells without exposure to AMF as a control and (B) 30min exposure to MnIO75TC+ HeLa cells.....	96
<b>Figure 32:</b> ESEM images of HeLa cells loaded with HAIO (A) before and (B) after the application of the alternating magnetic field [AMF]. The corresponding images higher magnification represents in the right side. Most of the cell membrane structure collapse .....	97
<b>Figure 33:</b> (A) T2 weighted MR images of (A) HAIO50 with varying the concentration at 1.5 T clinical MRI system (B) Relaxivity rate graphs of 1/T2 against the Fe concentration of the HAIO50 .....	98
<b>Figure 34:</b> (A) T2 weighted MR images of different concentrations of HAIO50 incubated with HeLa cells during 24h (B) corresponding pixel intensity variation plotted against TE values.....	99
<b>Figure 35:</b> A schematic representation of Mn <sup>2+</sup> substituted SPION crystals. (a) SPION (b) MnIO25 (c) MnIO50 and (d) MnIO75.....	100
<b>Figure 36:</b> HRTEM images of various molar concentrations of Mn <sup>2+</sup> substituted iron oxide crystals. (a) SPION, (b) MnIO25, (c) MnIO50 and (d) MnIO75.....	101
<b>Figure 37:</b> TEM images and their corresponding size distribution curve shown in the inset for (a) SPION, (b) MnIO25, (c) MnIO50 and (d) MnIO75.....	102

<b>Figure 38:</b> X-ray diffraction pattern of a) SPION b) MnIO25 c) MnIO50 d) MnIO75 nanoparticle assemblies.....	103
<b>Figure 39:</b> XRD patterns for the samples recorded with Cu K $\alpha$ 1 radiation. a) SPION b)MnIO80 c)MnIO90.....	104
<b>Figure 40:</b> FTIR spectra of (a) SPION, (b) MnIO25, (c) MnIO50 and (d) MnIO75 nanoparticles in the 1900–400 cm-1 range.....	105
<b>Figure 41:</b> FTIR spectra of the freeze dried powder samples of a) SPION b) MnIO25 c) MnIO50 d) MnIO75 e) TC.....	106
<b>Figure 42:</b> TGA and DTA for (a) MnIO25, (b) MnIO50 and (c) MnIO75 under an N2 atmosphere.....	107
<b>Figure 43:</b> Surface composition of the Fe/Mn ratio of nanoparticle calculated via energy dispersive spectroscopy.....	108
<b>Figure 44:</b> Phase contrast microscopic view 400X (Scale bar 50 $\mu$ m ) of erythrocytes after incubation with a) Negative control (Normal saline) b) positive control (polyethylenimine) c) MnIO25 d) MnIO50 e) MnIO75 f)SPION.....	110
<b>Figure 45:</b> Phase contrast micrographs of leukocytes after incubation with MnIOs a) Negative control normal saline b) positive control (polyethylenimine) c) MnIO25 d) MnIO50 e) MnIO75 f) SPION. Scale bar 50 $\mu$ m.....	110
<b>Figure 46:</b> Phase contrast micrographs of platelets after incubation with MnIOs a) Negative control (normal saline) b) positive control (polyethylenimine) c) MnIO25 d)MnIO50 e) MnIO75 f)SPION. Scale bar 50 $\mu$ m .....	111
<b>Figure 47:</b> Cell Activity at 24hrs contact with SPION and MnIOs evaluation via Alamar Blue assay.....	112
<b>Figure 48:</b> Phase Contrast Micrographs of HeLa cells after 24h incubation with nanoparticles. (A) Control, (B) SPION, (C) MnIO25, (D) MnIO50, (E) MnIO75 and (i), (ii), (iii), (iv) are 0.5mg/mL, 1mg/mL, 2mg/mL, 3mg/mL concentrations of corresponding material.....	112

<b>Figure 49:</b> HeLa cells incubated for 24 h with SPION and MnIOs nanoparticles and stained with Prussian Blue. Blue indicates iron based nanoparticle uptake. Samples are (a) Control (b) SPION (c) MnIO25 (d) MnIO50 (e) MnIO75 respectively. Uptake of the SPIONs .....	113
<b>Figure 50:</b> Measurement of the magnetic properties of MnIOs particles at room temperature (a) SPION, (b) MnIO25, (c) MnIO50 and (d) MnIO75 with their corresponding remanence and coercivity.....	113
<b>Figure 51:</b> (I) T2 weighted MR images of A) MnIO75 B) MnIO50 C) MnIO25 varying concentrations at 1.5T MRI system (II) Relaxivity rate Graphs of 1/T2 against the Fe+Mn concentrations of MnIOs.....	115
<b>Figure 52:</b> (I) The wide angle XRD patterns of the (a)IOTC (b)MnIO25TC (c)MnIO50TC and (d)MnIO75TC (II) Corresponding particles crystallite size calculation via scherrer equation.[ IO PDF= 01-071-6336] .....	116
<b>Figure 53:</b> FT-IR spectra of trisodium citrate modified manganese ferrite nanoparticles (a) Trisodium citrate (b) IOTC (c) MnIO25TC (d) MnIO50TC and (e) MnIO75TC.....	118
<b>Figure 54:</b> Thermogravimetric analysis of MnIOTCs (a) characteristic weight loss pattern and (b) the percentage amount of weight remained in temperature range.....	118
<b>Figure 55:</b> TEM micrographs and corresponding particles distributions in the insets (a)IOTC (b)MnIO25TC (c)MnIO50TC and (d)MnIO75T C .....	119
<b>Figure 56:</b> Field dependent magnetization curves of MnIOTCs at 300K and corresponding coercivity and remanence shown at inset.....	120
<b>Figure 57:</b> Cytotoxicity effect of MnIOTCs on Hela cells treated with various concentrations of nanoparticles during 24 h incubation and analyzed via Alamar blue assay kit.....	121

**Figure 58:** Confocal microscopic images of HeLa cells incubated with ferrite nanoparticles concentration 2mg/mL during 24h and without particle as control. In the images, cell nucleus stained with DAPI (blue), F-actin filament detected using TRITC-conjugation.....121

**Figure 59:** Prussian blue staining of HeLa cells after 24h incubation of 50µgs of MnIOTCs and counter stained with nuclear fast red (A) Control (Hela cell alone) (b)IOTC (c)MnIO25TC (d)MnIO50TC (e)MnIO75TC, scale bar 50 µm.....122

**Figure 60:** (A) T2 weighted MRI images of various concentrations of MnIOTCs dispersed in water and (B) corresponding relaxation rate graph plotted 1/T2 against Fe+Mn concentrations.....24

**Figure 61:** (A) T2 weighted MR images of different concentrations of MnIO75TC incubated with HeLa cells during 24h (B) Corresponding pixel intensity variation plotted against TE values.....124

**Figure 62:** Time-temperature graphs of MnIO75TC concentrations (A) 5mg/ml and (B) 10mg/ml on exposure of 200A to 450A alternating current at 275kHz frequency.....125

**Figure 63:** Typical dot plot obtained from FACS data showing HeLa cells distribution Annexin V/ Propidium Iodide (PI) staining (A) MnIO75TC+ HeLa cells without exposure to AMF as a control and (B) 30min exposure to MnIO75TC+ HeLa cells.....127

**Figure 64:** Representative images of Annexin V and PI fluorescent staining showed HeLa cells apoptosis after 30 min MnIO75TC hyperthermia treatment. In the images Annexin V visualized by a green signal, Differential interference contrast mode visualization.....128

**Figure 65:** ESEM images of HeLa cells loaded with MnIO75TC (A) before and (B) after the application of the alternating magnetic field [AMF]. The corresponding images higher magnification represents in the right side. Most of the cell membrane structure .....129

## LIST OF TABLES

Table No.	Title	Page No.
<b>Table 1</b>	Hemolysis analysis of HAIO50 nanocomposites various concentrations.....	74
<b>Table 2</b>	Percentage Gated Population of P1 & P2: time & dose based variance clearly expressed. P1= cells gated as Control indicated by no change in values, P2= Cells in interaction with HAIO50 indicated by linearly correlated intensity of SSC channel.....	76
<b>Table 3</b>	Percentage Gated Population of P1 & P2: time & dose based variance clearly expressed. P1= cells gated as Control indicated by no change in values, P2= Cells in interaction with HAIO50 indicated by linearly correlated intensity of SSC channel.....	77
<b>Table 4</b>	The coulter counter cell count of supernatant from HAIO50 magnetically separated cells done at room temperature (25°C) and low temperature (4°C). Cells separated from suspension linearly decreased with concentration of material.	79
<b>Table 5</b>	Hemolysis analysis of HAIO PCL microspheres various sizes on 1mg/ml.....	89
<b>Table 6</b>	Representation of hyperthermia studies based on the applied alternating current, magnetic field strength and corresponding specific loss power of HAIO50 and SPIONs calculated from time-temperature graphs.....	94
<b>Table 7</b>	Partial weight loss determined by TGA analysis.....	107
<b>Table 8</b>	The initial Fe/ Mn metal composition ratio compared with ratios as determined by ICP-OES analysis.....	108
<b>Table 9</b>	Percentage hemolysis values of blood cells after 2hrs incubation with MnIOs at 37°C and clotting time measurement assessing the MnIOs contacted blood samples..	109
<b>Table 10</b>	Measurement of magnetic saturation and relaxivity values of MnIOs nanoparticles compared with SPION particles.....	114
<b>Table 11</b>	Zeta potential and hydrodynamic measurement of bare and trisodium citrate surface modified manganese ferrite particles.....	117
<b>Table 12</b>	Percentage hemolysis values of blood cells after 2hrs incubation with MnIOTCs at 37°C and clotting time measurement assessing the MnIOTCs contacted blood samples.....	123
<b>Table 13</b>	Representation of hyperthermia studies based on the applied alternating current, magnetic field strength and corresponding specific loss power of MnIO75TC calculated from time-temperature graphs.....	126

## **ABBREVIATION**

MRI	Magnetic resonance imaging
SPION	Superparamagnetic iron oxide nanoparticles
HSPs	Heat shock proteins
vdW	van der Waals force
HA	Hydroxyapatite
HAIO	Iron Oxide embedded Hydroxyapatite Composites
HRTEM	High resolution transmission electron microscopy
EDS	Energy dispersive X-ray spectra
ESEM	Environmental scanning electron microscopy
XRD	X-ray diffraction
DLS	Dynamic light scattering
FTIR	Fourier transform infrared spectra
VSM	Vibrating sample magnetometry
FBS	Fetal bovine serum
AB	Alamar blue
PBS	Phosphate buffered saline
FACS	Fluorescence-activated cell sorting
cLSM	Confocal laser scanning microscopy
DAPI	4',6- diamidino-2-phenylindole
PCL	Polycaprolactone
SLP	Specific loss power
AMF	Alternating magnetic field
MnIO	Manganese substituted SPION
MnIOTC	Trisodium citrate modified MnIO

## SYNOPSIS

In general nanotechnology deals with the engineering or manipulation of materials with structural features in between those of atoms and bulk materials, which has applications in the real world. The term “nano” relates to the scale of size in nanometers [ $1\text{nm} = 10^{-9}\text{m}$ ] of small particles which serve as the fundamental building blocks for intended application.

Nanoparticles are defined as particles with size in the range of 1 to 100nm at least in one of the three dimensions. In this size range, the physical, chemical and biological properties of particles change in fundamental ways. It differs from the properties of molecular sub-units or its corresponding bulk material.

Nanoparticles play a major role in many fields of medicine especially in diagnosis, therapeutic and regenerative medicinal applications. The basic unit of biological systems are cells that are approximately 10 microns in size with intracellular proteins in the 5nm range. This is comparable with the dimensions of the smallest synthetic nanoparticles. Understanding of biological processes at the nanoscale level is a strong driving force behind development of nanotechnology for clinical and biological applications.

During the last one decade, several nanoparticles have been synthesised and evaluated successfully for different biomedical applications. Among them, magnetic nanoparticles are considered as a potential candidate due to their unique magnetic properties. Less than 100nm size, these particles exist as a single magnetic domain and respond to the direction of magnetic moment at room temperature. This type of

magnetism is termed as superparamagnetism. Several materials that exhibit superparamagnetic property exist. With magnetite particles gaining considerable attention due to their all round performance and were termed as superparamagnetic iron oxide [SPION]. In biomedical applications, SPION usage has been reported as targeted drug delivery, cell therapy, gene therapy, non-invasive biomolecule controlling, MRI contrast agent, hyperthermia therapy and theranostic applications.

SPIONs have been evaluated by numerous authors on their multi-faceted applications. There is still a lack of distinct information on magnetic nanoparticles development, surface modification and magnetic property alterations to fit actual clinical needs and address biological safety issues.

One of the major problems associated with SPIONs are their instability in colloidal condition due to the large surface area along with poor surface charge potential. As a result the particles aggregate and form large clusters. Aggregates perform sub-optimally when compared to uniform colloidal suspension of nanoparticles. Aggregated particles resist cellular uptake, promote clearance *via* the reticuloendothelial system and generate uncontrolled temperature variations in hyperthermia applications. Thus cell separation, therapeutic application of guided delivery; contrasting applications in MRI are rendered non – feasible. To reduce the aggregation potential, several molecules and crystals were studied as surface protection and stabilization agent for SPIONs. Among them, use of an inorganic matrix, hydroxyapatite (HA), was recognized as effective for imparting surface modification. HA surface modification was proposed to regulate the magnetic property of SPION *via* its nonmagnetic nature.

The magnetic nanoparticle should have good magnetic susceptibility and magnetic response for diagnostic and therapeutic application. However, common spinel ferrites SPIONs have intrinsic magnetic properties with standards far below than optimum. In order to improve their magnetic property, the best method is to substitute  $\text{Fe}^{2+}$  ions in the SPIONs crystal with a biocompatible magnetic ion having maximum magnetic moment. The 'd' block elements such as Co, Ni, Mn, Zn and Cu were evaluated and Mn identified as a suitable candidate for substitution. Thermal decomposition, microemulsion, hydrothermal and sonochemical processes were reported for ionic substitution in SPIONs. In these techniques, particles obtained are hydrophobic due to the non-polar hydrocarbon molecules at the surface and therefore are insoluble in aqueous media.

Main requirements for a MRI contrast agent are aqueous dispersion ability and colloidal stability. The relaxivity of nanoferrites are based on the ease of its surface contact with water molecules and proton relaxation. Also unstable ferrite particles get aggregated and act as a ferromagnetic system, which would adversely affect the application in targeted delivery and therapy. Hence a stable surface modification is essential for nanoferrite particles which can impart high aqueous dispersion ability and colloidal stability.

In a conventional route, the biocompatible polymeric molecules were used for nanoferrite stabilization. However due to the weak interactions like hydrogen bonding and physical force surface interactions, the polymeric molecules may easily detach from the nanoparticles surfaces under harsh *in vivo* condition. The recent studies revealed that inorganic molecule like trisodium citrate can possibly be

used as a dispersion agent which form stable chemical bonding to nanoparticle surface and act as a suitable nanoferrite stabilizer.

Based on an exhaustive literature review and current work in the biomedical field, our **main objectives** were defined as follows

1. To prepare surface modified superparamagnetic iron oxide particles *via* an aqueous method.
2. To evaluate the magnetic field guided cell delivery and culturing *via* magnetic nanocomposite.
3. To explore the feasibility of above nano particles for therapeutic hyperthermia & MRI contrast enhancement.
4. To enhance theranostic [MRI contrast and hyperthermia] properties of SPION *via* aqueous crystal modification and stabilization.

The thesis is divided into following chapters: Introduction, Literature Review, Materials and methods, Results and Discussion, Summary and Conclusion.

## **Chapter 1- Introduction**

This chapter provides an introduction to the field of nanotechnology, nanoparticles, importance of magnetic nanoparticles and up to date details of its potential applications. Major part deals with the current challenges, modification of nanoparticles and limitation associated with SPIONs. The demand for crystals substitution, surface modification along with stability, efficiency and compatibility issues are addressed. An introduction to stable surface coating and its importance in

application level is also discussed. Further the magnetic metal ion substitution into SPION crystal and its relevance in therapeutics has been discussed.

## **Chapter 2- Literature review**

The literature review addresses the field, tracing out the origin and importance of SPION and to its potential biomedical applications. The use of Magnetic Resonance Imaging as a diagnostic tool, role of nanoparticle contrast agents, nanoparticle application in cell manipulation, 3D culturing & SPION based hyperthermia applications have been addressed. More over the development of different preparation methods of SPION, their surface modification and limitations, importance of inorganic moiety stabilizers are also described. The crystal substitutions for magnetic property improvement were addressed along with the emergence novel processing methods.

## **Chapter 3 – Materials and Methods**

### **3.1 Synthesis of superparamagnetic iron oxide embedded hydroxyapatite composites [HAIOs] and SPION**

The synthesis of HAIO has been carried out by co-precipitating iron salt and calcium phosphate precursors in alkaline medium. The iron salts were taken in such way as to get a molar ratio of ferric and ferrous 1:2. The  $\text{Ca}(\text{NO}_3)_2 \cdot 4\text{H}_2\text{O}$  and  $(\text{NH}_4)\text{H}_2\text{PO}_4$  solutions were taken in such a way as to get the Ca/P ratio of 1.67. The calcium solution was mixed with iron salt precursors and deoxygenated at elevated temperature. Followed by increases the pH of solution *via* addition of 25% ammonia solution along with  $(\text{NH}_4)\text{H}_2\text{PO}_4$ . The precipitate was washed, freeze dried and

characterized. The HAI0 samples having weight percentage ratios of 10–90 were synthesised using the same method. In an ascending order of iron oxide weight percentage in the composite, the samples are termed as HAI010, HAI020, HAI030, HAI040, HAI050, HAI060, HAI070, HAI080 and HAI090. Bare SPION was also prepared using a co-precipitation method.

#### Physicochemical characterization of HAI0s and SPION

High-resolution TEM (HRTEM) along with EDS and ESEM along with EDS analysis was performed to evaluate the morphology, particle size, and composition analysis. The phase purity of crystals was analyzed using an X-ray diffraction and functional group analysis using FT-IR technique. The size and zeta potential measured by DLS measurement and magnetic property analyzed through VSM technique.

#### Biological evaluations of HAI0s and SPION

The cell *viability* and haemocompatibility of HAI0s and SPION were analyzed *via* MTT assay, alamar blue assay and hemolysis analysis studies in various concentrations. Cell uptake of HAI0s was assessed through Prussian blue staining. Further; HAI0 particles post exposed cellular response was evaluated by flow cytometry, phase contrast light microscopy and confocal laser scanning microscopy.

#### 3.2 Cell separation or manipulation and its culturing

HeLa cells were treated with HAI0 particles and were concentrated and separated from suspension *via* an external magnetic field. The separation efficiency, cellular morphology, *viability* were evaluated by various techniques such as coulter counter

cell counting, UV transilluminator, cLSM and ESEM. Further the separated cells were cultured under *in vitro* condition and assessed the cell proliferation, morphology and cytoskeleton structures.

### 3.3 Three dimensional model cell culture using HAIO and HAIO based magnetic microsphere

The HAIO incorporated cells were levitated with the aid of external magnetic field and cultured in a 3D model under *in vitro* condition. Cells proliferation, morphology, cytoskeleton structure has been evaluated. Further the magnetic microspheres were developed using HAIO and polycaprolactone through solvent evaporation technique. The developed microspheres were characterized using physicochemical techniques such as SEM, XRD, and FTIR and followed by carried out biological evaluations cytotoxicity and hemolysis. Moreover these microspheres were used for magnetic levitated 3D cell culture system and evaluated the morphology, *viability* and cytoskeleton.

### 3.4 Theranostic evaluation of HAIO [Magnetic hyperthermia and MRI contrast agent]

Evaluation of hyperthermia: Hyperthermia potential of various concentrations of HAIO was investigated using Ambell Easy Heating system and measured the time-temperature profile and specific loss power [SLP]. Hyperthermia efficiency of HAIO to cancer cells destruction was assessed under *in vitro* condition. The cell death was estimated through flow cytometry and ESEM techniques.

Evaluation of MRI contrast: Contrast efficiency of HAIO in MRI imaging was measured by aqueous phantom studies under 1.5T clinical MRI system. Relaxivity coefficient and *in vitro* pixel intensity variation of HAIO were also calculated.

### 3.5 Synthesis of manganese [Mn<sup>2+</sup>] substituted SPION crystals [MnIO]

The Mn<sup>2+</sup> substituted SPIONs were synthesized using aqueous co-precipitation method. The experimental procedure was repeated for various molar compositions of Mn<sup>2+</sup> to Fe<sup>2+</sup> ratios of 1:3, 1:1 and 3:1 keeping the concentration of ferric salt solution constant, (represented as MnIO25, MnIO50 and MnIO75, respectively). Bare SPIONs were prepared according to a previously reported procedure using ferrous and ferric chlorides in a 1:2 molar ratio under the same reaction conditions.

Physicochemical characterizations: The crystal structure, particle size, morphology were analyzed by using XRD, HRTEM and ESEM techniques. Further chemical composition identified through ICP-OES and EDS analysis and the chemical bonding evaluated by FT-IR spectroscopy. Followed by the chemical decomposition, magnetic properties, surface potential, hydrodynamic sizes were measured through TG-DTA, VSM, DLS techniques.

Biological evaluation: Cytotoxicity, haemocompatibility and cellular uptake of MnIOs were measured through Alamar Blue assay, hemolysis test, and Prussian blue staining respectively. The MnIOs post exposed cell morphology and cell *viability* were examined using cLSM, ESEM and light microscopic techniques.

### 3.6 MRI contrast efficiency of MnIOs

The relaxivity coefficients of MnIOs were measured *via* aqueous phantom studies. Various concentrations of MnIOs dispersed in deionized water and carried out the MRI phantom studies. Followed by the pixel intensity of images plotted against concentration of material and calculated the relaxivity.

### 3.7 Colloidal stabilization of MnIOs by surface modification and theranostic evaluation [MRI contrast and hyperthermia therapy]

In order to stabilize the MnIOs in colloidal condition; particles were surface modified *via* trisodium citrate molecules and termed as MnIOTCs. Stabilized particles were characterized using TEM, SEM, TG-DTA, FT-IR, and VSM techniques. MnIOTCs biocompatibility was studied through assessing the cytotoxicity, hemolysis, cell uptake, material exposed cytoskeleton evaluations.

MRI contrast analysis: The relaxivity of MnIOTCs were calculated using MRI aqueous phantom experiment. The MnIO75TC was selected and conducted *in vitro* cellular MRI studies.

Hyperthermia study: to evaluate the heating efficiency of MnIO75TC, sample was subjected to an alternating magnetic field, time-temperature profile observed and SLP values calculated. Ability of hyperthermia mediated by MnIO75TC to induce cell death in a cancer cell line was examined under *in vitro* condition and characterized using flow cytometry, cLSM, ESEM techniques.

## Results and discussion (Chapter 4 & 5)

A homogeneous dispersion of Superparamagnetic iron oxide nanoparticle embedded in hydroxyapatite (HAIO) particles were synthesised by a co-precipitation method. The *in-situ* generated dispersion of the composite powders showed nanosize HA particles with ~5 nm sized superparamagnetic iron oxide embedded inside. The XRD phase analysis results revealed the presence of HA and SPION with no tertiary phase. The ascending molar compositions [SPION concentrations] such as 10, 20, 30, 40, 50, 60, 70, 80 and 90 were developed using same method and labelled as HAIO10, HAIO20, HAIO30, HAIO50, HAIO60, HAIO70, HAIO80 and HAIO90. Depending on the molar concentration of SPION with respect to HA, the enhancement of corresponding crystal relative peak intensities in XRD demonstrated the phase pure formation of crystals. HRTEM and SEM results of the HAIO composite having lesser content of SPION shows needle like nanocrystal and on increasing the SPION concentration the particle morphology gradually changes from needle form to spherical shape. In FTIR spectra, characteristic phosphate peaks indicating the HA crystal and peaks at  $572\text{ cm}^{-1}$  confirm the presence of magnetite phase of SPION. EDS spectra, ICP-OES analysis confirms molar compositions and VSM measurement demonstrated the superparamagnetic property of HAIOs. Biological evaluation *via* MTT assay, Alamar Blue assay, Hemocompatibility, blood cell aggregation tests, Prussian blue staining, material exposed flow cytometric analysis, and cytoskeleton evaluations demonstrated that the HAIOs are non - toxic in nature. However our interest was on lesser content of SPION embedded HA

crystals having good magnetic property and compatibility, which was observed in HAlO50 and was selected for potential application studies such as cell therapy, MRI contrast and hyperthermia.

In a cell therapy, efficient delivery of cells to targeted sites at optimal concentrations within rational limits of damage to normal tissue is a major challenge. Cell conjugated magnetic nanoparticles enable external field based mobility & location management in biological systems. Based on these studies, the HAlO50 was selected for separation of cells and the concentration of HAlO50 for efficient cell separation was optimized. The magnetically separated cells were cultured and evaluated the proliferation, viability and cytoskeleton structure. In order to explore the possibility of cell manipulation and control, the HAlO50 tagged HeLa cells were levitated using an external magnetic field and cultured in a 3D model condition. The cells morphology, proliferation and structures were assessed through ESEM, cLSM and light microscopy. The results demonstrated that HAlO50 can be considered as an ideal vehicle for 3D model cell culturing. Moreover magnetic microspheres were made with the aid of polycaprolactone in a solvent evaporation technique. The structure, shape and chemical bonding were confirmed by XRD, FTIR and ESEM analysis. Alamar Blue assay, hemolysis and cell adhesions tests affirmed the cell friendly nature of microspheres. Furthermore, cells attached to magnetic microspheres were used for 3D culturing *via* magnetic levitation. These cells were characterized using ESEM & fluorescent microscopy. The results suggested that the magnetic microspheres are useful for tissue engineering application.

Hyperthermia efficiency of SPION & HAIO50 was measured using Ambell Easy induction heating system at various concentrations. The SLP values of materials were calculated using time temperature profiles. HAIO50 showed controlled temperature generation due to the nonmagnetic HA surface coating over SPION. Effects of particle mediated hyperthermia on cancer cell lines was examined under *in vitro* condition and characterized using FACS and ESEM techniques. The results revealed that more than 75% of cells were non – viable with reduced cellular integrity. It was found that the HAIO50 based hyperthermia induced cell death *via* apoptosis and not *via* necrosis. The MRI contrast effect of HAIO50 was examined in aqueous phantom study and the relaxivity constant was calculated. Also *in vitro* cellular imaging has been carried out with various concentrations of HAIO50. The results demonstrated that HAIO50 can possibly be used as a contrast agent in MRI. The combined effect of MRI contrast efficiency and hyperthermia property suggested that HAIO50 may be considered as a future theranostic agent for cancer treatment.

In order to improve the contrast effect in MRI technique of spinel ferrite, an *in situ* substitution of  $Mn^{2+}$  was performed in SPION and a series of ferrite particles,  $Mn_xFe_{1-x}Fe_2O_4$  with a varying molar ratio of  $Mn^{2+} : Fe^{2+}$  where ‘x’ varies from 0–0.75 were developed. Manganese substituted ferrite nanocrystals (MnIOs) were synthesized using a novel, one-step aqueous co-precipitation method based on the use of a combination of sodium hydroxide and trisodium citrate (TC). This approach yielded the formation of highly crystalline, superparamagnetic MnIOs with good control over their size and bivalent Mn ion crystal substitution. Primary

characterizations such as structural, chemical and magnetic properties demonstrated the successful formation of manganese substituted ferrite. More significantly, the MRI relaxivity of the MnIOs improved fourfold when compared to SPION crystals imparting high potential for use as an MRI contrast agent. Further, the cytocompatibility and blood compatibility evaluations demonstrated excellent cell morphological integrity even at high concentrations of nanoparticles supporting the non-toxic nature of nanoparticles.

However the poor surface potential of MnIOs showed instability in aqueous system. Hence their surfaces were modified using trisodium citrate molecules and termed as MnIOTCs. The MnIOTC was analyzed by physicochemical and biological characterization techniques. Size distribution calculation from TEM and SEM morphological analysis suggests that the particle size is below 20nm. Further, the FTIR, TGA, DLS and zeta potential measurements support the presence of citrate molecule on the crystal surface. XRD and SEM-EDS patterns confirmed the phase pure spinel structure. Superparamagnetic property of MnIOTCs was measured by vibrating samples magnetometer. Materials on evaluation exhibited good cytocompatibility & hemocompatibility. Upto 75 %  $Mn^{2+}$  substituted ferrites having good magnetic property and stability was prepared. This was obtained in the molar concentration of  $Mn^{2+}$  to  $Fe^{2+}$  as 3:1 and it termed as MnIO75TC and selected for theranostic evaluations. MnIO75TC exhibited high  $T_2$  relaxivity of  $184.6 \text{ mM}^{-1}\text{s}^{-1}$  in MRI phantom experiment and showed excellent signal intensity variation in the *in vitro* cell studies. Hyperthermia *via* application of an alternating magnetic field to MnIO75TC in a HeLa population induced apoptosis. FACS evaluation and post-

hyperthermia imaging by confocal laser scanning microscopy confirmed the observation. ESEM imaging showed significant disruption in the morphological structures in post-hyperthermic cells. The potential of MnIO75TC for contrast enhancement in MRI and hyperthermia therapy was demonstrated confirming its utility in the burgeoning field of theranostics.

## **Chapter 6- Summary & Conclusion**

Novel SPION embedded hydroxyapatite nanocomposites [HAIOs] were developed which showed excellent stability in aqueous medium, optimum responses to the external magnetic field and non toxicity under *in vitro* condition. The HAIO50 exhibit high concentration of cellular uptake and can be guided through a magnetic field and can be used for high through put cell culture system in a 3D model *via* magnetic levitation. HAIO50 demonstrated stable hyperthermia temperature generation and good contrast effect in MRI technique. Further manganese substituted iron oxide nanoparticles were synthesized *via* an aqueous co-precipitation method. The surface modified manganese ferrite particles showed excellent contrast effect in MRI imaging and hyperthermia therapy. Thus we have developed surface modified and stabilized two superparamagnetic nanoparticles [HAIO and MnIO] for functional biomedical applications.

# Chapter 1

## INTRODUCTION

### 1.1 Nanotechnology

Nanotechnology is technology at the nanoscale. It involves the creation and development of materials with structural features in between those of atoms and bulk materials, which has applications in the real world. The term “nano” refers to the scale of the observed area in nanometer [ $1\text{nm} = 10^{-9}\text{m}$ ]. The importance of nanotechnology was pointed out by Feynman as early as 1959, in his often-cited lecture titled “*There is plenty of room at the bottom*” (Feynman, 1960). Properties of materials of nanometric dimensions are importantly varied from those of atoms as well as those of bulk materials (Varadan, 2010). Modulation of structural properties of materials at the nano scale can lead to new science as well innovative devices and advanced technologies. The underlying theme of nanotechnology is miniaturization. It covers the production and application of physical, chemical and biological systems as size scales, ranging from individual atoms or molecules to submicron dimensions as well as the integration of the resulting nanostructure into larger systems. There has been an explosive growth of nanoscience and technology in the last few years, as new strategies for the synthesis of nanomaterials and new tools for characterization and manipulation have been developed. There are many examples to determine the current creation and paradigm shifts in this area. Evolving surface qualities as compared with volume of materials plays an ever increasing role, and the cumulative quantum physical effects must be given adequate consideration in nanotech.

In the last decade nanotechnology based interventions have been at the forefront of engineering, medical and biological fields of research and application. Improvement of existing technologies, development of new techniques and cost effective delivery of the same is expected from nanotech based applications.

In the biomedical field it is poised to make potentially revolutionary innovations in the theranostics & imaging (Labhasetwar and Leslie-Pelecky, 2007). Nanotechnology based diagnostic tools can detect abnormalities even at molecular level that potentially lead to disease progression. Nanoparticles serve as the key building blocks in several applications, improving on specification and accuracy.

## **1.2 Nanoparticles**

Nanoparticles are defined as particles in the range of 1 to 100nm at least in one of three dimensions. Nanomaterial properties based on the “size effect” are most intriguing to researchers. The effects determined by size relate to the evolution of structural, thermodynamic, electronic, spectroscopic, electromagnetic and chemical features of these finite systems. In nanosize range, the particle’s physical, chemical and biological properties change in fundamental ways from properties of atoms/molecules and of the corresponding bulk material. Nanoparticle structure and properties play a key role in fundamental studies and practical applications in a range of disciplines (Rotello, 2012a).

Nanoparticles can be made of materials of distinct chemical nature, the most common being metals, metal oxides, polymers, silicates, non-oxide ceramics, organics, carbon and biomolecules. Nanoparticles exist in various morphologies such as cylinders, spheres, platelets, tubes etc. Normally, they are designed with surface

modifications to meet the needs of specific applications. The extended diversity of the nanoparticles arise from their disparate chemical origins, shapes and morphologies, medium of dispersion, state of dispersion and the possible surface modifications, which make this an important field of science (Nogi et al., 2012).

At the nanoscale, particle surfaces indicate the presence of a high fraction of constituent atoms/molecules. Thus the material exhibits a large surface area to unit volume ratio. Nanoparticles display interesting optical properties since the absorption and/or emission wavelengths can be controlled by particle size and surface functionalization. Whenever the nanoparticle size is below the critical wavelength of light, then transparency can be achieved. The chemical nature and size of the nanoparticle control the ionic potential or electron affinity and thereby the electron transport properties. Further, in some metal and metal oxides, decrease in particle size results in improved magnetic property. Metal nanoparticles are considered to be the building blocks of the next generation of electronic, optoelectronic and chemical sensing devices (Rotello, 2012b).

Nanoparticles are broadly classified into two types, organic: and inorganic molecule-based systems. Major issue associated with organic molecule-based nanoparticles in contrast to inorganic systems during application in the biomedical field are:

(i) Oral route non - tolerance (ii) Poor encapsulation efficiency, (iii) Outflow of water-soluble drugs in the presence of blood components, (iv) Batch-to-batch reproducibility issues (v) Aggregation and poor storage stability (vi) Difficult scale-up processes & (vii) Toxicity (Fuente and Grazu, 2012).

Mainly there are two techniques for the development of inorganic nanoparticles; the first one is ‘top-down’ approach, which involves breaking down large pieces of material, generally by attrition or milling, to generate nanoparticles. Etching and lithography are probably the most typical examples of this approach. But the biggest problem of the ‘top-down’ approach is the heterogeneity of the resulting product. Particles produced in this way usually present broad size distribution and varied particle shape. They might contain a significant amount of impurities from the milling medium. Also, the material surface presents important defects and crystallographic damage. The second approach is known as ‘bottom-up’ and implies assembling single atoms and molecules into larger nanostructures. In this way, we have a better chance to obtain particles with less defects, more homogeneous chemical composition and narrower size and shape distribution. There are several inorganic nanoparticles such as gold, iron oxide, carbon nanotubes and quantum dots etc. reported in different ways of synthesis-based on their application potentials (Rotello, 2012b), (Cao and Wang, 2011).

### **1.3 Importance of Nanoparticles in the Biomedical Field**

Nanoparticles are projected to play a major role in the biomedical field, especially in diagnosis, therapeutic and regenerative medicine applications. The basic unit of biological system are cells and is approximately 10 microns in size. Even the intracellular proteins size with a typical size of just 5 nm, are comparable with the dimensions of the smallest manmade nanoparticles This simple size comparison gives an idea of using nanoparticles as very small probes that would allow us to spy

on cellular machinery without introducing too much interference (Wang et al., 2012), (Treuel et al., 2013).

In-depth understanding of biological processes at the nanoscale level is fuelled by advances in nanotechnology. There are several reports on nano-engineered tissue scaffolds and nanostructured biomaterials and coatings for implants and prostheses for tissue design, reconstruction, and reparative medicine (Liao et al., 2008), (Khademhosseini et al., 2010). In bone implants, a smooth surface is likely to cause production of a fibrous tissue covering the surface of the implant. This reduces the bone - implant contact, resulting in loosening of the implant and leads to implant failure. Nano-sized features on the surface of implants could reduce the chances of rejection as well as stimulate the attachment and proliferation of osteoblasts (Bose et al., 2012),(Lv et al., 2013). Nanoparticles have potential applications in drug delivery systems, as it's possible to deliver minimum quantity of drugs to a specific site *via* targeted delivery. The fluorescent nanoparticles such as quantum dots, gold nanoparticle and magnetic nanoparticle have been reported for diagnostic purposes. These particles have showed excellent photo stability, narrow range of emission, broad excitation wavelength, and multiple possibilities of modifications. Nanoparticles aid in specific site based *in vivo* imaging. Surface engineered nanoparticles have been studied for early detection of cancer cells (Nune et al., 2009). Also, the gold and carbon nanotube crystals under NIR laser, magnetic nanoparticles under alternating magnetic field can generate heat energy and is useful for noninvasive cancer therapeutic purposes (Shi Kam et al., 2004).

Recently, the theranostics approaches to treatment have evoked interest in interventional medicine. Theranostics is based on using drugs or specifically developed methods for simultaneous diagnosis and treatment. The integrated nano - therapeutic system which can diagnose, deliver targeted therapy and monitor the response to therapy is envisaged. It is assumed that a combined technique will result in the acceleration of drug development, improved disease management and reduce risks at decreased cost. Prime causes of mortality and morbidity require targeted approaches as described above at the earliest. (Yoo et al., 2011), (Ho et al., 2011).

#### **1.4 Magnetism and Superparamagnetic Nanoparticles**

Magnetic materials are those materials that show a response to an external magnetic field. Depending on the nature of response, they are mainly classified into paramagnetic, diamagnetic, ferromagnetic, anti - ferromagnetic and ferrimagnetic. In paramagnetic materials, magnetic domains are absent and the magnetic moments are generated by unpaired electrons. These materials do not retain magnetic property after the removal of the external magnetic field. A diamagnetic material has no unpaired electron and shows zero net magnetic moment under external magnetic field. In the case of ferromagnetic materials, atoms have net magnetic moment due to unpaired electron. Also, the materials composed of domains [a region having uniform direction of magnetization] and each domain containing large number of atoms, whose magnetic moments are parallel to producing a net magnetic moment and a residual magnetic moment exists even after the removal of the external magnetic field. The antiferrromagnetic materials are compounds of two different atoms that occupy different lattice positions, which have equal magnetic moment

with opposite directions and the net magnetic moments becomes zero. Ferrimagnetic materials having different atoms reside on different lattice sites with anti - parallel magnetic moment and shows net magnetism in the presence of external magnetic field(Coey, 2010), (Jiles, 1998).

Ferromagnetic particles which are less than 100nm size exhibit a special type of magnetism termed as “superparamagnetism”. In this size the coercivity drops down which results in corresponding reduction in anisotropy energy with size. The anisotropy energy, which holds the magnetization along an easy direction is given by the product of the anisotropy constant,  $K$ , and the volume,  $V$  of the particle. As the volume gets reduced,  $KV$  becomes comparable to the thermal energy,  $k_B T$ . As a result, the thermal energy can overcome the anisotropy “force” and spontaneously reverse the magnetization of a particle from one easy direction to the other, even in the absence of an external magnetic field. This phenomenon is termed as *superparamagnetism*. The magnetic moment of superparamagnetic particles is so much larger than that of atoms. Iron oxide particles contain magnetite and maghemite phases. At nanosize iron oxide particles are superparamagnetic in nature. Superparamagnetic nanoparticles have considerable interest in the biomedical field compared to other types of nanoparticles (Getzlaff, 2007), (Alez, 2012).

## **1.5 Potential Application of Superparamagnetic Nanoparticles in the Biomedical Field**

### **1.5.1 Targeted Cell Therapy**

Tissue Engineering depends on targeted delivery of cells & cellular components and facilitators as part of path breaking Regenerative Medicine applications. However,

the treatment modality faces several problems due to the lack of specificity and targeting ability. The SPION shows excellent response to external magnetic field guidance in a non-invasive manner. SPIONs utilization has been reported for several targeted drug delivery, gene delivery and therapeutic agents. Cells combined with magnetic nanoparticles can be easily guided, concentrated and delivered to a selected area. This could address the non-essential accumulation of administered therapeutic cells and ensures better efficiency (Gupta and Gupta, 2005), (Parsa et al., 2015).

### **1.5.2 Diagnostic Tool- Magnetic Resonance Imaging (MRI) Contrast Agent**

MRI is a premier non – invasive imaging technology utilized in the clinical diagnosis of disease. Imaging proficiency is adequate to obtaining tomographic images of living subjects with high spatial resolution as a result of perturbation of tissue water protons in the presence of an external magnetic field (Westbrook, 2014).

Among existing imaging tools, new and amended techniques are continuously deployed. Implementation of new imaging technologies in an accessible diagnostic environment requires massive investment in terms of time, cost & skill acquisition. Development of accessories that maximize existing devices or image tools are therefore preferred (Na et al., 2009). A highly efficacious add-on is an imaging probe or contrast agent, which is innovative to amend its visibility in the image. Superparamagnetic iron oxide (SPION) shows excellent contrast enhancement in MRI images. As these particles have large value of magnetic susceptibility, which can generate large magnetization in local area and can alter the spin-spin ( $T_2$ ) relaxation of environmental protons. This property creates good contrast enhancement

in MRI images and is possible to ease disease diagnosis (Lee et al., 2006),(Wang et al., 2001).

### **1.5.3 Therapeutic Agent – Magnetic Hyperthermia Cancer Treatment**

Hyperthermia therapy involves exposure to slightly higher temperatures, to damage, kill or make cancer cells more sensitive to the effects of radiation & chemotherapy. Cancer cells with inherently poor heat shock protein activation are susceptible to temperature fluctuations. Hyperthermia *via* traditional methods may lead to uncontrolled temperature generation and cause collateral damage to normal tissues.

Localized cancer therapy mediated by magnetic nanoparticles is therefore possible. Reducing collateral tissue damage results in lack of side effects and ensures delivery of therapy to targeted cell population alone. Superparamagnetic nanoparticles targeted to tumor tissue are excited at the target site *via* application of an alternating external magnetic field. This induces controlled temperature generation at desired site inducing apoptosis in malignant cells (Kobayashi, 2011), (Giustini et al., 2010).

### **1.6 Limitation of the Current Approaches**

The use of magnetic nanoparticles has been explored in several studies in the biomedical field. However there is a serious deficit of information in the development, stabilization and magnetic property modifications of magnetic nanoparticles aimed at the biomedical niche. The major limitations are outlined below.

1. Biomedical and Bioengineering applications require high magnetization values and particle size smaller than 100nm. Size distribution should be narrow to ensure

that the particles showed uniform physical and chemical properties. Lack of stability of particles in colloidal solutions is a grave issue. Aggregation is prominent in cases where particles have a large surface area coupled with poor surface potential leading to increased hydrophobic interactions. In these cases the van der Waals forces between particles are greater than electrostatic repulsive forces produced by the nanostructure surface. This causes the particles to form large clusters and increase measured particle sizes. In the case of iron oxide nanoparticles these clusters exhibit strong magnetic dipole -dipole interactions and showed ferromagnetic behaviour (Mohamed, 2014), (Hu and Apblett, 2014).

2. The Reticular Endothelial System (RES) is an immune system component, utilizing macrophages, monocytes, Kuffer cells, spleen and the lymphatic system to remove foreign bodies. Nanoparticles with poor surface potential and high aggregation rates are more prone to clearance *via* the RES. Anomalous surface charge on particles may impede circulation *via* occlusion of circulatory vessels (Longmire et al., 2008), (Singh et al., 2010).

3. Cellular manipulation *via* nanoparticles is based on the ability of the particles to remain in suspension with non-significant levels of aggregation. Cells conjugated with nanoparticles *via* surface charge interaction can be guided by a non-invasive magnetic field. In case of nanoparticle aggregation, the surface potential decreases to zero and causes failure of cell surface interactions. This lack of colloidal stability may lead to failure of cell – manipulation procedures. (Kolosnjaj-Tabi et al., 2013), (Yang et al., 2012).

4. When nanoparticles in suspension are placed in the presence of an alternating magnetic field, hyperthermia generation is induced. Heat generated *via* this process depends on the magnetic identity of the particles involved. Aggregated particles with strong interaction exhibit ferromagnetic nature. It retains magnetic property even in the absence of external magnetic field. Non-aggregated particles exhibit superparamagnetic nature in an alternating external magnetic field and does not retain magnetic property in the absence of an applied field. Moreover, for hyperthermia applications aggregated particles materials are not preferred due to possible overheating. This could damage non – malignant tissues. (Lao and Ramanujan, 2004), (Yoo et al., 2011).

5. Surface modifications are widely utilized to improve stability of nanoparticles in solution. Conventional approach uses coatings based on biocompatible polymers. However, due to the weak interactions like hydrogen bonding and opposite charged physical surface interactions, the polymeric molecules may detach under harsh *in vivo* condition. (Moghimi et al., 2001),(Gupta and Gupta, 2005), (Zhang et al., 2002).

6. The most essential property of magnetic nanoparticles for biomedical applications is good magnetic property and excellent field response. However, common spinel ferrite SPION has intrinsic magnetic property far below that of the optimal level. To improve efficiency; modifications are incorporated during the synthesis process. One among the best techniques for magnetic property modification is crystal ion substitution with appropriate candidate. Several d-block elements are suitable for ionic substitution. However, based on elemental toxicity, hydrophobic nature, & leaching property a suitable candidate has to be selected. Furthermore, various

methods have been evolved for preparing iron oxide crystal modification. Conventional techniques are non-polar or organic solvent based high temperature decomposition. The hydrophobic hydrocarbon molecules at the surfaces of nanoparticles inhibit proper dispersion in polar solvents. Hence, the current challenge in this area is to develop a novel synthetic method for aqueous dispersed magnetic particles with enhanced magnetic properties (Sun et al., 2004), (Pereira et al., 2012).

This thesis is a detailed investigation into the development of superparamagnetic iron oxide particles in an aqueous condition, followed by addition of a stable surface protection *via* an *in-situ* technique. These surface modified magnetic nanocomposite particles are used to assess potential applications such as cell manipulation, 3D model cell culture & theranostics. Crystal substitution is executed and examined *via* detailed characterizations. The substituted particle was also evaluated for application in theranostics.

### **Hypothesis**

Surface modified and stabilized superparamagnetic nanoparticles for biomedical applications.

### **Objectives of the Study**

SPION's with surface modifications *via* aqueous *in-situ* technique have not been widely reported. Reported abilities include drug delivery and gene delivery applications. However cell concentration, site targeting, regenerative medicine applications and 3D culture methods have not been widely explored. Also reports of magnetic hyperthermia and MRI contrast agent applications have not been

investigated in detail. This study undertakes a closer look at controlled temperature generation, mechanism of cancer cell destruction and corresponding MRI contrast efficiency.

The study aims to address the concerns above *via* the following pathways:

- 1. To prepare surface modified superparamagnetic iron oxide particles via an aqueous method.*
- 2. To guide cell delivery and culturing via magnetic nanocomposite.*
- 3. To explore theranostic properties such as therapeutic hyperthermia and MRI contrast enhancement.*
- 4. To enhance theranostic properties of superparamagnetic iron oxide particle via aqueous crystal modification and stabilization.*

The thesis has been divided into six chapters for a holistic overview of the problem at hand. Chapter 1 provides a brief glimpse at the terminology, technology and the major issues in play. Chapter 2 undertakes a comprehensive literature analysis, covering technical approaches, current limitations and possible avenues of approach backed up with latest citations. Chapter 3 lays down the protocols used through out the study, details of techniques developed and parameters of experimental design. Chapter 4 lays out the results and observations gleaned from experimental analysis in prescribed formats, with critical discussion of results making up Chapter 5. Chapter 6 draws together important findings of this study, provides comparison with the current state of the art and teases out new directions for the work ahead.

## Chapter 2

### LITERATURE REVIEW

#### 2.1 Superparamagnetism and Superparamagnetic Iron Oxide Nanoparticles

##### [SPION]

The scale of reduction in materials shows changes in their basic structure, which in turn greatly modifies the electronic, optical and magnetic properties (Varadan, 2010). Generally, considering magnetic materials, ferromagnetic substances exhibit permanent magnetic properties. This is because of the large number of magnetic domain [magnetic domain: the small area of material having same direction of magnetization] are aligned in an easy direction. On decreasing the particle size, the numbers of domain formations decrease. At less than 100nm particle size it acts as a single domain. Frenkel and Dorfman were the first to predict that a ferromagnetic material below a critical size would consist of a single magnetic domain. From the Neel and Brown theories, these particles' magnetization vector can change its orientation with the aid of thermal fluctuation (Getzlaff, 2007). When the size of the magnetic particles is small enough, then the anisotropy energy becomes comparable to the thermal energy. The thermal instability of magnetization gives rise to *superparamagnetism*. *Superparamagnetism* is defined as a form of magnetism, which appears in small ferromagnetic or ferrimagnetic nanoparticles. Particles can randomly flip direction under the influence of temperature and their susceptibility is between that of ferromagnetic and paramagnetic materials (Alez, 2012). The term superparamagnetism was first introduced by Bean and Livingston in 1959. Iron oxide

particles having less than 100nm size exhibit superparamagnetism and are termed as superparamagnetic iron oxide nanoparticles [SPION] (Bean and Livingston, 1959).

SPION exist as inverse spinel structure containing ferrous [ $\text{Fe}^{2+}$ ] and ferric [ $\text{Fe}^{3+}$ ] ions. The basic crystal structure is formulated by thirty two oxygen anions forming a face-centred cubic unit cell. The iron atoms are situated on 8 tetrahedral sites (surrounded by four oxygen ions) and 16 octahedral sites (surrounded by 8 oxygen ions). The tetrahedral sites are exclusively occupied by  $\text{Fe}^{3+}$  ions although  $\text{Fe}^{2+}$  and  $\text{Fe}^{3+}$  ions alternately occupy octahedral sites. This organization of ions in crystals is generally represented as  $\text{Fe}_{\text{Td}}^{3+} [\text{Fe}^{2+} \text{Fe}^{3+}]_{\text{oh}} \text{O}_4$ . The magnetic property is generated by superexchange oxygen mediated coupling. All magnetic moments of the tetrahedral iron ions are aligned in the same direction. While the octahedral ions magnetic moment is aligned in the opposite direction. Since there are an equal number of octahedral and tetrahedral  $\text{Fe}^{3+}$  ions, they compensate for each other and the resulting superparamagnetic property of crystal arises only from uncompensated octahedral  $\text{Fe}^{2+}$  ions (Gossuin et al., 2009).

## **2.2 Different Method of SPION Synthesis and Importance of Co-precipitation**

There are several chemical methods for synthesis of SPION such as microemulsion, sonochemical reaction, hydrothermal reaction, sol-gel synthesis, hydrolysis and thermolysis, electrospray synthesis and flow injection synthesis. The main challenge consists of designing experimental conditions for monodisperse particles with uniform size. The second major problem is to select a reproducible process that can be easily industrialized without any complex purification procedure, such as size exclusion chromatography, magnetic filtration, ultracentrifugation, flow field

gradient etc. In non-polar solvents like organic reagent-based methods hydrophobic particles are produced even if it is homogeneous and of uniform particle sizes. For biomedical applications, these particles require further surface modification and stabilizations. Hence, the most common method of synthesis of SPION is chemical co-precipitation technique of iron salts (Laurent et al., 2008),(Gupta and Gupta, 2005).

The co-precipitation technique is likely the simplest, most efficient and versatile synthesis route to prepare nanocrystals. In this technique, SPION are usually prepared by aging stoichiometric mixtures of ferric and ferrous salts in an aqueous medium. The main advantage of this method is that a large quantity of nanoparticles can be synthesized. It is cost effective, provides high yields and is less time consuming. It is an eco-friendly route because there is no use of hazardous solvents or chemicals, high temperature and pressure (Wu et al., 2008).

### **2.3 Versatile Applications of SPION and Importance in Potential Biomedical Field**

SPIONs are of great interest in applications ranging from catalysis to data storage and biomedical applications. Due to their biocompatibility, FDA approval and absence of toxicity, these particles are intensively studied for potential applications studies in biology and biomedicines such as magnetic targeted delivery, theranostics and cancer therapy by magnetic fluid hyperthermia etc (Laurent et al., 2010).

#### **2.3.1 Targeted Delivery and Therapy**

The magnetic nanoparticles assisted targeted therapy has emerged as one among the best ways of disease treatment. Targeted delivery reduces the unwanted

accumulation of therapeutic agent from normal tissues, which reduces the toxicity as well as quantity of curing agent. The mainly reported areas are gene delivery, bio-separation, cells sorting and drug delivery (Singh and Lillard Jr., 2009). Literature revealed that a great deal of effort has been made to design novel therapeutic agents with targeted modality, specificity, minimize the side effects and good efficiency (Kamaly et al., 2012).

Similarly, the cell-based therapy has emerged as a new frontier in medicine. Cell therapy provides more promising solution for several diseases and injuries compared to most conventional medicines and therapies. Cells can perform better physiologic as well as metabolic duties than any of the mechanical devices, recombination proteins or chemical compounds (Wang et al., 2013), (Mooney and Vandenberg, 2008). However, there are a lot of hurdles to systemic administration of cells, causing significant difficulties for effective retention of the therapeutic cells at the target site. In order to achieve greater efficiency and optimum performance, a higher cell dose or higher engraftment of cells is inevitable (Li et al., 2009). Nevertheless, higher cell doses induce larger systemic circulation, which in turn raises safety concerns. Since the fundamental requirement associated with the success of cell therapy is the ability of cells to migrate and engraft (Singh, 2009), (Huang et al., 2010) the inability to achieve the desired level of cell homing and engraftment is a basic challenge for cell-based therapy.

Cells tagged with SPION can migrate easily and enhance accumulation by magnetic actuation (Chen et al., 2013). Recent literature puts forth several interesting research attempts at magnetic nanoparticle-conjugated stem cell delivery towards tissue repair

as well as hyperthermia applications (Edmundson et al., 2013),(Kubinová and Syková, 2010), (Bulte et al., 1999). Andreas et al. reported citrate-modified SPION-labelled stem cell delivery and its MRI trafficking (Andreas et al., 2012). Kyrtatos et al. reported that ferridex-labelled endothelial progenitor cells efficiently targeted an arterial injury with the help of an external magnetic field (Kyrtatos et al., 2009). Basically, labelling techniques utilize either of the following two approaches: (a) immobilizing magnetic nanoparticles onto the cell surface (Gaipa et al., 2003) or (b) internalization of biofunctional magnetic nanoparticles, for example *via* endocytosis (Schoepf et al., 1998). In receptor , mediated endocytosis, more particles will have the opportunity to accumulate inside the cells are cause cell stress (Kou et al., 2013). Therefore, surface-charge enhanced nanoparticle cell labelling may be considered as a suitable option.

The prerequisites for magnetic nanoparticles to be used for such applications are as follows: (a) should be stable enough to retain its physical integrity (b) retain its chemical stability, and (c) remain in the colloidal suspension. More significantly, it should not induce any un-favoured reactions in the biological milieu; nevertheless, it should facilitate faster and efficient binding to the required biomolecular component. In addition, feasibility of large-scale production without compromising its fundamental superparamagnetic nature is essential for clinically significant magnetic nanoparticles (Xu et al., 2011).

### **2.3.1.1 Three Dimensional Cell Culturing and Magnetic Microspheres**

Potential applications of non-invasive cell manipulation is three dimensional cell culturing (Lei et al., 2014). At present, 2D cell cultures, in general are restricted in

their capability to replicate the molecular gradients, substrate stiffness, the spectrum of cell-cell and cell-matrix interactions observed in living tissue. But there is a prominent break in complexity and originality to native tissue properties between simple two dimensional cell culture experiments and human tissues of interest. As a result, there exists a demand to create more representative environments using three-dimensional cell culture, toward which biological research has moved. The three dimensional cell culture techniques extend the ability to control shape, structure and biochemical environment than existing 2D,(Pampaloni et al., 2007). Three dimensional cell culture techniques generally depends on encouraging direct cell-cell interactions, using cell aggregation method like spheroids and pellet cultures or cell matrix interactions such as protein gels or synthetic polymer scaffolds. In general, these methods have been successful in producing improved *in vivo* like condition, yet there is a lack to generate proper 3D cell culture techniques in the current scenario (Tseng et al., 2013).

The application of magnetic nanoparticles-based magnetic levitation technique is a hopeful approach for 3D cell culture development. It is based on the use of magnetic nanoparticles that self assemble into networks based on electrostatic interactions. Cellular uptake of the biocompatible nanoparticles renders the cell amenable for magnetic manipulation of cells. Cells in culture can be levitated within the culture medium (Haisler et al., 2013). These cells interact, self assemble and proliferate without the demand or influence of an artificial extracellular matrix. Jialong *et al* in 2013 reported the magnetic nanoparticles loaded cells controlled *via* non-invasive technique and delivered it in the *in vivo* model (Chen et al., 2013). Similarly, Dmitry

*et al* in 2014 demonstrated the magnetic nanoparticles loaded stem cells delivery for spinal cord injury therapy (Tukmachev et al., 2015). These results revealed that the magnetic nanoparticle tagged cells were easily manipulated with the aid of external magnetic field which will help the development of magnetically levitated 3D cell culture system.

However, in the regenerative medicine, a synthetic extracellular matrix is crucial for supporting the differentiation process and for integration of the tissue formation. To overcome the limitations of existing 2D techniques there are several types of organic, inorganic, polymeric-based systems reported. One among the potential candidates for scaffold application is polymeric-based microspheres (Park et al., 2013) . Recently several groups have reported the microsphere based regenerative and selective separation in biological applications. Tsunehiro *et al* in 2013 demonstrated the magnetic nanoparticles embedded beads used for the selective separation of phosphorylated biomolecules from suspension (Tsunehiro et al., 2013). Also, Gong *et al.* in 2013 studied the surface-engineered magnetic microsphere for fast separation of phosphorylated biomolecules (Cheng et al., 2013). These reports revealed that the biocompatible magnetic microspheres are useful candidates for potential biomedical application.

### **2.3.2 MRI Contrast Agent**

#### **2.3.2.1 Magnetic Resonance Imaging**

Magnetic resonance imaging (MRI) is among the best non-invasive imaging methodologies today. It has long been used as a powerful technique in the clinical diagnosis of diseases. MRI is capable of obtaining three dimensional tomographic

images of living subjects with high spatial resolution as a result of perturbation of tissue water protons in the presence of an external magnetic field (van Gelderen et al., 1995). Although there are several imaging tools such as micro CT, X-ray, Positron emission tomography etc new and significant techniques are continually employed for a wide range of biomedical applications. Both in economic and virtual terms, it is more viable to develop accessories that can maximize the ability of the present devices or imaging tools. One of the most efficacious is an imaging probe or contrast agent, which helps in finer image acquisition (Na et al., 2009).

### **2.3.2.2 Magnetic Resonance Imaging- Importance of Contrast Agent**

Disease diagnosis *via* MRI imaging is positively enabled by contrast agents. Superparamagnetic iron oxide and paramagnetic gadolinium complexes are the commonly used contrast agents. However, the gadolinium-based contrast agent has pitiable target-specific biodistribution, fast exertion and undesired side-effects in patients (Kim et al., 2011). Form the recent study reports that the “nephrogenic systemic fibrosis” has created increased concern over the use of gadolinium-based contrast agents, which later induced chronic kidney disease in the patients (Grobner, 2006). Spinel ferrite SPION crystals have long been used as superparamagnetic T<sub>2</sub> contrast agents for magnetic resonance imaging (MRI). However, the common spinel ferrite iron oxides have intrinsic magnetic properties that are below the required standard. To improve their efficiency for various applications, the spinal ferrite nanoparticles with particular physical and magnetic properties were modified during the synthetic process (Lee et al., 2007), (Carta et al., 2009), (Lu et al., 2009).

### 2.3.2.3 Spinel Crystal Structure and its Modification

One among the best techniques for magnetic modification is crystal ion substitution with appropriate candidates, which can provide a versatile strategy to tune the SPION crystal structure (Jang et al., 2009). It is known that the SPION crystals exist as a cubic spinel structure with the oxygen atoms forming an fcc close packing and  $\text{Fe}^{2+}$ ,  $\text{Fe}^{3+}$  occupying tetrahedral or octahedral interstitial sites, and is generally represented as  $\text{MFe}_2\text{O}_4$  (O'Handley, 1999). By altering the chemical identity of  $\text{M}^{2+}$ , the magnetic properties of  $\text{MFe}_2\text{O}_4$  can be considerably increased (Sun et al., 2004).

There are several d-block elements such as Mn, Co, Ni, Cu and Zn, which when incorporated into the crystal structure of SPIONs favor spinel crystal formation. This results in enhanced magnetic properties and relaxivity when compared to bare SPION (Stuber et al., 2007), (Bárcena et al., 2008). Spinel structures developed by doping SPION with  $\text{Ni}^{2+}$  and  $\text{Cu}^{2+}$  are sensitive to leaching and can cause cytotoxicity. Hence, these systems require further treatment for stability, while doping  $\text{Zn}^{2+}$  to SPION produces hydrophobic nanoparticles with superior magnetic moment and a negative contrast effect (Chen et al., 2011). The major drawback of this system is its high solubility in acidic and basic pH conditions. It is noteworthy to mention that  $\text{Co}^{2+}$  doping with SPION is not preferred due to the non - superparamagnetic nature of the resultant crystal structure and high toxicity of Co ions (Horev-Azaria et al., 2013). However, manganese ion ( $\text{Mn}^{2+}$ ) doped SPION crystals possess the highest magnetization value when compared to other doping agents reported till date. Moreover, these  $\text{Mn}^{2+}$  doped SPION crystals also

demonstrate higher transverse relaxivity values (Berry et al., 2004a), (Veranth et al., 2007).

#### **2.3.2.4 Synthesis of Spinel Ferrite**

Various methods have been evolved for preparing SPION crystal modification, including thermal decomposition (Carta et al., 2010), co-precipitation, microemulsion, hydrothermal and sonochemical processes (Lu et al., 2007), (Bhasarkar et al., 2013). The most common protocols for their preparation are the thermal decomposition and co-precipitation techniques. The former method can easily produce size controlled ferrite nanoparticles under high temperature in an organic medium (Sun et al., 2004). However, these particles are hydrophobic with hydrocarbon molecules at the periphery of the surfactants, and therefore are insoluble in aqueous media. To transform the nanoparticles into water dispersible, one requires different steps. In this context, the current challenge is to develop a novel and synthetic method for aqueous dispersed magnetic nanoparticles with enhanced magnetic properties and biocompatibility. An aqueous-based co-precipitation method represents a simple and versatile tool to prepare nanocrystals not readily achievable using other methods. It is cost effective, provides high yields, is less time-consuming and easily scalable for large scale production. In addition to these advantages, it is an eco-friendly route because there is no use of hazardous solvents or chemicals and high temperature or pressure (Li et al., 2012), (Li et al., 2008).

#### **2.3.3 Hyperthermia Cancer Therapy – Importance of Magnetic Field**

Hyperthermia (controlled temperature) application has been used as a crucial self defence approach in biological system. For example, in an effort to fight injury,

including viral and bacterial infection, there is an increase in body temperature, thus creating the well-recognized symptoms of fever (Kyle, 2008). Hyperthermia as therapy has been realized with the aid of near-infrared light, microwave ablation, hot water bath, ultrasound waves and magnetic field by increasing localized temperature in a targeted region (Baronzio and Hager, 2008). Near infrared radiations have poor tissue penetration ability and it is difficult to modulate temperature at target sites. Magnetic nanoparticle assisted hyperthermia gained considerable attention compared to the other technical modalities due to the potential advantages. This is due to their capability to generate heat on exposure to an alternating magnetic field without a penetration depth limit (Nemala, 2015). Heat thus generated is *via* a non-invasive magnetic field and prevents collateral tissue damage due to precise temperature control.

### **2.3.3.1 Temperature Sensitivity of Cancer Cells**

Cancer therapy by hyperthermia is based on the variation in response of normal and cancerous cells to increase in environmental temperature. In general, normal cells show better resistance to elevated temperature and easily recover from injury than the cancer cells. This is based on the production of heat shock proteins (Storm et al., 1979).

Hyperthermia has long been used to activate the synthesis of heat shock proteins and it has been recently demonstrated that mild hyperthermia can also induce apoptosis (O'Neill et al., 1998). In culture cells react to environmental stressors in a graded fashion. At the initial stages of stress the heat shock or stress response is started. This response involves the rapid synthesis of an evolutionarily stored family of proteins

called heat shock proteins (HSPs). The primary function of these proteins is to enable cell survival till the stress element is removed. When the stressor is eliminated, the amount of intracellular HSPs quickly returns its normal level. If stress remains constant over a prolonged period of time or if its intensity is increased, the presence of HSPs may not suffice to ensure survival. Then HSP production ceases and apoptosis is initiated (Chu and Dupuy, 2014), (Vertrees et al., 2005).

### **2.3.3.2 Hyperthermia Heating Mechanism of Magnetic Nanoparticles**

The magnetic induction heating of ferrite materials is developed from their power loss in an alternating magnetic field. The total power loss is composed of hysteresis loss, eddy current loss, residual loss and relaxation loss. In the case of nanoparticle the hysteresis loss, eddy current generations and residual loss contributions are negligible due to the absence of remanence and coercivity. The major contributions of heat generation in superparamagnetic particles from relaxation process are associated with the Neel relaxation and Brownian relaxation. The Neel relaxation process refers to the heat-assisted domain rotations in the particles by the alternating magnetic field. Brownian relaxation refers to the rotation of the magnetic particle as a whole because of the torque exerted on the magnetic moment by the external alternating magnetic field (Pearce et al., 2013).

The energy barrier for changing the direction of particles is determined by rotational friction in the surrounding liquid. In general, the heating effects usually proceed through one of the two mechanisms: Neel and Brownian relaxation process, or both together. The relaxation losses due to both mechanisms could be calculated by the following equation:

$$P = (mH\omega\tau_{eff})^2 / [2\tau_{eff}kTV(1 + \omega^2\tau_{eff}^2)] \dots\dots\dots (1)$$

Here,  $m$  is the particle magnetic moment,  $H$  is the ac field amplitude,  $\omega$  is the AC field frequency,  $V$  is the nanoparticle volume, and  $\tau_{eff}$  is the effective relaxation time. When the AC magnetic field is applied to magnetic nanoparticles, their magnetic moments attempt to rotate following the magnetic field with time lag. The effective relaxation time ( $\tau_{eff}$ ) is given by

$$\tau_{eff} = \frac{\tau_B \tau_N}{\tau_B + \tau_N} \dots\dots\dots (2)$$

in which the Brownian relaxation is

$$\tau_B = 3\eta V_H / kT \dots\dots\dots (3)$$

Where  $V_H$  is the hydrodynamic volume of particle,  $\eta$  is the viscosity of the carrier fluid,  $T$  is the absolute temperature and  $k$  is the Boltzmann constant. Neel relaxation is

$$\tau_N = \tau_0 \exp(KV / kT) \dots\dots\dots (4)$$

Where  $\tau_0 =$  on the order of  $10^{-9}$  s,  $K =$  anisotropy constant of magnetic nanoparticle (Deatsch and Evans, 2014),(Chris Binns, 2014).

### **2.3.4 Theranostic Application of Magnetic Nanoparticles**

Theranostics is a newly emerging concept that combines diagnostics and therapeutics property in single unity. Numerous classes of nanomaterials have been explored and studied for their potential applications in cancer theranostics. Among them the SPION is considered a most appealing candidate due to their intrinsic physical and chemical properties (Wadajkar et al., 2013), (Gobbo et al., 2015). Based on the recent studies, the SPION has evaluated for use simultaneously as a diagnostic tool for cancer detection and hyperthermia tool for cancer therapy. Li *et al* in 2013 and Yen *et al* in 2013 have reported the possibility, advantages and efficiency of SPION nanoparticles for theranostic applications (Li et al., 2013).

### **2.4 Problems Associated with Bare SPION Particles in Biomedical Applications**

One of the major problems associated with the bare particles is aggregation. This is due to the fact that nanoparticles in colloidal suspension will tend to irreversible inter-particles adherence. This leads to the formation of large and irregularly shaped clusters and proceeds to aggregate. In biomedical applications, the stability of particles is one among the major challenges. As aggregates may lead to misrepresentative results and impedes experimental reproducibility by changing cellular response and toxicity profile of the particle (Mahmoudi et al., 2012).

There are several factors --physical and biological-- influencing the aggregation and sedimentation velocities (Jiang et al., 2010). Most of the nanoparticles have surface charge in aqueous environment due to the ionization/dissociation of surface groups, and adsorption of charged molecules or ions to the particle surface. The colloidal stability is decided by inter-particle behaviour resulting from intermolecular and

surface attractive forces (van der Waals force (vdW)), interacting with repulsive electrostatic double layer (EDL) and structural forces such as depletion attraction. The attractive vdW forces are repelled by EDL of particle surface, which stabilizes the dispersion (Min et al., 2008). The equilibrium between these forces determines the colloidal stability of particles. In the case of magnetic nanoparticle the magnetic dipole-dipole attraction also influences the colloidal stability. In the case of bare magnetic nanoparticle, at pH values near the isoelectric point or the point of zero charge, the overall surface potential of the particles tends to be neutral. As a result the repulsion of the nanoparticles caused by EDL decreases and the attractive forces such as vdW and dipole-dipole magnetic forces are dominated, this promoting the aggregation (Street et al., 2014).

In the case of targeted therapy, cell manipulation, cell separation *via* nanoparticles that tend to aggregate fail. This is because of the difficulty in appropriate contact between the cell surfaces and nanoparticles (Peng et al., 2008). Ugelstad *et al.* in 1993 has reported the criteria required for magnetic nanoparticles in cell separation experiments. One of the main conditions noted is based on particle colloidal stability (Ugelstad et al., 1993). Gupta *et al* in 2005 reported that the surface functionalized and stabilized magnetic particles can easily attach to cell surfaces and be taken up, thus allowing efficient manipulation or concentration of floating cells (Gupta and Gupta, 2005).

For use as a MRI contrast agent, stability and dispersion are important. Dispersed particles effectively interact with protons and increase proton relaxivity. Yoo *et al* in 2011 reported that magnetic particles with poor surface potential displayed artifacts

or limited sensitivity in MRI images due to aggregation (Yoo et al., 2012). Increase in cluster size of particles causes exclusion of water molecules from the inner surface of the particles. Thus altering the relaxivity even if it has good magnetic susceptibility. Balasubramaniam *et al.* in 2011 investigated controlled aggregation of magnetic nanoparticles *via* thermoresponsive polymer surface functionalization (Balasubramaniam et al., 2011). The report demonstrated that controlled aggregation and stable particles exhibited excellent contrast efficacy in MR images.

Hyperthermia mediated by magnetic nanoparticles also relies on their dispersed status in solution. In 2003 Hamley et al has reported that the aggregated particles or clumps may act as ferromagnetic systems under external magnetic field (Hamley, 2003). A ferromagnetic system always retains magnetization or hysteresis loss even after removal of external field. In hyperthermia application, ferromagnetic characteristics of particles may cause uncontrolled temperature generation leading to non-targeted tissue damage. There are few reports on the basis of controlled aggregation and hyperthermia therapeutic approaches for efficient cancer treatment. Lao *et al* in 2004 reported that aggregated particle and large magnetic susceptibility crystals overshoot therapeutic temperature under alternating magnetic field and cause damage the normal tissues (Lao and Ramanujan, 2004).

#### **2.4.1 Importance of Surface Modification**

Storage stability and efficient *in vivo* targeting are major challenges in nanoparticle development. In colloidal storage, physicochemical attractions dominate and induce particle aggregation. Similarly, in the *in vivo* administration a major requirement is to minimize the non-specific adsorption of plasma protein on the nanoparticle surfaces

(Wilhelm et al., 2003). These non-specific events can drastically hamper molecular identification processes at the surface of the nanoparticles and reduce the efficiency in targeted application (Fang et al., 2009). The particles should also resist non-specific adsorption of opsonins. Opsonisation of magnetic nanoparticles by plasma proteins results in rapid elimination from the blood by the mononuclear phagocyte system with subsequent accumulation in the RES. The nature and amount of plasma protein adsorbing on nanoparticles is directly related to the physicochemical characteristics of the surfaces. Adsorbed opsonins potentially conduct specific interactions with receptors on the surface of macrophages and hepatocytes with subsequent excretion of the nanoparticles (Sigmund et al., 2008).

To reduce opsonisation and improve the colloidal stability, a critical requirement is to surface engineer the nanoparticles with molecules that provide repulsive forces large enough to counter the attractive ones in the collision process. The repulsive forces can be attained in the presence of an electrical double layer on the particles or in the presence of polymeric chains providing steric stabilization (Neoh and Kang, 2011).

#### **2.4.2 Inorganic Molecules Used as Surface Coating Agent – Hydroxyapatite**

##### **Crystals**

There are several types of polymers, ceramics and other materials used for surface modification of iron oxide particles. The polymers include dextran (Berry et al., 2004b), polyethylene glycols and polyvinylpyrrolidone, all of which are known to be biocompatible and promote good dispersion of iron oxide in aqueous medium (Kohler et al., 2005), (D'Souza et al., 2004). However, the possibility that the

polymer coating can disappear under harsh *in vivo* conditions has been a concern (Zhang et al., 2002), (Moghimi et al., 2001). Among diverse coating techniques, the use of an inorganic matrix as a host for nanocrystalline particles has been shown as an effective means for tailoring a uniform particle size and controlling the homogeneous dispersion of ultra-fine clusters (Moreno et al., 2002). These coatings not only provide stability to the nanoparticles in solution but also help in binding various biological ligands to the nanoparticles' surface (Ashokan et al., 2010). These nanoparticles have an inner iron oxide core with an outer ceramic shell of inorganic materials. Several studies have reported potential use of iron oxide ceramics, especially the magnetite or maghemite phase. For biomedical applications of magnetic nanoparticles, it is crucial to develop biocompatible protection strategies against oxidation and agglomeration (Lu et al., 2007). Recent research has focused on the synthesis of silica stabilized iron oxide nanoparticles for various catalytic and biomedical applications (Sunil et al., 2009). Bretcanu *et al.* reported that iron oxide-containing ferrimagnetic bioglass ceramics (FBC) could be used for hyperthermia treatment of bone cancer (Leventouri et al., 2005). Although distinct inorganic biocompatible materials are reported, hydroxyapatite (HA) ( $\text{Ca}_{10}(\text{PO}_4)_6(\text{OH})_2$ ), which is the main inorganic phase of human bones has been widely used as an inorganic material for bone filling and augmentation application. It is bioactive and supports bone ingrowth and osteointegrate when used in orthopedic, dental, and maxillofacial applications (Liu et al., 2008). Better biocompatibility of HA prompts its use as an inorganic host matrix for seeding iron oxide nanoparticles. One of the advantages of calcium phosphate as an embedding material relative to its polymeric nanoparticles or liposomes is its variable solubility in cells (Kester et al., 2008).

Few studies have evaluated HA-nano iron oxide and its effect on biological system. A recent report suggests increased osteoblast density in the presence of nano iron oxide (maghemite) and hence favors its use as a potential candidate in bone tissue engineering applications (Hou et al., 2009), (Pareta et al., 2008). But there is a dearth of suitable synthetic strategy and proper microstructure evaluation in all the reported methods (Silva et al., 2008).

#### **2.4.3 Surface modification – Trisodium citrate (TC) Molecules**

Nanoparticles can be stabilized through surface modification *via* small polar molecules like citrate moieties. As the nanoparticles surface coating thickness has great importance in the efficiency in biomedical field (Andreas et al., 2012). The high molecular weight polymer and other crystal molecules thicken particle surfaces, which reduce the magnetic property. Moreover, the higher density of particles reduces the colloidal stability and increases the chance for settling or clustering under gravitational force for long term storage (Khandhar et al., 2015). The addition of citrate molecules in the synthesis of magnetic nanoparticles can control the nucleation, crystal growth, structure, stability, size and crystallinity. Depending upon the concentration of citrate molecules, the core size gets varied (Laurent et al., 2008). Carboxylic group have importance on the growth of magnetic nanoparticle and magnetic properties. Bee *et al* in 1995 have investigated the effect of concentration of citrate ions on size variation (Bee et al., 1995). Liu and Huang have studied the effect of the presence of citrate during magnetic nanoparticle synthesis (Chen Liu, 2003). Increasing concentrations of citrate cause significant decrease in the crystallinity of the iron oxides formed. Krishnamurti and Huang have studied the

influence of citrate on the kinetics of  $\text{Fe}^{2+}$  oxidation and the ensuing hydrolytic products of  $\text{Fe}^{3+}$  (P.M. HUANG, 1991). Moreover the citrate molecules are highly water soluble and biocompatible. Khlebtsov *et al* reported that the citrate molecules stabilized gold nanoparticles showed good biocompatibility in *in vitro* condition and excellent stability under *in vivo* system (Khlebtsov and Dykman, 2011).

## Chapter 3

### MATERIALS AND METHODS

#### 3.1 Development of Superparamagnetic Iron Oxide Embedded Hydroxyapatite Nanocomposite

##### 3.1.1 Materials

Samples of  $\text{FeCl}_2 \cdot 4\text{H}_2\text{O}$  (Merck, Darmstadt, Germany),  $\text{FeCl}_3$  (Merck),  $\text{Ca}(\text{NO}_3)_2 \cdot 4\text{H}_2\text{O}$  (Rankem, New Delhi, India),  $(\text{NH}_4) \text{H}_2\text{PO}_4$  (Rankem), and 25% aqueous  $\text{NH}_4\text{OH}$  (SD Fine Chemicals, Mumbai, India) and 35%  $\text{HCl}$  (SD Fine Chemicals) were used as obtained. 3-(4,5-Dimethyl thiazol-2-yl)-2,5-diphenyltetrazolium bromide (Sigma-Aldrich, USA), streptomycin (Invitrogen, USA) and fetal bovine serum (Invitrogen, USA) were used for the MTT assay. All chemicals used for the experiments other than those mentioned in the materials section were obtained from Sigma-Aldrich, USA.

##### 3.1.2 Synthesis of Nano Iron Oxide Embedded Hydroxyapatite Composites (HAIO)

The synthesis of HAIO was carried out by co-precipitating iron salt and calcium phosphate precursors in alkaline medium. The iron salt solution was freshly prepared in an acidic medium of  $\text{HCl}$  using  $\text{FeCl}_2 \cdot 4\text{H}_2\text{O}$  and  $\text{FeCl}_3$  in the ratio of 1:2. The  $\text{Ca}(\text{NO}_3)_2 \cdot 4\text{H}_2\text{O}$  and  $(\text{NH}_4) \text{H}_2\text{PO}_4$  solutions were taken in such a way as to get the Ca/P ratio of 1.67. The  $\text{Ca}(\text{NO}_3)_2 \cdot 4\text{H}_2\text{O}$  solution was mixed with iron salt solution with constant stirring until the required temperature  $70^\circ\text{C}$  was reached. The pH of the above solution was then slowly increased up to 11 by adding 25% ammonia solution

together with  $(\text{NH}_4)\text{H}_2\text{PO}_4$  for a period of 1 h. The addition and mixing of reagents were done under  $\text{N}_2$  atmosphere. After the addition was completed, temperature was increased to  $80^\circ\text{C}$  for a period of 1 h to eliminate excess ammonia. The suspension was aged for 24 h at room temperature, after which the precipitate was washed three times with distilled water and centrifuged at 3500 rpm. The particles were further collected after centrifuging at 6000 rpm followed by magnetic separation. Bare iron oxide particles were also prepared by 1:2 ratios of ferrous, ferric chlorides in the same reaction condition for size, phase purity, and chemical structure comparison.

The HAIO samples at molar percentage ratios of 10–90 were synthesised using the same method. In ascending order of molar percentage of iron oxide in the composite, the samples are described as HAIO10, HAIO30, HAIO50, HAIO70, and HAIO90. Bare SPION was also prepared using a 1:2 ratio of ferrous: ferric chlorides at the same reaction conditions for size, phase purity, and chemical structure comparison.

### **3.1.3 Physicochemical Characterizations HAIOs and SPION**

#### **3.1.3.1 High Resolution Transmission Electron Microscopy (HRTEM) and Energy Dispersive X-ray Spectra (EDS)**

High-resolution TEM (HRTEM) analysis was performed to evaluate the morphology and crystal size, and for composition analysis. The HRTEM images and energy dispersive X-ray spectra (EDS) were collected on a JEOL JEM-2010F microscope operated at 300 kV. HAIO magnetic nanocomposite samples at low concentration were dropped onto a formvar coated copper grid, dried and analyzed.

### **3.1.3.2 Environmental Scanning Electron Microscopy (ESEM) and Energy Dispersive X-ray Spectra (EDS)**

The micro-scale morphology and the composition analysis of the HAIO nanocomposite were investigated with the aid of ESEM (ESEM; Quanta 200, The Netherlands). Samples were prepared by dispersing in distilled water with ultrasonication for 2 minutes. A single drop of the above suspension was put on an aluminium stub and dried at room temperature, followed by coating with gold. The composition of the magnetic nanocomposites was evaluated using energy dispersive X-ray spectroscopy.

### **3.1.3.3 X-ray Diffraction Analysis (XRD)**

The phase purity of crystals of HA, SPION and HAIOs nanocomposites was analyzed using an X-ray diffractometer (Bruker, D8 Advance, Karlsruhe, Germany) using  $\text{CuK}_{\alpha 1}$  radiation operating at 40 kV and 30 mA current strength. The crystal structure was determined by analyzing the position and intensities of the diffraction peaks typically observed in the range of diffraction angle  $2\theta = 20\text{--}70^\circ$  and at a scan rate of  $4^\circ \text{ min}^{-1}$  with a step of  $0.1^\circ$ .

### **3.1.3.4 Dynamic Light Scattering (DLS) and Zeta Potential Measurements**

The hydrodynamic size and surface charge of the nanocomposite particles were analyzed using a Dynamic Light Scattering (DLS) Particle Size Analyzer (Malvern Instruments Ltd, Worcestershire, UK) by dispersing the sample in distilled water using ultrasonic probe sonication.

### **3.1.3.5 Fourier Transform Infrared Spectra (FTIR)**

The Fourier transform infrared (FTIR) spectra of the samples were collected using a Thermo-Nicolet 5700 spectrometer. As the ceramic powder was found to be opaque to IR, the diffuse reflectance (DRIFT) technique was used for measurement. Samples were dried and the powder thus obtained was thoroughly mixed with IR grade KBr powder and the reflectance spectrum recorded in the range of 400 to 4000  $\text{cm}^{-1}$  at a resolution of 4  $\text{cm}^{-1}$ . KBr powder alone was used for background spectra.

### **3.1.3.6 Vibrating Sample Magnetometry (VSM)**

Freeze-dried powder samples were used for the magnetic property analysis. Vibrating sample magnetometry (VSM) was used to measure the magnetic properties of the SPION and HAIOS using a PAR EG&G Model 4500 magnetometer with an external field varying from -15 to 15 kOe at room temperature. The magnetization of each sample was obtained as a function of the applied field.

## **3.1.4 Biological Evaluation of HAIOS**

### **3.1.4.1 *In vitro* Biocompatibility - Cell Culture**

HeLa (human cervical carcinoma) cells were cultured in Dulbecco's Modified Eagle Medium-High Glucose (DMEM-HG) with 10% fetal bovine serum (FBS), 50 units per ml of penicillin and 50  $\text{mgml}^{-1}$  of streptomycin. All reagents were sourced from Invitrogen, India and cell culture lab ware from NUNC, Denmark. Cells were seeded and maintained at 37°C and 5%  $\text{CO}_2$  atmosphere and experiments were performed at 80% confluence.

#### **3.1.4.2 Cell viability MTT Assay**

The *viability* of HeLa cells was ascertained using the standard methyl thiazol tetrazolium bromide (MTT) assay as per Mosmann *et al.* (Mosmann, 1983) using HeLa fibroblasts. The nanocomposites HAIO10, HAIO30, HAIO50, HAIO70, HAIO90, SPION and control were added to wells at final concentrations of 0.75 mg ml<sup>-1</sup> and 1.5 mg ml<sup>-1</sup>. After 24 hours incubation with the above concentrations of nanoparticles, MTT was added to each well, the resulting formazan was dissolved and the optical density was evaluated at 570 nm using a Chameleon Microplate Reader. The control in the MTT experiment was HeLa cells without exposure to particles. Control MTT activity was taken as 100 % and test values were plotted against it.

#### **3.1.4.3 Cell viability Alamar blue Assay**

The cytotoxicity of HAIO50 particles various concentration were evaluated *via* alamar blue (AB) assay. The AB assay was used to assess cell *viability* and proliferation based on the reduction potential of metabolically active cells. The mitochondrial reductase enzymes in living cells are active and it changes the alamar blue to pink color on the basis of live cell activity. In this study, HeLa cells were seeded in a transparent 96 well plates and exposed to the different concentrations [0.5mg/ml, 1mg/ml, 2mg/ml and 3mg/ml] of HAIO50. After the exposure, 100 µl of alamar blue reagent (invitrogen assay protocol) was added in each well and incubated for 4h at 37°C. The fluorescence was measured at 560 nm excitation and 590 nm emission wavelengths using a plate reader (HIDEX Chameleon) and

expressed in percentage activity of live cells versus control. The experiments were carried out in six duplicates for each concentration.

#### **3.1.4.4 *In vitro* Hemocompatibility**

Samples were diluted with PBS (pH 7.4) to 10 mg ml<sup>-1</sup> hemoglobin concentration and the test was then performed. Samples as listed (HAIO10, HAIO30 and HAIO50) were used for the test and each sample at different test concentrations (0.1 mg, 0.3 mg and 0.5 mg) was incubated individually with 100 µl of whole blood with a hemoglobin concentration of 10 mg/ml for 3 h at 37°C in a shaking water bath. The samples were centrifuged at 700 – 800g for 15 min, and the supernatant was then observed for any released hemoglobin at 540 nm using the methemoglobin test. The test was validated against Triton X100 as the positive control and polyethylene glycol as the negative control. The percentage of hemolysis was calculated by a relative method based on optical density (OD). The experiments were run in triplicate and repeated twice.

Percentage hemolysis =  $\frac{\text{Supernatant Hb released}}{\text{Total Hb conc. of dil. Blood}} * 100 * 8(\text{dilution factor})$

Total Hb conc. of dil. Blood

The calculated percentages of hemolysis for all the samples were compared with ASTM standard, which defines samples as highly hemocompatible (<5% hemolysis), hemocompatible (within 10% hemolysis) and nonhemocompatible (>20% hemolysis).

### **3.1.4.5 Cellular Uptake: Prussian blue Staining and Flow Cytometry Evaluations**

Cells post-incubation with nanoparticles were visualized using the Prussian blue staining method to detect the presence of iron. HeLa cells were grown on round glass coverslips (Blue Star, India) and incubated with HAI050 nanoparticles (120 µg) for 4 hours. After incubation, the coverslips were washed with sterile phosphate buffered saline and fixed with 95% ethanol. Prussian blue staining was carried out with equal volumes of 2% hydrochloric acid and potassium ferricyanide trihydrate for 15 min followed by washing with distilled water, and images were captured using a Leica DMIL microscope. Cell interactions with the nanomaterial were analyzed using flow cytometry. HAI050 was used for analysis at varying concentrations (30 µg, 60 µg, 120 µg, 240 µg, 480 µg and 960 µg).  $1 \times 10^6$  HeLa cells in suspension were treated with the nanoparticles for 15 min, and the forward scatter (FSC) and side scatter (SSC) were measured using a Becton Dickinson FACS Aria instrument using FACS ARIA software.

## **3.2 HAI050 Assisted Cell Separation, Manipulation and Culturing using External Magnetic field for Introducing Targeted Cell Delivery and Therapy**

### **3.2.1 Cell Separation**

HeLa cells ( $1.4 \times 10^3$  cells per ml) were added to seven tubes (A– G) and incubated for 15 minutes with varying concentrations of HAI050 (C1 to C6) in PBS. Cells were pre-stained with Acridine orange and magnetic separation was carried out with an external magnet (0.3 T) for 1 minute on all tubes. The supernatant and the pellet were collected into separate tubes. Cell numbers were evaluated using Coulter

counting (Sysmex K- 4500). The supernatant and pellet were resuspended in 500  $\mu$ l of PBS and placed on a UV transilluminator (Bangalore, Genei).

### **3.2.2 Morphological Study: Cell Separation**

To understand the effect of the cell separation dynamics on the cell morphology, imaging studies were carried out. A pellet isolated *via* magnetic separation was fixed in 1% glutaraldehyde (Electron Microscopy Sciences) overnight. The pellet was prepared as a thin film on a clean glass slide (Blue Star, India) and dried at room temperature. The film was fixed in 100% methanol, airdried and then stained with Giemsa Stain (1 : 20 volume dilution). Excess stain was removed by washing with diluted buffer solution, and the sample was then dried and imaged under an inverted phase contrast microscope (Leitz DMIL, Leica, Germany). Environmental scanning electron microscopy (FEI QUANTA 200) was carried out on fixed pellets dehydrated in an ascending alcohol series and placed on a glass coverslip.

### **3.2.2 Cell Culture of Magnetically Separated Cells**

Cell pellets collected by magnetic separation were transferred into culture wells under aseptic conditions and provided with growth medium (DMEM-HG) and then cultured for 24 hours and characterized.

#### **3.2.2.1 Cytoskeleton, Morphology Evaluations by Confocal Laser Scanning Microscopy (cLSM)**

The F-actin structure and morphology of the magnetically separated cells, after 24 h culture, were observed by confocal laser scanning microscopy and environmental scanning electron microscopy. For cLSM evaluation, the monolayered cells were fixed in 3.7% paraformaldehyde and permeabilized with 0.25% Triton X-100 for

F-actin staining in the cells. F-actin was stained with Alexa-fluor- 488-phalloidin and the nucleus was counterstained with 4',6- diamidino-2-phenylindole (DAPI). The control and HAI050- labeled HeLa cells were investigated using a confocal laser scanning microscope (Carl Zeiss LSM 510 META equipped with differential interference contrast optics). Images of the samples were prepared in multi-track mode with separate excitation of DAPI and Alexa-fluor-488-phalloidin.

### **3.2.3 HAI050 Aided Three Dimensional Cell Culture**

The HeLa cells were grown in six well plate to 70-80% confluence, at which point, they were treated with HAI050 magnetic nanocomposite particles at a concentration of 2 mg/ml and incubated overnight. The next day, treated cells were enzymatically detached with trypsin and resuspended 3 ml of fresh medium in a six well plate. A neodymium magnet was placed on top of the plate to levitate the cell to the medium. The HAI050 particles attached or up taken cells were levitated and incubated another 72 h. To understand the nature of structure and morphology of cultured cells were analyzed by environmental scanning electron microscopy, fluorescent imaging and phases contrast imaging.

#### **3.2.3.1 Morphological Evaluation-ESEM Technique**

The magnetically levitated 3D cultured cell sheet was separated from the medium with the help of external magnetic field and transferred to clean glass coverslip. Then the cells were fixed with 1% glutaraldehyde overnight. The cells sheet was dehydrated with ascending alcohol series and placed on a cover slip and gold coated. The morphology was analyzed by ESEM analysis.

### **3.2.3.2 DAPI Nuclear Staining and Phase Contrast Imaging**

Cell sheet were fixed with 3.7% paraformaldehyde at overnight followed by washed with PBS solution. Diluted (1:100 dilution) DAPI solution was added to cell sheet and incubated for up to 5min. Rinse the cell sheet with PBS solution for removing the excess DAPI stain and mounted with the antifade reagent to reduce fluorescence quenching and imaged *via* fluorescence microscope. The same cell sheet phase contrast images captured by using a Leica DMIL inverted microscope.

### **3.2.4 Magnetic Microsphere Synthesis**

The magnetic microspheres were developed by solvent evaporation technique. Briefly, the polycaprolactone polymer (PCL) was dissolved in dichloromethane [DCM] to get 10% weight percentage and 2mg of magnetic powder HAI080 [80% SPION and 20% HA] were dispersed into them. The precursor was magnetically stirred at room temperature for 24h in a closed vessel. It was drop wise adding into continuously stirring aqueous solution containing 0.05% polyvinyl alcohol. After complete addition of magnetic slurry, the suspension was stirred continuously to another 24h and washed with distilled water and dried under room temperature. The same synthetic technique was followed with out addition of HAI0 powder to development of 7.5 wt% and 5wt% in PCL microspheres, which were termed as PCL5 and PCL7.5 respectively.

### **3.2.5 Physicochemical Characterizations**

#### **3.2.5.1 ESEM and EDS Analysis**

The size, surface texture and elemental compositions of HAIOPCL were evaluated by scanning electron microscope. For this analysis, the microspheres were dispersed over the aluminum stub and images were captured in various magnification. Followed by the corresponding areas elemental compositions analyzed through energy dispersive spectra.

#### **3.2.5.2 XRD and FTIR Analysis**

To understand the crystallinity and nature of bonds of HAIO and PCL in composite form has been evaluated *via* XRD and FT-IR technique. The separate phases of each crystal were analyzed and compared with HAIOPCL. The method of analysis and parameters used as same as that mentioned in the section 3.1.3.3 and 3.1.3.5.

### **3.2.6 Biological Characterizations**

#### **3.2.6.1 Cell Culture**

HeLa (human cervical carcinoma) cells were cultured as per mentioned in the section 3.1.4.1

#### **3.2.6.2 Cytotoxicity - Alamar Blue Assay and Light Microscopic Technique**

The cytotoxicity of HAIOPCL10 (short termed as HAIOPCL) containing various size ranges were evaluated *via* Alamar blue (AB) assay as per the procedure mentioned in section 3.1.4.3. In this study, HeLa cells were seeded in a transparent 96 well plates and exposed to the different sizes of HAIOPCL microspheres [sizes ranges 100-250  $\mu\text{m}$ , 250-350  $\mu\text{m}$ , 350-500  $\mu\text{m}$ , 500-1000  $\mu\text{m}$ ] dispersions at

concentration of 2mg/mL for 24h. After the exposure, 100  $\mu$ l of alamar blue reagent (invitrogen assay protocol) was added in each well and incubated for 4h at 37°C. The fluorescence was measured at 560 nm excitation and 590 nm emission wavelengths using a plate reader (HIDEX Chameleon) and expressed in percentage activity of live cells versus control. The experiments were carried out in six duplicates for each size of microsphere. Further the cell was exposed to microspheres for 24 h and structure was also evaluated *via* bright field Leica DMIL microscope (Leica, Germany).

### **3.2.6.3 Hemolysis and RBC Morphology Analysis**

Blood from human volunteer was collected into the anticoagulant, ACD (acid citrate dextrose). ACD blood was prepared by adding 1mL of ACD solution to 9 mL of fresh human blood. The blood compatibility experiments were based on the standard protocol ISO10993- 4:2002(E). 1mgs of various sizes of microspheres [sizes ranges 100-250 $\mu$ m, 250-350 $\mu$ m, 350-500 $\mu$ m, 500-1000 $\mu$ m] and saline control [2ml] were added into each of the 10 mm<sup>2</sup> polystyrene wells, followed by addition of 1ml blood and incubated for a period of 2 h under agitation at  $70 \pm 5$  rpm using an environ shaker thermostat (Kuhner shaker, Switzerland) at  $35 \pm 2^{\circ}$ C. Three empty polystyrene culture dishes were exposed to blood as reference. The total hemoglobin in the whole blood samples were measured using automatic hematology analyzer (sysmex-K 4500). The free hemoglobin liberated into the plasma after exposure to materials was measured using Diode array spectrophotometer (Hewlett Packard 8453) and the percentage hemolysis was calculated using the formula (Free Hb/ total Hb)<sup>\*</sup> 100. Hemolysis expressed as a percentage of hemoglobin release was performed to assess the effect of microspheres on blood cell membranes.

### **3.2.7 Three Dimensional Cell Culture using Magnetic Microsphere**

HeLa cells were seeded over magnetic microspheres in six well plates and incubated for 24h to attach the cell on microsphere surfaces. The cell culture medium was changed after 24h and microspheres were levitated with the help of neodymium magnet placed over the plate. The microspheres were incubated another 72 h in a levitated condition and evaluated the cells morphologies, live-dead analysis *via* various microscopic methods.

#### **3.2.7.1 ESEM Analysis**

3D cell cultured microsphere were fixed with 1% gluteraldehyde for 24h and dehydrated using ascending order of alcohol. Followed by the cell over microsphere was fixed in aluminum stubs. The morphologies of cells as well as microsphere were imaged by Environmental scanning electron microscopy (FEI QUANTA 200).

#### **3.2.7.2 Live- Dead Staining and DAPI Nuclear Staining Evaluation**

In order to evaluate the efficacy of magnetic microsphere in maintaining cell viability over time, the 3D cultured cells were evaluated through a live- dead assay using acridine orange and ethidium bromide (sigma). The 3D cultured magnetic microsphere was washed in PBS and incubated with 100  $\mu$ l dye mixer for 30min. Excess stain was removed with PBS and the sphere was viewed under a fluorescent microscope. Live cells were determined by the uptake of acridine orange green fluorescence (502/526) and the exclusion of ethidium bromide red fluorescence (518/605) stain. The cells over microsphere were evaluated by DAPI nuclear staining. For this analysis the 3D cultured magnetic microsphere were fixed with 3.7% paraformaldehyde for 24h followed by washed with PBS solution. 100 times

diluted DAPI solution were added to magnetic spheres and imaged by fluorescent microscope.

### **3.3 Theranostic Efficiency Evaluation of HAIO50 (Hyperthermia Therapy and MRI Contrast Agent)**

#### **3.3.1 Magnetic Hyperthermia Evaluation of HAIO50 and SLP Calculation**

In order to investigate the therapeutic hyperthermia potential of HAIO50, the samples were subjected to induction heating studies. For this analysis, the Ambell EASY HEAT laboratory induction system was used. It's containing induction coil with 4 cm diameter, 2.6 cm length and a total of 6 turns was set at magnetic field frequency 275 kHz for this experiment. The induction coil was thermalized to room temperature with a closed circuit water chiller. HAIO50 was subjected to an alternating magnetic field through induction heating system and temperature of nanoparticles was measured as a function of time. The temperature change in sample was monitored with a non contact mode IR thermometer (Fluke 572).

To examine the specific loss power [SLP] of material, different concentrations of HAIO50 dispersed in aqueous solution in a 1.5mL plastic centrifuge tube and insulated with ceramic wool. The entire assembly was placed within the centre of a water cooled copper coil and measured the time-temperature profile *via* alternating magnetic field (AMF) applications. The SLP was calculated by the equation,

$$S.I.P = \frac{CV_s}{m} \frac{dT}{dt} \dots\dots\dots(5)$$

Where ‘C’ is the volume specific heat capacity of the sample ( $C_{\text{water}} = 4185 \text{ J L}^{-1} \text{ K}^{-1}$  C),  $V_s$  = is the sample volume, and  $m$  is the mass of the magnetic nanocomposite present in the sample volume.  $dT/dt$  initial slope of the change in temperature versus time curve ( $\text{Ks}^{-1}$ ).

### 3.3.2 HAIO50 *in vitro* Hyperthermia Evaluation

HeLa cells ( $1 \times 10^6$ ) and HAIO50 material at a concentration of 2mg/ml were suspended in a 1.5 ml eppendorff tube with a final volume of 200 $\mu$ l. An alternating magnetic field [AMF] of 33.8mT and 275 kHz was applied to the test tube containing HeLa cell suspensions for 30min. The material-cell suspension placed to maximum field strength of the induction coil and carried out the AMF hyperthermia. The temperature of the suspension was monitored by an infrared thermometer. After AMF application material-cell suspension was incubated for 1h at 37°C. Cell suspension containing 2mg/ml HAIO50 without AMF application was taken as control.

#### 3.3.2.1 Quantitative Estimation of Dead Cell Population – FACS Analysis

In this analysis, the control and test material-cell suspensions were washed twice in 1X PBS and re-suspended in PBS. Cells were stained with 200  $\mu$ l of (50  $\mu$ g/ml stock solution) Ethidium bromide solution for half an hour. Further the cells suspension washed in 1X PBS solution to remove the excess stain and was evaluated through

flow cytometric analysis [FACS ARIA, BD Biosciences, San Jose, CA,USA] and percentage of stain expressed cells was calculated by using BD FACS Diva software (BD Biosciences, San Jose, CA, USA).

#### **3.3.2.2 Quantitative Estimation of Cell Death Mechanism - FACS Analysis**

After hyperthermia experiment, the control and test material-cells suspensions were washed twice in 1X PBS and re-suspended in PBS. Cells were further stained with live-dead staining kit [Invitrogen FITC Annexin V/Dead Cell Apoptosis cat no:V13242]. Post - staining, cell population was evaluated *via* flow cytometric analysis [FACS ARIA, BD Biosciences, San Jose, CA,USA] and percentage of stain expressed cells was calculated by using BD FACS Diva software (BD Biosciences, San Jose, CA, USA).

#### **3.3.2.3 Hyperthermia Treated Cells Morphology Evaluation – ESEM Technique**

To understand the hyperthermia treated HeLa cells morphological analysis, cells were grown adherent on round glass coverslips (Blue Star, India) and exposed to 2 mg/ml of HAI050 particles, followed by AMF exposure for 30min and incubated for 1h at 37°C. Cells alone grown over glass coverslip were used for control of the experiment. The cells were fixed in 1% glutaraldehyde for 2 h and dehydrated in an ascending alcohol series and evaluated by Environmental scanning electron microscopy (FEI QUANTA 200).

#### **3.3.3 Magnetic Resonance Imaging Contrast Efficiency of HAI050**

Relaxivity measurements: To assess the magnetic characteristics of the HAI050 nanoparticles with respect to their potential use as MRI contrast agents, the HAI050

$r_2$  relaxivity (relaxation of transverse magnetization, i.e. spin–spin interaction) was measured.

The magnetic relaxivity measurements phantom study were performed on a 1.5 T entire body MRI scanner (MAGNETOM Avento Tim, Siemens, Munich, Germany) using a 12 channel head coil. Different concentrations of the HAIO50 particles dispersed uniformly in DI water and enclosed in non-magnetic containers served as the phantoms. The relaxation times ( $T_2$ ) using different concentrations of nanoparticles (0 to 0.25 mM of Fe) were measured. The concentrations of the nanoparticles in containers were fixed *via* serial dilution. From a stock concentration of HAIO50, different dilutions were made using DI water. The scanning parameters used were: temperature = 22 °C, field of view = 20 cm x 40 cm and slice thickness = 6 mm. For  $T_2$  relaxometric measurements, a spin echo sequence from three different planes of the phantoms was used. The MR signal was measured for various echo times of 15–120 ms with a fixed repetition time of 2000 ms.  $T_2$  relaxation time was calculated from the resulting MRI pixel intensity maps with respect to each concentration. The relaxivity ( $r_2$ ) value calculated *via* pixel intensity plotted against the HAIO50 concentrations and  $r_2$  value was determined by the linear fit.

#### **3.3.3.1 *In vitro* MRI Analysis**

HeLa cells ( $1 \times 10^6$ ) were incubated with HAIO50 in a DMEM medium for 24h at Fe concentrations of 0.05, 0.1, 0.15, 0.2 and 0.25mM. After exposure time, the cells were washed twice with 1X PBS and re-suspended 1mL PBS in an Eppendorf tube. MR imaging was performed with a 1.5T MRI.  $T_2$  weighted images were acquired

using the following parameters: temperature = 22°C, FOV = 8 cm x 8cm, slice thickness 3mm. The T<sub>2</sub> signal intensities were measured within the region of interest.

### **3.4 Improve the Theranostic Efficiency of Superparamagnetic Nanoparticles Through Crystal Modification**

#### **3.4.1 Development of Manganese Substituted SPION (MnIO) Nanocrystal *via* an Aqueous Co-precipitation**

##### **3.4.1.1 Materials:**

FeCl<sub>2</sub>.4H<sub>2</sub>O (≥99%), FeCl<sub>3</sub> anhydrous (≥98%), MnCl<sub>2</sub>.4H<sub>2</sub>O (≥99%), NaOH, 35% HCl and Trisodium citrate (TC) were purchased from Merck (Germany/India). The chemicals used for the cell culture studies are 3-[4,5-dimethylthiazol-2yl]-2,5-diphenyltetrazolium bromide (MTT), F12K medium, sodium bicarbonate, Gentamicin (Himedia, India), amphotericin B solution and fetal bovine serum (Sigma-Aldrich, Germany). The chemicals used for the nanoparticle cell uptake and blood compatibility evaluations are from Sigma-Aldrich, Germany. Deionized water was used for the synthesis and subsequent washing of the MnIO. All the reagents were used without further purification.

##### **3.4.1.2 Synthesis of MnIO**

MnIO with varying Mn<sup>2+</sup> molar concentrations were synthesized using an aqueous co-precipitation method. Briefly, the precipitation was carried out in the precursor composed of a 0.1 M solution of ferric salt in deionized water and 0.05 M solution of ferrous and manganese salts in 1 M HCl. A solution of 0.03 M trisodium citrate was added to this solution to restrict particle aggregation and to control the crystal

growth. This precursor was magnetically stirred at a temperature of 80°C under an inert atmosphere followed by the dropwise addition of 1 M NaOH, continuously monitoring the pH. At a pH ~12, a black precipitate was observed indicating the formation of MnIO. After completing the addition of the NaOH solution, the reaction was allowed to continue for another 2 h to complete the precipitation of stable MnIO. The black precipitate obtained was magnetically separated, washed initially with deionized water followed by washing with 0.001 M HCl to achieve complete dispersion of the nanocrystals in the aqueous solution. This was further washed with deionized water to attain a neutral pH.

#### **3.4.1.3 Development of Various Concentration of Mn<sup>2+</sup> Substituted SPION**

The experimental procedure in section 3.4.1.2 was repeated for various molar compositions of Mn<sup>2+</sup> to Fe<sup>2+</sup> ratios of 1 : 3, 1 : 1 and 3 : 1 keeping the concentration of ferric salt solution constant, (represented as MnIO25, MnIO50 and MnIO75, respectively). Bare SPIONs were prepared according to a previous section 3.1.2 using ferrous and ferric chlorides in a 1:2 ratio under the same reaction conditions.

#### **3.4.1.4 Physicochemical Characterizations of MnIOs**

##### **3.4.1.4.1 TEM and HRTEM analysis**

The size and morphology of the prepared nanoparticles were studied by transmission electron microscopy (TEM, JEM-2010, JEOL, Tokyo, Japan) at 100 kV and the histogram of TEM particles evaluated using ImageJ software by counting 50 number. The corresponding average particle sizes were calculated with the help of a Gaussian fit. HRTEM images were obtained using a Hitachi HF 2200 TU field emission microscope operating at an accelerating voltage of 200 kV.

#### **3.4.1.4.2 Powder X-ray Diffraction**

Nanocrystal phase analysis was carried out using powder X-ray diffraction. The powder X-ray diffraction measurements were taken using an X-ray diffractometer (Bruker, D8 advance, Karlsruhe, Germany) with  $\text{CuK}_{\alpha 1}$  radiation operating at 40 kV and 30 mA current strength performed at room temperature.

#### **3.4.1.4.3 Fourier Transform Infrared Spectra (FTIR)**

FTIR spectra for all the samples were recorded on a Thermo- Nicolet 5700 spectrometer (Thermo Nicolet 5700, USA) using the diffuse reflectance (DRIFT) mode and to obtain high signal to noise ratio, 64 scans were collected at a resolution of  $4 \text{ cm}^{-1}$ .

#### **3.4.1.4.4 Thermogravimetric Analysis**

Thermogravimetric analysis (TGA) was performed for freeze dried MnIOs samples with a SDT 2960 V2.2B instrument (Simultaneous TGA-DTA, TA Instruments, Delaware, USA) under the nitrogen atmosphere at a heating rate of  $10^{\circ}\text{C min}^{-1}$ .

#### **3.4.1.4.4 Inductively Coupled plasma-Optical Emission Spectroscopy**

The total atomic percentage of iron and manganese were determined by inductively coupled plasma-optical emission spectroscopy (ICP-OES, Perkin Elmer 5300DV, USA). An aliquot (typically 2 mL) of the MnIO nanoparticles dispersion with 1 mL of 3 N analytical grade HCl were used for ICP measurements. The sample solutions were pre-heated to boiling, and then cooled to room temperature, followed by adjusting the volume to 50 or 100 mL as per the required analysis conditions and measurements were conducted.

#### **3.4.1.4.5 ESEM and EDS spectrum**

An environmental scanning electron microscope (Quanta 200, The Netherlands) equipped with energy dispersive X-ray (EDS) spectrum was used to determine the composition of the as-prepared MnIOs samples.

#### **3.4.1.4.5 Magnetic Property Measurement of MnIOs**

Magnetic measurements were carried out on a PAR EG&G Model 4500 Vibrating sample magnetometer (VSM) varying the field between -15 kOe and +15 kOe. Powder samples of MnIOs were placed in a uniform magnetic field and its magnetic properties, saturation magnetization and magnetic hysteresis nature studied at room temperature.

#### **3.4.1.4 Biological Evaluations of MnIOs**

##### **3.4.1.4.1 Cell Culture**

HeLa (human cervical carcinoma) cells were cultured as per mentioned in the section *3.1.4.1*

##### **3.4.1.4.2 Cytotoxicity - Alamar Blue Assay and Light Microscopy**

Alamar blue (AB) assay was carried out as per the procedure mentioned in section *3.1.4*. In this study, HeLa cells were seeded in a transparent 96 well plates and exposed to the nanoparticle [SPION and MnIO<sub>25</sub>, MnIO<sub>50</sub> and MnIO<sub>75</sub>] dispersions at concentrations ranging from 0.5mg to 3mg for 24h. After the exposure, 100µl of alamar blue reagent (invitrogen assay protocol) was added in each well and incubated for 4h at 37°C. The fluorescence was measured at 560 nm excitation and 590 nm emission wavelengths using a plate reader (HIDEX Chameleon) and

expressed in percentage activity of live cells versus control. The experiments were carried out in triplicate for each nanoparticle concentrations. The 24h material exposed cell structure was also evaluated *via* bright field microscopy. Microscopic observations and cell imagery acquired with a Leica DMIL microscope (Leica, Germany) support the non – cytotoxic nature of the particles.

#### **3.4.1.4.3 Hemolysis Assay**

The experiment was conducted as per the section 3.2.6.3. In this study, the MnIOs and controls (1mg) were added into each of the 10 mm<sup>2</sup> polystyrene wells, followed by addition of 1ml blood and incubated for a period of 2h under agitation at  $70 \pm 5$  rpm using an environ shaker thermostat (Kuhner shaker, Switzerland) at  $35 \pm 2^\circ\text{C}$ . Three empty polystyrene culture dishes were exposed to blood as reference. The total hemoglobin in the whole blood samples were measured using automatic hematology analyzer (sysmex-K 4500). The free hemoglobin liberated into the plasma after exposure to materials was measured using Diode array spectrophotometer (Hewlett Packard 8453) and the percentage hemolysis was calculated using the formula  $(\text{Free Hb} / \text{total Hb}) \times 100$ . Hemolysis expressed as a percentage of hemoglobin release was performed to assess the effect of nanocrystals on the blood cell membranes.

#### **3.4.1.4.4 Clotting Time**

Whole human blood was collected from an un-medicated healthy donor without anticoagulant and was transferred immediately to glass tubes for clotting time analysis. Briefly, 1mg of each sample (SPION & MnIOs) was mixed with 1ml of whole blood and time required for clot formation was observed manually by tilting the tube at fixed time intervals measured using a stopwatch. The time period between

the addition of the samples to whole blood and first visible clot formation was taken as the clotting time. Negative (saline) and positive (polyethylenimine) controls were also treated identically.

#### **3.4.1.4.5 RBC Aggregation**

Red blood cell concentration was collected from whole blood in ACD by centrifugation at 3000 rpm for 15min. 1 mg of each of the samples (SPION & MnIOs), positive (polyethylenimine) and negative (saline) control were added to 1ml of 1:10 normal saline diluted red cell concentrates and were incubated in Environ shaker thermostat for 30 min at  $35 \pm 2^\circ\text{C}$ . Aggregation was observed using 40x objective of Leica phase contrast DMIL microscope (Leica, Germany) after 1: 100 dilution of the mixture with normal saline.

#### **3.4.1.4.6 WBC Aggregation**

WBCs were isolated from citrate human whole blood by gradient centrifugation using Histopaque (sigma-1077). Cells were carefully collected and diluted with normal saline to obtain a concentration of 5000-10000 cells per microlitre. 1mg of each samples, positive and negative controls were then added to 1ml of count adjusted WBC and were incubated in Environ shaker thermostat for 30min at  $35 \pm 2^\circ\text{C}$ . Aggregation was observed using 40x objective of Leica phase contrast microscope after 1: 100 dilution of the mixture with normal saline.

#### **3.4.1.4.7 Platelet Aggregation**

Platelets were isolated from citrate human whole blood *via* gradient centrifugation using Histopaque. Cells were carefully collected and diluted with platelet poor plasma to obtain a concentration of  $2.0 - 2.5 \times 10^8/\text{cells}$ . 1mg each of the samples,

positive and negative controls were then added to 1ml of count adjusted platelet solution and were incubated in Environ shaker thermostat for 30min at  $35 \pm 2^\circ\text{C}$ . Aggregation was observed using 40x objective of Leica phase contrast microscope after 1: 100 dilution of the mixer with normal saline.

#### **3.4.1.4.8 Cell Uptake**

To evaluate the cell uptake of SPION and MnIOs, the cells were incubated with 50  $\mu\text{g}$  of SPION and MnIOs at  $37^\circ\text{C}$  for 24h. After incubation, the cells were washed with sterile PBS buffer and fixed with 3.7% paraformaldehyde for 4h. The prussian blue staining was carried out with 7:3 volume ratios of 10% potassium ferrocyanide and 10% hydrochloric acid. After 20 min the cells were washed thrice with distilled water. Further, cells were counterstained by nuclear fast red (NFR) to visualize cell nuclei. Coverslip was mounted in DPX and images were captured on a Leica DMIL microscope.

#### **3.4.1.5 MnIOs Contrast Effect in Magnetic Resonance Imaging**

Relaxivity measurements was executed as per mentioned in the section 3.3.3

In this study, different concentrations of the MnIOs dispersed uniformly in DI water and enclosed in non-magnetic containers served as the phantoms. The relaxation times ( $T_2$ ) using different concentrations of nanoparticles (0 to 0.25 mM) were measured. The concentrations of the nanoparticles were calculated with the help of ICP-OES analysis.  $T_2$  relaxation time was calculated from the resulting MRI pixel intensity maps with respect to each concentration. The relaxivity ( $r_2$ ) value calculated *via* pixel intensity plotted against the MnIO concentrations and  $r_2$  value was determined by the linear fit.

### **3.4.2 Development of Surface Modified Manganese Substituted SPION**

#### **3.4.2.1 Materials**

FeCl<sub>2</sub>.4H<sub>2</sub>O (≥99%), FeCl<sub>3</sub> anhydrous (≥98%), MnCl<sub>2</sub>.4H<sub>2</sub>O (≥99%), NaOH, 35% HCl and trisodium citrate were purchased from Merck (India). Chemicals used for cell culture were exclusively sourced from Invitrogen, India. Alamar Blue, Annexin V/dead cell apoptosis kit was commercially sourced and company prescribed protocol followed (Invitrogen, CAT # DAL1100 and CAT #V13242). The chemicals used for the nanoparticle cell uptake and blood compatibility evaluations were from Sigma-Aldrich, Germany. Nuclear fast red and potassium ferrocyanide were from Carl Roth (Karlsruhe, Germany). Actin cytoskeleton and focal adhesion staining kit (FAK100) and goat anti-mouse IgG FITC conjugate were from Chemicon (Millipore, USA). All the reagents were used without further purification.

#### **3.4.2.2 Synthesis of Surface Modified MnIO Nanoparticles (MnIOTCs)**

The manganese ferrite nanoparticles were synthesized by co-precipitation according to the previous section 3.4.1.2.

In order to stabilize the nanoparticle, the colloidal suspensions MnIO<sub>25</sub>, MnIO<sub>50</sub>, MnIO<sub>75</sub> and SPIONs were dispersed in 10 M trisodium citrate [TC] and stirred at room temperature around 12h. The colloids were centrifuged and washed several times with deionized water to remove un-reacted citrate molecules and re-dispersed in neutral pH. Finally the synthesized aqueous suspensions were freeze-dried and used for physicochemical characterizations and termed as MnIO<sub>25</sub>TC, MnIO<sub>50</sub>TC, MnIO<sub>75</sub>TC and IOTC.

### **3.4.2.3 Physicochemical Characterizations**

#### **3.4.2.3.1 Dynamic Light Scattering**

Dynamic light scattering (DLS) was executed on an aqueous dispersion of ~0.01% w/v in MnIOTCs. Hydrodynamic size and zeta potential values of the particles were estimated with Malvern Instruments Ltd, Malvern, UK.

#### **3.4.2.3.2 X-ray Diffraction Technique**

X-ray diffraction (XRD) was performed on a Bruker, D8 advance, Karlsruhe, Germany, diffractometer with Ni- filtered Cu K $\alpha$  radiation. Samples were dried on a glass petridish, collected, ground and spread on the Bruker sample holder. The instrument was operated at 40kV and 30mA current strength. The crystal structure was determined by analyzing the position and intensities of diffraction peak typically observed in the range of diffraction angle  $2\theta = 20^{\circ}$ – $75^{\circ}$  and at a scan rate of  $4^{\circ}\text{min}^{-1}$  with a step wise of  $0.1^{\circ}$ .

#### **3.4.2.3.3 Thermogravimetric Analysis**

The citrate content in the manganese ferrite samples was determined with thermogravimetric analysis [TGA] using SDT 2960 V2.2B Delaware, USA.

#### **3.4.2.3.4 Transmission Electron Microscopic Analysis**

Samples for TEM were prepared by casting a droplet of a dilute aqueous suspension of MnIOTCs on formvar-coated copper TEM grids and observed in TEM (H-7650, 120kV, Hitachi, Japan).

#### **3.4.2.3.5 Fourier Transform Infrared Spectra**

Fourier transform infrared (FTIR) spectra of samples were recorded using Thermo Nicolet 5700 FTIR spectrometer (USA) in the diffuse reflectance mode. To alter high signal to noise ratio, 64 scans were acquired at a resolution of  $\text{cm}^{-1}$ .

#### **3.4.2.3.6 Vibrating Sample Magnetometry analysis**

The magnetic property of MnIOTCs was analyzed at room temperature using Vibrating sample magnetometry (VSM). The measurements were taken by PAR EG&G Model 4500 magnetometer with an external field varying from -15 to 15 kOe. The magnetization of each samples were obtained as a function of the applied field.

#### **3.4.2.4 Biological Evaluations**

##### **3.4.2.4.1 Cell Culture**

HeLa (human cervical carcinoma) cells were cultured as per mentioned in the section 3.1.4.1.

##### **3.4.2.4.2 Cytoskeleton Evaluation**

Samples for cytoskeletal staining were assessed as follows; cell monolayer on glass cover slip was incubated with MnIOTCs for 24h. Cells were then washed three times with PBS before fixation in 3.7% paraformaldehyde for 24h and stored at 4°C. Further processing was as per kit protocol of Invitrogen. Secondary antibody from Millipore (Millipore Goat Anti-Mouse IgG Antibody, (H+L) FITC Conjugated, CAT # AP124F) conjugated with FITC was used to illuminate cell junctions. Actin was visualized with TRITC conjugated phalloiding and nuclei stained using DAPI. Cover

slips were mounted using light diagnostics mounting fluid [Millipore] and imaged using confocal laser scanning microscope (Carl Zeiss LSM 510 META).

#### **3.4.2.4.3 Cytotoxicity- Alamar blue Assay and Light Microscopic Technique**

Alamar blue (AB) assay was performed as per the procedure mentioned in section 3.1.4. In this study, HeLa cells were seeded in a transparent 96 well plates and exposed to the nanoparticle [IOTC and MnIO25TC, MnIO50TC and MnIO75TC] for 24h and alamar blue was added in each well as per protocol. The fluorescence was measured at 560nm excitation and 590 nm emission wavelengths using a plate reader (HIDEX Chameleon). Experiments were carried out in six times for each nanoparticle concentrations.

#### **3.4.2.4.4 Cell Uptake**

To verify the cell uptake of IOTC and MnIOTC, cell monolayers were incubated with 50 µg of each particle at 37°C for 24h. After incubation, cells were thoroughly washed with sterile PBS buffer and fixed with 3.7% paraformaldehyde for 4h. Prussian blue staining was carried out with 7:3 volume percentages of 10% potassium ferrocyanide and 10% hydrochloric acid for 20min. Stained samples were washed thrice with distilled water, counterstained with nuclear fast red; mounted and imaged on a Leica DM 6000 microscope.

#### **3.4.2.4.5 Blood Compatibility Studies**

Hemolysis and clotting time assay of MnIOTCs were evaluated as per the procedure in previous sections 3.4.1.4.3 and 3.4.1.4.4. In our studies saline and polyethylenimine were used as negative and positive controls respectively. Using

Diode array spectrophotometer (Hewlett Packard 8453) absorbance at 541 nm was considered for percentage hemolysis evaluation.

#### **3.4.2.5 Contrast Efficiency in MRI**

Magnetic relaxivity measurement of samples was performed as per the previous sections 3.3.3 and 3.3.3.1. Various concentrations [0.05 to 0.25 mM] of MnIO75TCs were prepared in aqueous solution. The images from three different planes were acquired and T<sub>2</sub> relaxation times were calculated from the resulting MRI pixel intensity maps with respect to concentrations. Similarly for *in vitro* assessment, the cells were incubated for 24h with different concentrations of MnIO75TC nanoparticle at 37°C and washed with centrifugation for removing excess material. The cells were then re-dispersed in PBS solution and MRI was carried under above conditions.

#### **3.4.2.6 Hyperthermia Studies**

The hyperthermia investigation of MnIO75TC has been carried out as per the previous section 3.3.1. In this study, various concentrations of aqueous dispersed MnIO75TC were used for hyperthermia and calculated the SLP values.

#### **3.4.2.7 Hyperthermia – Cell Death Evaluation**

Hela cells ( $1 \times 10^6$ ) and material at a concentration of 2mg/ml were suspended in a 1.5 ml eppendorff tube with a final volume of 200 $\mu$ l. An alternating magnetic field of 33.8mT and 275 kHz was applied to the test tube containing cell suspensions for 30min. Cell suspension placed to maximum field strength of the induction coil and temperature of the suspension monitored by an infrared thermometer. After AMF

application cell suspension was incubated for 1h at 37°C. Cell suspension containing 2mg/ml MnIOTC without AMF application was taken as control.

#### **3.4.2.7.1 Hyperthermia Cell Death – FACS Analysis**

Cells were then washed twice in 1X PBS and re-suspended in PBS. Cells were further stained with live dead staining kit [Invitrogen FITC Annexin V/Dead Cell Apoptosis cat no:V13242]. Post - staining, cell population was evaluated *via* flow cytometric analysis [FACS ARIA, BD Biosciences, San Jose, CA,USA] and percentage of stain expressed cells was calculated by using BD FACS Diva software (BD Biosciences, San Jose, CA, USA).

#### **3.4.2.7.2 Hyperthermia Cell Death – ESEM Analysis**

For morphological analysis HeLa cells were grown adherent on round glass coverslips (Blue Star, India) and exposed to 2mg/ml of MnIO75TC followed by AMF exposure for 30min and incubated for 1h at 37°C. The cells were fixed in 1% glutaraldehyde for 2h and dehydrated in an ascending alcohol series and evaluated by Environmental scanning electron microscopy (FEI QUANTA 200).

## Chapter 4

### RESULTS

#### 4.1 Development of SPION Embedded HA Nanocomposites (HAIO)

##### 4.1.1 Synthesis of HAIO and Physicochemical Characterizations

By an *in situ* co-precipitation we prepared the SPION embedded HA nanocomposite (HAIO) particles. The iron oxide precursors such ferrous and ferric salts in a molar ratio 1:2 and hydroxyapatite precursor calcium salts and phosphate salts to get a Ca/P ratio of 1.67 were employed for the preparation of HAIO. The detailed synthesized conditions described in the materials and methods (section 3.1.2). Reaction parameters such as pH, temperature and atmospheric condition were optimized. HAIO synthesis was followed by developing various concentrations of SPION embedded HA composites. To determine crystal structure XRD evaluation of SPION, HA & HAIO was carried out. Results as in figure 1A for crystal structure and cell parameter analysis were obtained. The major peaks of HA (002), (211), (112), (300), (310), (222), and (213) and SPIONs of (220), (311), (400), (422), (511), and (440) can be clearly seen in the HAIO composites. XRD patterns of HAIO containing HA was in good agreement with the reference HA pattern (PDF=09-0432) and SPION pattern (PDF= 01-071-6336). Upon changing the molar concentration of SPION and HA, various compositions of HAIO were developed and the corresponding XRD patterns are depicted in figure 1B.

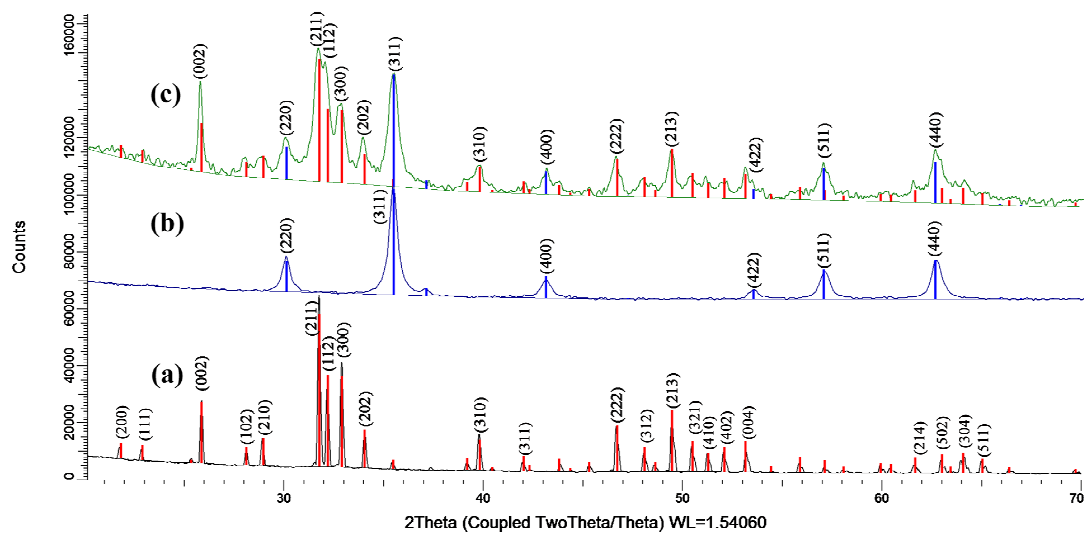


**Figure 1A:** X-ray diffraction (XRD) pattern of (a) HA, (b) SPION and (c) HAIO;

[ - HA PDF = 00-009-0432, - SPION PDF = 01-071-6336]

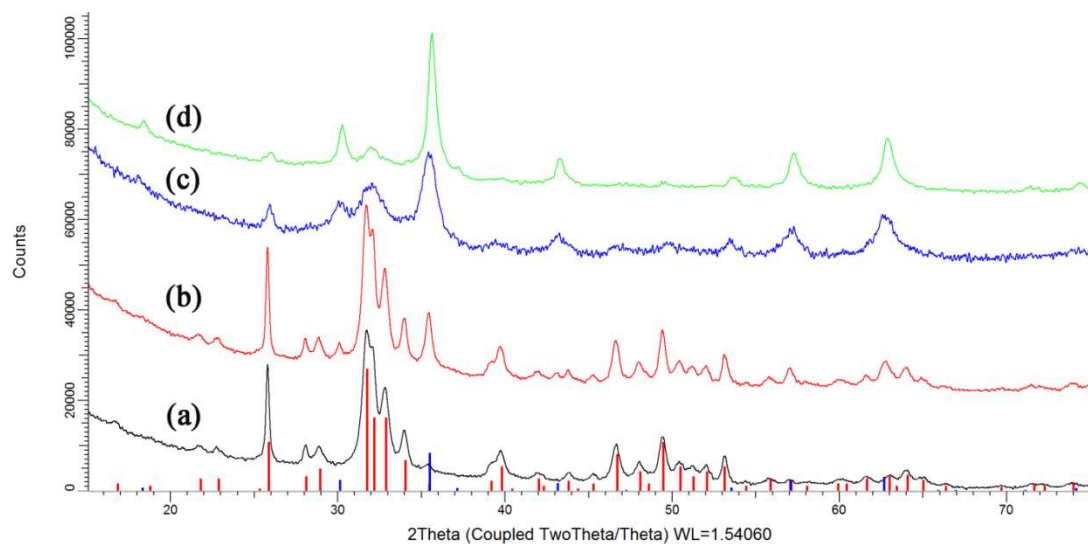


**Figure 1B:** XRD pattern of a) HAIO10 b) HAIO30 c) HAIO70 d) HAIO90;

[ - HA PDF= 00-009- 0432, - SPION PDF= 01-071-6336]

However the molar compositions of HAIOs have great importance in the crystal structure, shape and morphologies. Transmission electron and scanning electron microscopic evaluation provides interesting information on the morphological features of the various compositions of magnetic nanocomposite. Figure 2 and figure 3 are the respective TEM and SEM micrographs, depicting the acicular or needle shaped crystals of hydroxyapatite containing SPION nanoparticles within it.

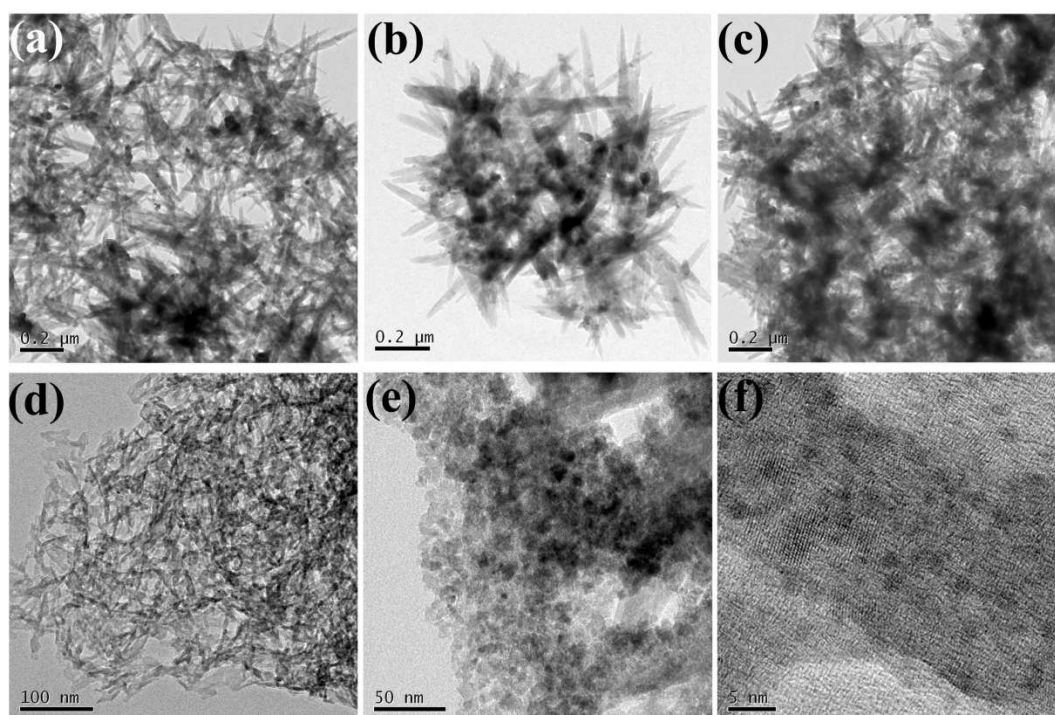


**Figure 2:** Transmission Electron Micrographs of various weight percentage of SPION embedded HA samples (a) HAIO10, (b) HAIO20, (c) HAIO30, (d) HAIO40, (e) HAIO50 and (f) Higher magnification of HAIO50

It was observed that with increased concentration of SPION particles, the shapes and crystal growth patterns were altered, transforming from needle to spherical. The lower concentrations of SPION of 10, 20 and 30 wt% show acicular nature crystals (as seen from Figure. 2a–c and 3a–c), while higher concentrations of 40 and 50 wt% changed from acicular to spherical shaped HAIO composites (Figure. 2d and e and 3d and e).

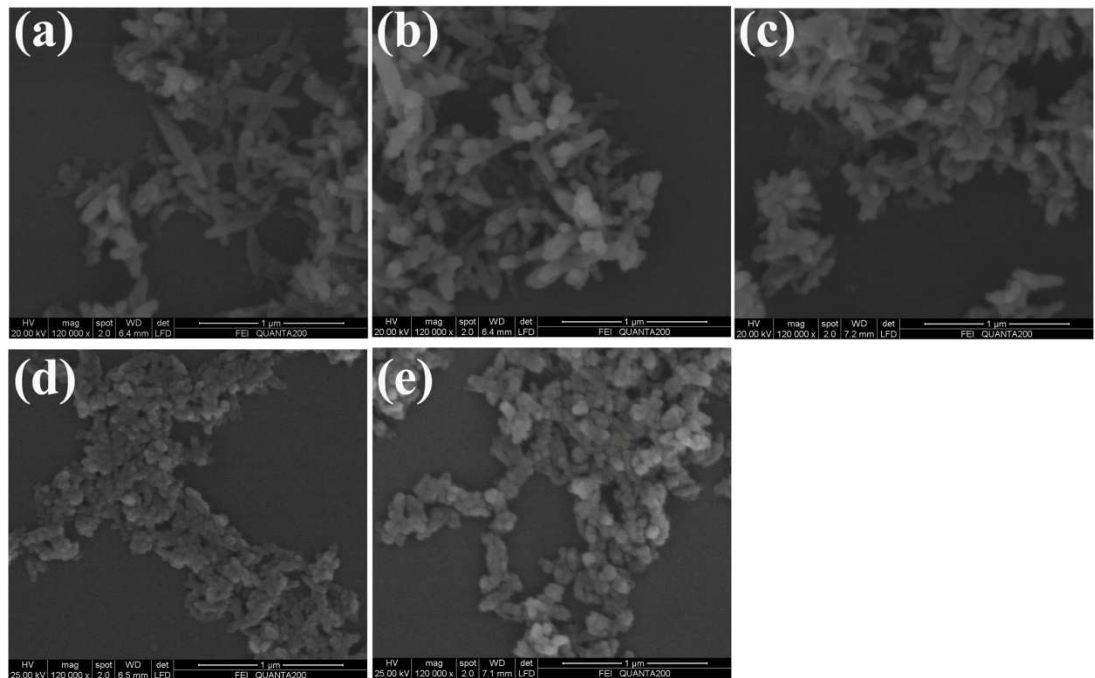


**Figure 3:** Scanning Electron Micrographs of HAIOs a) HAIO10 b) HAIO20 c) HAIO30 d) HAIO40 and e) HAIO50

Figure 4a–e and Figure 5a–e present the EDS spectra of various compositions of HAIOs taken from the respective TEM and SEM micrographs. The corresponding peak intensities of iron, calcium and phosphorous elements in the EDS spectra were in good agreement with the formation of all weight percentage compositions.

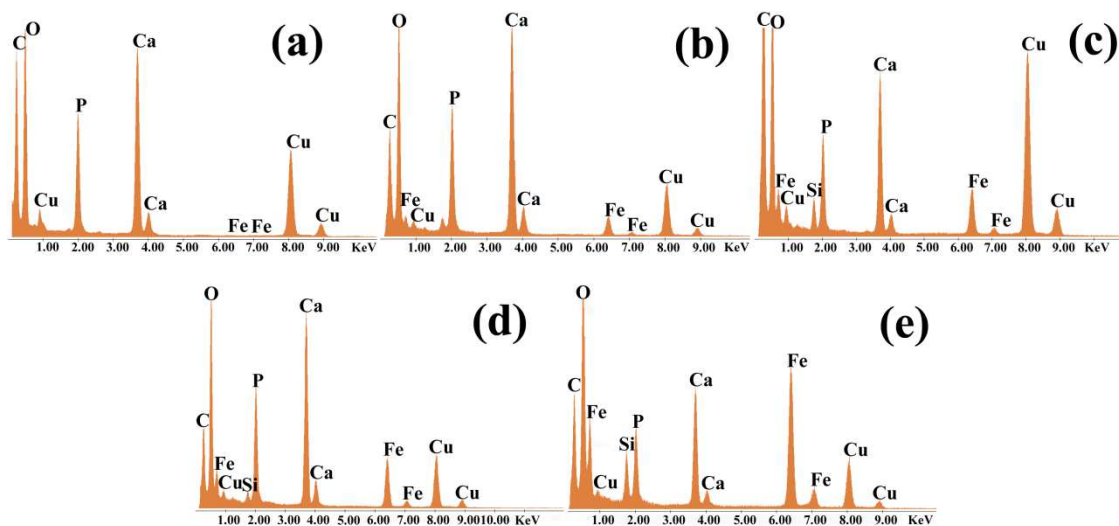


**Figure 4:** Energy Dispersive Spectra (EDS) of (a) HAIO10, (b) HAIO20, (c) HAIO30 (d) HAIO40 and (e) HAIO50 from TEM grid

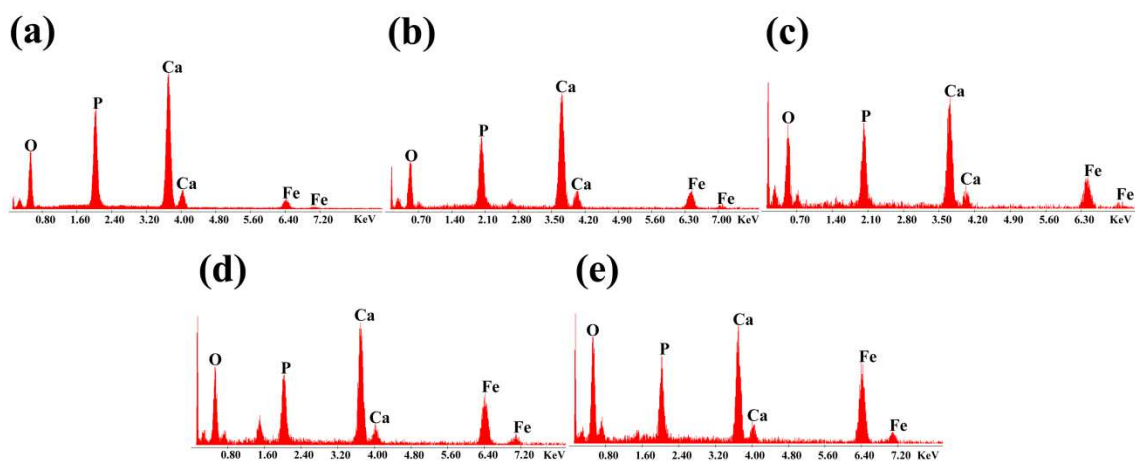


**Figure 5:** Energy Dispersive Spectra (EDS) of a) HAIO10 b) HAIO20 c) HAIO30 d) HAIO40 and e) HAIO50 from SEM stub

The vibrational spectroscopic evaluation of the samples was carried out with FTIR technique and the results are presented in Figure 6A and 6B. The FTIR spectrum of

the HAIO50 composites has a characteristic peak at  $572\text{ cm}^{-1}$  corresponding to stretching frequency of the Fe–O bond of the  $\text{Fe}_3\text{O}_4$  crystals (Chen et al., 2013). Moreover, the vibration of hydroxyapatite, such as the  $\nu_1$  (P–O) vibration of phosphate, is observed as a peak at  $\sim 962\text{ cm}^{-1}$ . A peak at  $\sim 471\text{ cm}^{-1}$  is identified as the  $\nu_2$  (O–P–O) vibration of the phosphate group. The peaks observed at  $\sim 1090$  and  $\sim 1040\text{ cm}^{-1}$  have been identified as  $\nu_3$  (P–O anti-symmetric) vibrations. The  $\nu_4$  vibrations have been observed at  $\sim 604$  and  $567\text{ cm}^{-1}$ . These characteristic peaks show the formation of the pure magnetite phase embedded hydroxyapatite nanocomposite. In addition, from analysis of the FTIR spectra various weight percentage compositions of HAIOs, there were no significant differences between the HA peaks and the SPION peaks observed.

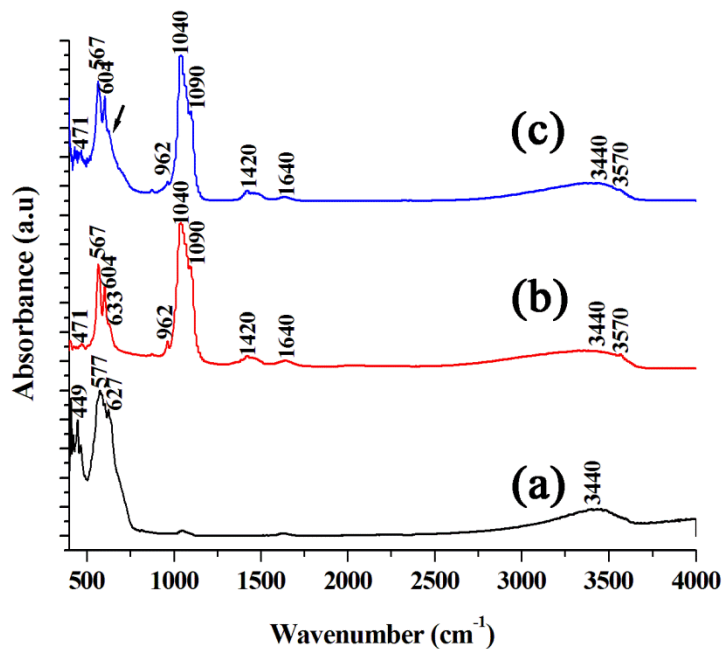


**Figure 6A:** Fourier Transform Infra red Spectra of a) SPION b) HA c) HAIO50

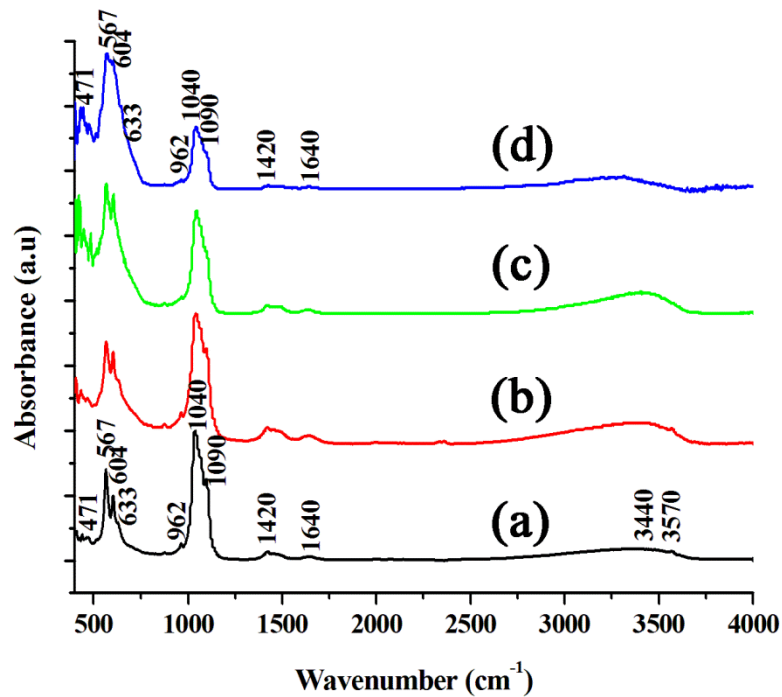


**Figure 6B:** Fourier Transform Infra red Spectra (FTIR) of various weight percentages of HAIOs a) HAIO10 b) HAIO30 c) HAIO70 and d) HAIO90

Magnetic measurements of HAIOs and SPION measured at room temperature are given in Figure 7. The bare iron oxide expresses highest magnetization value (73emu/g), and its corresponding composites decreases with lesser content of magnetic crystals in the composites nanoparticles.

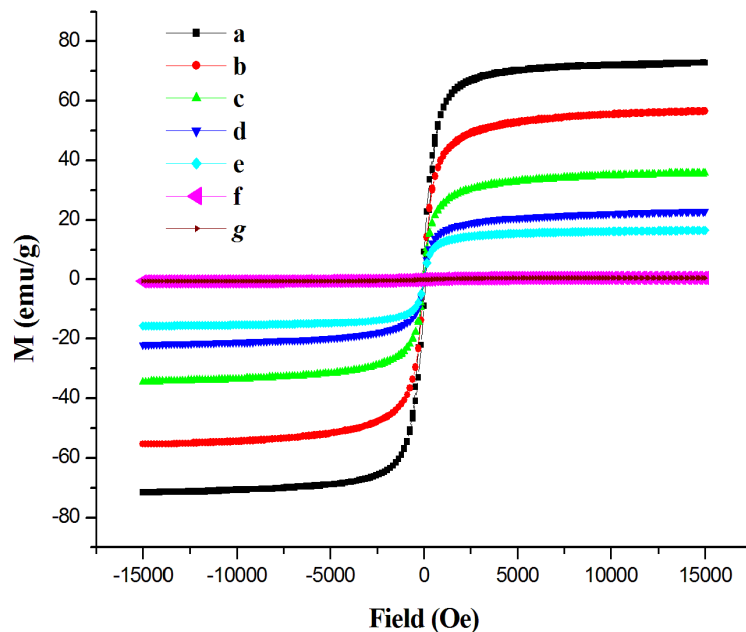


**Figure 7:** Field-dependent magnetization curves (M-H) at 300K for magnetic composite with compositions of a)HAIO10 b)HAIO30 c) HAIO50 d)HAIO70 e)HAIO90 f)SPION and g) HA

From an application point, interest was on minimum concentration of SPION embedded HA having good magnetic property. In our study the HAIOS with lesser content of SPION with good magnetic response were observed in HAIO50. The HAIO50 shows magnetization value 23emu/g, which is suitable for potential biomedical application and it shows optimal response and accumulates in the presence of external magnet. Moreover surface potential and hydrodynamic size of HAIO50 was measured using DLS technique and values were observed as -20.2 mV and 150–170 nm respectively and are depicted in the figure 8.

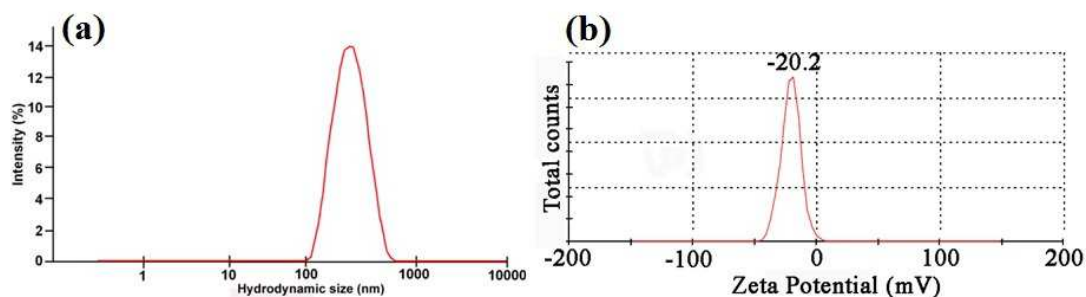


**Figure 8:** (a) hydrodynamic size and (b) zeta potential value of HAIO50 particles.

#### 4.1.2 Biological Evaluation of HAIOs

Preliminary cytocompatibility of HAIOs was evaluated by MTT assay and hemocompatibility test. The MTT assay was used to measure cell viability after incubation with HAIO's. Cells were incubated with test samples for 24 hours and viability index was measured in percentage scale based on formazan production.

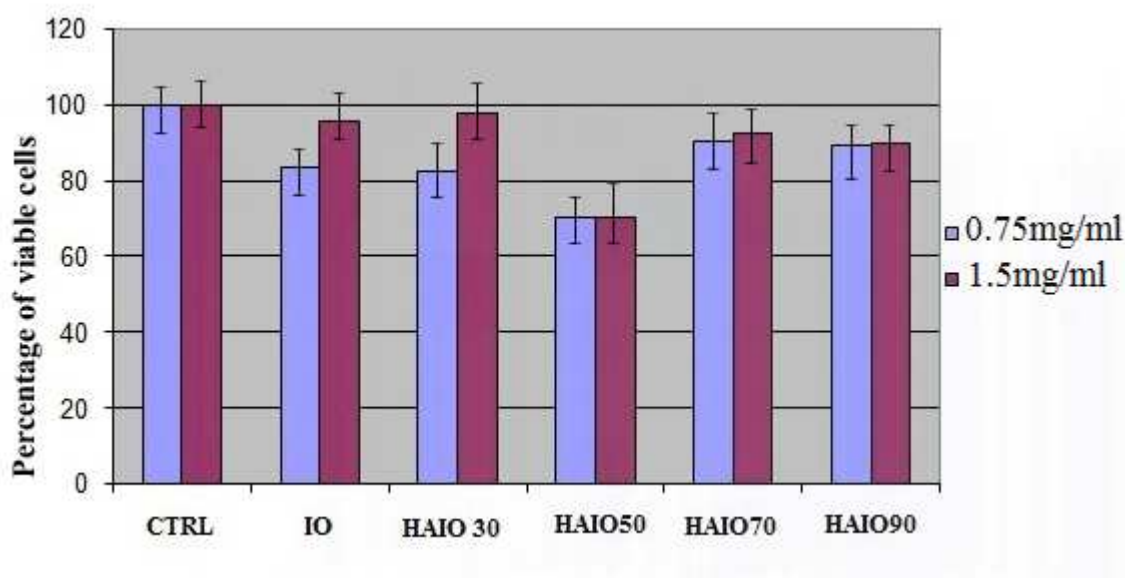


**Figure 9:** MTT test of HeLa cells treated with 0.75mg/ml & 1.5mg/ml of SPION and HAIOs ( $p < 0.05$ )

Figure 9: demonstrate that HAIO30, HAIO50, HAIO70 and HAIO90 nanoparticles are associated with very low toxicity when concentrations 0.75mg/ml and 1.5mg/ml were used over a period of 24 hours of exposure.

A detailed biological evaluation was performed on lower weight percentage SPION compositions of HAIOs. Hence the various concentrations of HAIO50 cytocompatibility assessed *via* Alamar Blue assay and depicted in Figure 10. Followed by hemolysis study was performed to assess the blood compatibility of the candidate materials, since the intravenous route is the most commonly explored way of administration in practical scenarios. The resulting damage, if any, is expressed as percentage of hemoglobin release in Table 1.

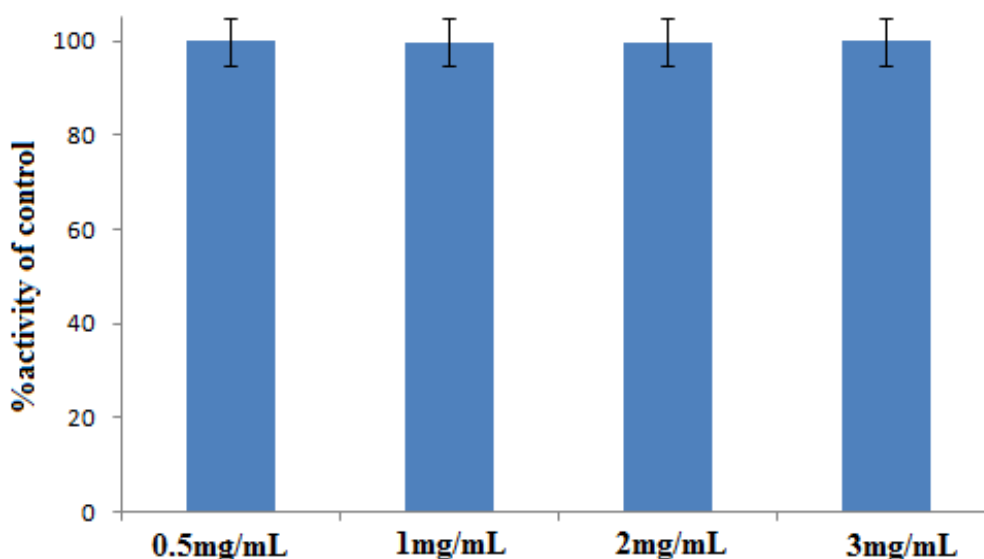


**Figure 10:** Cell Activity at 24hrs contact with HAIO50 various concentration evaluation *via* Alamar Blue assay ( $p < 0.05$ )

Concentration of HAI050 (mg/ml)	0.1	0.3	0.5	Positive control	Negative control
% Hemolysis	0.79 ± 0.13	0.96 ± 0.20	1.05 ± 0.13	75.08 ± 0.86	0.70 ± 0.07

**Table 1:** Hemolysis analysis of HAI050 nanocomposites various concentrations

To evaluate the cell uptake of HAI050 particles, Prussian blue staining was done. For this analysis, iron staining was carried out to evaluate the presence of magnetic nanoparticles. 120 µg/mL of the HAI050 nanocomposite was incubated with HeLa cells followed by Prussian blue staining. As per Figure 11, positive Prussian blue staining does not affect the morphology of the cells and they retain their native cellular structure *in vitro*, thus proving to be non-cytotoxic.

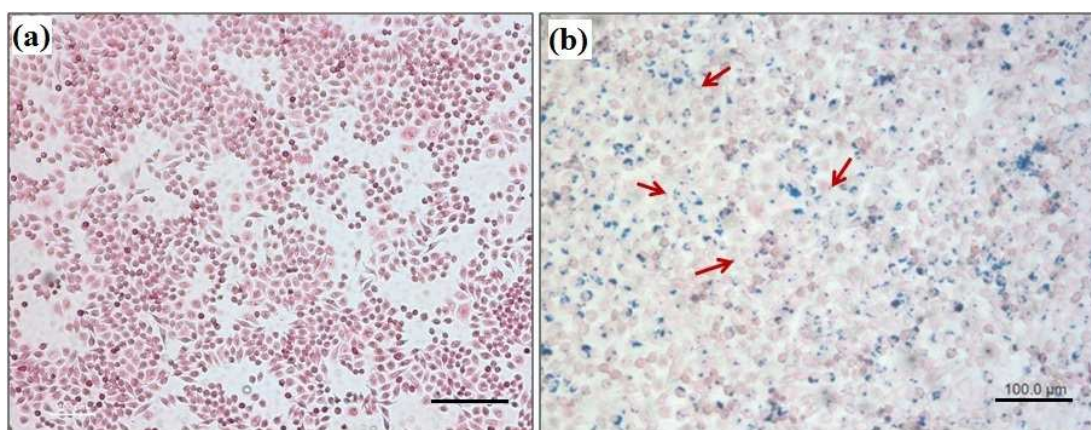


**Figure 11:** Phase contrast light micrographs of HeLa cells incubated with 120µg of HAI050 - a) Control and b) stained with Prussian Blue

Flow cytometric analysis was used to estimate cell–material interactions as a function of time with exposure to different doses of the nanoparticles. Side scatter (SSC) is generally thought to be related to both the granularity of the cell and the cell mass. The SSC signal is affected by the refractive index of the cytoplasm and the

number of organelles present in the cell (Tzur et al., 2011), (Zucker et al., 2010).

Generally, FSC provides information on the overall size of the cells.

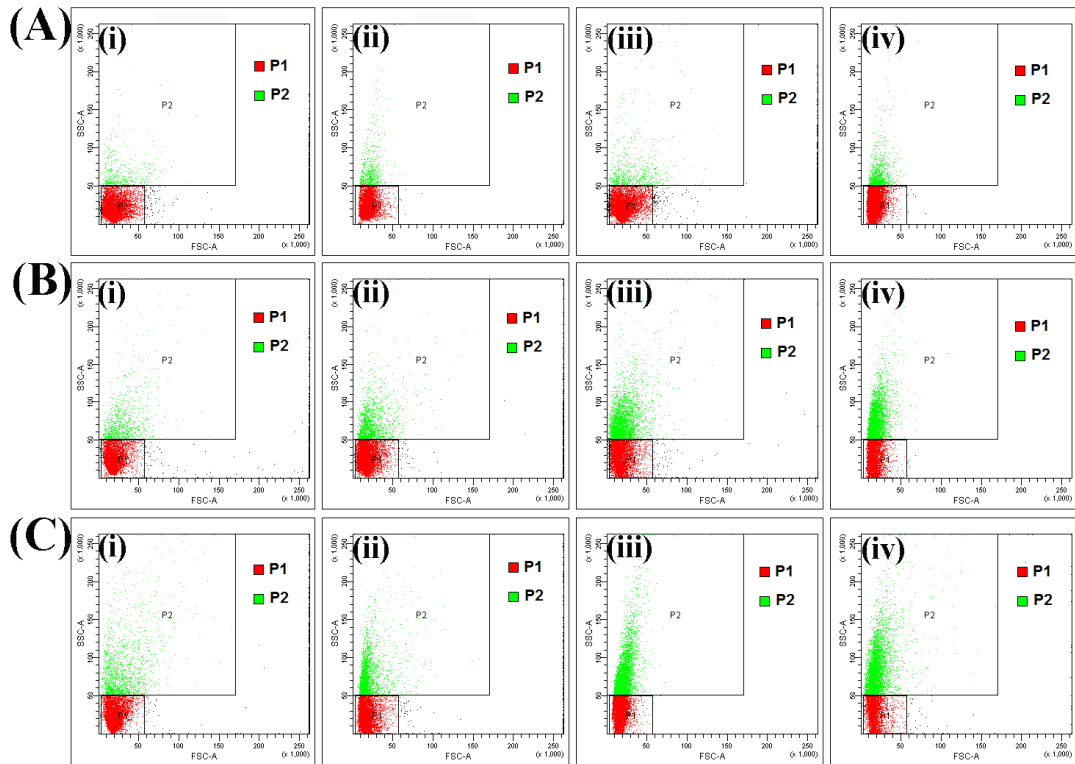


**Figure 12A:** FSC vs SSC plots of Flow Cytometric measurement of granularity change in HeLa cells; A, B & C are represents 120 $\mu$ g, 240  $\mu$ g & 480  $\mu$ g of HAI050 in contact with 10<sup>6</sup> cells and (i), (ii), (iii) & (iv) indicated analysis at time points - 0,5, 10 & 15 min. ■P1= cells gated as Control indicated by no change in values ■P2= Cells in interaction with HAI050 indicated by linearly correlated intensity of SSC channel. Plots indicate increase in uptake of HAI050 from zero to fifteen min & a dose dependent response at longer time period with higher dosage.

Time (min)	Control		HAIO50 120 $\mu$ g		HAIO50 240 $\mu$ g		HAIO50 480 $\mu$ g	
	P1	P2	P1	P2	P1	P2	P1	P2
0	99.2	0.8	81.4	3.8	61.9	8.9	73.5	15.3
5	99.2	0.8	94.2	5.7	70	15.5	64.8	24.7
10	99.5	0.5	78.4	6	63.4	34	61.3	38.6
15	99.6	0.4	90.6	9.4	59.2	40.7	43.2	52.8

**Table 2:** Percentage Gated Population of P1 & P2: time & dose based variance clearly expressed. P1= cells gated as Control indicated by no change in values, P2= Cells in interaction with HAIO50 indicated by linearly correlated intensity of SSC channel.

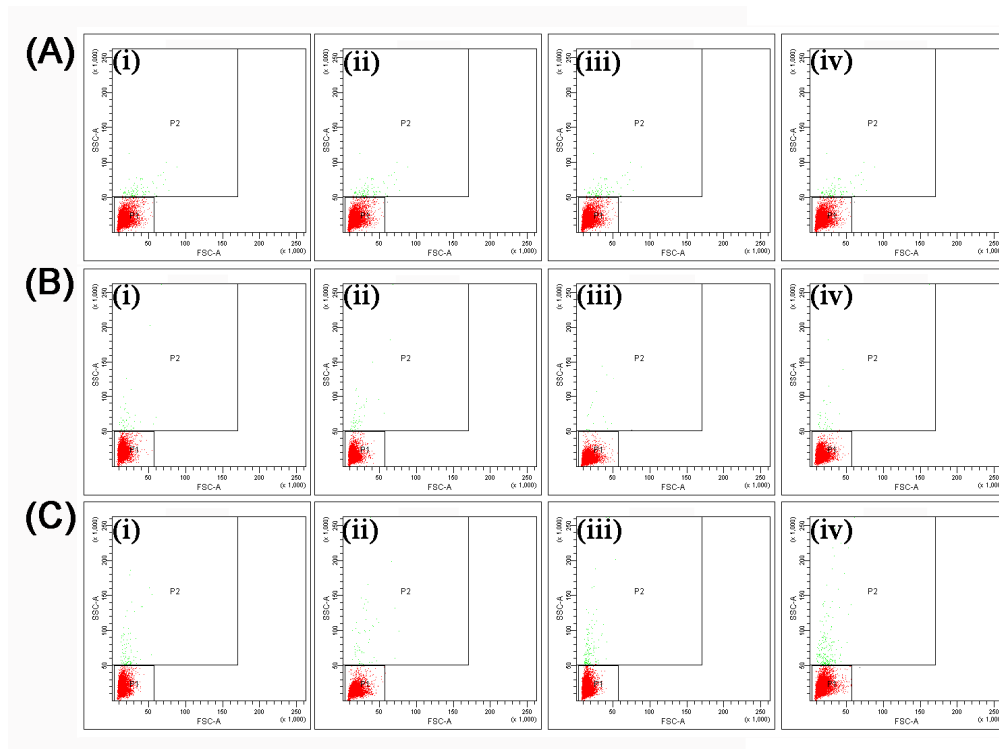


**Figure 12B:** FSC vs SSC plots of Flow Cytometric measurement of granularity change in HeLa cells; A control, B & C are represents 30 $\mu$ g & 60 $\mu$ g of HAIO50 in contact with  $10^6$  cells and (i), (ii), (iii) & (iv) indicated analysis at time points - 0.5, 10 & 15 min. ■ P1= cells gated as Control indicated by no change in values ■ P2= Cells in interaction with HAIO50

Time (min)	Control		HAIO50 30µg		HAIO50 60µg	
	P1	P2	P1	P2	P1	P2
0	99.2	0.8	99.6	0.4	99.2	0.8
5	99.2	0.8	99.6	0.4	99.5	0.5
10	99.5	0.5	99.8	0.2	98.1	0.1
15	99.6	0.4	99.4	0.6	98.2	1.2

**Table 3:** Percentage Gated Population of P1 & P2: time & dose based variance clearly expressed. P1= cells gated as Control indicated by no change in values, P2= Cells in interaction with HAIO50 indicated by linearly correlated intensity of SSC channel

Approximately  $1 \times 10^6$  HeLa cells were treated with 30, 60, 120, 240 and 480 µg doses of HAIO50 and held for time periods varying from T0 to T15 (minutes). The corresponding cellular interactions were assessed *via* changes in forward scatter (FSC) and side scatter. As indicated in Figure 12A and Figure 12B. However, in cells treated with higher concentrations of HAIO50 of 240 and 480 µgs, FSC was constant but SSC intensity was higher depending on the incubation time, as presented in Table 2 and Table 3.

## **4.2 HAI050 Assisted Cell Separation, Manipulation and Culturing Using External Magnetic Field for Introducing Targeted Cell Delivery**

### **4.2.1 HAI050 Aided Cell Separation Experiment**

The cell separation experiment has been carried out with HAI050 nanoparticles with the aid of external magnetic field.  $1 \times 10^6$  HeLa cells were incubated with Acridine Orange and exposed to HAI050 particles. Cells were separated using an external magnet, which has been demonstrated in the Figure 13. Cells with HAI050 uptake were responsive to magnetic field within 2 min and concentrated to form a pellet within 10 min.

To better explore HAI050 as an efficient probe for floating cell separation from suspension and evaluate its potential as a carrier for cell therapy, low doses of HAI050 nanoparticles (30, 60, 120, 240, 480, and 960  $\mu\text{g}$ ) were incubated with Acridine orange stained  $1 \times 10^6$  HeLa cells. The supernatant after magnetic separation as well as the pellet were subjected to population analysis using a Coulter Cell Counter. A concentration of 480  $\mu\text{g}$  of HAI050 efficiently separated from all cells from suspension with 15 min incubation. To elucidate the mechanism of interaction with the nanoparticles, separation experiments were carried out at a temperature of 4 °C. The separation efficiency of the 480 $\mu\text{g}$  dose was preserved at 4°C on comparison to that at room temperature (Table 4).

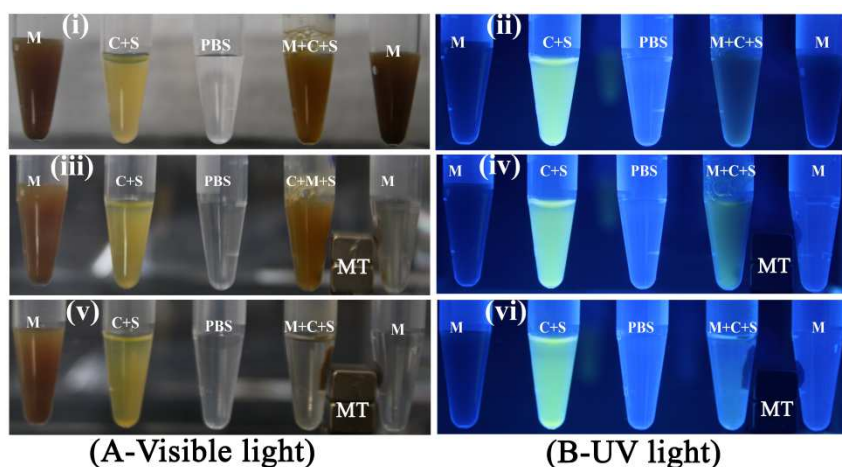


**Figure 13:** Visible Light (A- i, iii, v) & UV (B - ii, iii, vi) Illumination of Acridine Orange (AO) stained HeLa cells incubated with HAI050 for 15min and separated with an external magnet (MT) placed in the vicinity between 4<sup>th</sup> and 5<sup>th</sup> tubes [0.3T]: M=HAI050 alone, C+S= cells stained with AO, PBS= buffer, M+C+S= stained cells and HAI050. (i) & (ii) zero min (iii) & (iv) 2min, (v) & (vi) 10min, post magnetic exposure

Concentrations of HAI050 ( $\mu\text{g}$ )	Supernatant cell count (HeLa $\times 10^3$ cells)	
	Temperature (25°C)	Temperature (4°C)
30	1.4	2
60	0.8	1.6
120	0.6	1.4
240	0.3	0.6
480	0.2	0
960	0	0

**Table 4:** The coulter counter cell count of supernatant from HAI050 magnetically separated cells done at room temperature (25°C) and low temperature (4°C). Cells separated from suspension linearly decreased with concentration of material.

As cells are tagged with Acridine orange, to ascertain the fluorescent intensity of supernatant and pellet, the magnetically separated stained HeLa cells were placed under a UV transilluminator. Images in Figure 14 show that there was strong green fluorescence in the control tube while fluorescence was absent in the supernatant from tubes B and C, corresponding to 480  $\mu\text{g}$  and 960  $\mu\text{g}$ , respectively. The supernatant from tubes D through G, 240, 120, 60 and 30  $\mu\text{g}$ , respectively, showed increasing levels of fluorescence, which further corroborate the Coulter counter observations of a residual cell population at lower particle concentrations. To confirm cell separation into the pellet compartment, pellets were re-suspended and observed under UV illumination. A dose-dependent decrease in fluorescence with lowering the dose could be visualized in Figure 14.

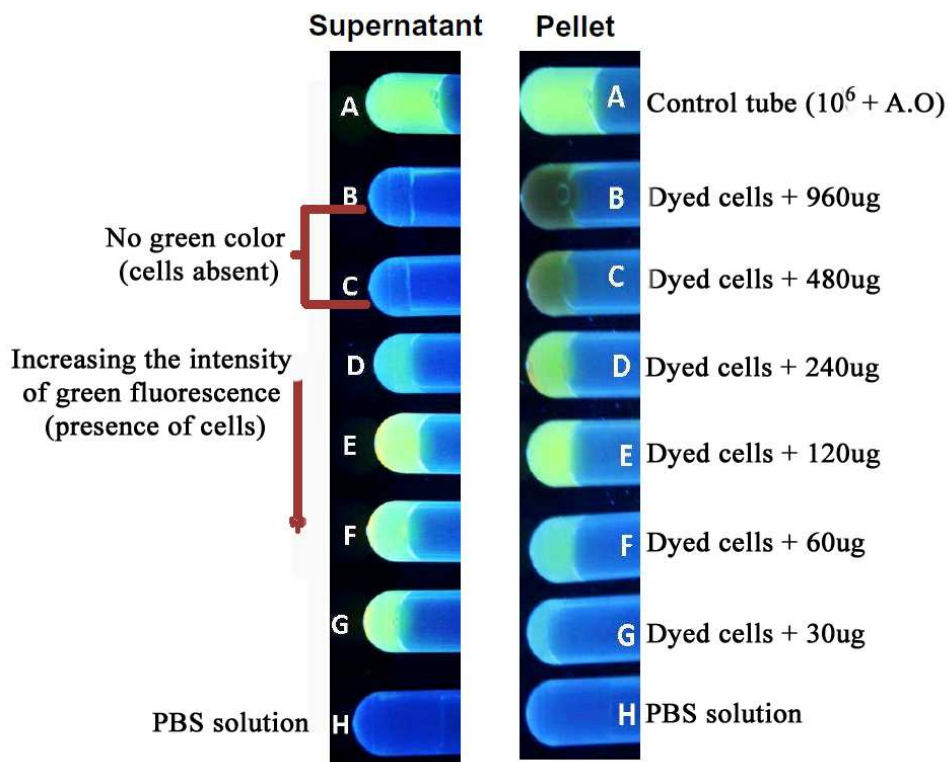


**Figure 14:** The Acridine Orange (AO) pre-stained HeLa cells were incubated with various concentrations of HAI050 for 15min and magnetically separated. Supernatant collected and the corresponding pellets were re-dispersed in PBS buffer. Images of dispersion were taken on UV transilluminator

#### 4.2.2 Structure and Morphology Evaluation of Magnetically Separated Cells

Separated cell morphology was evaluated *via* Giemsa staining and ESEM techniques. Giemsa-stained cells were viewed as a dark purple colour under light microscopy, as represented in Figure15, while the unattached cells on the glass slide were observed as spherical units with a dark violet colour in both the control and the pellet. HAI050 clumps appeared as a dark yellow colour in both the pellet and the bare sample.

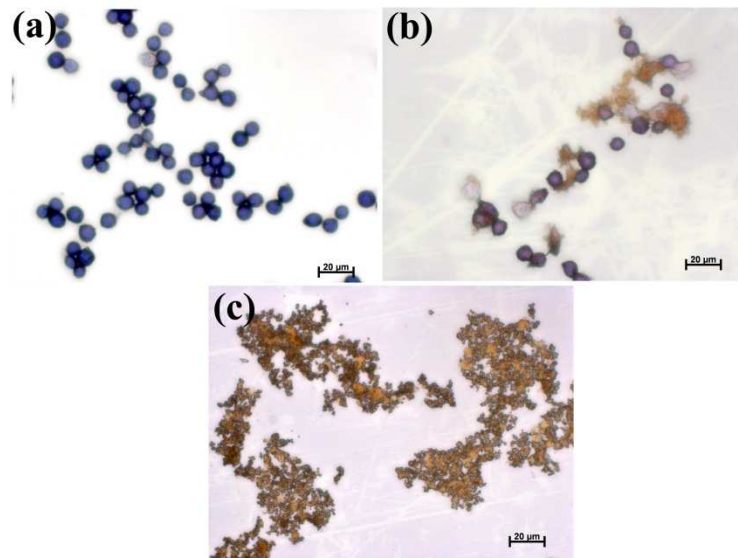


**Figure 15:** Giemsa Stained HeLa cells: (a) cells alone indicated by clear blue spheres (b) Magnetically separated HAIO50 pellet containing cells identical to (a); and (c) HAIO50 alone

Environmental scanning electron microscopy (ESEM) and energy dispersive spectrum (EDS) were further used to evaluate the smears of the control and the pellet recovered cells, as depicted in Figure 16.

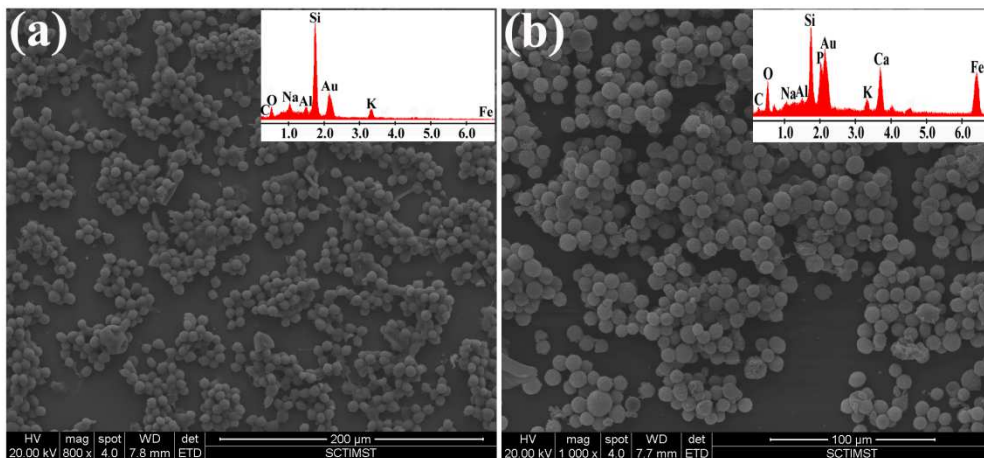


**Figure 16:** Scanning Electron Micrographs: (a) Cells alone and (b) Magnetically Separated HAIO50 Cell pellet. The corresponding energy dispersive spectra are in inset

#### **4.2.3 Magnetically Separated Cells were Cultured under *In vitro* Condition**

Cells were separated using a 60  $\mu\text{g}$  HAIO50 dose and maintained under standard cell culture conditions for 24 hours post separation. Actin staining and visualization using confocal laser scanning microscopy studies confirmed the normal cytoplasmic skeletal organization (Figure 17).

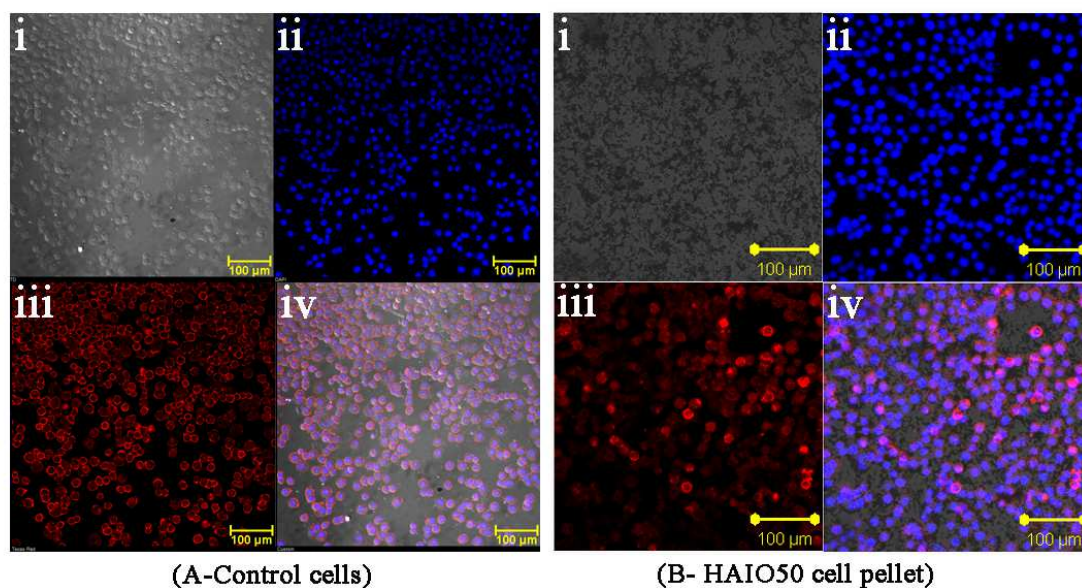


**Figure 17:** Confocal Laser Scanning Micrographs of magnetically separated HAI050 Cell pellet in culture for 24 hrs (i) in DIC mode (ii) DAPI (nuclei) stained cells (iii) Rhodamine Phalloidin stained Actin and (iv) merged image of (ii) & (iii). A – Control of cells alone and (B) Magnetically separated HAI050 Cell pellet

#### **4.3 HAI050 Conjugated HeLa Cells were Magnetically Levitated and used for Three Dimensional [3D] Culturing**

In order to investigate the HAI050 and levitation, HAI050 conjugated HeLa cells were levitated in a cell culture medium using an external magnetic field.

We observed that the magnetic field concentrated clusters of levitated cells in solution, triggering cell–cell interactions in a mode consistent with tissue engineering scaffolds designed to enhance cell growth advantage. After 72h the 3D cell cultured viability, proliferation and cytoskeletal structures were evaluated using ESEM, fluorescent microscope and phase contrast microscopy.

Morphological analysis using ESEM is depicted in the Figure 18. Cells proliferated to form a sheet like structure and the higher magnification clearly showed the cellular integrity and cells attached magnetic HAIO50 particles. Nuclear staining has been carried out with DAPI staining and phase contrast light microscopic images were taken and depicted in the Figure 19. The morphology and cell-cell interaction revealed efficiency and the nontoxic nature of the HAIO50 aided 3D model cell culture.

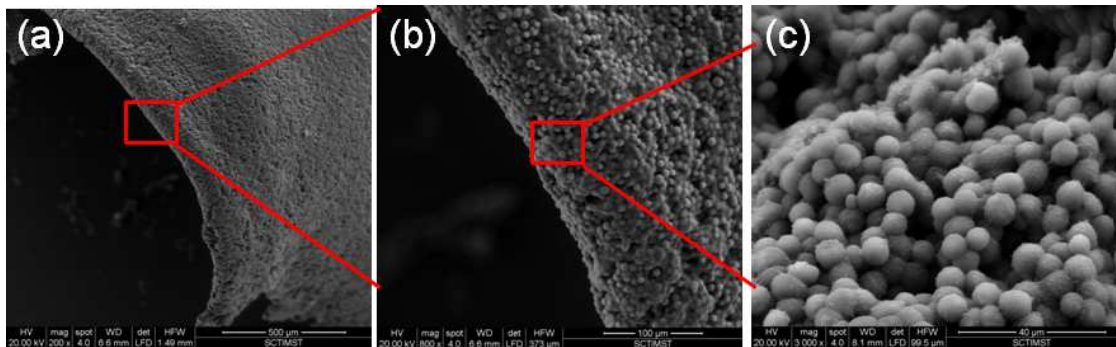


**Figure 18:** (a) 200X (b) 800X, (c) 3000X images of three dimensionally cultured HeLa cells sheet on 72h

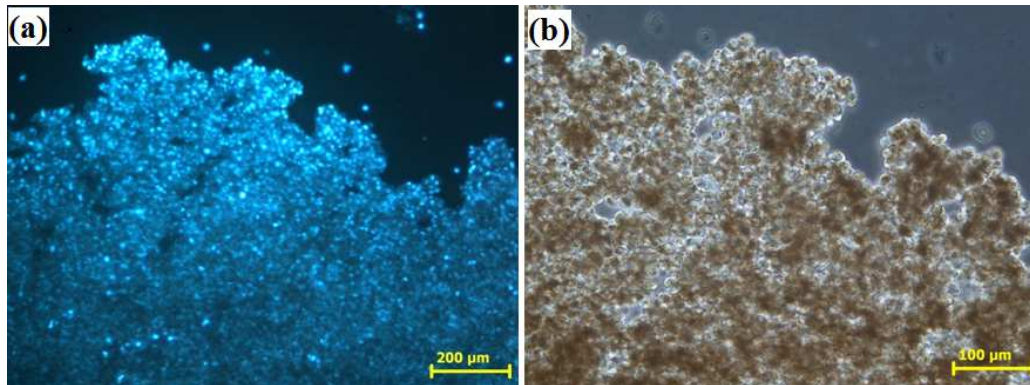


**Figure 19:** cell sheet construct ruction after 72h 3D culturing (a) DAPI nuclear staining (b) phases contrast light microscopic image

#### **4.3.1 Synthesis of HAIO Embedded Polycaprolactone Magnetic Microspheres [HAIO PCL] and Physicochemical Characterization**

The HAIO embedded polycaprolactone magnetic microspheres were developed *via* solvent evaporation techniques. HAIO particles were an inorganic magnetic material with the property of hydrophilic surface while PCL was an organic hydrophobic material. Here we used dichloromethane as a solvent, the magnetic microsphere could be formed as HAIO embedded PCL magnetic microspheres.

The size of the microspheres were optimized by varying the concentration of PCL polymer (5, 7.5 and 10 wt %). The morphology and microsphere size was evaluated through SEM technique and depicted in the Figure.20. The results showed that at a lower polymeric concentration, microsphere size was smaller and on increasing the polymeric concentration, microsphere size gradually increases. Magnetic microsphere synthesis using 10wt% of polymer was carried out and spheres evaluated by SEM Figure 21.

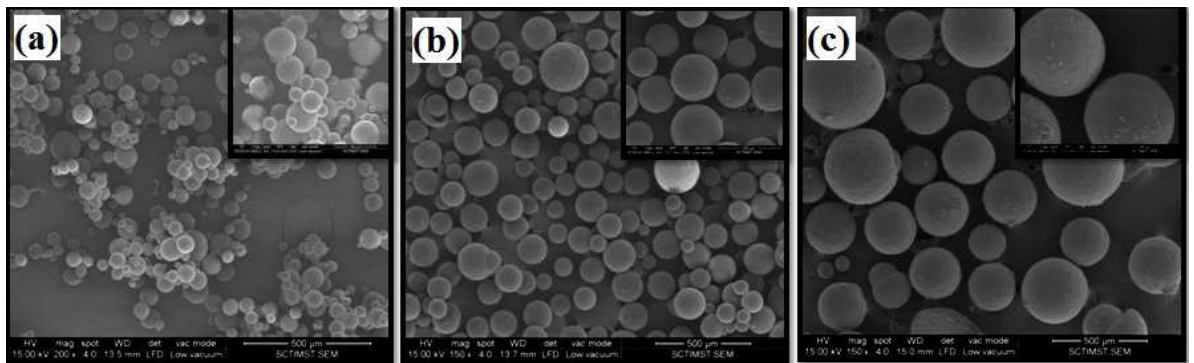


**Figure 20:** SEM images of polycaprolactone microsphere (a) PCL 5 (b) PCL 7.5 (c) PCL10

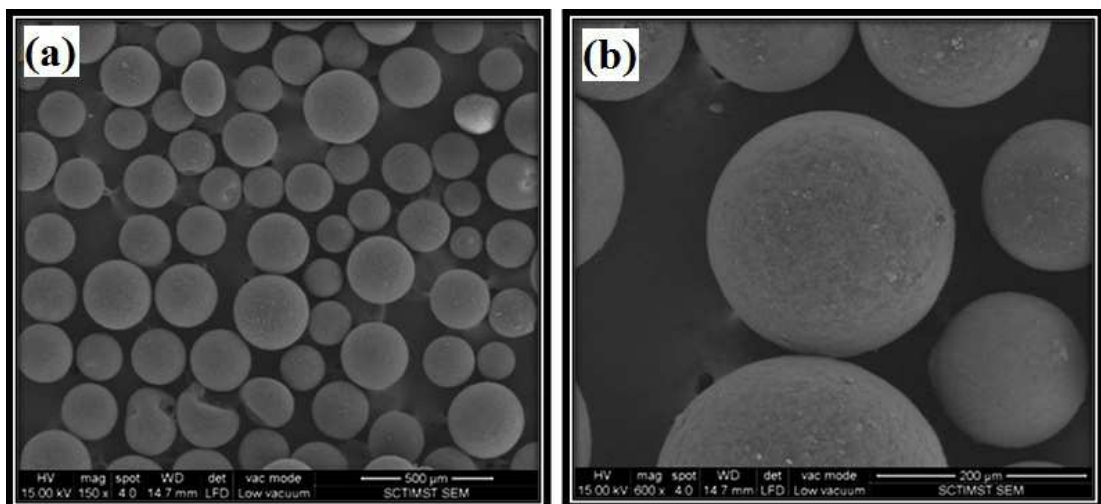


**Figure 21:** (a) & (b) are Low and high magnification SEM images of HAIO PCL magnetic microsphere

The crystallinity and bonding in HAIOPCL was evaluated via XRD & FTIR. Coresponding spectra are as in Figure 22 & 23. However, HA and iron oxide spectral intensity were suppressed by the presence of PCL polymer in compoite.

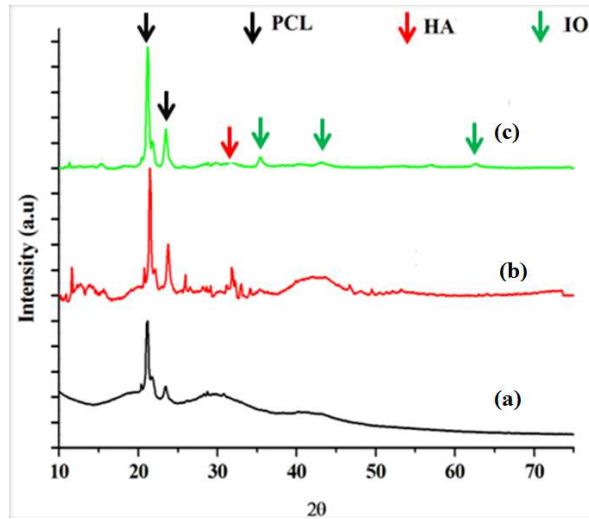


**Figure 22:** XRD measurement of magnetic microspheres (a) PCL (b) HAPCL (c) HAIOPCL

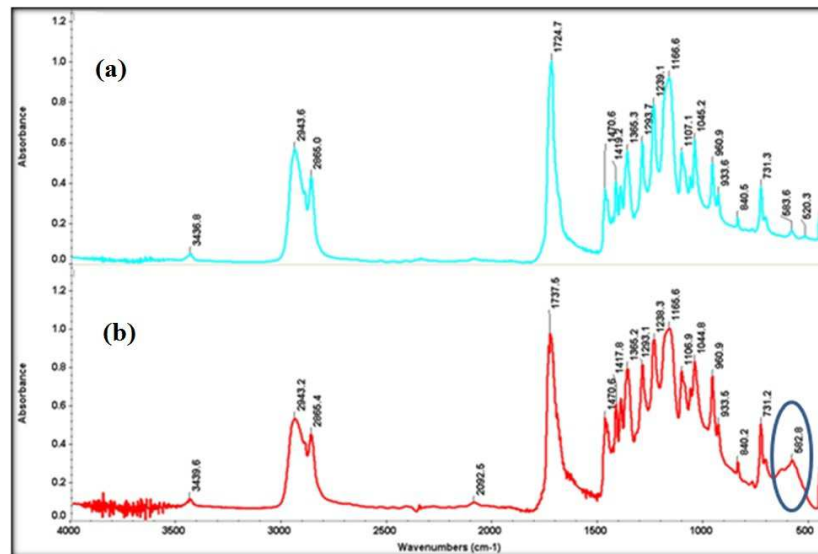


**Figure 23:** FTIR measurement of magnetic microspheres (a) PCL (b) HAIOPCL

In XRD spectra, the green arrow represented (311), (400) and (440) patterns showed the presence of iron oxide and red arrow marked (211) pattern suggested the presence of HA crystals. Further, the presence of broad peak at  $580\text{cm}^{-1}$  from FTIR spectra confirmed the iron oxide crystals in HAIOPCL composite.

### 4.3.1.1 Biological Evaluation and 3D culture of HAIO PCL

The preliminary cytocompatibility and hemocompatibility evaluation of HAIO PCL was carried out using Alamar Blue assay and hemolysis test. Almar blue assay results in the Figure 24 revealed that more than 95% viability of cells with on exposure to HAIO-PCL structures with varying size at 2mg/mL concentration. Also the percentage hemolysis value and ESEM image of RBCs after microspheres post exposure have been represented in table 5 and Figure 25 respectively.

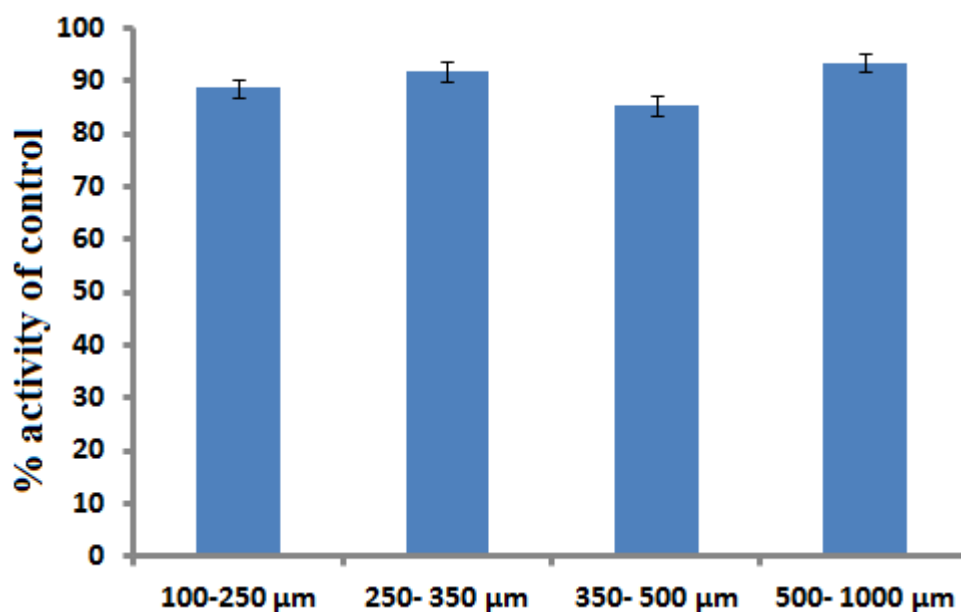


**Figure 24:** Cell Activity at 24hrs contact with HAIO PCL various size range having 2mg/ml concentration evaluation *via* Alamar Blue assay ( $p < 0.05$ )

Microsphere size (1mg/ml)	100-250 μm	250- 350 μm	350- 500 μm	500-1000 μm	Negative control	Positive control
Hemolysis (%)	0.08±0.002	0.05±0.001	0.07±0.008	0.09±0.007	0.00±0.000	0.65±0.06

**Table 5:** Hemolysis analysis of HAIO PCL microspheres various sizes on 1mg/ml

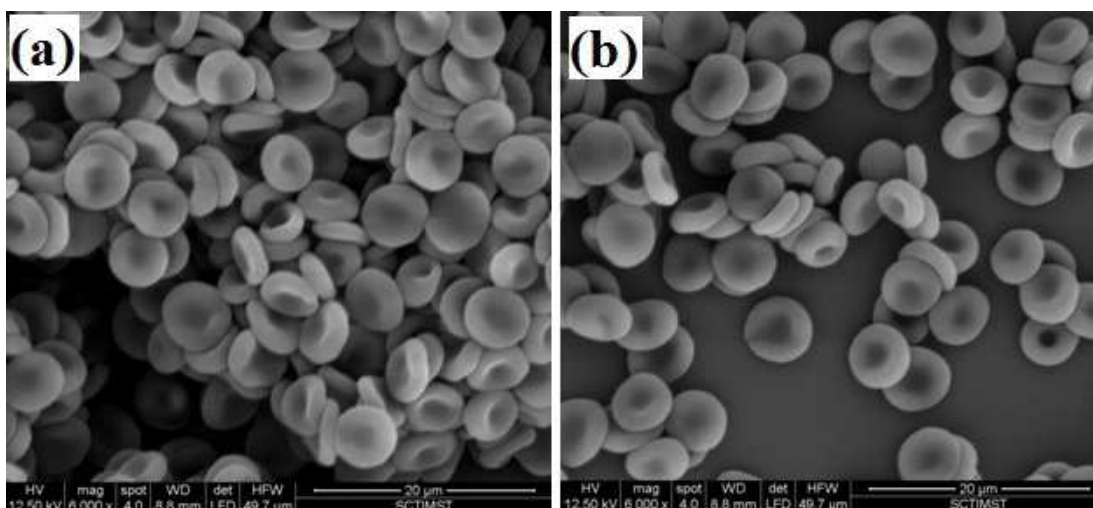


**Figure 25:** Scanning Electron Micrographs: (a) RBC cells alone and (b) 1mg/ml of 250- 350  $\mu\text{m}$  size HAIO PCL exposed RBC cells

The HAIO PCL 250-350  $\mu\text{m}$  sizes were selected for cell adhesion and 3D culture evaluations. HeLa cells were incubated with HAIO PCL for 24h and was levitated with the aid of external magnetic field and cultured under *in vitro* condition for 72h. The cells over microsphere were examined using ESEM and fluorescent microscopic technique. ESEM images from the Figure 26 showed that cells were well attached and proliferated over microsphere. The live-dead experiment has been carried out using Acridine orange- Ethidium bromide staining and represented in the Figure 27 (a). An intense green fluorescence observed from the sphere surface demonstrated the viability and proliferation of cells. Moreover the DAPI nuclear staining support the cell over microsphere and clearly visible from the Figure 27 (b).

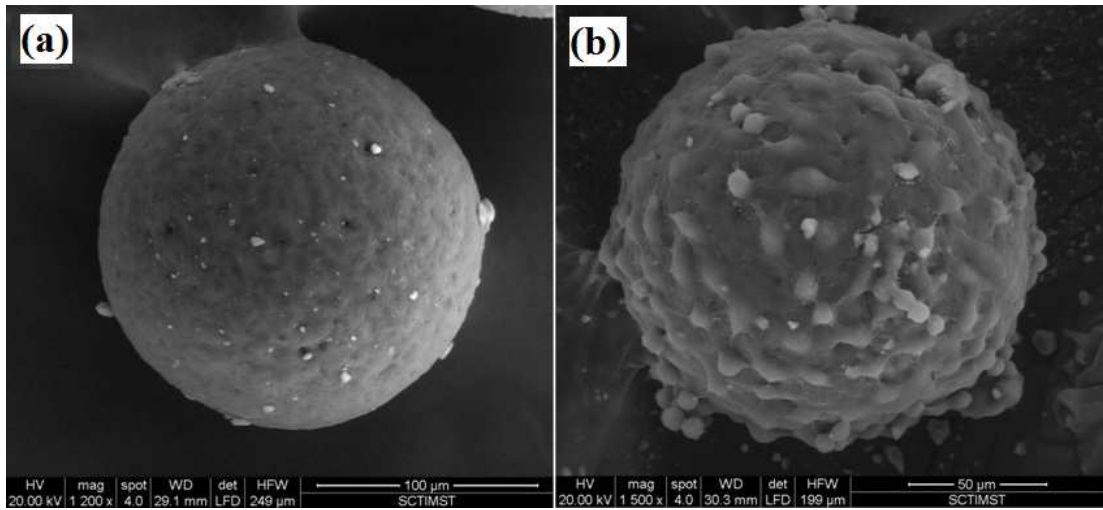


**Figure 26:** Scanning Electron Micrographs: (a) HAIO PCL microsphere (b) HeLa cell seeded over HAIO PCL microsphere and cultured under 3D model condition

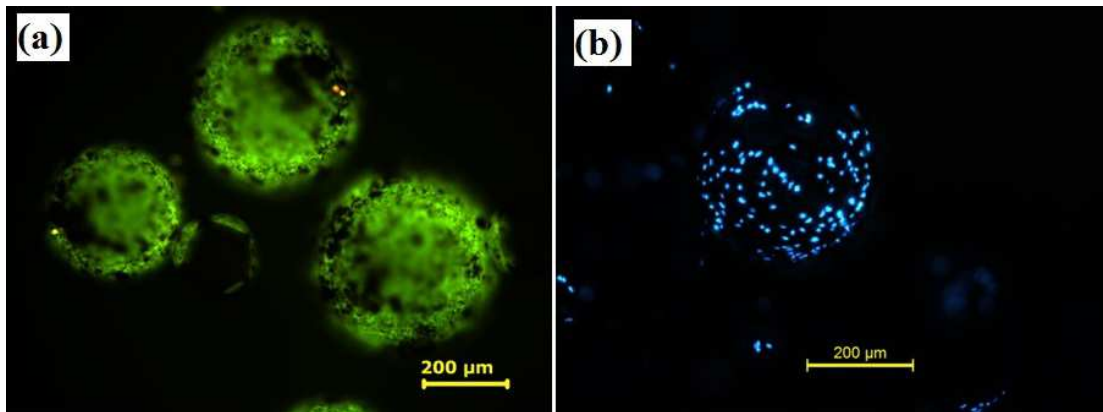


**Figure 27:** Fluorescence microscopic images of cells over microspheres (a) Live-dead analysis using Acridine orange ethidium bromide (b) DAPI nuclear staining

## 4.4 Theranostic Efficiency Evaluation of HAIO50 (Hyperthermia Therapy and MRI Contrast Agent)

### 4.4.1 Hyperthermia Therapeutic Evaluation of HAIO50

In order to investigate the hyperthermia performance of HAIO50 particles, the powder forms as well as aqueous dispersed material of various concentrations were tested. The AMF heating study was carried out with field ranging from 14.4 to 38.6mT for a period of 15min. SPIONs particles powder and aqueous dispersed forms were also investigated in the AMF studies and compared with the HAIO50 time-temperature profiles. The temperature variation with respect to exposure time, strength of the magnetic field and concentration of HAIO50 and SPIONs powder form is illustrated in Figure 28.

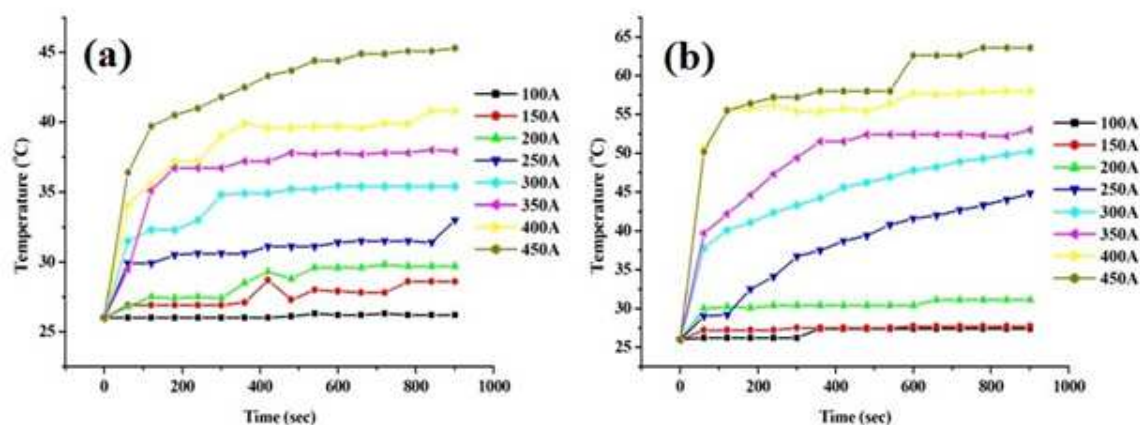


**Figure 28:** Heat profile of 5mg of samples (a) HAIO50 and (b) SPION for different currents.

However the hyperthermia therapeutic capabilities of samples are decided on the basis of specific loss power [SLP]. Hence to examine the therapeutic heating efficiency of particles, we have conducted the AMF analysis of HAIO50 and SPIONs at various

concentration in aqueous medium. The corresponding samples time-temperature graphs has been illustrated in the Figure 29.

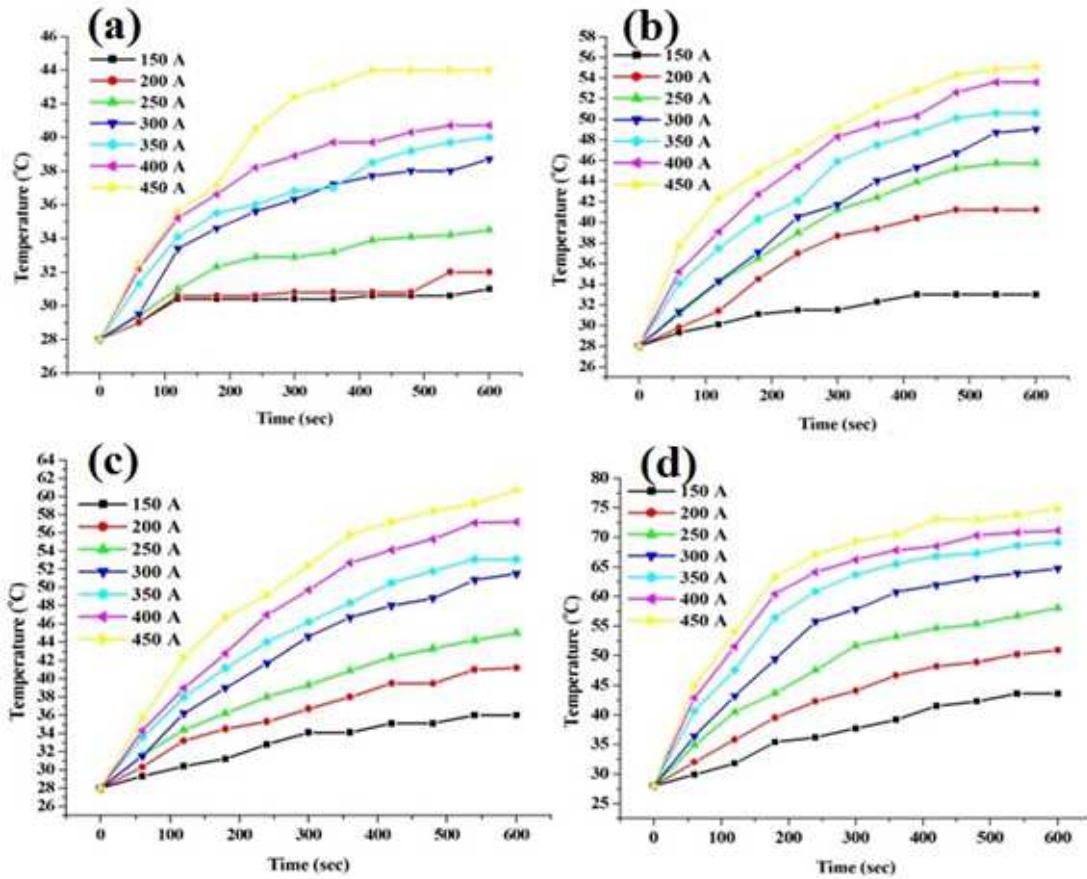


**Figure 29:** Time versus temperature graphs for various suspensions having different concentrations of samples (a) 5mg/ml, (b) 10mg/ml of HAIO50 and (c) 5mg/ml, (d) 10mg/ml of SPION

The SLP value has been calculated using below equation number (1) and the values are presented in the table 6.

$$\text{Calculation of Specific loss of power [SLP]} \dots\dots\dots = \frac{C}{m} \frac{dT}{dt} \quad (1)$$

C = specific heat capacity of water per unit volume ( $C = 4.184 \text{ J K}^{-1} \text{ mL}^{-1}$ )

$m$  = concentration of the magnetic particles

$(dT/dt)$  = slope of the temperature Vs time graph

No	Current passing through the coil (A)	Magnetic field strength (mT)	SLP			
			HAI050 5mg/ml	HAI050 10mg/ml	SPION 5mg/ml	SPION 10mg/ml
1	200A	14.4	10.48299	9.885275	18.46549	19.0167
2	250A	19.33	13.79341	11.12668	25.63121	33.5778
3	300A	24.166	15.44862	23.03499	48.78198	51.72176
4	350A	28.99	16.00035	24.50629	50.89495	62.19473
5	400A	33.83	41.93196	39.21925	66.88	88.0556
6	450A	38.66	53.70233	46.34585	73.86198	101.744

**Table 6:** Representation of hyperthermia studies based on the applied alternating current, magnetic field strength and corresponding specific loss power of HAI050 and SPIONs calculated from time-temperature graphs.

#### 4.4.1.1 Hyperthermia Therapeutic Evaluation of HAI050 under *In vitro* Condition

The literature suggested that cancer cells are more sensitive to elevated temperature or hyperthermia than normal cells (Storm et al., 1979). Magnetic nanoparticles have gained extensive attention for hyperthermia applications owing to their capacity to produce heat effectively when exposed to an alternating magnetic field (AMF) without an incursion depth limit. Hyperthermia, the artificially induced heat medication of disease, usually uses temperature ranging between 42°C and 47°C. Normally, the cancer cells are induced to apoptosis at a temperature range of 43-45°C. Based on reported protocols HAI050 was utilized to carry out hyperthermic

intervention on a controlled population *in vitro*. Post – exposure cells were evaluated through flow cytometric analysis and ESEM technique.

In flow cytometric analysis, hyperthermia applied cells were stained with ethidium bromide (EB), a fluorescent dye used as an indicator of cell membrane permeability. The hyperthermia applied cells were stained with 2  $\mu$ l of 0.5mg/ml of EB for 15min, then washed and tested by FACS analysis. Material treated HeLa cells were used for control of the experiment. Dead cell population was estimated *via* usual dot-plot gating technique and expressed in Figure 30.

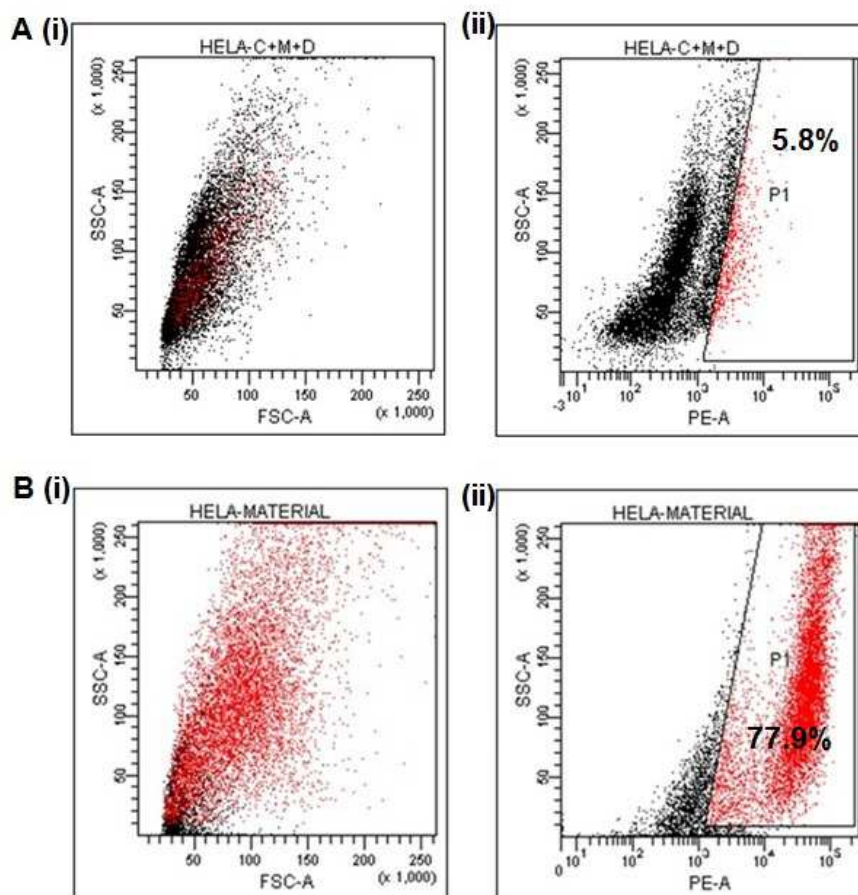


**Figure 30:** Dot-plots obtained from FACS data showing HeLa cells distribution post ethidium bromide after hyperthermia exposure (A) Control sample [Hela cell +

HAIO particles without AMF application] (B) Test sample [Hela cells + HAIO particle + 30min hyperthermia treatment]

In order to investigate the cell death mechanism through hyperthermia treatment, the cells were stained with Annexin V and propidium iodide (PI). The HAIO50 exposed hyperthermia treated HeLa cells were stained with Annexin V and PI and evaluated using flow cytometric analysis. The results have been depicted in the figure 31. Further morphological analysis of treated cells has carried out *via* ESEM techniques and compared to control cell structure. The observations were depicted in the figure 32, which demonstrated that most of the cells lost their cellular integrity after hyperthermia treatment.

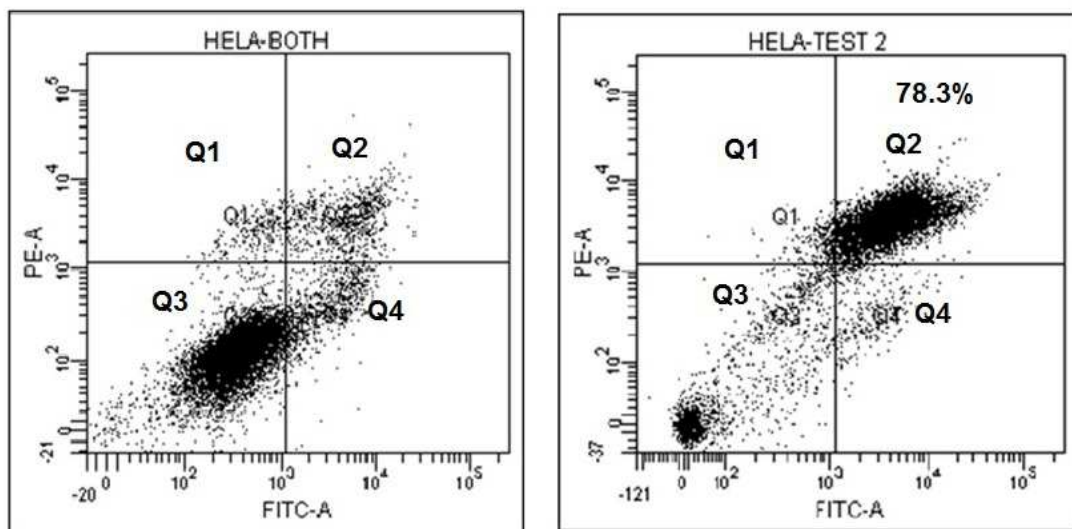


**Figure 31:** Typical dot plot obtained from FACS data showing HeLa cells distribution Annexin V/ Propidium Iodide (PI) staining (A) HAIO+ HeLa cells without exposure to AMF as a control and (B) 30min exposure to MnIO75TC+ HeLa cells. The image quadrants designated as Q1=PI alone, Q2=Annexin V+PI, Q3=unstained cells and Q4= Annexin V alone positivities respectively

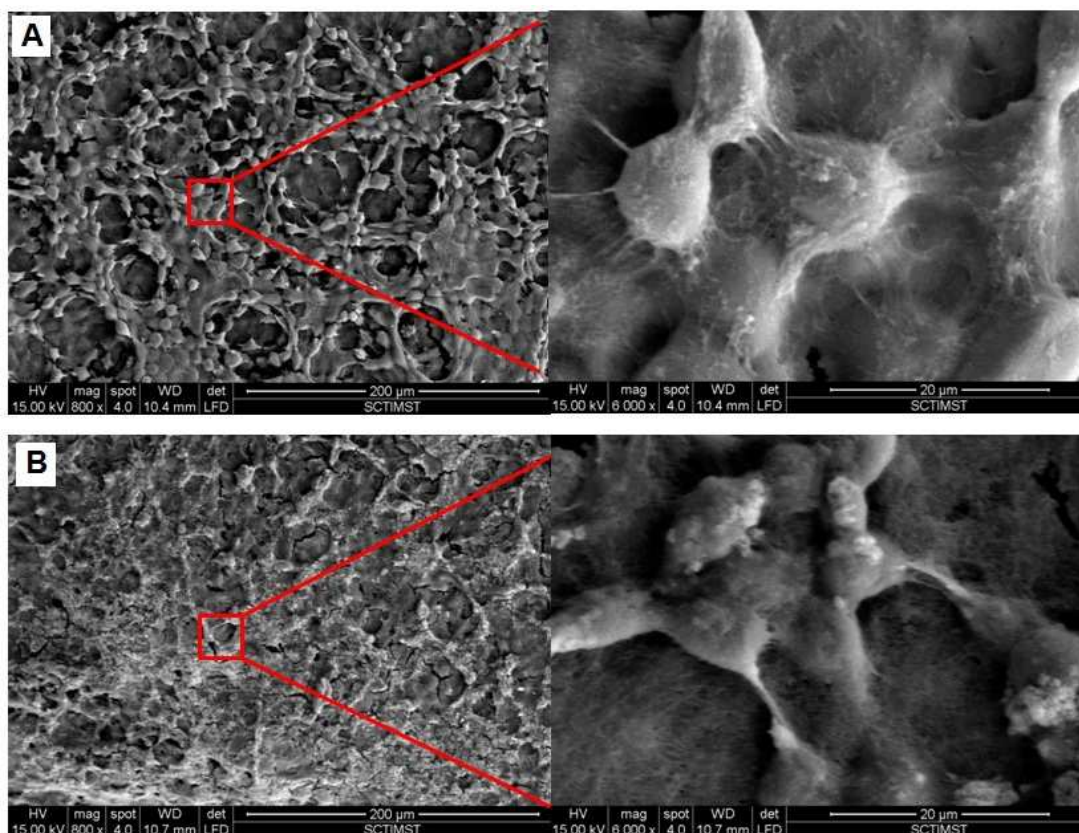


**Figure 32:** ESEM images of HeLa cells loaded with HAIO (A) before and (B) after the application of the alternating magnetic field [AMF]. The corresponding images higher magnification represents in the right side. Most of the cell membrane structure collapse after exposure to the AMF

#### 4.4.2 MRI Contrast Efficiency Evaluation of HAIO50 Particles

In order to demonstrate MRI contrast efficiency of HAIO50, the material was imaged *via* aqueous phantom study performed on a 1.5T entire body MRI scanner. Different concentrations of the samples were dispersed uniformly in deionized water and corresponding relaxation times were measured. We obtained the spin-spin relaxations time of  $T_2$  weighted MR images for each sample. Figure 33 shows the contrast efficiency and relaxivity of the HAIO50 having different concentrations.

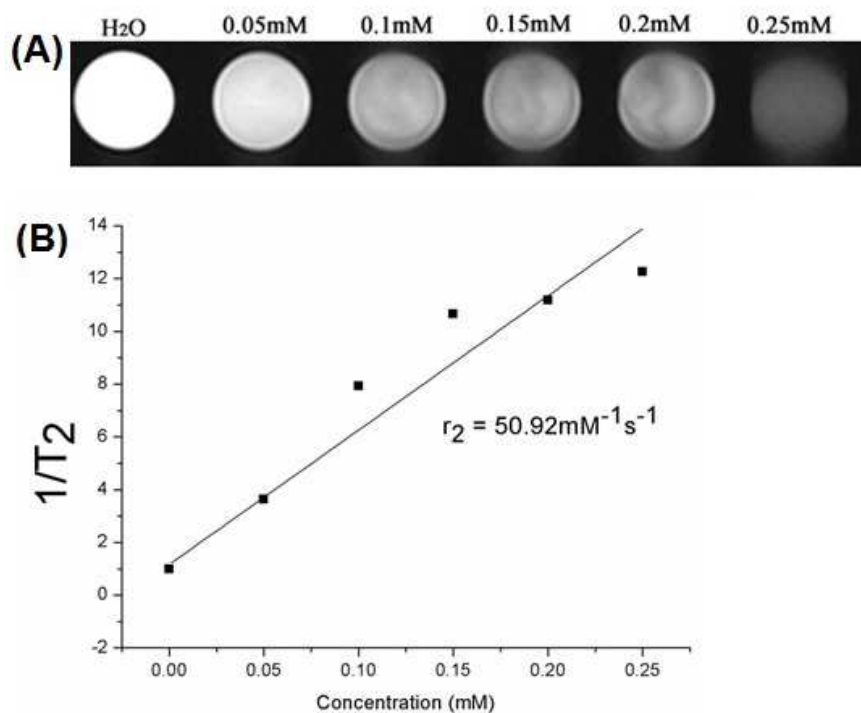


**Figure 33:** (A) T<sub>2</sub> weighted MR images of (A) HAI050 with varying the concentration at 1.5 T clinical MRI system (B) Relaxivity rate graphs of 1/T<sub>2</sub> against the Fe concentration of the HAI050

As a part of demonstrating the use of HAI050 as a plausible contrast agent, contrast efficiency of HeLa cells labelled HAI050 (various concentrations) was evaluated *via in vitro* MRI evaluation. Change in contrast with respect to the concentrations has been observed and pixel intensity versus echo time was plotted and recorded in Figure 34.

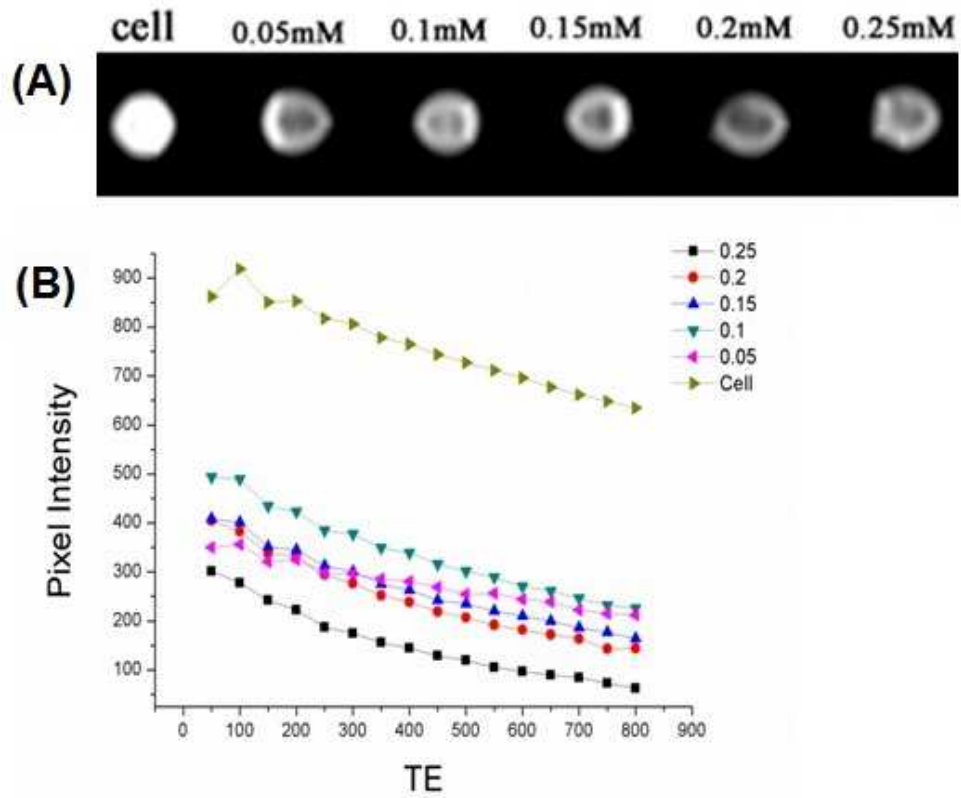


**Figure 34:** (A) T<sub>2</sub> weighted MR images of different concentrations of HAIO50 incubated with HeLa cells during 24h (B) corresponding pixel intensity variation plotted against TE values

## 4.5 Improve the Theranostic Efficiency of Superparamagnetic Nanoparticles Through Crystal Modification

### 4.5.1 Development of Manganese Substituted SPION (MnIO) Nanocrystal *via* an Aqueous Co-precipitation

The co-precipitation synthesis route has enabled the *in situ* formation of bivalent Mn substituted superparamagnetic nanoparticles as a colloidal suspension and is schematically represented in figure 35.

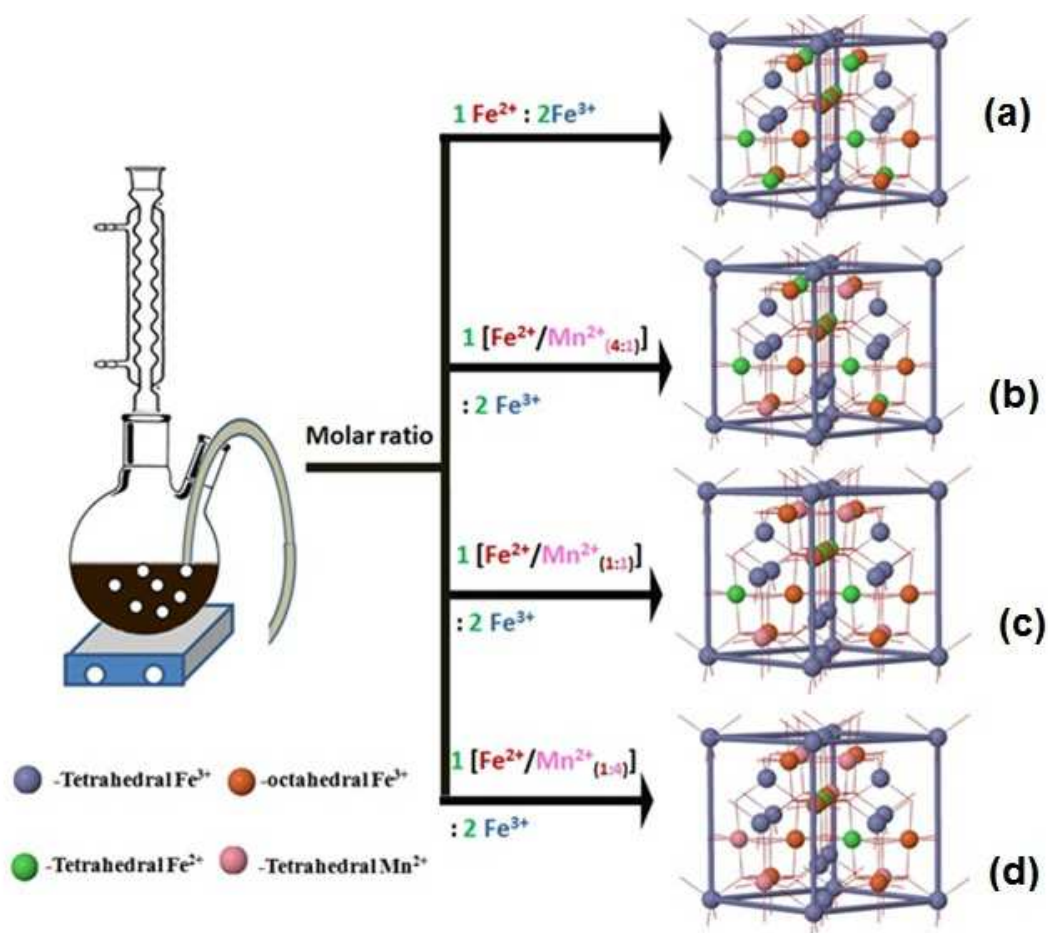


**Figure 35:** A schematic representation of  $\text{Mn}^{2+}$  substituted SPION crystals. (a) SPION (b) MnIO25 (c) MnIO50 and (d) MnIO75

In an earlier study, cation-substituted superparamagnetic nanocrystals were synthesized using co-precipitation in a high temperature organic media (Lee et al., 2007). However, the present study has focused on the easiest aqueous co-precipitation route for making nanoparticles with a maximum concentration of  $Mn^{2+}$  substitution in the SPION crystals.

The precipitation of nanocrystals was carried out in the presence of trisodium citrate solution. This favoured homogeneous nanoparticle formation of the manganese ferrite crystals. The detailed physicochemical and biological evaluations of developed manganese ferrite nanocrystals were examined.

#### 4.5.1.1 Physicochemical Characterization of MnIOs

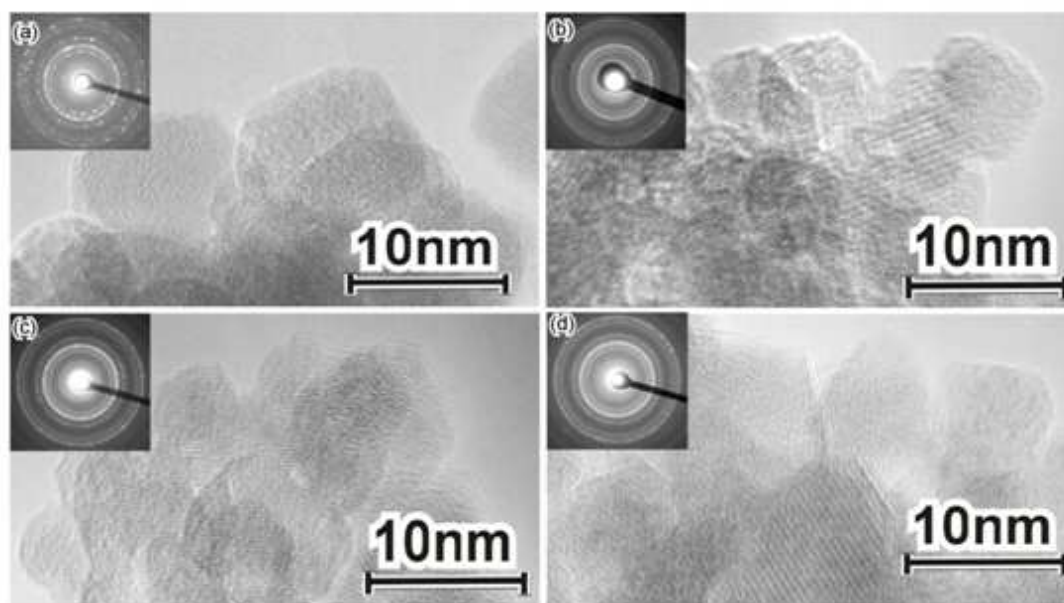


**Figure 36:** HRTEM images of various molar concentrations of  $Mn^{2+}$  substituted iron oxide crystals. (a) SPION, (b) MnIO25, (c) MnIO50 and (d) MnIO75

The HRTEM images show the size and shape of the MnIOs and are depicted in Figure. 36. The HRTEM and its FFT investigations indicate that nearly all of the nanoparticles form single crystals of ferrite containing a highly crystalline structure.

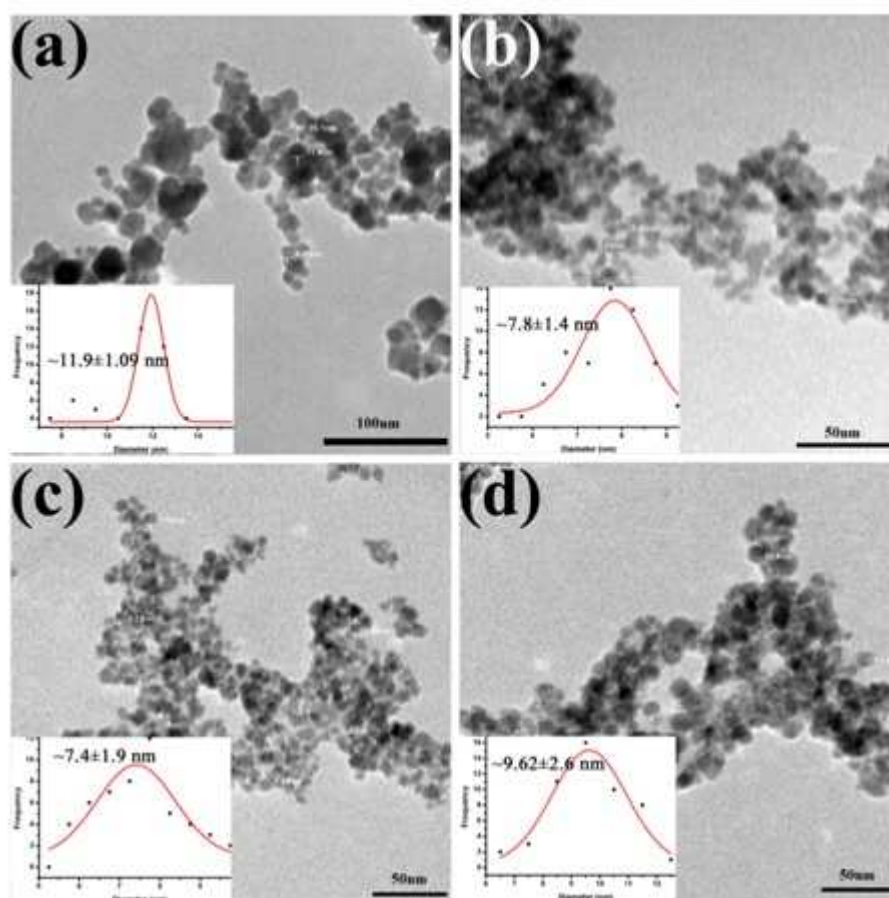


**Figure 37:** TEM images and their corresponding size distribution curve shown in the inset for (a) SPION, (b) MnIO25, (c) MnIO50 and (d) MnIO75

The TEM images as described in Figure 37 demonstrate that the samples consist of polygonal faceted spherical nanoparticles and have narrow size distribution with average values of  $\sim 11.9 \pm 1.09$  nm for SPION,  $\sim 7.8 \pm 1.4$  nm for MnIO25,  $\sim 7.4 \pm 1.9$  nm for MnIO50, and  $\sim 9.62 \pm 2.6$  nm for MnIO75.

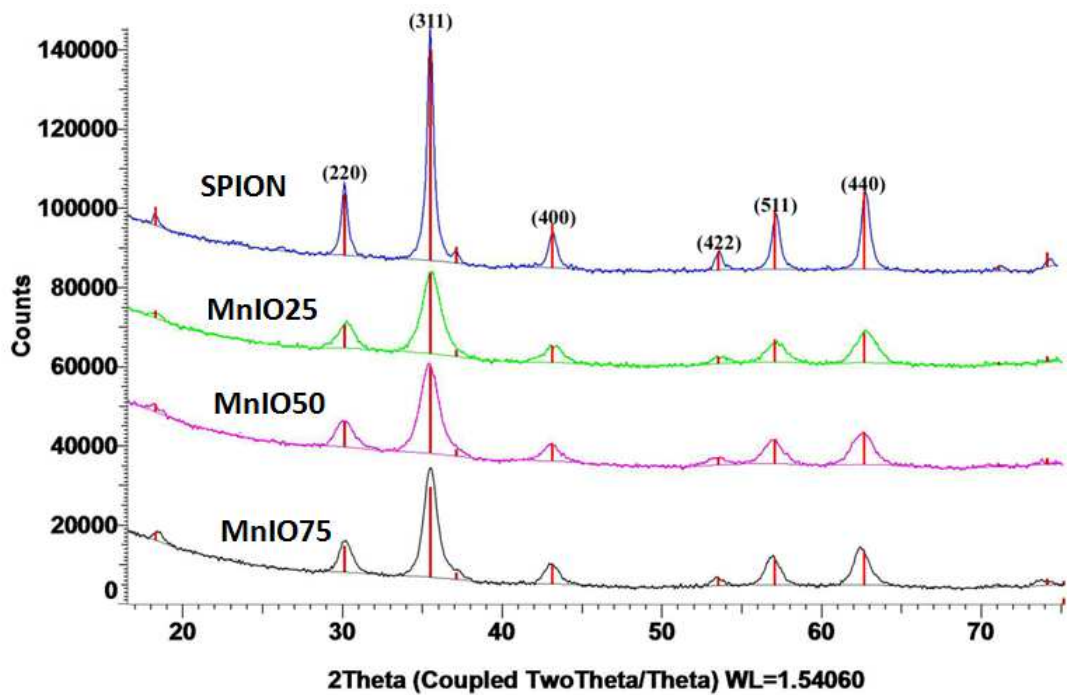


**Figure 38:** X-ray diffraction pattern of a) SPION b) MnIO25 c) MnIO50 d) MnIO75 nanoparticle assemblies

XRD analysis was performed to identify the crystallographic structure and to estimate the crystallite size (Figure 38 and figure 39). The various molar concentrations of  $Mn^{2+}$  of 25%, 50%, 75%, 80% and 90% of ferrous ions in the SPION crystal substituted and termed as MnIO25, MnIO50, MnIO75, MnIO80 and MnIO90 respectively.

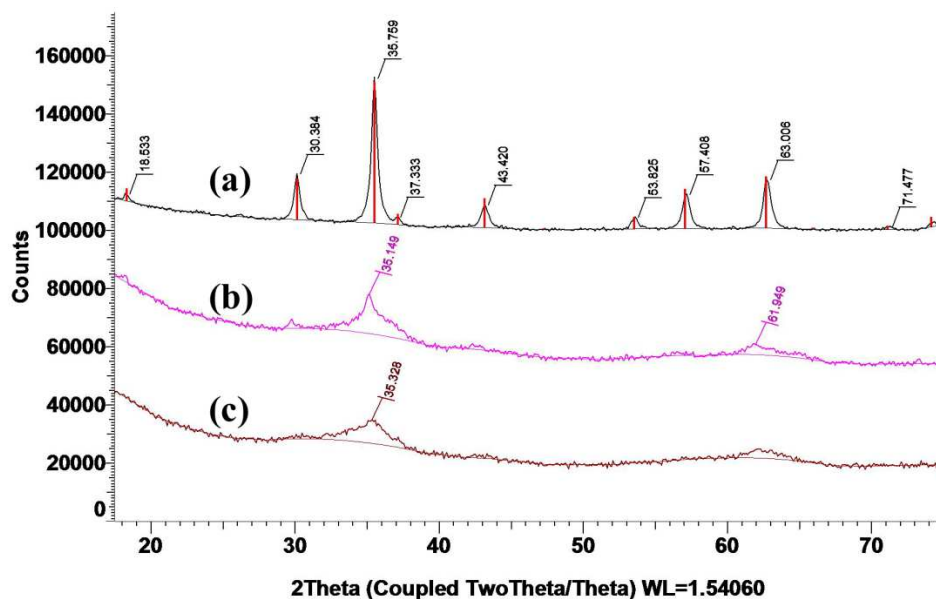


**Figure 39:** XRD patterns for the samples recorded with Cu  $K\alpha 1$  radiation. a) SPION b)MnIO80 c)MnIO90

The XRD patterns of MnIOs presented in the Figure 38 support that no phases other than nanocrystalline manganese ferrite are present up to a critical concentration. On the other hand, beyond the critical molar concentration (75% of ferrous ion) of  $Mn^{2+}$ , the final system did not support crystal formation in which the major peaks of spinel disappears (figure 39). The average crystal size of the nanoparticles range from  $\sim 11.5 \pm 0.8$  nm for SPION,  $\sim 8.6 \pm 0.9$  nm for MnIO25,  $\sim 8.1 \pm 0.6$  nm for MnIO50 and  $\sim 9.7 \pm 0.9$  nm for MnIO75, and the crystal size of the nanoparticles calculated by the Scherrer formula using the (311) peak matches with size calculated using TEM.

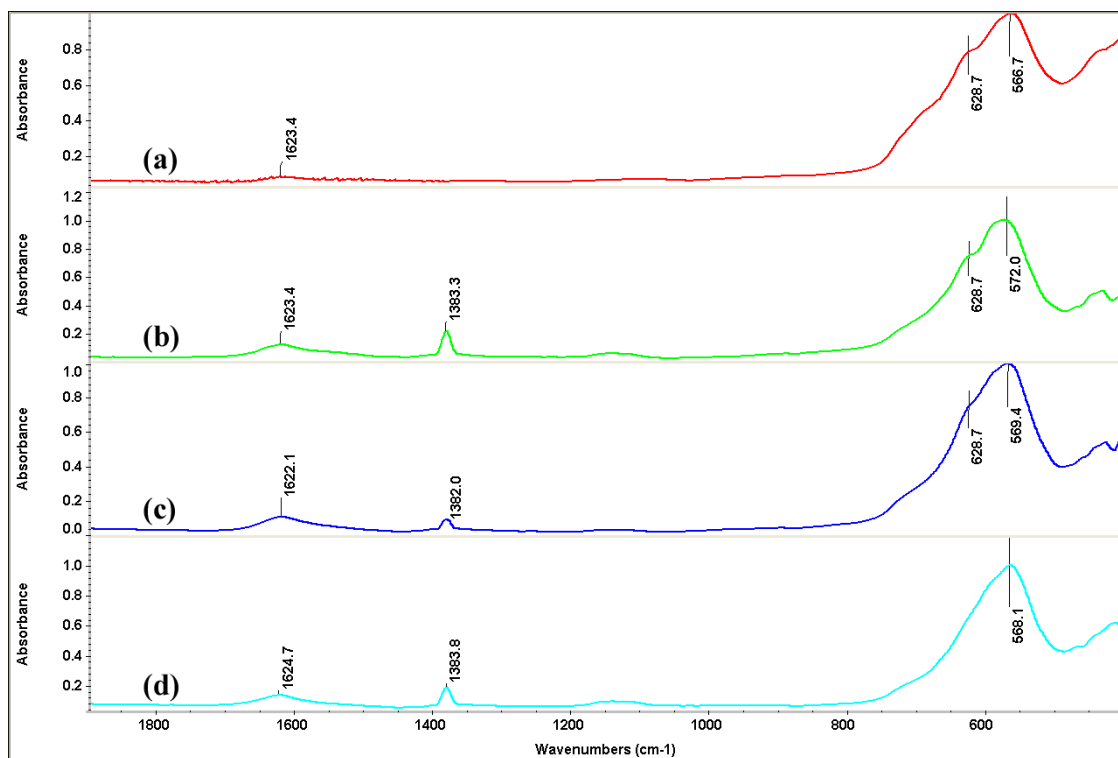


**Figure 40:** FTIR spectra of (a) SPION, (b) MnIO<sub>25</sub>, (c) MnIO<sub>50</sub> and (d) MnIO<sub>75</sub> nanoparticles in the 1900–400 cm<sup>-1</sup> range

The FTIR spectra of (a) SPION, (b) MnIO<sub>25</sub>, (c) MnIO<sub>50</sub> and (d) MnIO<sub>75</sub> in the range of 1900–400 cm<sup>-1</sup> are depicted in Figure 40. Generally, iron oxide and manganese ferrite shows a M<sub>T</sub>-O-M<sub>O</sub> stretching band at ~600-500 cm<sup>-1</sup>, in which M<sub>T</sub> and M<sub>O</sub> correspond to the tetrahedral and octahedral positions, respectively.

In Figure 41, the peaks at ~3395 and ~1595 cm<sup>-1</sup> are characteristic bands for metal ferrites with O–H stretching and bending vibrations, respectively. In addition to the vibrational peaks of metal oxides, the MnIOs shows additional peaks at 1618 and 1397 cm<sup>-1</sup> corresponding to the asymmetric and symmetric stretching of the carboxyl group in citrate. Tri-sodiumcitrate also shows corresponding infrared bands at 1668 and 1390 cm<sup>-1</sup>.

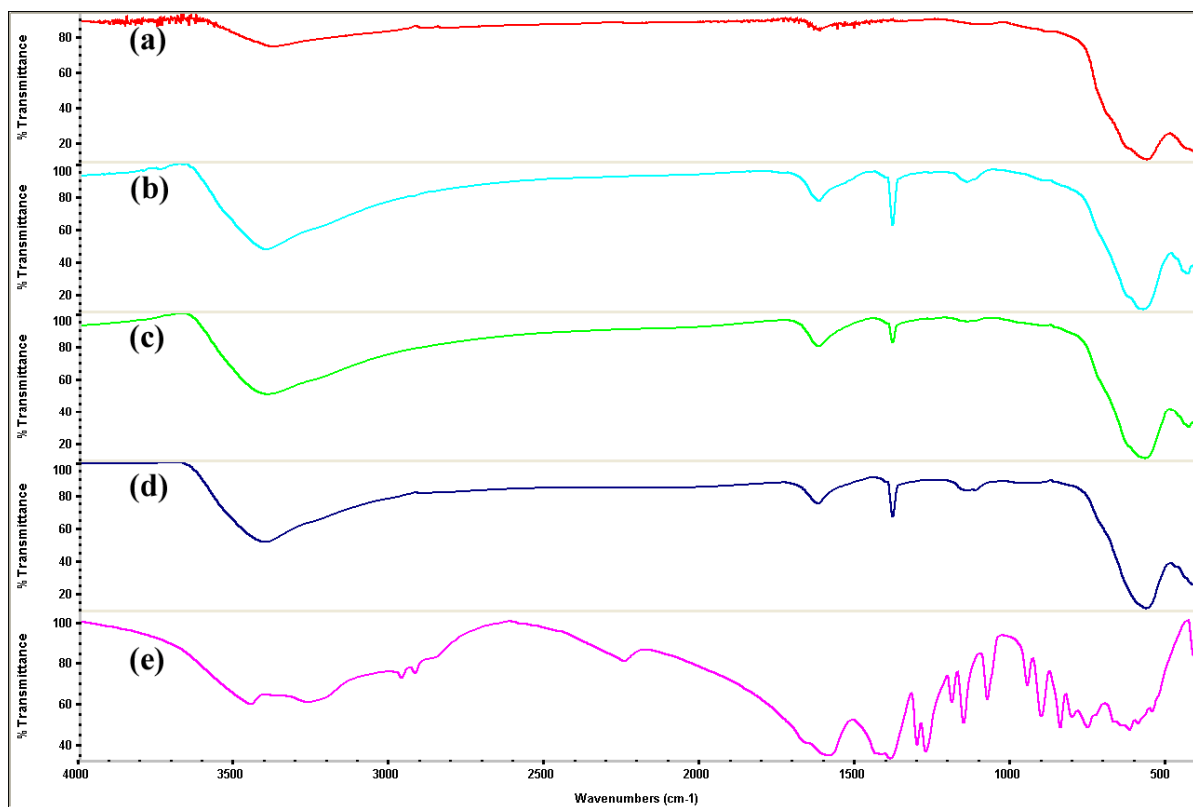


**Figure 41:** FTIR spectra of the freeze dried powder samples of a) SPION b) MnIO25 c) MnIO50 d) MnIO75 e) TC

The amount of trisodium citrate adsorbed on the nanomaterial surface was quantified using TGA-DTA and the results presented in Figure 42. The TGA plot represents four distinct stages of thermal decomposition at temperatures of 143°C, 350°C, 605°C and 900°C. The total and partial weight losses are summarized in Table 7.

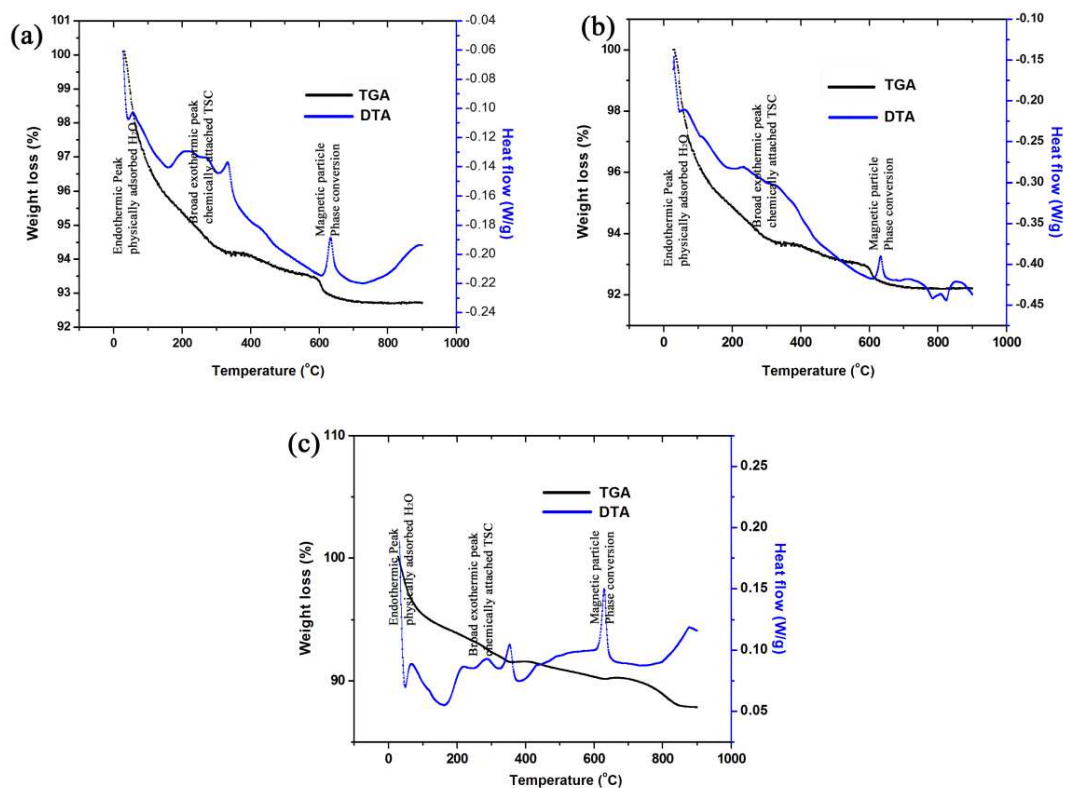


**Figure 42:** TGA and DTA for (a) MnIO<sub>25</sub>, (b) MnIO<sub>50</sub> and (c) MnIO<sub>75</sub> under an N<sub>2</sub> atmosphere

Temp (°C)	Weight % remaining		
	MnIO <sub>25</sub>	MnIO <sub>50</sub>	MnIO <sub>75</sub>
143	96.37	95.47	94.6
350	94.62	93.72	91.56
605	93.63	92.73	90.29
900	93.12	92.22	87.83

**Table 7:** Partial weight loss determined by TGA analysis

The different molar compositions of manganese ferrite nanocrystal Fe/Mn ratios were evaluated by EDX and ICP analysis. It is well known that EDX analysis gives

the effective atomic concentration of different constituents on the surface layer of the solid investigated. Energy dispersive X-ray analysis of the prepared specimens was carried out at same voltage and at various areas on the surface of the solid, and is represented as the Fe/Mn ratio in Figure 43. Similarly, the relative atomic percentage of Mn, Fe and oxygen species present in the solid from the theoretical calculation and ICP analysis are presented in Table 8.

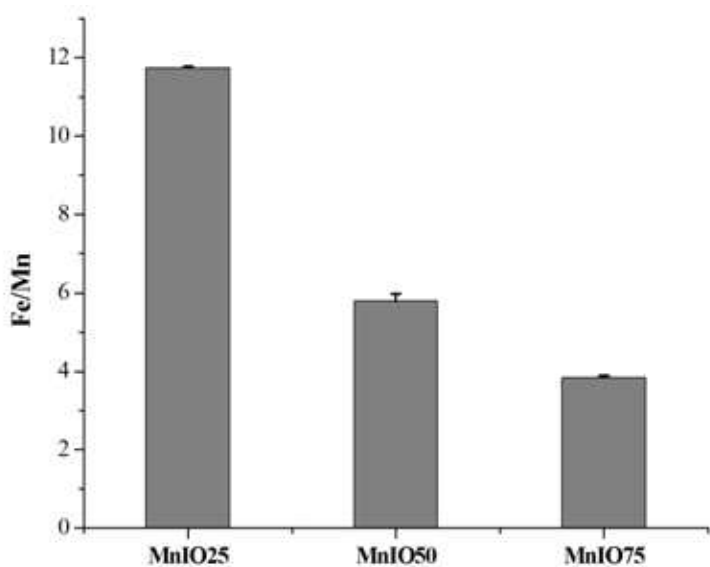


**Figure 43:** Surface composition of the Fe/Mn ratio of nanoparticle calculated *via* energy dispersive spectroscopy

	Theoretical	Fe/Mn (ICP)
MnIO25	11.18	11.60
MnIO50	5.08	5.43
MnIO75	3.05	3.28

**Table 8:** The initial Fe/ Mn metal composition ratio compared with ratios as determined by ICP-OES analysis

#### 4.5.1.2 Biological Evaluations of MnIOs

Hemocompatibility is of prime importance for nanoparticles used in imaging, as the vasculature provides primary access and distribution in a living system. To ensure their compatibility, hemolysis and clotting time evaluations were carried out (Table 9). It is apparent that the nanoparticles at concentrations up to 1 mg/mL of blood did not induce hemolysis. MnIOs nanoparticles in a final concentration of 1 mg/mL were used in the aggregation test. Particle induced aggregation was not observed in the case of RBC, WBC and platelets (Figure 44, 45 and 46).

Sample	Hemolysis (%)	Clotting time (s)
MnIO25	0.01±0.002	220±28
MnIO50	0.01±0.001	245±34
MnIO75	0.04±0.005	245±27
SPION	0.03±0.003	235±26
Negative control	0.00±0.000	255±30
Positive control	0.52±0.008	165±28

**Table 9:** Percentage hemolysis values of blood cells after 2hrs incubation with MnIOs at 37°C and clotting time measurement assessing the MnIOs contacted blood samples

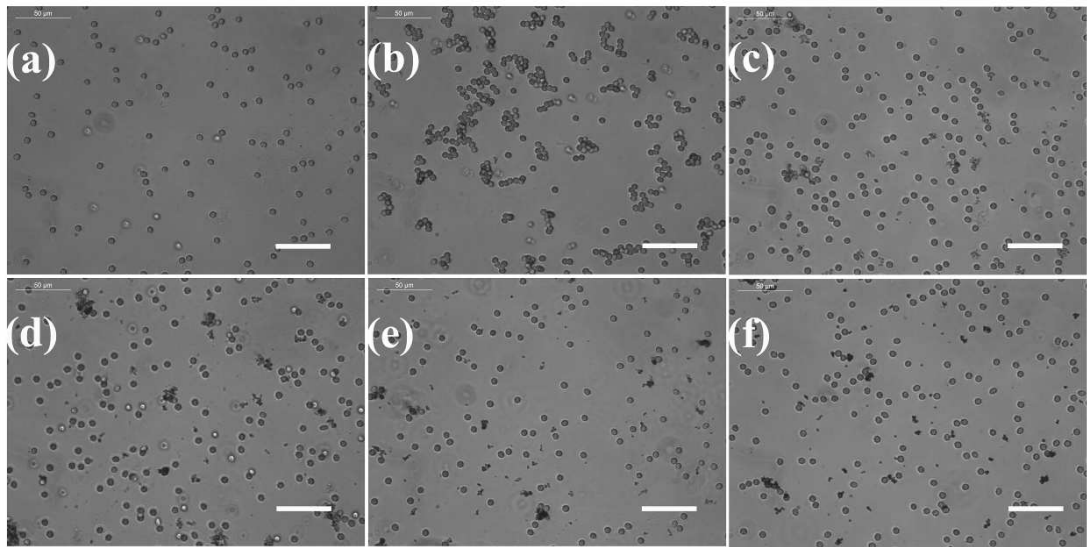


**Figure 44:** Phase contrast microscopic view 400X (Scale bar 50µm ) of erythrocytes after incubation with a) Negative control (Normal saline) b) positive control (polyethylenimine) c) MnIO25 d) MnIO50 e) MnIO75 f)SPION

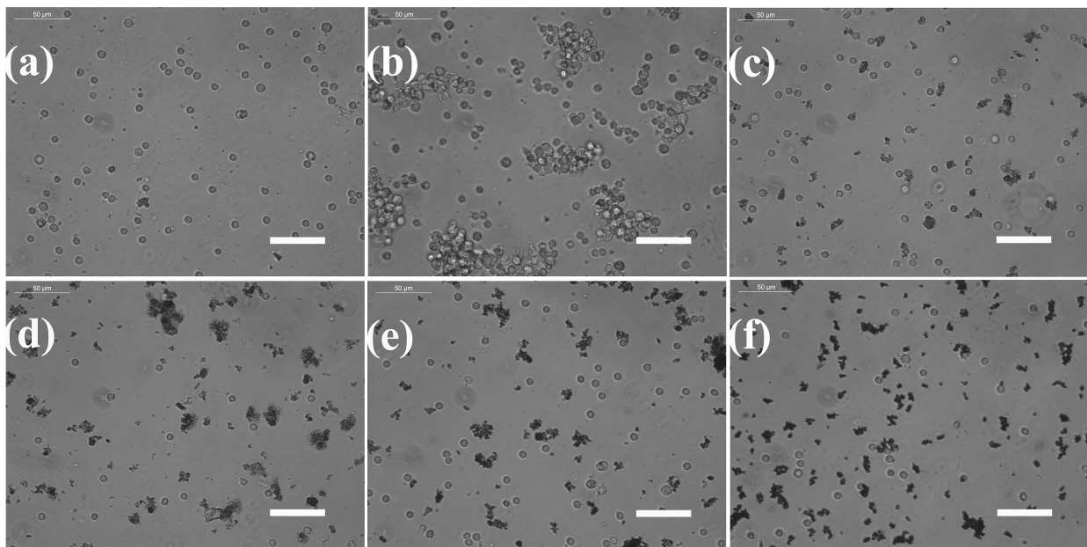


**Figure 45:** Phase contrast micrographs of leukocytes after incubation with MnIOs a) Negative control normal saline b) positive control (polyethylenimine) c) MnIO25 d) MnIO50 e) MnIO75 f) SPION. Scale bar 50µm

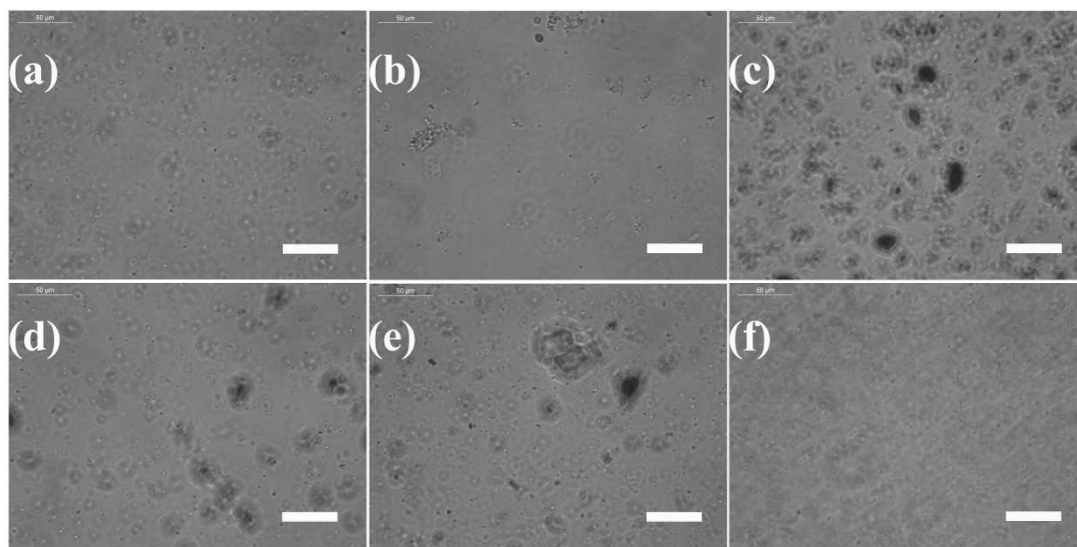


**Figure 46:** Phase contrast micrographs of platelets after incubation with MnIOs a) Negative control (normal saline) b) positive control (polyethylenimine) c) MnIO25 d)MnIO50 e) MnIO75 f)SPION. Scale bar 50 $\mu$ m

Alamar Blue assay was carried out to evaluate cellular activity in the presence of the nanoparticles at varying concentration levels. HeLa cells were evaluated at 24 hours post exposure to the nanoparticles, the data collected indicates more than 95% cellular activity across the concentration levels used (Figure 47). Phase contrast images (figure 48) of cells in contact with the nanomaterials also provide evidence on the preservation of the morphological characteristics of cells under the influence of the nanoparticles. Furthermore, microscopic study on cellular uptake of SPION and MnIOs in HeLa cells visualized by Prussian blue staining shows the internalised particles of SPION and MnIOs (Figure 49).

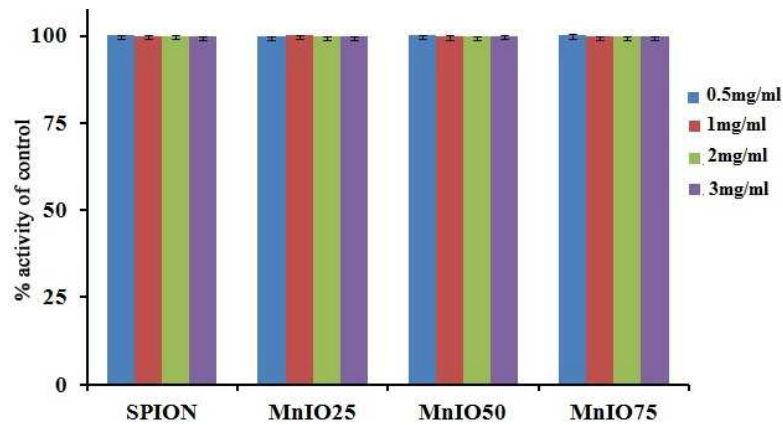


**Figure 47:** Cell Activity at 24hrs contact with SPION and MnIOs evaluation *via* Alamar Blue assay ( $p < 0.05$ )

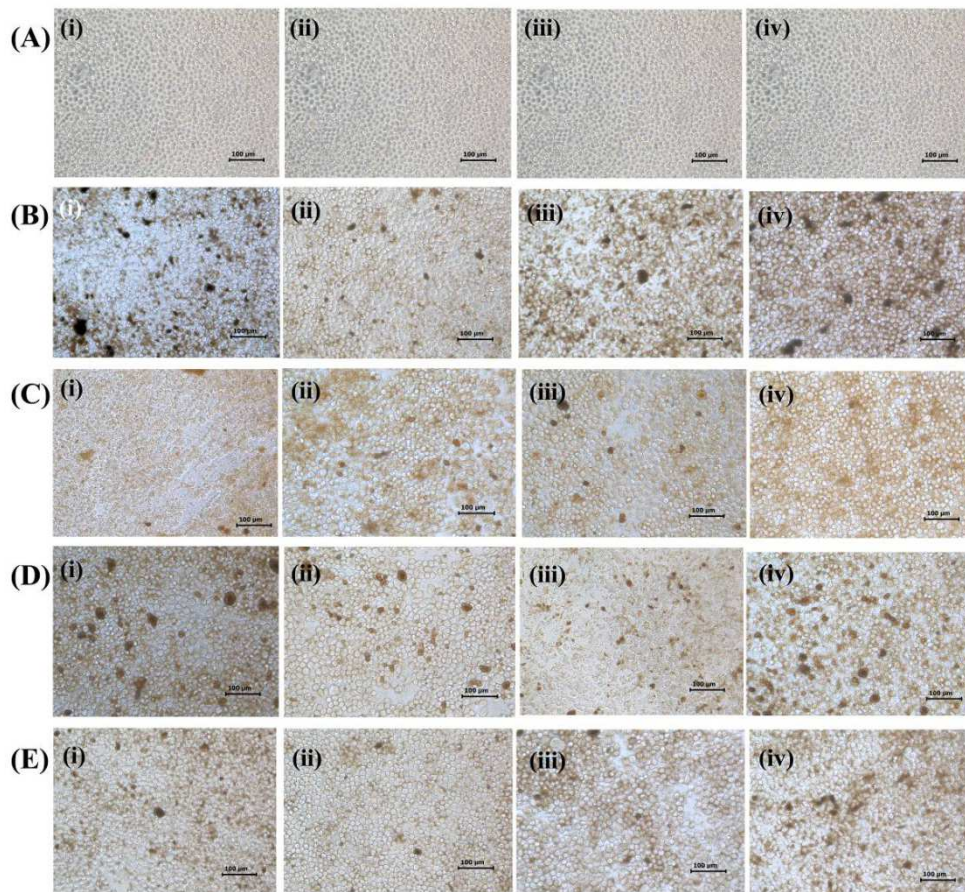


**Figure 48:** Phase Contrast Micrographs of HeLa cells after 24h incubation with nanoparticles. (A) Control, (B) SPION, (C) MnIO25, (D) MnIO50, (E) MnIO75 and (i), (ii), (iii), (iv) are 0.5mg/mL, 1mg/mL, 2mg/mL, 3mg/mL concentrations of corresponding material

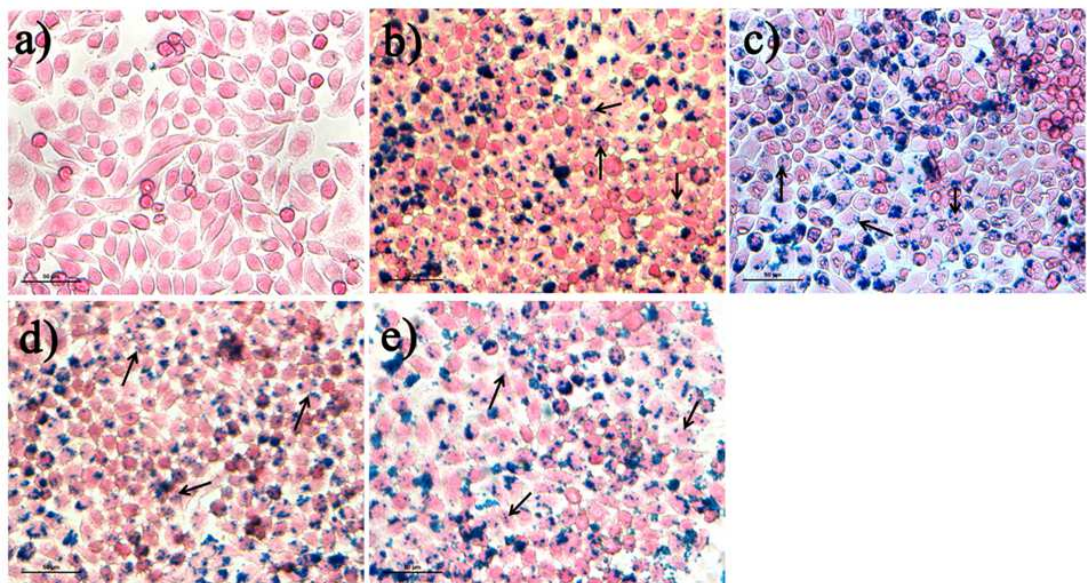


**Figure 49:** HeLa cells incubated for 24 h with SPION and MnIOs nanoparticles and stained with Prussian Blue. Blue indicates iron based nanoparticle uptake. Samples are (a) Control (b) SPION (c) MnIO25 (d) MnIO50 (e) MnIO75 respectively. Uptake of the SPION and MnIOs are clearly seen and it marked by arrows

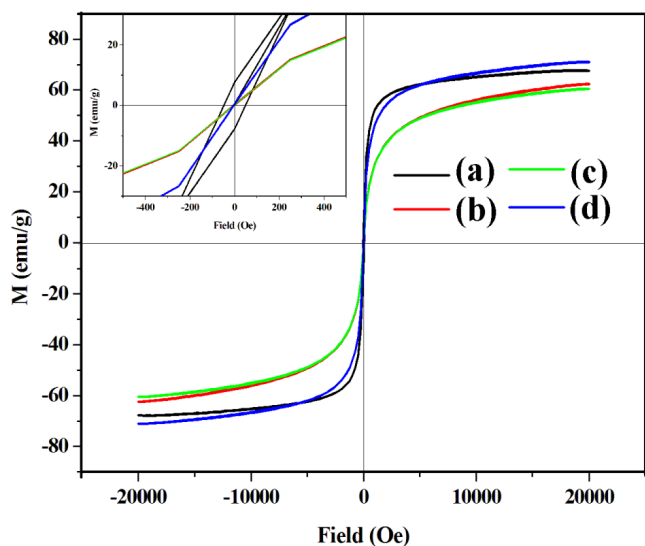


**Figure 50:** Measurement of the magnetic properties of MnIOs particles at room temperature (a) SPION, (b) MnIO25, (c) MnIO50 and (d) MnIO75 with their corresponding remanence and coercivity, shown in the inset

#### 4.5.1.3 Magnetic measurement and relaxivity calculation of MnIOs

The magnetic property of MnIOs was evaluated using VSM analysis at room temperature. The (M–H) loop of various compositions of ferrite nanoparticles are shown in Figure 50. It could be observed from the hysteresis loop that all the composition of nanoparticles shows negligible remanence and coercivity, which confirms the superparamagnetic behavior of the nanoparticles. However, the hysteresis curve of SPION shows minor remanence and coercivity when compared with the MnIOs, where they are nil.

Sample	Magnetic saturation M(emu/g)	Relaxation ( $r_2$ ) $\text{mM}^{-1}\text{s}^{-1}$
MnIO25	62.4	236.6
MnIO50	60.55	203.9
MnIO75	71.13	202.1
SPION	67.63	57

**Table 10:** Measurement of magnetic saturation and relaxivity values of MnIOs nanoparticles compared with SPION particles

The values of saturation magnetization of pure SPION and MnIOs are represented in Table 10. Herein, the saturation magnetization of nanocrystals slightly varies for the  $\text{Mn}^{2+}$  substituted SPION crystals.

Various molar composition of  $\text{Mn}^{2+}$  modified magnetic MnIO nanoparticles were tested as a MRI contrast agent. Due to the large magnetic moment, nanoparticles can modulate the MR signal enhancement effects. The spin–spin relaxation time was

measured using  $T_2$  weighted MR images for each sample at 1.5 T clinical MRI system (Figure 51).

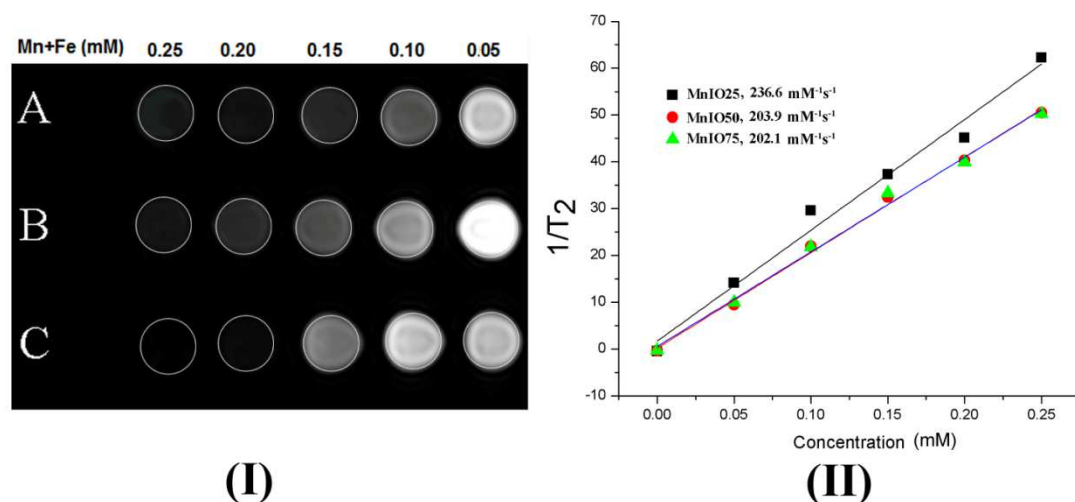


**Figure 51:** (I)  $T_2$  weighted MR images of A) MnIO75 B) MnIO50 C) MnIO25 varying concentrations at 1.5T MRI system (II) Relaxivity rate Graphs of  $1/T_2$  against the Fe+Mn concentrations of MnIOs

The magnetic relaxivities were calculated from the pixel intensity maps with different concentrations of SPION, MnIO25, MnIO50 and MnIO75 corresponding to  $57\text{mM}^{-1}\text{s}^{-1}$ ,  $236.6\text{mM}^{-1}\text{s}^{-1}$ ,  $203.9\text{mM}^{-1}\text{s}^{-1}$  and  $202.1\text{mM}^{-1}\text{s}^{-1}$ , respectively (Saraswathy et al., 2014).

#### 4.5.2 Surface Modified Manganese Ferrite (MnIOTCs) Nanoparticle for MRI Contrast Efficiency and Hyperthermia Theranostic Evolutions

In order to investigate the theranostic application of MnIOs, the particles were developed *via* previously reported aqueous co-precipitation method. In a previous section 4.5.1, we reported the development of manganese ion ( $\text{Mn}^{2+}$ )-substituted ferrite crystals with various molar concentrations (substituted concentration 25%, 50% and 75% of  $\text{Fe}^{2+}$  ions) *via* an aqueous co-precipitation method. The

nanoparticles were obtained by precipitation of ferrite nanocrystals in the presence of a  $Mn^{2+}$  ion precursor at a higher pH of  $\sim 12$ . Further, the colloidal suspensions were surface modified to obtain magnetic nanoparticles that had a stable crystal structure with enhanced magnetic property, improved MRI contrast enhancement and hyperthermia effect. Based on the previous reports, the MnIO crystals were surface modified using trisodium citrate molecules. MnIO crystals were dispersed and magnetically stirred in 10 M trisodium citrate stirred at room temperature for 12 h to ensure coating and stabilization. The excess citrate molecules were washed from the colloidal suspension by repeated centrifugation.

#### 4.5.2.1 Physicochemical Characterizations of MnIOTCs

The surface-modified magnetic nanoparticles were characterized by X-ray diffraction [Figure 52] and compared with the spinel structure PDF [01-071-6336] data.

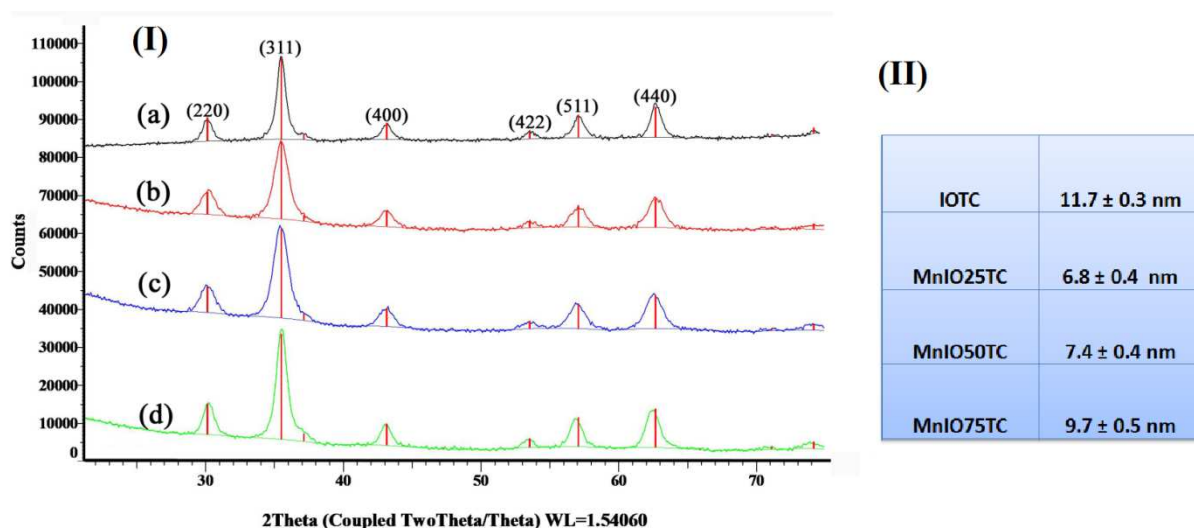


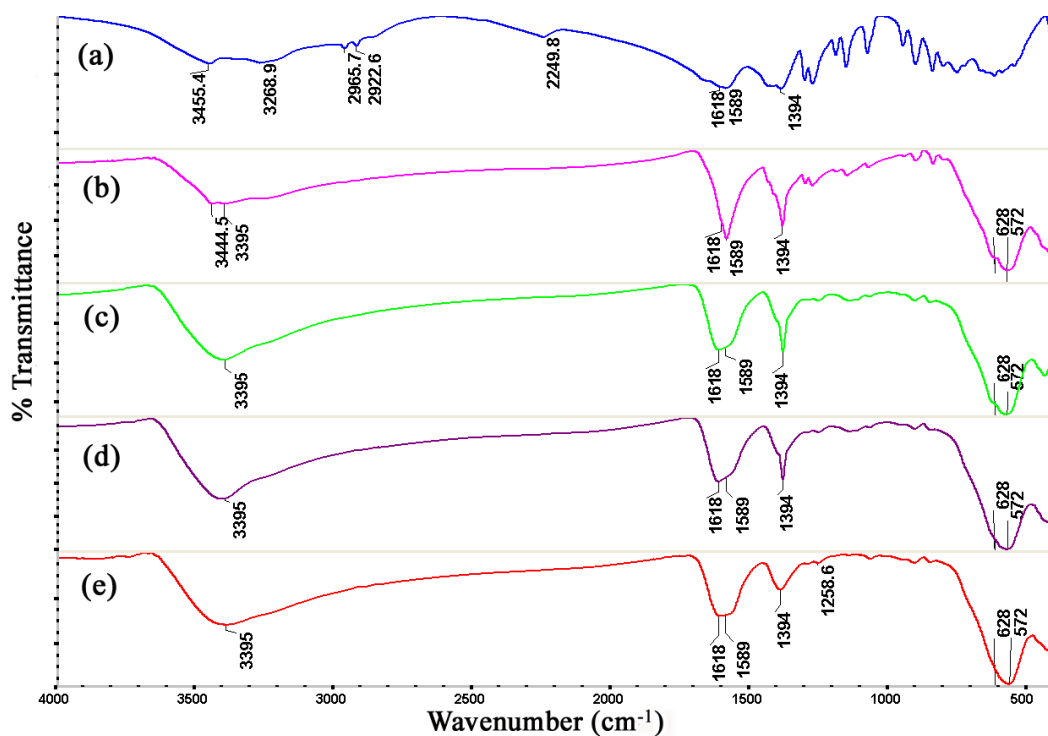
**Figure 52:** (I) The wide angle XRD patterns of the (a)IOTC (b)MnIO25TC (c)MnIO50TC and (d)MnIO75TC (II) Corresponding particles crystallite size calculation *via* scherrer equation.[ IO PDF= 01-071-6336]

Furthermore, the nanoparticles were characterized by DLS, FTIR, TGA, TEM, and VSM. The DLS data and zeta potential values displayed in Table 11 showed large hydrodynamic size and higher zeta potential values due to the presence of citrate molecules on the surface-modified samples compared with those of bare particles.

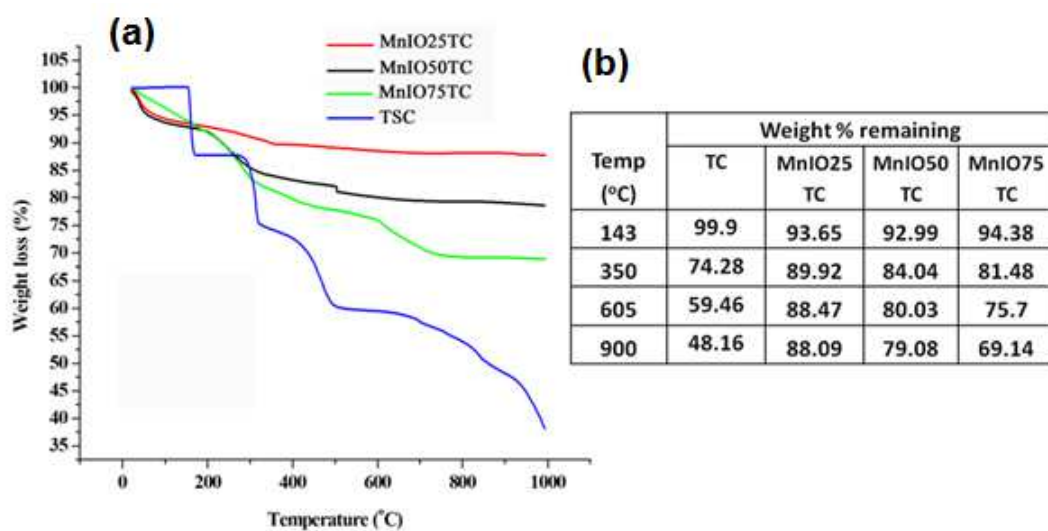
Sample	Zeta potential (mV)	Hydrodynamic size (nm)
IO	-15.3±0.8	
IOTC	-25.5±1.2	107.8±8.4
MnIO25	-12±0.7	
MnIO25TC	-16.3±1.8	72.44±4.9
MnIO50	1.45±0.3	
MnIO50TC	-21.5±2.2	85.56±9.2
MnIO75	5.06±0.8	
MnIO75TC	-27.1±1.8	105.2±7.3

**Table 11:** Zeta potential and hydrodynamic measurement of bare and trisodium citrate surface modified manganese ferrite particles

The vibrations observed at  $1394\text{ cm}^{-1}$  and  $1589\text{ cm}^{-1}$  in the FT-IR spectra of Figure 53. The amount of citrate coated on the particles was estimated *via* the TGA measurements represented in Figure 54(a) and the corresponding percentage of weight remaining in Figure 54 (b).



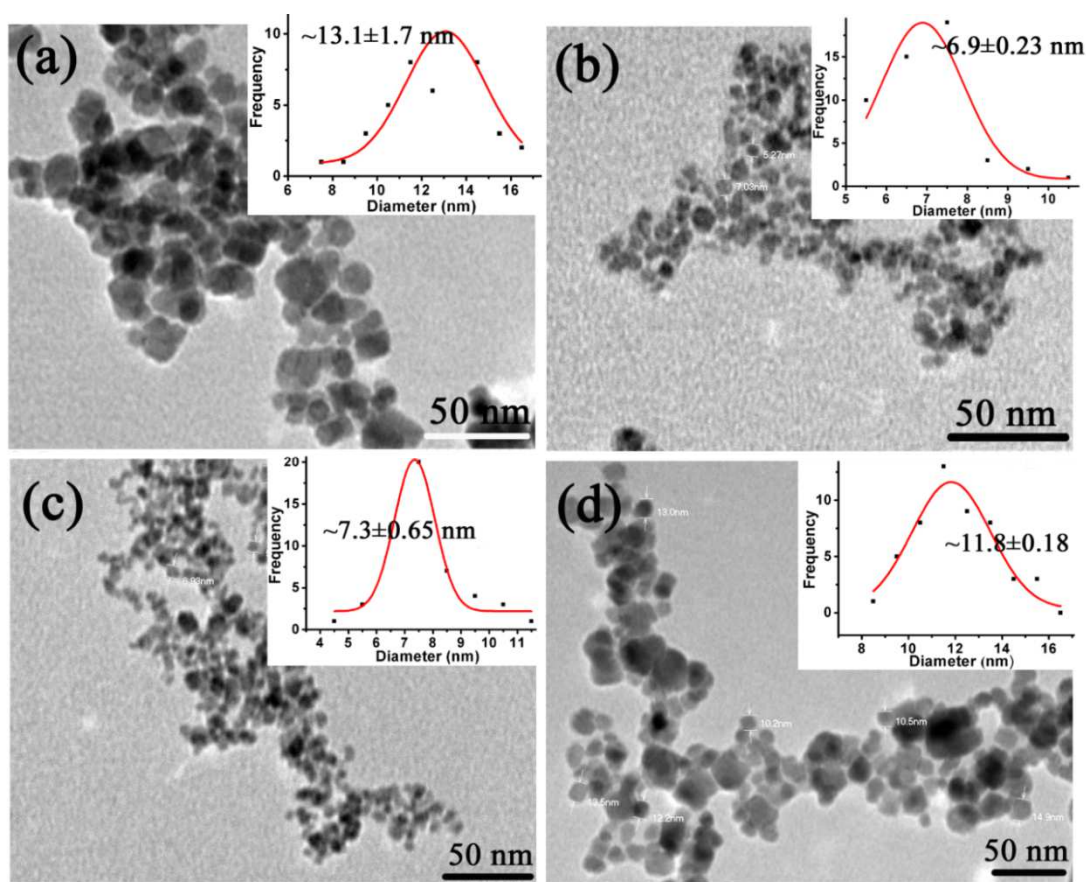
**Figure 53:** FT-IR spectra of trisodium citrate modified manganese ferrite nanoparticles (a) Trisodium citrate (b) IOTC (c) MnIO25TC (d) MnIO50TC and (e) MnIO75TC



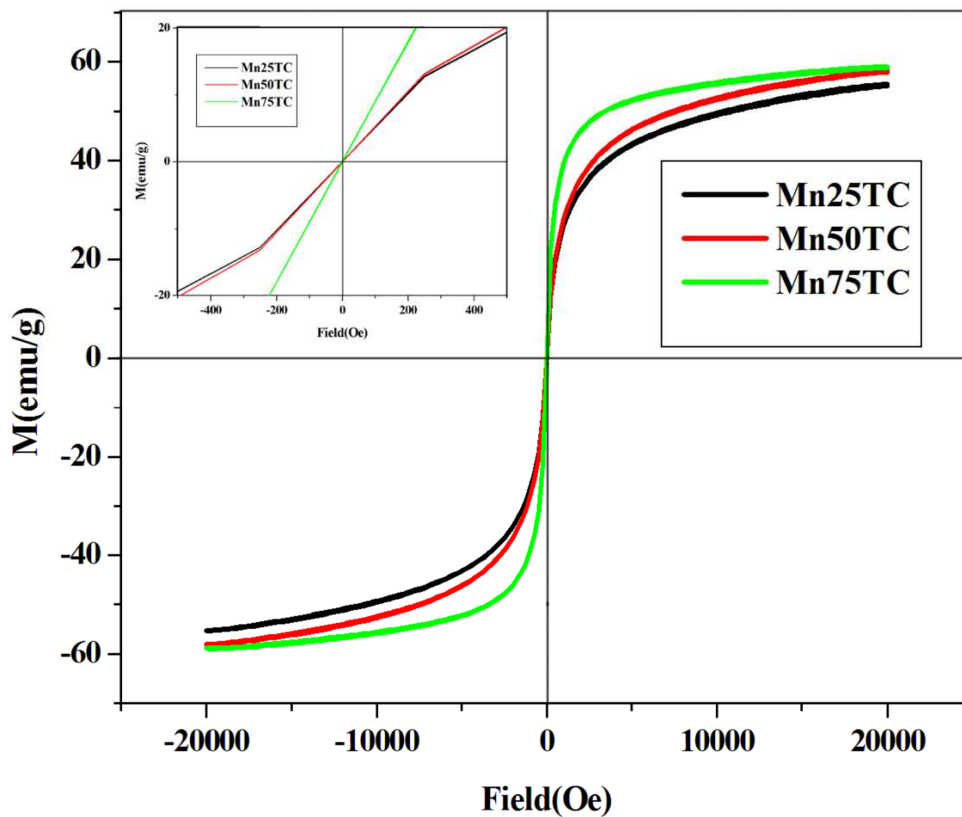
**Figure 54:** Thermogravimetric analysis of MnIOTCs (a) characteristic weight loss pattern and (b) the percentage amount of weight remained in temperature range

Figure 55 shows a typical TEM image of MnIOTCs deposited on a grid from a water suspension and subsequently dried in air. The average particle ( $n=50$ ) diameters are  $\sim 13 \pm 1.7$  nm for IOTC,  $\sim 6 \pm 0.23$  nm for MnIO25TC,  $\sim 7 \pm 0.65$  nm for MnIO50TC and  $\sim 11 \pm 0.18$  nm for MnIO75TC.

The VSM data (Figure 56) indicate saturation magnetization values of 55.4, 58, 58.8 emu/g for MnIO25TC, MnIO50TC and MnIO75TC, respectively, showing substantial superparamagnetic behavior for all MnIOTCs.



**Figure 55:** TEM micrographs and corresponding particles distributions in the insets (a)IOTC (b)MnIO25TC (c)MnIO50TC and (d)MnIO75TC



**Figure 56:** Field dependent magnetization curves of MnIOTCs at 300K and corresponding coercivity and remanence shown at inset

#### 4.5.2.2 Biological Evaluations of MnIOTCs

Preliminary biocompatibility evaluation studies of MnIOTCs were performed *via* alamar blue assay (Figure 57) and hemocompatibility testing. The cytotoxicity of MnIOTCs with varying compositions was further confirmed by observation of the variation in cell morphology after treatment of the cells with these particles. Figure 58 shows confocal microscopic images of HeLa cells treated with a higher concentration (2 mg/mL) of MnIOTCs.

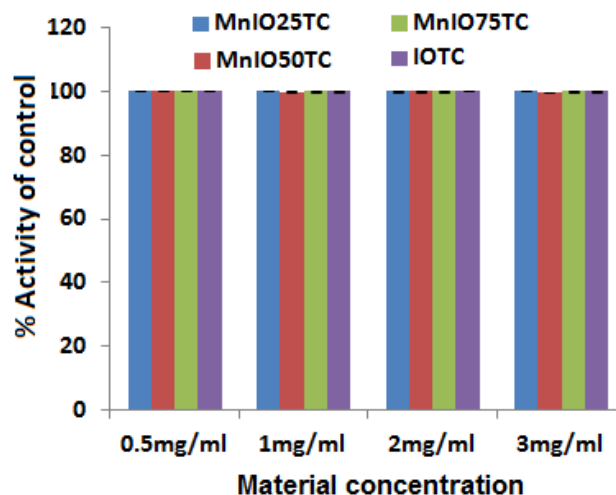


**Figure 57:** Cytotoxicity effect of MnIOTCs on HeLa cells treated with various concentrations of nanoparticles during 24 h incubation and analyzed *via* Alamar blue assay kit, ( $p < 0.05$ )

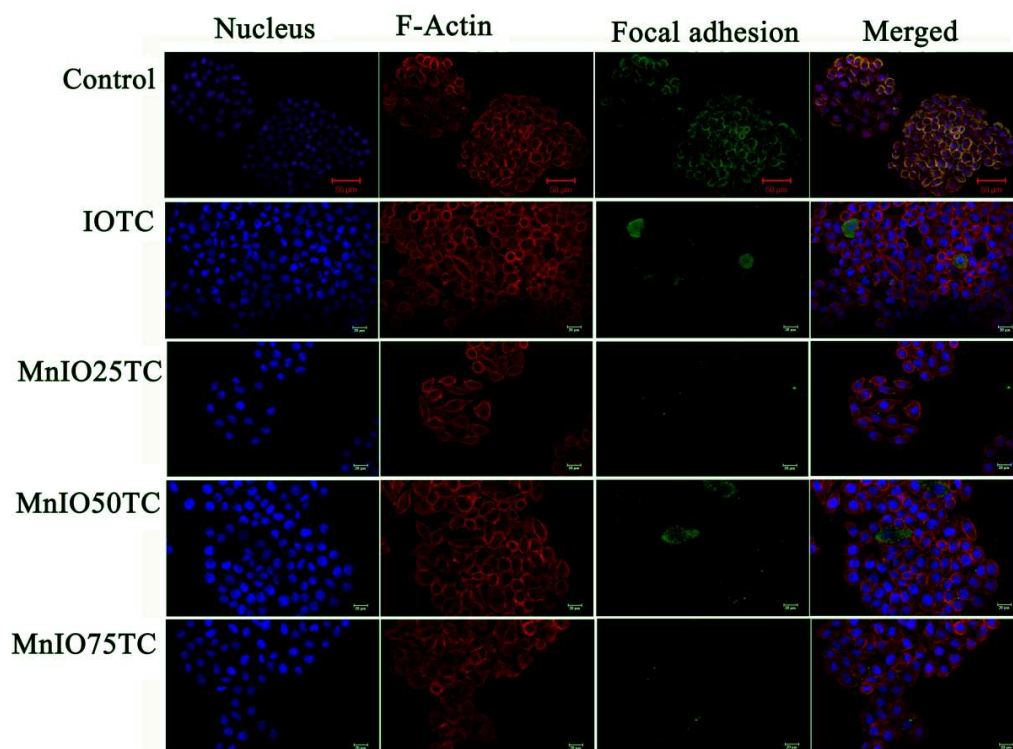


**Figure 58:** Confocal microscopic images of HeLa cells incubated with ferrite nanoparticles concentration 2mg/mL during 24h and without particle as control. In the images, cell nucleus stained with DAPI (blue), F-actin filament detected using

TRITC-conjugated Phalloidin (red), focal adhesion analyzed using anti-Vinculin monoclonal antibody and a FITC-conjugated secondary antibody (green) and merged all images

MnIOTCs are uptaken by cells, as affirmed by their localization in cells visualized using Prussian Blue (PB) staining, as indicated in Figure 59. Positive PB staining was due to the presence of ferric ions, which signals cell uptake of nanoparticles.

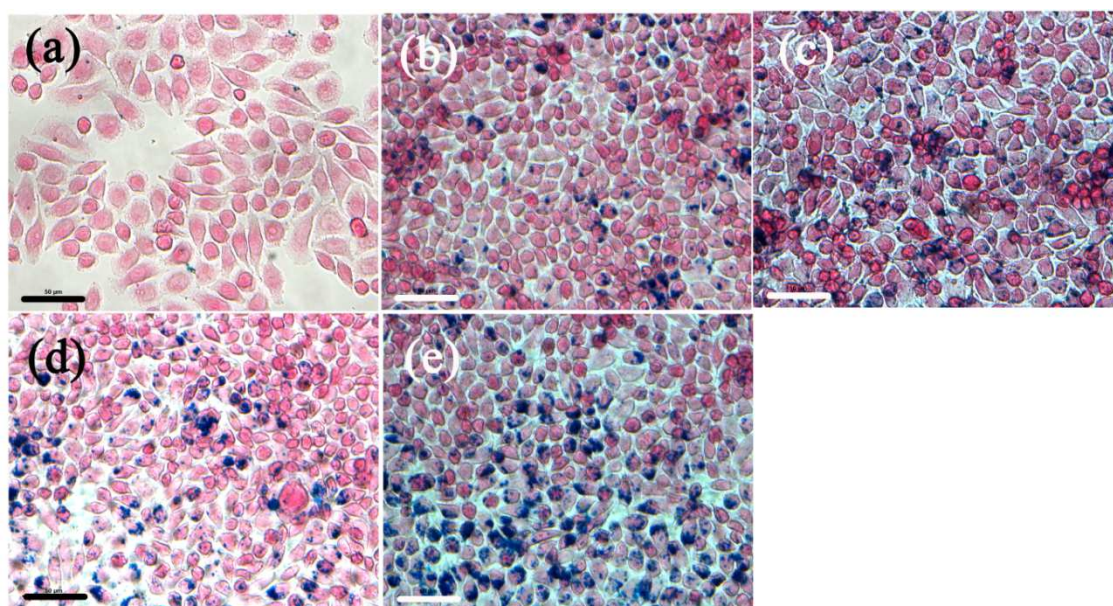


**Figure 59:** Prussian blue staining of HeLa cells after 24h incubation of 50µgs of MnIOTCs and counter stained with nuclear fast red (A) Control (Hela cell alone) (b)IOTC (c)MnIO25TC (d)MnIO50TC and (e)MnIO75TC, scale bar 50 µm

In a detailed analysis of MnIOTC interaction with blood, studies were performed with respect to hemolysis and clotting time. Table 12 indicates preliminary hemocompatibility characteristics.

Sample	Hemolysis	Clotting time
MnIOTC	0.01±0.003	235±28
MnIO50TC	0.01±0.002	250±22
MnIO75TC	0.04±0.006	255±20
IOTC	0.09±0.005	245±26
Negative control	0.00±0.000	255±30
Positive control	0.52±0.008	165±28

**Table 12:** Percentage hemolysis values of blood cells after 2hrs incubation with MnIOTCs at 37°C and clotting time measurement assessing the MnIOTCs contacted blood samples

#### 4.5.2.3 Theranostic Evaluation of MnIOTCs

The potential applications of MnIOTC lie in the area of MRI contrast enhancement and hyperthermia. Recently, few superparamagnetic iron oxide contrast agents have been reported as clinically approved (Wang, 2011), (Matuszewski et al., 2005). The quality of the current products is constrained due to their poor contrast efficacy and the toxicity associated with excess iron (Jang et al., 2009). In the current work, the MRI behavior of MnIOTCs was evaluated in an aqueous medium and is represented in Figure 60. The prime importance was on maximum concentration of Mn<sup>2+</sup> substituted iron oxide particles.

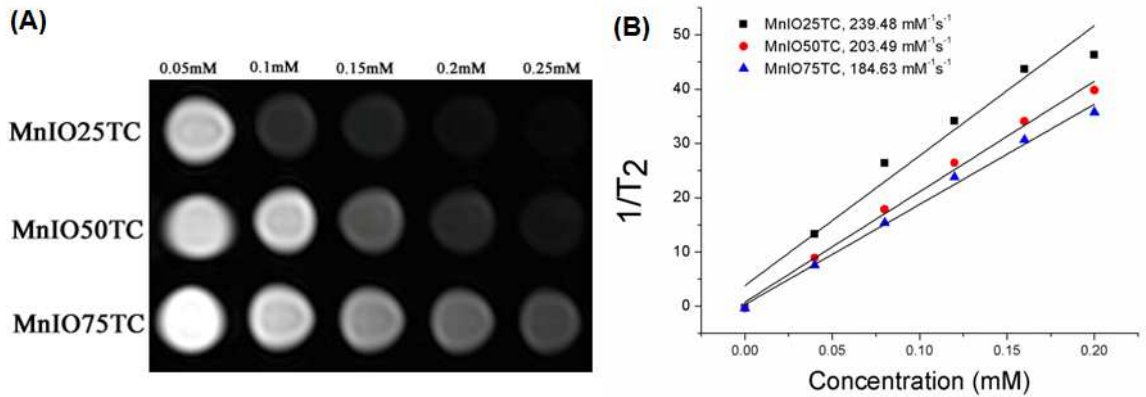


**Figure 60:** (A) T<sub>2</sub> weighted MRI images of various concentrations of MnIOTCs dispersed in water and (B) corresponding relaxation rate graph plotted 1/T<sub>2</sub> against Fe+Mn concentrations

To demonstrate the use of maximum Mn<sup>2+</sup>-substituted iron oxide as a plausible contrast agent, the contrast efficiencies of MnIO<sub>75</sub>TC and HeLa cells labeled with MnIO<sub>75</sub>TC (various concentrations) were evaluated *via in vitro* MRI evaluation. A change in contrast with respect to concentration was observed and is illustrated in Figure 61.

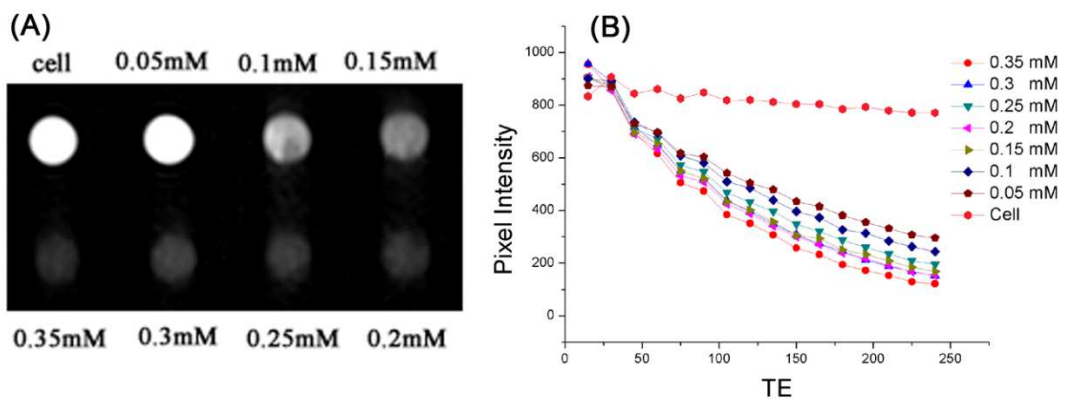


**Figure 61:** (A) T<sub>2</sub> weighted MR images of different concentrations of MnIO<sub>75</sub>TC incubated with HeLa cells during 24h (B) Corresponding pixel intensity variation plotted against TE values

To assess the hyperthermia efficiency, different concentrations of MnIO75TC were exposed to an alternating magnetic field with a field strength ranging from 14.4 mT to 38.6 mT for a period of 15 minutes. Temperature variation with respect to exposure time, strength of the magnetic field, and concentration is depicted in Figure 62.

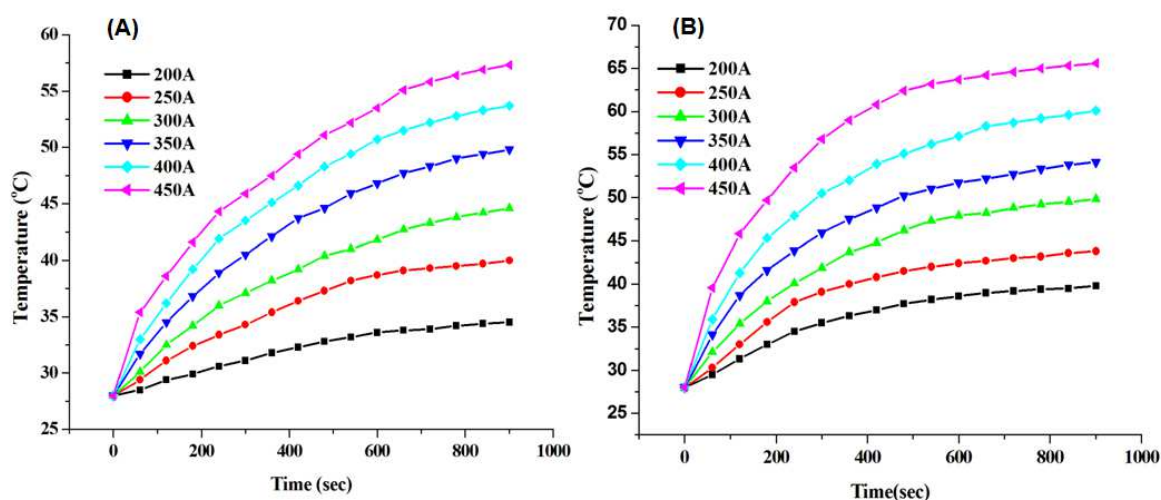


**Figure 62:** Time-temperature graphs of MnIO75TC concentrations (A) 5mg/ml and (B) 10mg/ml on exposure of 200A to 450A alternating current at 275kHz frequency

The time–temperature profile indicates a lack of hyperthermia activity at low field intensity. As a continuous magnetic field is applied, the temperature increases from 28 to 57 °C and from 28 to 65 °C for an MnIO75TC sample with concentrations of 5 mg/mL and 10 mg/mL, respectively. The heating efficiency of the magnetic material was measured using the specific loss power [SLP] (Yoo et al., 2012), which is defined as the amount of energy converted into heat per time and mass. The SLP is calculated using equation [1], and the values are presented in the Table 13.

No.	Current passing through the coil	Magnetic field strength (mT)	Specific loss power (SLP) of material concentrations	
			5 mg/ml	10 mg/ml
1	200 A	14.4	6.97±1.32	10.46±1.71
2	250 A	19.33	19.52±2.1	16.03±1.68
3	300 A	24.166	29.28±1.86	28.59±2.3
4	350 A	28.99	51.60±1.54	42.53±2.45
5	400 A	33.83	69.73±2.4	55.08±2.81
6	450 A	38.66	103.20±3.83	80.89±3.21

**Table 13:** Representation of hyperthermia studies based on the applied alternating current, magnetic field strength and corresponding specific loss power of MnIO75TC calculated from time-temperature graphs [SLP values with standard deviation; n=3]

In order to investigate the hyperthermia potential of MnIO75TC, the particles were applied to cancer cells and further exposed to AMF for 30 minutes. Cells treated with particles and not exposed to AMF were used as control. Post-AMF exposure cells were analyzed by flow cytometry, confocal laser scanning microscopy and scanning electron microscopy.

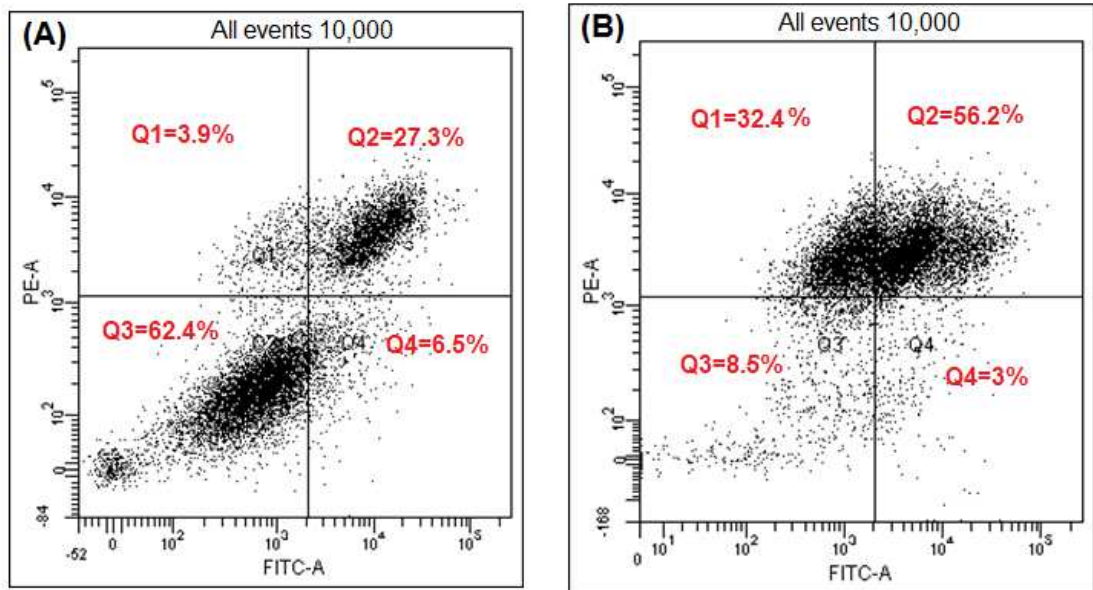


**Figure 63:** Typical dot plot obtained from FACS data showing HeLa cells distribution Annexin V/ Propidium Iodide (PI) staining (A) MnIO75TC+ HeLa cells without exposure to AMF as a control and (B) 30min exposure to MnIO75TC+ HeLa cells. The image quadrants designated as Q1=PI alone, Q2=Annexin V+PI, Q3=unstained cells and Q4= Annexin V alone positivities respectively

Figure 63 displays FACS evaluation of hyperthermia-treated HeLa cells. A steep decline in cell viability was observed with 90% of cell death, and 55% of the dead cell population stained positive for Annexin V-PI.

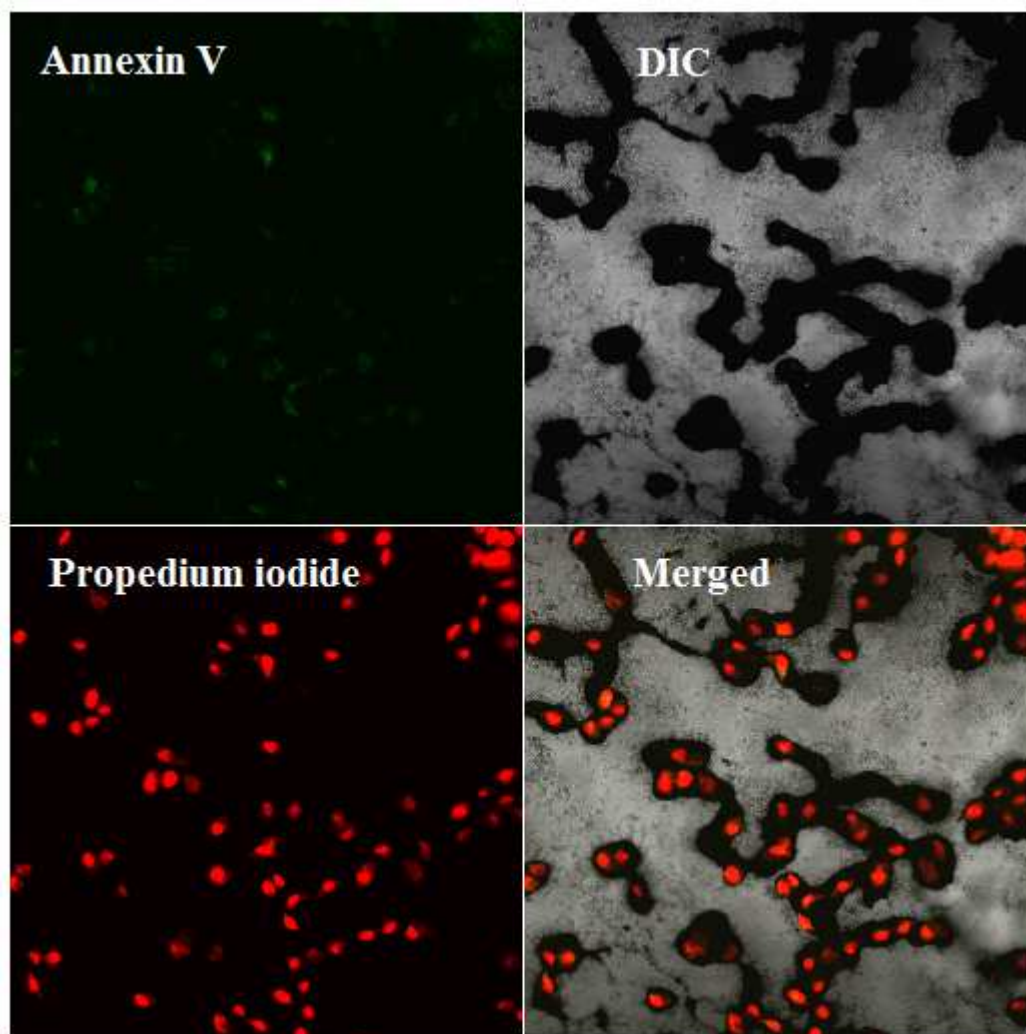


**Figure 64:** Representative images of Annexin V and PI fluorescent staining showed HeLa cells apoptosis after 30 min MnIO75TC hyperthermia treatment. In the images Annexin V visualized by a green signal, Differential interference contrast mode visualization (DIC), PI visualized by red signal and merged all images.

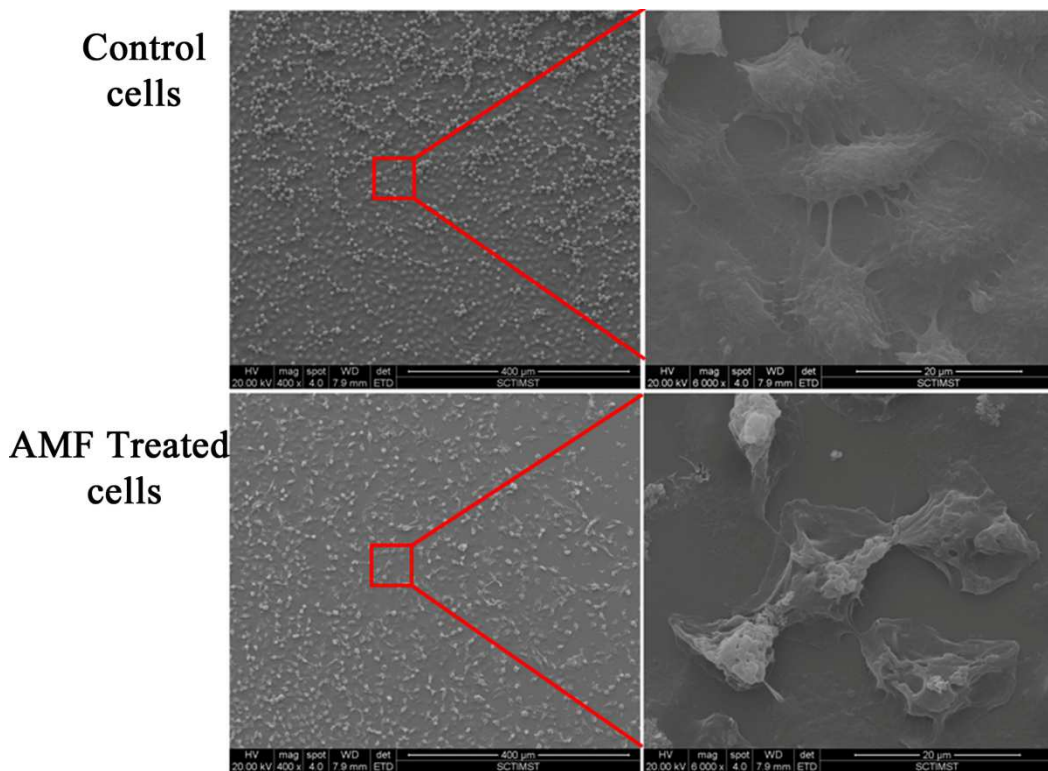


**Figure 65:** ESEM images of HeLa cells loaded with MnIO75TC (A) before and (B) after the application of the alternating magnetic field [AMF]. The corresponding images higher magnification represents in the right side. Most of the cell membrane structure collapse after exposure to the AMF

Further analysis of the treated cell population *via* cLSM confirmed (Figure 64) that nearly all cells stained positively for both Annexin V and PI. Again, morphology changes in the cells after AMF exposure were evaluated using the ESEM technique. Figure 65 indicates visible cellular damage after MnIO75TC hyperthermia.

## Chapter 5

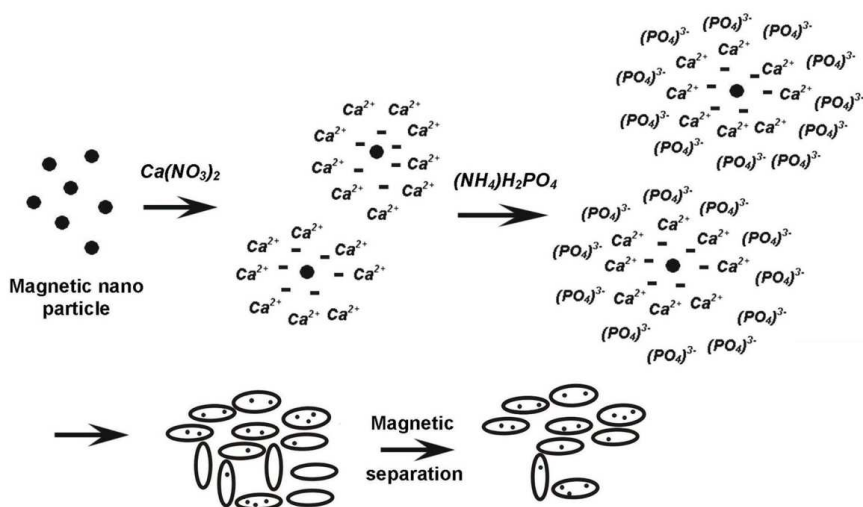
### DISCUSSION

Stable nanoparticles provide versatile approaches to remedy short falls in advanced biomedical applications. Combining knowledge and techniques from biotech & nanotech provides innovative designs for cell delivery systems, enhanced MRI contrast agents and adds teeth to therapeutic hyperthermia. Based on the observations made and experimental results recorded in this thesis the following possibilities are outlined:

1. Development of stable superparamagnetic nanocomposite (HAIO) particles *via* an aqueous co-precipitation method.
2. Evaluating targeted cell delivery and therapy applications mediated by magnetic nanocomposites (HAIO50) under *in vitro* condition.
3. Assessment of contrast enhancement in MRI imaging and hyperthermia therapeutic efficiency of HAIO50 particles in an *in vitro* condition.
4. Development of manganese ion substituted magnetic property modified superparamagnetic nanocrystal (MnIO) *via* an aqueous coprecipitation method.
5. Evaluation of contrast enhancement in MRI imaging and hyperthermia therapeutic efficacy of MnIO particles in an *in vitro* condition.

## 5.1. Development of Stable Superparamagnetic Nanocomposite (HAIO) Particles *via* an Aqueous Co-precipitation Method

Among a broad diversity of nanoparticles based on a plethora of materials, SPION have been intensively developed for several biomedical and technological applications. However, it is essential to minimize the aggregation *via* surface modification using suitable molecules for effective application. There are several types of polymers, ceramics materials utilized for surface modification of SPION particles. Among the diverse coating agent, the inorganic hydroxyapatite ceramic moiety consider as a desirable molecule because these molecules not only provide stability to the nanoparticles in solution but also help to improve the biocompatibility of particles. This is due to the innate biocompatibility of hydroxyapatite crystals. But there is a lack in appropriate synthetic strategy and microstructure evaluation in all the reported methods. Based on the literature survey, we have developed a novel technique: an *in situ* simultaneous synthesis strategy for the development of SPION hydroxyapatite nanocomposite (HAIO) *via* an aqueous method.



Scheme 1: Representation of the mechanism of formation of HAIO crystallization

In an *in situ* simultaneous co-precipitation technique, the SPION as well as HA nanocrystals were simultaneously formed. In principle, iron oxide (SPION) nanoparticles are primarily formed and their charged surfaces subsequently initiate the nucleation of amorphous calcium phosphate. Scheme 1 shows the representation for the nucleation and growth mechanism of calcium phosphate on the surface of nano-sized SPION (magnetite phase) particles. This initial  $\text{Ca}^{2+}$  growth has attributed to the size restriction of the SPION nanoparticles to ~5 nm as depicted in the scheme 1. Also the initial calcium phosphate precursor layer is the key step that facilitates the embedding of SPION particles, which later on transform to the apatite matrix. In addition, the initial adsorption of calcium phosphate prevents self-agglomeration of SPION particles and hence uniformly distributed SPION nanoparticles embedded in the calcium phosphate matrix could be achieved. Followed by the same experimental conditions were applied to the development of various molar compositions of SPION and HA composite (HAIOS) particles.

### **5.1.1 Physicochemical Characterizations of Developed HAIOS**

The phase purity analysis revealed that the nanocomposites particles exhibit no secondary phases than magnetite and hydroxyapatite. Because the comparison with ICDD card number 01-071-6336 for on SPION and 00-009-0432 for HA further confirms the presence of the cubic spinal phase of SPION ( $\text{Fe}_3\text{O}_4$ ) and hexagonal HA crystal structures. Further the percentage of SPION increased, the peaks in the spectra broadened and decreased in intensity. This phenomenon was probably due to the poor crystallinity and small crystallite size of synthesized HAIOS. The size and morphology evaluation revealed that the lower percentage of SPION nanocomposites

exhibit acicular structure, while at higher concentrations the acicular structure gradually changes to polygonal faceted spherical structures, which is confirmed from HRTEM and SEM images. The presence of iron, calcium and phosphorous peaks clearly observed from EDS patterns derived from HRTEM and SEM techniques. The EDS spectrum having Fe/Ca ratios closely matches with ICP-OES values of Fe/Ca ratios and the peak intensities from EDS spectrum also suggested phase pure formation of nanocomposites. Moreover the vibrational spectroscopic analysis revealed the nature of bonding in the HAIO nanocomposites. The peak at  $572\text{ cm}^{-1}$  observed from the spectrum was corresponding to the stretching frequency of Fe-O bond of the SPION crystals. Also the characteristic phosphate group vibrations are clearly visible in the FTIR pattern which demonstrated the presence of HA and SPION crystal existence in the nanocomposites.

The magnetic property of HAIOs was analyzed *via* vibrating sample magnetometer (VSM) and the values were compared with SPION crystals. The results affirmed that the material shows superparamagnetic property because the VSM spectrum exhibits zero value of remanence and coercivity and large value of saturation magnetizations for all compositions of HAIOs. The superparamagnetic nature signifies that the magnetic particles embedded in the system are consisting of single domain characteristic features.

Based on the literature survey (Singh et al., 2010) and considering the application efficacy of magnetic materials, our prime importance was to select a lesser content of SPION embedded HA having good magnetic property and was observed in HAIO50. Further the stability, hydrodynamic size and external field

response to magnetic has been examined. The results proved that the HAI050 particles exhibit excellent stability in neutral pH due to the surface potential and showed hydrodynamic size of 150-170nm and these particles were immediately responsive to the presence of an external magnetic field.

### **5.1.2 Biocompatibility Evaluations of HAI0s**

The preliminary toxicity evaluations of HAI0s were assessed using cytotoxicity and hemolysis analysis. The cytotoxicity effect of HAI0s compared with control values indicated not much variation with percentage of compositions and concentrations. It is noteworthy to mention that all the HAI0s concentration and compositions showed greater than 70% viability. In order to investigate applications potential efficiency nanocomposites, the HAI050 has been selected and examined the detailed biological characterizations. The higher concentrations of HAI050 particle's cytotoxicity was assessed using Alamar Blue assay. It is noteworthy to mention that, at higher concentration (3mg/mL) of HAI050 used in the study has illustrated excellent viability and this concentration was very high dose than which further highlight the superior cell tolerance with these nanocomposite formulations. The blood compatibility of the HAI050 estimated using hemolysis analysis *via* various concentrations, since the intravenous route is the most commonly explored way of administration in practical scenarios. Literature revealed that (Fornaguera et al., 2015) inherent negative charged nanoparticles may cause damage to blood cells. In our study, the HAI050 hemocompatibility analysis results demonstrated the nontoxic nature of particle.

The cell uptake of HAI050 particle was analyzed *via* Prussian blue iron staining. The presence of iron is evidenced by a blue colour within cells. Also the cellular uptake of HAI050 particles did not affect the morphology of cells and they retain their native cellular structure *in vitro*, thus proving to be non-cytotoxic. The material cell-material interaction was examined through flow cytometric analysis. Cell interactions, indicated by an increase in flow cytometric side scattering, are related to HAI050 concentration and incubation time. A control experiment was performed on a non-exposed population of cells, and cells marked as P1 (control) and P2. This helps differentiation of the cells with no internalization of nanoparticles (P1) from those where there was a strong cell– material interaction. At lower concentrations of 30, 60 and 120  $\mu\text{g}$  the granularity changes [P2 = 0.3, 0.6 and 1.2] were comparable to the control population, even after 15 minutes of incubation. However the higher concentrations of 240 and 480 $\mu\text{g}$ , the forward scattering was constant but the SSC changes with respect to time. That is cells took up higher doses of nanoparticles showed higher intensities of SSC. FSC is routinely used as a measure of cellular size comparison, irregular cell shape or damage to the cell membrane. It could be presumed from the results that the surface charge enhanced uptake of HAI050 without adversely affecting the cell cytoskeleton, as confirmed from the FSC intensities.

## **5.2 HAI050 Assisted Cell Separation, Manipulation and Culturing using External Magnetic Field for Introducing Targeted Cell Delivery**

Cell therapy based solutions for various disease and injuries are high performing compared to most conventional medicines and therapies. Especially because cells

can perform better physiologic as well as metabolic function than any of the mechanical devices, recombination proteins or chemical compounds. However, there are a lot of difficulties to systemic administration of bare cells, causing significant obstacles for sufficient retention of the therapeutic cells at the target site. In order to achieve greater efficiency and optimum performance, a higher cell dose or higher engraftment of cells is inevitable. Magnetic nanoparticle based cell therapy is one encouraging area where cells are effectively labelled, separated and concentrated from a biological suspension and delivered to the specific site with the aid of an external magnetic field.

### **5.2.1 HAI050 Nanocomposites Cells Separation using External Magnetic Field and Characterizations**

Based on the literature reports, targeted cell delivery for therapy was studied using magnetic nanoparticles. In our previous method, the newly developed magnetic nanocomposite having good magnetic property and lesser content of SPION termed as HAI050 was selected for the cells controlling and separation application. The experiment was executed through floating HeLa cells treated with HAI050 particles and separated over external magnetic field. In order to investigate the cell separation ability, the Acridine orange fluorescent dye was used and it provide evidence for cell separation *via* supernatants and pellets fluorescent intensity difference in a UV Trans illuminator. The minimum concentration of HAI050 particles required for efficient cell separation optimized, which demonstrates that a concentration of  $1 \times 10^6$  cells can effectively separated from suspension using 480  $\mu\text{g}$  of HAI050 particle and was confirmed from coulter counter analysis. To understand the mechanism of HAI050-

cell interaction, the experiments were carried out at a temperature of 4°C, which would suppress the energy consuming process such as direct endocytosis of HAIO50 to the cells (Sokolova et al., 2013). The results demonstrated that the cell surface-HAIO50 interactions are independent of temperature.

### **5.2.2 Magnetically Separated Cells Morphological Analysis and *in vitro* Culturing**

The structure and morphology of magnetically separated cells were evaluated through Giemsa staining and ESEM technique. Giemsa-stained cells imaged *via* light microscopy revealed that the characteristic spherical morphology of the cells was preserved in the control cells and cells from pellet, indicating a cell-friendly separation method. The ESEM and EDS examinations showed that the separated cells were similar to the corresponding control cell structure. Cells with adhered HAIO50 nanoparticles were visible confirmed by the corresponding calcium, phosphorous peaks intensities from the EDS spectrum.

Through magnetic accumulation-induced cell therapy, an increase in the number of cells accumulating at the injury site is reported (Polyak et al., 2008), (Riegler et al., 2010) but it is important to note that a continuous reduction in cell survival and localization at the target site occurs over time in previous studies (Li et al., 2009), (Terrovitis et al., 2010). In order to establish the efficacy of magnetic separated cells for cell therapy, and to demonstrate a non-deleterious effect to cellular structure and functions, cells post-separation were maintained in culture. Hence the magnetically separated cells were cultured in an *in vitro* condition for 24h and assessed the cytoskeleton structure using confocal laser scanning microscopy studies. From the

images, the individual actin fibres appeared as organized well-defined and clearly visible and HAIO50 particles are viewed as black intracellular spots. The depth and diameter of the cells were calculated from the 3-D reconstructed image of the cells obtained from z-axis scans. From the actin cytoskeleton distribution evaluation, no structural changes were observed in the magnetically separated cells compared to the control cells, and the fibrous structure with cell–cell contact is observed only in biocompatible conditions. Therefore, magnetic composite-based cell separation and subsequent culture could be employed as an efficient technique for cell transplantation therapy.

### **5.2.3 Three Dimensional Cell Culture using Magnetic Levitation Technique**

In a biomedical research field the native tissue model are developed through tissue engineering techniques. However there is a large gap in complexity and originality between native tissue properties and simple two dimensional cell culture experiments compared to human tissues of interest. Recent studies revealed that the three dimensional cell culture techniques extend the ability to control shape, structure and biochemical environment than existing 2D. To the extent of magnetic nanoparticle application potential, the newly developed HAIO50 particle was studied for the three dimensional cell cultures *via* magnetic levitation technique.

An *in vitro* experiment has been performed for the investigation of magnetic levitation 3D cell culture. The HeLa cells were conjugated with HAIO50 particles and levitated in the cell culture medium-air interface *via* external magnetic field and cultured for 72h. The HeLa cells rose to the air-medium interface, but were unable to leave the medium, presumably due to surface tension. The detected cell levitation in

the liquid medium affirmed that the field from a permanent magnet is sufficient to overcome the gravitational force to reach a steady state. The detailed morphology and cytoskeletal structure of 3D cultured cells were analysed through ESEM and phase contrast light microscopic techniques. The cells were well proliferated and form a sheet like structure. Moreover the cellular structure, integrity and cell –cell interaction has not changed with the presence of HAIO50 particles in three dimensional levitation methods. This is confirmed from the ESEM images, DAPI nuclear stained fluorescent images and phase contrast light microscopic images. We expect that this simple design of magnetic levitation could be further expanded to for the development of *in vitro* level tissues and organs.

#### **5.2.4 Magnetic Microsphere Development and 3D Cell Culturing**

Further exploring the possibility of magnetic levitation 3D culturing techniques, the magnetic microspheres were developed. The microsphere was synthesized using polycaprolactone and magnetic HAIO nanocomposites *via* a solvent evaporation technique. In this technique, the size of the microsphere depends on the reaction conditions such as concentration of reactants, stirring speed, addition rate etc. Hence the polymeric microspheres sizes were optimized *via* preliminary reaction parameters variations and loaded with HAIO nanocomposite particles. The developed magnetic microspheres were characterized through ESEM, XRD and FTIR techniques. The incorporation of HAIO particles in the microspheres retained the shape and sizes. The XRD and FTIR techniques confirmed the phase purity and chemical bonding in the microsphere structure. The main peaks of HA and SPION crystals are clearly

visible in the corresponding spectra and it confirmed the phase pure existence of crystals in the magnetic microspheres.

The biocompatibility of developed magnetic microspheres was examined using Alamar blue assay and hemolysis test. Alamar blue assay shows more than 95% cell viability and the percentage hemolysis was comparable to the negative control values. The results indicate that the magnetic microspheres are nontoxic irrespective of the sizes. Further magnetic microspheres were examined the 3D cell culture *via* the magnetically levitation technique. The size range of 250-350  $\mu\text{m}$  microspheres was selected and performed the cell adhesion and magnetically levitated cell culture. The cell proliferation and morphology after 72h analyzed using ESEM, which revealed that the cells were grown over the microsphere and form a spheroid shape with good cellular integrity. Viability was examined through DAPI nuclear staining and live-dead analysis. The DAPI stained cell showed intense blue colour dots from the sphere surface and an intense green colour observed from the Acridine orange-ethidium bromide staining. The results demonstrated the confirmation of live cells strongly attached over the sphere surfaces.

### **5.3 Assessment of Contrast Enhancement in MR imaging and Hyperthermia Therapeutic Efficiency of HAI050 Particles in an *In vitro* Condition**

#### **5.3.1 Hyperthermia Therapeutic Efficiency**

Over the last decade magnetic nanoparticles have been intensively studied for the hyperthermia cancer therapy and MRI contrast agent applications. The magnetic nanoparticles can produce elevated temperature in the presence of the alternating magnetic field. Also the presence of magnetic field creates more contrast effect in

MRI images, which is useful for the ease of diagnosis. The cancer cells are more sensitive to hyperthermia compared to normal cells due to the poor production of heat shock proteins. Hence recently several researchers have reported magnetic nanoparticles based theranostic approach to cancer tissues such as targeted hyperthermia and simultaneous diagnosis. In order to investigate the newly developed HAIO50 particles theranostic efficiency (hyperthermia effect and MRI contrast), the detailed *in vitro* analysis has been executed.

The temperature profile graph has been observed to the assessment of hyperthermia effect of HAIO50 particles and the values were compared to the SPION crystal. Time-temperature profile indicated the absence of hyperthermia activity at low magnetic field intensity. But on increasing the field strength the particles showed high temperature generation with respect to time. The SPION particles exhibit high temperature formation than HAIO50 under AMF application. However the therapeutic performance based on the specific loss of power (SLP), which is defined as the amount of energy converted into heat per time and mass.

Further to determine the SLP values of magnetic particles HAIO50 and SPION, various concentrations of particles were dispersed in aqueous medium and performed the hyperthermia experiment. The particle dispersions time-temperature profiles illustrate the temperature generation depends on the alternating magnetic field strength. At low field strength the hyperthermia effect was poor and on increasing the field strength, the particles produce elevated temperature and saturations. Two major mechanisms explain the temperature generation of magnetic nanoparticles on the basis of relaxations. The mechanisms which decide the relaxation of the

magnetization are (1) Neel relaxation, corresponding to the magnetic moment reversal over the energy barrier, characterized by  $T_N = T_0 \exp(KV/k_B T)$ , where  $T_0$  is the constant,  $K$  is the anisotropic constant,  $k_B$  is the Boltzmann constant and (2) Brownian relaxation, corresponding to the mechanical rotation of the whole particle, described by  $T_B = 3\eta V_H/k_B T$  where  $\eta$  is the viscosity of media and  $V_H$  is the hydrodynamic volume.

From the time-temperature profile observations the SLP values has been calculated. The SLP values of HAI050 particles depreciate with respect to increasing concentration while that of SPIONs particles rise with respect to concentration. This may depend on the stability and surface modification of SPIONs. In HAI050 nanocomposite, the SPIONs surfaces were covered with nonmagnetic HA crystals. Moreover the particle surface potential and magnetic dipolar interactions are compensated and reduced the aggregation. Therefore at higher particle concentration HAI050 exhibit good dispersion and reduces the uncontrolled temperature generation under AMF application. But in SPIONs particles at higher concentrations, the dipolar interaction and surface charge attractions dominated and form clusters, which was showing uncontrolled temperature production at AFM. Hence the SPIONs were exhibit higher SLP values at higher concentrations.

The therapeutic application to cancer, controlled temperature generation has considerable attention. The controlled temperature production could induces cancer cells elimination *via* activation of the apoptosis path way. Uncontrolled temperature treatment induces cancer tissues to eliminate through necrotic pathway, which may induce for cancer in another part of the body. Moreover the uncontrolled temperature

production may chance to damage normal tissues. In our preliminary evaluations, the HAI050 particles exhibit controlled temperature production under AMF application than SPIONs. Based on previous magnetic hyperthermia studies (Jordan et al., 1999), the HAI050 particles treated with HeLa cancer cells and examined the hyperthermia therapeutic efficiency *via* AMF application for 30min. The temperature generation on the sample was measured using noncontact mode IR thermometer. Hyperthermia efficiency of HAI050 sample to cancer cells was evaluated *via* flow cytometric analysis and ESEM technique.

Preliminary examination of cell death analysis using ethidium bromide (EB), the hyperthermia treated cells exhibit more than 75% positivity to EB staining compared with control cell, which is due to the membrane disruption through hyperthermia and permeability to EB stains. Further the cell death mechanism has been assessed using Annexin V and propidium iodide (PI) staining. The combination of both dyes normally used approach for studying apoptotic cells. In the apoptotic cells, the cell membrane phospholipid phosphatidylserine (PS) is translocated from the inner to the outer leaflet of the plasma membrane there by opening PS to the peripheral cellular environment. Annexin V is a  $\text{Ca}^{2+}$ - dependent phospholipid- binding protein with high affinity for PS, and reacts to exposed apoptotic cell surface PS. The Annexin V can be conjugated to fluorochromes while preserving its high affinity for PS and thus serves as a sensitive probe for flow cytometric studies of cells go through apoptosis. PI is utilized more frequently than other nuclear stains because it is stable and a good indicator of cell viability, based on its capability to not penetrate viable cells and also economical. The ability of PI to enter a cell is contingent to the permeability of the

membrane. Moreover the PI does not stain live or early apoptotic cells due to the existence of an intact plasma membrane. However in the late apoptotic cells, the integrity of plasma membrane and nuclear membrane decreases and permit PI to move through the membrane bind into nucleic acids and display fluorescence.

In our study, the HAI050 exposed hyperthermia treated cells were showed more than 75% both positivity to Annexin V and PI as compared with control populations in flow cytometric analysis. This could be due to the late apoptosis of HeLa cells by the HAI050 exposed hyperthermia treatment. Followed by the morphological observation has been examined with ESEM technique after hyperthermia, the images affirmed that the detected cell death after HAI050 loaded HeLa cells is lead by concurrent loss of the intact structure of the cell membrane as compared with control cells. It can also be detect that the appearance of membrane channels as an effect of AMF application, which is probably the mechanism to render the membrane permeable. The results obtained from flow cytometry and ESEM techniques demonstrated that the HAI050 exposed hyperthermia treatment eliminated the cancer cells *via* late apoptosis path way.

### **5.3.2 Contrast Enhancement in Magnetic Resonance Imaging**

The contrast enhancement of HAI050 in MRI imaging has been evaluated in aqueous phantom studies. The results revealed that a negative contrast enhancement in MR images is distinctly observed in the presence of HAI050 particles. The contrast enhancement in MRI is based on proton relaxation with respect to the local magnetic field (Chavhan et al., 2009). The proton relaxation usually occurs on spin-lattice relaxation ( $T_1$ ) and spin-spin relaxations ( $T_2$ ). In a spin-spin relaxation occurs

on the basis of loss of transverse coherence, which produces the true and characteristic relaxation, which is highly sensitive to environmental magnetic property. Hence the superparamagnetic contrast agent can make large fluctuation in relaxation time. In our study, the HAIO50 crystal containing  $\text{Fe}^{2+}$  ions are magnetically ordered within the crystal to create large susceptibility character in MRI field and create local inhomogeneous magnetic field, which reduces the  $T_2$  relaxation time and produces contrast enhancement in MR images. Furthermore the image contrast increases with an increase in the material concentration. The  $T_2$  relaxivity ( $r_2$ ) can be incurred as the slope of the plot of spin-spin relaxation rate ( $1/T_2$ ) versus the molar concentration of iron in the corresponding samples, was determined to be  $50.92\text{mM}^{-1}\text{s}^{-1}$  from the  $T_2$  measurement. In order to investigate the existence of contrast effect in biological condition, the contrast enhancement of HAIO50 were examined under *in vitro* condition using HeLa cell line. Results demonstrated that significant reduction in the signal intensity of  $T_2$  weighted MRI images as compared to untreated cells. Further, pixel intensity of their  $T_2$  weighted images decreased with increase of HAIO50 concentration. These results indicated that HAIO50 nanoparticles could be exploited as novel negative contrast enhancement agent for MRI.

Ultimately, the therapeutic hyperthermia efficiency and MRI contrast enhancement evaluation of HAIO50 particles exhibit excellent efficiency under *in vitro* investigation. The results demonstrated that the HAIO50 could be useful for the theranostic application of cancer treatment.

## **5.4 Development of Manganese ion Substituted Magnetic Property Modified Superparamagnetic Nanocrystal (MnIO) via an Aqueous Co-precipitation Method**

### **5.4.1 Synthesis and Characterization of MnIO**

The superparamagnetic nanoparticle for functional application required good magnetic property and high efficiency. If not, the magnetic nanoparticles required higher concentration for application potential. When cells are treated to nanoparticles at high concentration, it causes the production of ROS with high chemical activity (Fu et al., 2014). High ROS production can damage cells by peroxidizing lipids, modulating gene transcription, disrupting DNA, altering proteins and resulting in failure of physiological function and preceded to cell death. Hence the application of suitable magnetic particles containing minimum dosage having maximum efficiency is challenging part. However, the common spinel ferrites such as SPION have intrinsic magnetic properties with standards far below that of optimal requirement for diverse biomedical applications. In order to improve their efficiency, the spinel ferrite nanoparticles with particular physical and magnetic properties were modified during synthetic process. One among the best procedure for magnetic property modification is crystal ion substitution with appropriate candidate, which can provide a versatile strategy to tune the SPION crystal structure.

Based on the literature reports revealing advantages and economical strategy, we have developed a novel method for the  $Mn^{2+}$  substituted SPION crystal using the ideal aqueous co-precipitation route (Gupta and Gupta, 2005). SPION nanocrystal formation is highly sensitive to the percentage substitution of foreign ions because an

excess amount of bivalent oxidation does not support spinel crystal formation. Therefore, with this in regard, we have further extended the study to optimize the maximum feasible quantity of  $\text{Mn}^{2+}$  incorporation into the SPION crystals using an aqueous synthetic route. The maximum substitution of  $\text{Mn}^{2+}$  in the SPION ( $\text{MnIO}$ ) was optimized to a 75% molar concentration of ferrous ions ( $3 : 1 \text{ Mn}^{2+} : \text{Fe}^{2+}$ ); beyond which the manganese ions could not form superparamagnetic nanocrystals.

The SPION have an inverse spinel crystal and its cation distributions are  $\text{Fe}^{+3}_A[\text{Fe}^{+3}\text{Fe}^{+2}]_B\text{O}_4$ , in which A and B are tetrahedral and octahedral sites, respectively. This was attributed to the smaller size and favorable orbital splitting energy of  $\text{Fe}^{3+}$  ions occupied in the tetrahedral and the octahedral interstitial sites proportional to the  $\text{Fe}^{3+}$  and  $\text{Fe}^{2+}$  ions. The incorporation of bivalent manganese ions changed the occupancy of the inverse spinel arrangement of cations in the  $\text{Fe}_3\text{O}_4$  crystals and favoured the formation of a mixed spinel structure in the ferrite crystals. In the MnIOs, the spinel with a cubic oxygen lattice of cation distribution was formed with an expected chemical formula of  $(\text{Mn}^{2+}_{1-c}\text{Fe}^{3+})_A[\text{Mn}^{2+}_c\text{Fe}^{3+}_{2-c}]_B\text{O}_4$ .

The  $\text{Mn}^{2+}$  substitution in SPION crystals was carried out in the presence of trisodium citrate (TC) molecules. The absence of citrate ions caused the formation of large clumps of manganese ferrites, which caused significant difficulty in dispersing these particles in water, hindering their use as contrast agents (Sperling and Parak, 2010), (Dubois et al., 1999). Moreover, in magnetic nanocrystal formation, after the nucleation step, van der Waals and electrostatic forces govern the formation of the clusters. In the presence of TC, nanoparticles gain a negative surface potential, which could overcome these attractive forces. Herein, the  $\text{Mn}^{2+}$  ions have a maximum

number of unpaired electrons and similar size to that of the iron ions, and favour the isomorphous substitution of ferrous cations by manganese ions in the co-precipitation process. By this argument, we can make ferrite with very high substitution efficiency (75% molar concentration of the ferrous ion) for achieving high quality superparamagnetic nanostructure formation. Indeed the typical syntheses of MnIOs were carried out to produce a large quantity of nanoparticles using a one-pot reaction without sacrificing the characteristics of the superparamagnetic nanoparticles.

In physicochemical characterization, phase analysis *via* XRD revealed that the molar concentrations of  $\text{Mn}^{2+}$  25%, 50% and 75% of ferrous ions in the compositions of MnIOs matches with (PDF = 01-071-6336) SPION diffraction pattern, the positions and relative intensities of the strong peaks confirm the Bragg reflections indexed inverse cubic spinel structure ( $Fd3m$ ). Each sample contains identical peaks regardless of the bivalent Mn content, and there are no peaks corresponding to  $\text{MnO}_2$  or  $\text{Mn}_3\text{O}_4$ , confirming that the bivalent Mn is incorporated into the ferrite structure rather than precipitating as a manganese oxide or hydroxide along with the SPION. This could be attributed to the similarity in ionic charge and radii for  $\text{Fe}^{2+}$  and  $\text{Mn}^{2+}$ . However, the scenario changes when the  $\text{Mn}^{2+}$  concentration is more than 75% molar concentration of ferrous ions. Beyond the critical concentration (75% of ferrous ion) of  $\text{Mn}^{2+}$ , the final system did not support crystal formation in which the major peaks of spinel disappears (figure 37). The shape, structure and size distribution was evaluated using HRTEM and TEM analysis. A careful inspection of the HRTEM image further revealed the presence of some crystal defects in a few particles.

However, the d-spacing measurements obtained from HRTEM and the corresponding FFT generations are in good agreement with the interplanar distances derived from the XRD studies. The selected area diffraction patterns are very similar for all the samples, comparable to spinel ferrite and reveals that these nanoparticles are highly crystalline. Further the uniform size distribution of particles observed from the TEM images and the values are in good agreement with the calculated values of crystallite sizes from the X-ray diffraction technique. Moreover, the peak broadening in XRD is in good agreement with the variation in particle size detected by TEM. These results revealed that the reactants trisodium salt & NaOH plays a dual role in controlling the particle size in addition to acting as a co-precipitation agent. However, these molecules did not induce any complex formation other than the magnetic phase of the nanocrystals.

In chemical bonding analysis, the FT-IR spectra of the different ferrites exhibit an intense peak at  $575\text{-}550\text{ cm}^{-1}$ , corresponding to the characteristic peak of Fe–O stretching in iron oxide and Fe–O or Mn–O stretching of manganese ferrite. In addition to this intense peak, an additional weak shoulder peak at  $\sim 628\text{ cm}^{-1}$  that appears in nanoparticles also shows the presence of a magnetite phase in the nanocrystals (Ming Ma, 2003). The Fe–O vibration band widens and weakens with an increase in manganese concentration and is slightly shifted towards the lower wavenumber region. There is no oxyhydroxide peak of Fe or Mn observed in the characteristic regions, which further corroborates to the pure phase formation of manganese ferrite (Yathindranath et al., 2011), (Daou et al., 2008). Moreover the presence of tri-sodiumcitrate molecules was also confirmed by the presence main

peaks. The band at  $1668\text{ cm}^{-1}$  for tri-sodium citrate, which corresponds to the asymmetric stretching of the carboxyl group, is shifted to  $1618\text{ cm}^{-1}$  in the FTIR spectra of MnIOs. The shift in the peak position to a lower wavenumber region indicates the presence of strong hydrogen bonding, which gives an indication of the strong binding of citrate onto the MnIOs surface (Srivastava et al., 2011).

The amount of citrate molecules in MnIOs were examined through TG-DTA analysis. In the TGA curves for all the bare samples display an initial weight loss of ~4-5wt% in the temperature range 30-143°C, assigned to the removal of physically adsorbed water and hydroxyl groups from trisodium citrate, which show an endothermic peak. The following weight losses are due to the decomposition of the citrate group adsorbed on the nanoparticle surface. The second major broad exothermic peak was observed between 143-350°C showing a weight loss of ~1.5-3%. Weight loss in the second step indicates the dissociation of the citrate-metal bond accompanied by the oxidative exothermic degradation of citrate from the nanoparticle surface at higher temperature. The last stage of TG-DTA resulted in the exothermic magnetic particle phase conversion region around 605°C and due to loss of residual carbon (Pati et al., 2012), (Srivastava et al., 1987).

The molar compositions of MnIOs investigated using EDX and ICP-OES analysis. In EDS estimation, the values indicate that the surface concentration of Mn increases with an increase in the percentage of substitution in the SPION crystal. It gives strong evidence for the effective incorporation of manganese ions into the spinel structure. Moreover, the surface concentration of Mn, Fe and O atoms at 20 keV on different areas over the surface of the specimen studied are very close to one another.

This finding supports the homogeneous composition of the synthesized MnIOs. Table 8 shows the quantitative manganese content present in each of the compositions of these magnetic nanocrystals confirmed by ICP analysis. The results indicate that the samples possess a slightly varied manganese content compared to stoichiometric manganese ferrite. However, the Mn/Fe ratio is approximately equal to the EDX composition, which confirms the pure phase substitution of manganese ions into the ferrite crystals (Muruganandham et al., 2010).

The preliminary biocompatibility evaluations of MnIOs were estimated *via* blood compatibility and cytocompatibility. Maintenance of blood rheology is of prime importance in most intravenous interventions. Surface charged ferrites may induce aggregation during interaction with leukocytes and platelet cells (Demiroglu, 1997). The MnIO nanoparticles in a final concentration of 1mg/mL were used in the hemolysis, clotting time, blood cell aggregation analysis and no toxicity was reported from these studies. The cytotoxicity was examined using Alamar blue assay and compared with control cells with the results demonstrating that more than 95 % of cellular activity across the concentration levels is used for various MnIOs. Cellular uptake was verified by Prussian Blue staining. Material exposed cells retained cellular integrity and demonstrated robust non – toxic nature of the material *in vitro*.

#### **5.4.2 Evaluation of Contrast Efficiency in Magnetic Resonance Imaging**

The magnetic property and MRI contrast efficiency of MnIOs were evaluated and compared with the SPION crystals. One of the most important factors for a nanoparticle based MRI contrast agent is its magnetic properties, which depend on the crystal constitution by metallic cationic distribution among A and B sites in the

crystal constitution. The magnetic behavior of the MnIOs is expected to vary with different  $\text{Mn}^{2+}$  and  $\text{Fe}^{2+}$  positions in the crystal structure because the  $\text{Mn}^{2+}$  ion is isotropic compared to other crystal atoms. In our study, the MnIOs exhibit negligible remanence and coercivity, but the SPION showed minor value of remanence and coercivity. Recent studies report (Kolhatkar et al., 2013) that manganese ferrite shows a lower blocking temperature and higher magnetic saturation. This is because the  $\text{Mn}^{2+}$  cation in the spinel structure has five unpaired electrons and they are all in the high spin state. Moreover, the weak interaction of spin-orbital coupling gives a smaller magnetic anisotropy energy barrier than SPION and results in the particles to thermally activate through superparamagnetism *via* random flipping of its magnetization. Furthermore, previous reports have revealed that small MnIOs exhibit non-interacting properties, which helps to speed up the relaxation of the particles. Hence, the particles do not show any remanence and coercivity even at a low field (Sun et al., 2004), (Rondinone et al., 2001). In our study, the MnIO25 and MnIO50, manganese substitution decreases the saturation magnetization when compared with bare SPION particles. However, the further increase in  $\text{Mn}^{2+}$  substitution in MnIO75 (where the concentration of  $\text{Fe}^{2+}$  to  $\text{Mn}^{2+}$  is 1 : 3) lead to a slight improvement in the saturation magnetization. The shape of the hysteresis curve was also found to vary with changes in the  $\text{Mn}^{2+}$  substitution concentration.

The bivalent manganese ion has five unpaired electrons in the outer shell and has a higher magnetic moment when compared to the bivalent iron ion. Moreover, MnIO25 and MnIO50 were found to be slightly small size compared to bare SPION crystals, and therefore have a greater spin canting effect than SPION (Kim et al.,

2011). Furthermore, the observed results in the magnetization studies for MnIO25 and MnIO50 were slightly distorted when compared to the slightly larger SPION particles resulting in a lower saturation magnetisation. This may be due to the smaller size and structural anisotropic nature of the particles. However, in the case of MnIO75, the crystallite size is almost similar to that of SPION and demonstrated zero remanence and coercivity when compared with SPION. This can be clearly viewed from the intersection of loop with vertical magnetization axis in the inset of Figure 46. In the case of magnetic materials, the coercivity field ( $H_c$ ) for crystal refers to the intensity of magnetic field required to reduce the magnetization of the magnetic sample to zero. It has been observed from the magnetic measurements that both the  $M_s$  and  $H_c$  values decrease with an increase in the concentration of bivalent Mn ions in the crystal. This indicates that the incorporation of  $Mn^{2+}$  ions into the SPION matrix greatly enhance the magnetic isotropy of the crystals. Therefore, in a simple model, the spinel ferrite of oxygen packed, face centered cubic lattice, the tetrahedral ( $T_d$ ) and octahedral ( $O_h$ ) sites were occupied by magnetic ions. In the case of manganese ferrite, with a mixed spinel structure, the majority of  $T_d$  sites are expected to be occupied by  $Mn^{2+}_{1-x}Fe^{3+}_x$  ( $0 < x < 1$ ) and  $O_h$  sites by  $Mn^{2+}_x Fe^{3+}_{2-x}$ . When an external magnetic field was applied to this structure, the magnetic spins ( $Mn^{2+}/Fe^{3+}$ ) in  $O_h$  are aligned parallel to the direction of the external magnetic field but those in  $T_d$  are aligned anti parallel (McCurrie, 1994). Moreover, the maximum magnetic susceptibility was shown by manganese ferrite due to the higher magnetic spin of manganese (contribution approximately  $5 \mu_B$ ), such that the higher concentration of manganese substitution in iron oxide replaces more and more

magnetization deciding  $\text{Fe}^{2+}$  ions from the crystal position and the crystal acquires a higher magnetic saturation.

The contrast efficiency of MnIOs in MR imaging has been examined and the corresponding crystals relaxivity ( $r_2$ ) values calculated. The values show that  $r_2$  is based on the composition of the nanocrystals. As MnIOs show a higher  $r_2$  value compared to iron oxide alone, even with a lower saturation magnetization. This suggests that the relaxivity coefficient is not only dependent on the magnetic saturation of the nanostructure but also its geometry (Rebolledo et al., 2010). Another possible explanation for the faster relaxation of protons may be due to the higher magnetic moment of the manganese ions in the crystals. Furthermore, the presence of citrate molecules on the MnIOs surface retards the  $r_2$  relaxivity. The increase in coating thickness decreases the outer-sphere contribution of the core towards  $r_2$  due to the distance of the closest approach for diffusing bulk water molecules to the superparamagnetic core of the particles (Pinho et al., 2010). Moreover, the relatively smaller size of MnIO25 and MnIO50 nanoparticles have a greater surface-to-volume ratio and a greater number of hydrogen nuclei of water in proximity when compared with MnIO75. Therefore, a decrease in the coating thickness results in an increase in the diffusing bulk water molecules to the superparamagnetic core of the particles. It plays a further role on  $r_2$  relaxivity and rapidly decreases the  $T_2$  relaxation time or the dephasing of the water protons.

## **5.5 Evaluation of Contrast Enhancement in MRI imaging and Hyperthermia Therapeutic Efficacy [theranostic] of MnIO Particles in an *In vitro* Condition**

### **5.5.1 Synthesis of Stable MnIOs using Trisodium Citrate Surface Modification**

The nanoparticles consider for therapeutic application must exhibit good stability and efficiency in colloidal condition. In our previous study we developed manganese substituted ferrite (MnIOs) nanoparticles and evaluated the MRI contrast efficiency under *in vitro* condition. However, the MnIOs synthesized using this method formed aggregates during long-term storage in colloidal suspension. This aggregation could be due to the poor surface potential of the synthesized particles. Hence, for theranostic applications, a comprehensive approach is essential for study of the structural, biophysical and dispersion properties of these manganese ferrites. Surface modification of manganese ferrite using trisodium citrate resulted in superior properties compared with those of previous synthesis methods.

Liu *et al.* and Campelj *et al* reported aggregation due to poor surface potential in cases of bare iron oxide nanoparticles (Liu et al., 2009), (Campelj et al., 2008). Addition of citrate moieties at a specific desired concentration increases the surface potential of the particles and stabilizes the suspension *via* electrostatic repulsion between the particles. Hence, citrate addition is a highly suitable and efficient pathway to stabilizing novel ferrofluids and ensuring enhanced functionality. Citrate molecules have been accepted as coating agent for magnetic iron oxide nanoparticles, and Fleige and co-workers reported that macrophages readily uptake citrate-modified magnetic particles, thus demonstrating the cytocompatible nature of these particles (Fleige et al., 2002). Effective coating with citrate moieties on

nanocrystals renders them unique in their structural and physicochemical characteristics with excellent contrast efficiency in the colloidal condition. Hence the MnIO particles were surface modified with 10 M trisodium citrate molecules and characterized.

In a phase analysis *via* XRD, the peak pattern matched well with the respective hkl indexes of spinel ferrite nanocrystals structure PDF [01-071-6336]. Further, the surface modified MnIOs exhibit large hydrodynamic size and higher zeta potential values due to the presence of citrate molecules on the surface-modified samples compared with those of bare particles. In FTIR spectra, the vibrations observed at  $1394\text{ cm}^{-1}$  and  $1589\text{ cm}^{-1}$  are due to the stretching vibrations of the carboxylic group in citrate. This evidence confirms the incorporation or attachment of citrate molecules on the magnetic particle surface. The amount of citrate in the MnIOs surface was evaluated through TG-DTA analysis. The free citrate molecules show distinct degradation stages at  $143^{\circ}\text{C}$ ,  $350^{\circ}\text{C}$ ,  $605^{\circ}\text{C}$  and  $900^{\circ}\text{C}$ . In the TGA measurement, a similar pattern of % weight remaining was observed with MnIO25TC, MnIO50TC and MnIO75TC, confirming the effective surface modification. The size analysis was executed with the TEM measurement. However, the average particle sizes obtained from DLS are higher than the values ascertained *via* TEM. The anomalous reading could be due to non-visibility of the surface-modified citrate coating under bright field TEM. The TEM analysis obtained average particle sizes at the nano level for the MnIOTCs, which were compared with the crystallite size calculated from XRD (Figure 52) using the Scherrer equation, which showed nearly the same size. Further the superparamagnetic property of MnIOTCs

was confirmed through VSM measurement and all the compositions showing substantial superparamagnetic behavior.

The preliminary biocompatibilities of MnIOTC's were performed *via* Alamar blue assay and hemocompatibility testing. The results showed no significant differences in the viability of cells treated by MnIOTCs at concentrations ranging from 0.5 mg/ml to 3 mg/ml compared with the control for a period of 24 h. This result suggested that higher concentrations of nanoparticles are non-inhibitory if cellular activity is considered. The MnIOTCs exposed cellular morphologies were examined through confocal laser scanning microscopic imaging. The treated cells maintained cellular integrity with a regular morphology similar to that of the control cells. Moreover, actin staining showed individual actin fibers similar to normal cell cytoplasmic skeletal organization. Furthermore, positive staining for vinculin indicated the presence of key focal adhesion complexes that are integral to cell – extracellular matrix contact. Further, the cell friendly nature MnIOTCs were confirmed by positive Prussian blue staining from cellular uptake evaluation. This is because, the cells containing ferric ions combined with ferrocyanide resulted in the formation of blue-colored ferric ferrocyanide. Ensuring hemocompatibility is of utmost importance for medical applications of novel nanomaterials. For hemolytic assessment, concentrations of up to 1 mg/ml were used, and the results demonstrated no discernible hemolytic effects due to the different MnIOTCs. The hemolytic effect was quantitatively estimated by measuring the absorbance of the supernatant at 541 nm. A notably low percentage of hemolysis was indicated, certifying their excellent hemocompatibility at higher concentrations.

### 5.5.2 Theranostic Evaluation of MnIO75TC

In order to investigate the theranostic potential of MnIOTCs, preliminary the MR contrast efficacy evaluated *via* aqueous phantom studies using various concentrations. The signal intensities of images vary significantly as the concentration of Fe+Mn varies from 0.05 mM to 0.25 mM. This effect is clearly due to the dipolar interaction of MnIOTCs with water protons. From the pixel intensity, the  $T_2$  relaxation rates ( $r_2=1/T_2$ ) of MnIO25TC, MnIO50TC and MnIO75TC are calculated as 239, 203 and 185  $\text{mM}^{-1} \text{s}^{-1}$ , respectively. The relaxivity values demonstrate that all MnIOTC variants exhibit excellent contrast effects in phantom studies. However the prime importance was on maximum concentration of  $\text{Mn}^{2+}$ -substituted iron oxide as a plausible contrast agent. Hence the contrast efficacy of MnIO75TCs various concentrations were assessed at *in vitro* condition. The results revealed a significant reduction in signal intensity in  $T_2$ -weighted MRI images compared with untreated cells. Furthermore, the pixel intensity of the  $T_2$ -weighted images decreased with increasing Mn+Fe concentration. These results indicated that MnIO75TC nanoparticles could be exploited as a novel negative contrast enhancement agent for MRI.

The hyperthermia temperature generation of MnIO75TC was investigated by alternating magnetic field experiment. The result demonstrated that the particles exhibit excellent temperature variation from 28 to 57 °C and from 28 to 65 °C with concentrations of 5 mg/ml and 10 mg/ml, respectively. Two different mechanisms that decide the relaxation of the magnetization are (1) the Neel relaxation, corresponding to the magnetic moment reversal over the energy barrier and

characterized by  $T_N = T_0 \exp(KV/k_B T)$ , where  $T_0$  is the constant,  $K$  is the anisotropic constant, and  $k_B$  is the Boltzmann constant, and (2) Brownian relaxation, corresponding to the mechanical rotation of the entire particle, described by  $T_B = 3\eta V_H/k_B T$ , where  $\eta$  is the viscosity of the media, and  $V_H$  is the hydrodynamic volume (Rosensweig, 2002), (Vamvakidis et al., 2014).

From the results, the figure 62: represents the variation in heat generated with a field strength ranging from 14.4 mT to 38.6 mT at a magnetic field frequency of 275 kHz. After 13-15 min of exposure to the magnetic field, the temperature of the particle suspension achieved saturation. At the saturation temperature point, the energy for maintenance of the saturation temperature is nearly equal to the energy generated by the application of an alternating magnetic field to the particles (Pham Hoai Linh, 2009). The saturation temperature and rate of increase of temperature necessary to reach saturation depend on the magnetic field strength and concentration of the suspension (Rosensweig, 2002). Hence, highly concentrated samples have elevated temperature generation capabilities and saturation rates, which is evident from Figure 62.

However, the SLP values appear to decrease with increasing concentration, even with application of constant field strength. A plausible explanation is the apparent reduction of the inter-particle distance with the increasing concentration of nanoparticles (Urtizberea et al., 2010), (Carlos Martinez-Boubeta, 2013). When the system is exposed to an alternating magnetic field, it becomes magnetized, and magnetic dipolar interaction becomes a significant factor that contributes to the magnetization value. Furthermore, the energy dissipation mechanism is strongly dependent on dipole-dipole interactions [Neel relaxation time]. At higher

concentrations, the dipolar interaction dependency on the Neel relaxation becomes greater. Therefore, the long-range collective magnetic behavior at increasing particle concentration causes a decrease in the SLP value at higher concentrations (Piñeiro-Redondo et al., 2011). This result confirms that the particles are stable and non-aggregating. Particle aggregates that are present due to unforeseen interactions might cause runaway temperature levels, and controlled elevation of temperature under an applied field indicates uniform particle dispersion (Wu et al., 2008). The results revealed that MnIO75TC produces effective and controlled heat generation under an alternating magnetic field and could be useful for hyperthermia applications.

Previous investigations suggested that cancerous cells are more sensitive to hyperthermia (Laurent and Mahmoudi, 2011). Thus, it is possible to destroy these cells *via* initiation of the apoptotic pathway *via* controlled temperature application. Apoptosis or programmed cell death is a specific mechanism by which cells initiate a programmed sequence leading to cell death with minimal side effects (Wang, 2011), (Marcos-Campos et al., 2011). In our study, the FACS evaluation of hyperthermia treated HeLa cells exhibit more than 90% cell death and majority of them showed both positivity to AnnexinV-PI, indicating translocation of phosphatidylserine and initiation of the apoptotic cell death process. Controlled hyperthermia promotes apoptotic cell death in cancer cell populations (Harmon et al., 1990), (O'Neill et al., 1998). Thus, a stable rise in temperature due to well dispersed and stabilized MnIO75TC particles is key to ensuring induction of apoptosis. The controlled temperature formation might occur *via* thermal conduction to the central surface area of cells, leading to apoptosis or irreversible cell injury, which further proceeds to apoptotic cell death. Further the structural integrity of hyperthermia exposed cells

was evaluated using the ESEM technique. The cells show loss of structural integrity with simultaneous shrinkage in size and decreased cellular organization compared with the control cells. Therefore, hyperthermia mediated by MnIO75TC particles is an efficient pathway for the induction of apoptotic cell death in malignant cells, which provides a ray of hope for cancer therapy. These results revealed that the MnIO75TC could be considering as a potential candidate for theranostic applications.

## Chapter 6

### SUMMARY

The present strategies for targeted cell delivery and therapy, cancer diagnosis and therapeutic approaches have several limitations as stated earlier. Parallel with the present approaches, focus was on the interdisciplinary area of nanobiotechnology to develop improved and uncomplicated nanoparticles for theranostic applications.

Primarily a homogeneous dispersion of nano iron oxide (SPION) crystallites inside the hydroxyapatite (HA) particles was achieved by a co-precipitation method. This highly stable colloidal dispersion of magnetic nano composite (HAIO) was made without the use of any surfactants. The *in-situ* generated dispersion of the composite powders showed submicron HA particles with ~5 nm SPION inside. The same experimental condition was applied for the synthesis of different compositions of magnetic nanocomposites. The phase analysis results showed the presence of hydroxyapatite (HA) and SPION with no tertiary phase. The enhancement of relative peak intensities with increased percentage of SPION phase in X-ray diffraction analysis suggests the formation of SPION together with HA without affecting the phase purity of the latter, which is important when the biological behaviour of HA is considered. The FTIR data further confirm that the introduction of SPION does not produce any considerable change in the chemical structure of HA. However, the weight percentage plays a critical role in determining the fundamental magnetic behaviour and also significantly influences the crystal shape and growth pattern of the particles. Further, the preliminary cytocompatibility and hemocompatibility of

HAIOS revealed non-toxic nature at *in vitro* condition. From the physicochemical and biological evaluations of HAIOS, the molar percentage ratios of 50:50 (HAIOS) with lower content of SPION showed better magnetic property, non-toxicity and blood compatibility and hence it was selected for further therapeutic applications.

The next attempt was to utilize HAIOS nanoparticles as a cell-binding agent for controlled targeted delivery in cell-therapy application. To this end, the cell uptake of nanoparticles was analyzed and the granularity variations quantitatively examined. The Prussian blue staining confirming the cell uptake of HAIOS particles and FACS analysis revealed the minimum concentration of HAIOS required for cellular uptake preceding to granularity changes of  $10^6$  cells in the suspension. Also, the surface charge enhanced cell uptake of HAIOS without adversely affecting the cytoskeleton, as confirmed from the flow cytometry FSC intensities. Further, various concentrations of HAIOS was used to execute magnetic separation of HeLa cells from the suspension. The magnetically separated pellets and supernatants were quantitatively as well as qualitatively based on evaluations by Coulter counter and UV transilluminator. The capability to reliably separate the cell assembly from suspension was quantified and illustrated. Moreover, the HAIOS uptake in cells could be controlled by a non-invasive magnetic field. The cells were concentrated, separated and cultured under *in vitro* condition with no detectable impact on cell growth, proliferation or intracellular structures. The results highlight the potential for using HAIOS-labelled cells as a new type of nanoprobe for remotely controlled cell therapies with better specificity and enhanced efficacy.

To examine the possibility of magnetic nanoparticle-based cell control, magnetically levitated three dimensional cell culture was developed using HAIO50 conjugated HeLa cells. Magnetically levitated cells were cultured for 72h, and the cytoskeletal structure, morphology and viability were evaluated. The ESEM images and light microscopic analysis confirmed that the cells retained structural integrity and proliferated to form sheet like structure. Further the HAIO50 material did not induce any alteration in nuclear component which was confirmed from the DAPI nuclear staining and imaging. In order to explore the opportunity of magnetic levitated cell culture, magnetic microsphere (HAIO-PCL) was developed using polycaprolactone and HAIO nanocomposite through solvent evaporation technique. The physicochemical evaluations of magnetic microspheres revealed the size confirmation, phase pure existence and retention of nature of bonding in molecules of HAIO and polycaprolactone. Preliminary biocompatibility of experiments such as Alamar blue assay and hemocompatibility suggested that the HAIO-PCL microspheres are non-toxic. Further, the cell adhesion and magnetically levitated 3D cell culture were executed using 250-350  $\mu\text{m}$  size microspheres. The ESEM images confirmed that the cells were attached and proliferated over microspheres. Moreover, the live-dead assay and DAPI nuclear staining demonstrated that the viability and structural integrity of cells over microspheres. The current study demonstrated that the HAIO based magnetically levitated 3D cell culture could be considered as a novel technique for tissue engineering.

The next attempt was to demonstrate the use of HAIO50 particles as a hyperthermia therapeutic application and MRI contrast agent. To demonstrate the hyperthermia

temperature production of HAI050 particles, various concentrations of powder and colloidal suspensions were used in the AMF experiment and time-temperature profile observed. The results confirmed that the HAI050 particles exhibit excellent temperature generation under *in vitro* condition. Further the efficacy of HAI050 hyperthermia potential was observed through specific loss power calculation and the values compared with SPION demonstrated that the HAI050 exhibit controlled temperature generation. Hence the HAI050 particles are suitable for cancer theranostic applications. To establish the therapeutic property, the HAI050 exposed cancer cells were exposed to hyperthermia and cell death levels examined qualitatively and quantitatively. Preliminary characterization *via* ethidium bromide exhibit more than 75% positivity FACS analysis revealing that the majority of the cells were dead. The Annexin V-PI assay showed more than 75% both positivity, which confirmed that most of the cells underwent the apoptotic pathway. Further the morphological observation examined *via* ESEM technique affirmed that hyperthermia treated cells had lost structural integrity and indicated increased morphological disruption as compared with control cells. The contrast enhancement property of HAI050 in MR images was assessed in a clinical MRI system *via* aqueous phantom studies and *in vitro* cell culture medium. The results proved that the HAI050 can be useful particles for T<sub>2</sub> weighted contrast agent in MRI technique. Hence, both properties such as hyperthermia therapeutic capability and MRI contrast efficacy of HAI050 under *in vitro* investigation revealed that the HAI050 particles could be considered as an ideal candidate for theranostic application.

Next, the manganese substituted superparamagnetic iron oxide nanoparticles called the manganese ferrite termed as MnIO was prepared to improve the efficiency of theranostic applications. In this context, an *in situ* substitution of  $\text{Mn}^{2+}$  was performed in SPION and a series of ferrite particles,  $\text{Mn}_x\text{Fe}_{1-x}\text{Fe}_2\text{O}_4$  with a varying molar ratio of  $\text{Mn}^{2+} : \text{Fe}^{2+}$  where 'x' varies from 0–0.75. The ferrite particles obtained were further studied in MRI contrast applications and showed appreciable enhancement in their MRI contrast properties. Manganese substituted ferrite nanocrystals (MnIOs) were synthesized using a novel, one-step aqueous coprecipitation method based on the use of a combination of sodium hydroxide and trisodium citrate (TC). This approach yielded highly crystalline, superparamagnetic MnIOs with good control over their size and bivalent Mn ion crystal substitution. The presence of a TC hydrophilic layer on the surface facilitated easy dispersion of the materials in an aqueous media. Primary characterizations such as structural, chemical and magnetic properties demonstrated the successful formation of manganese substituted ferrite. The newly developed manganese ferrite particles such as MnIO25, MnIO50 and MnIO75 exhibited  $r_2$  relaxivities of 236.6, 203.9 and 202.1  $\text{mM}^{-1} \text{ s}^{-1}$  at 1.5 T, respectively. More significantly, the MRI relaxivity of the MnIOs improved fourfold when compared to SPION crystals indicating a high potential for use as an MRI contrast agent. Further, the cytocompatibility test using alamar blue assay and blood compatibility evaluations *via* hemolysis and blood cell aggregation demonstrated excellent cell morphological integrity even at high concentrations of nanoparticles supporting the non-toxic nature of nanoparticles. This validates a cost-effective route for the high yield formation of water dispersible MnIOs, with

remarkable MRI contrast properties and biocompatibility, which can serve as a potential candidate in biomedical applications.

The stability of nanoparticle in biological conditions has been considered as of prime importance. However, the manganese ferrite synthesized using co-precipitation method formed aggregates during long-term storage in colloidal suspension. Hence the ferrofluid-based manganese ( $\text{Mn}^{2+}$ ) substituted superparamagnetic iron oxide nanoparticles stabilized by surface coating with trisodium citrate (MnIOTCs) were synthesized for enhanced hyperthermic activity and use as negative magnetic resonance imaging (MRI) contrast media intended for applications in theranostics. The synthesized MnIOTC materials were characterized based on their physicochemical and biological features. The crystal size and the particle size at the nano level were confirmed using XRD and TEM. The presence of citrate molecules on the crystal surface of the MnIOTCs were established by FTIR, TGA, DLS and zeta potential measurements. The magnetic property of MnIOTCs measurement revealed that the nanocrystals exhibit superparamagnetism. However the important aim was of obtaining a composition with fewer iron atoms for maximum theranostic efficiency. Hence MnIO75TC was selected for further application. The MnIO75TC exhibited a high  $T_2$  relaxivity of  $184.6 \text{ mM}^{-1}\text{s}^{-1}$  and showed excellent signal intensity variation *in vitro*. Hyperthermia *via* application of an alternating magnetic field to MnIO75TC in a HeLa cell population induced apoptosis, which was further confirmed by FACS and cLSM observations. The morphological features of the cells were highly disrupted after the hyperthermia experiment, as proved from ESEM images. Biocompatibility evaluation was performed using an Alamar blue assay and

hemolysis studies, and the results indicated good cytocompatibility and hemocompatibility for the synthesized particles. In the current study, the potential of MnIO75TC as a negative MRI contrast agent and a hyperthermia agent was demonstrated to confirm its utility in the burgeoning field of theranostics.

## **Conclusion**

The work focuses on the development of Iron oxide based nanoparticles with a high degree of stability and biocompatibility. Compatibility of particles were positively enhanced with addition of HA moieties. NP's thus developed were assessed successfully for cytocompatibility, hemocompatibility, cell – concentration and Theranostic capabilities. Significant enhancement in critical properties like magnetic susceptibility & Theranostic ability was achieved by Mn substitution and trisodium citrate coating. The study was based on developing novel nanoparticles for specific biomedical applications and assessing their ability to facilitate therapy, diagnostics and cell delivery within specified limits.

An *in situ* technique has been developed for the synthesis of hydroxyapatite-iron oxide nanocomposite. The results revealed that ~5nm superparamagnetic iron oxide particles were uniformly embedded in the HA crystals. The developed HAIOS were exhibit excellent magnetic field response and biocompatibility.

The targeted cell delivery method has been achieved *via* magnetic nanocomposite HAIOS and its derivatives. Based on evaluations, the non-invasive magnetic field, concentrated separated and cultured under *in vitro* condition with no detectable impact on cell growth, proliferation or intracellular structures. The results highlight

the potential for using HAI050 and its derivatives labelled cells as a new type of nanoprobe for remotely controlled cell therapies with better specificity and enhanced efficacy.

Further the HAI050 theranostic capability was assessed under *in vitro* condition. The results revealed that HAI050 aided hyperthermia treatment could destruct the cancer cells *via* apoptosis. Also the HAI050 uptake cells exhibit significant contrast enhancement in MRI images. Thus the HAI050 could be useful for the theranostic application of cancer treatment.

The bivalent manganese ion substituted SPION with molar concentrations of 25%, 50% and 75% of  $\text{Fe}^{2+}$  ion were successfully synthesized using an aqueous coprecipitation method. The incorporation of manganese ions changed their magnetic properties and significantly modified  $T_2$  MRI contrast when compared with conventional SPION.

Further the SPION substituted with  $\text{Mn}^{2+}$  with a 3:1 molar concentration of  $\text{Mn}^{2+}$  to  $\text{Fe}^{2+}$  crystals was surface modified and evaluated the theranostic property. The results revealed that the excellent contrast enhancement in MRI images. Also exhibited hyperthermia effect under alternating magnetic field and destruct cancer cells *via* apoptosis path way. Thus the potential of MnIO75TC as a negative MRI contrast agent and a hyperthermia agent was demonstrated to confirm its utility in the burgeoning field of cancer theranostics.

Nanoparticles thus developed have the innate potential to be developed further into multi-faceted therapeutic interventions that would surpass the current standards of

care. The current study has undertaken a comprehensive analysis of the existing solutions from the synthesis level and developed novel routes of compliance with current and future demands on nanotech based biomedical applications. The thesis has been able to address several issues related to acceptance of the developed technology but to exploit it fully concerns mentioned in the Future Directions are also be reviewed.

### **Future Directions**

Future application would require more data of nanoprobe stability and efficiency in human *in vitro* systems. Also would demand in-depth evaluation of concentration dependent nanotoxicity of developed magnetic particles under *in vivo* rat models. Develop a practical delivery method for use in *in vivo* models to assess the cell delivery for targeted therapy. Further the capability and efficiency of cancer theranostic potential of MnIOTC as well as HAI050 under *in vivo* rat model. Moreover to investigate the molecular level understanding of hyperthermia induced cell death, differences and advantages compared to standard processes.

## REFERENCES

1. Alez Gaby (2012) Superparamagnetism: Introduction, Effect of a Magnetic Field, Applications, and More. Webster's Digital Services, February 28.
2. Andreas Kristin, Georgieva Radostina, Ladwig Mechthild, Mueller Susanne, Notter Michael, Sittinger Michael, Ringe Jochen (2012) Highly efficient magnetic stem cell labeling with citrate-coated superparamagnetic iron oxide nanoparticles for MRI tracking. *Biomaterials* 33: 4515–4525. doi:10.1016/j.biomaterials.2012.02.064.
3. Ashokan Anusha, Menon Deepthy, Nair Shantikumar, Koyakutty Manzoor (2010) A molecular receptor targeted, hydroxyapatite nanocrystal based multi-modal contrast agent. *Biomaterials* 31: 2606–2616. doi:10.1016/j.biomaterials.2009.11.113.
4. Balasubramaniam Sharavanan, Pothayee Nikorn, Lin Yinnian, House Mike, Woodward Robert C, St. Pierre Timothy G, Davis Richey M, Riffle JS (2011) Poly(N-isopropylacrylamide)-Coated Superparamagnetic Iron Oxide Nanoparticles: Relaxometric and Fluorescence Behavior Correlate to Temperature-Dependent Aggregation. *Chem. Mater.* 23: 3348–3356. doi:10.1021/cm2009048. <http://dx.doi.org/10.1021/cm2009048>.
5. Bárcena Carlos, Sra Amandeep K, Chaubey Girija S, Khemtong Chalermchai, Liu J Ping, Gao Jinming (2008) Zinc ferrite nanoparticles as MRI contrast agents. *Chem. Commun.*: 2224–2226. doi:10.1039/B801041B. [http://pubs.rsc.org/en/content/\\_articlelanding/2008/cc/b801041b](http://pubs.rsc.org/en/content/_articlelanding/2008/cc/b801041b).
6. Baronzio Gian F, Hager E Dieter (2008) Hyperthermia In Cancer Treatment: A Primer. Springer Science & Business Media, May 8.
7. Bean CP, Livingston JD (1959) Superparamagnetism. *J. Appl. Phys.* 30: S120–S129. doi:10.1063/1.2185850. <http://scitation.aip.org/content/aip/journal/jap/30/4/10.1063/1.2185850>.

8. Bee A, Massart R, Neveu S (1995) Synthesis of very fine maghemite particles. *J. Magn. Magn. Mater.* 149. Proceedings of the Seventh International Conference on Magnetic Fluids: 6–9. doi:10.1016/0304-8853(95)00317-7. <http://www.sciencedirect.com/science/article/pii/S0304885395003177>.
  
9. Berry Catherine C, Charles Stuart, Wells Stephen, Dalby Matthew J, Curtis Adam SG (2004a) The influence of transferrin stabilised magnetic nanoparticles on human dermal fibroblasts in culture. *Int. J. Pharm.* 269: 211–225.
  
10. Berry Catherine Cecilia, Wells Stephen, Charles Stuart, Aitchison Gregor, Curtis Adam SG (2004b) Cell response to dextran-derivatised iron oxide nanoparticles post internalisation. *Biomaterials* 25: 5405–5413. doi:10.1016/j.biomaterials.2003.12.046.
  
11. Bhasarkar Jaykumar B, Chakma Sankar, Moholkar Vijayanand S (2013) Mechanistic Features of Oxidative Desulfurization Using Sono-Fenton–Peracetic Acid (Ultrasound/Fe<sup>2+</sup>–CH<sub>3</sub>COOH–H<sub>2</sub>O<sub>2</sub>) System. *Ind. Eng. Chem. Res.* 52: 9038–9047. doi:10.1021/ie400879j. <http://dx.doi.org/10.1021/ie400879j>.
  
12. Bose Susmita, Roy Mangal, Bandyopadhyay Amit (2012) Recent advances in bone tissue engineering scaffolds. *Trends Biotechnol.* 30: 546–554. doi:10.1016/j.tibtech.2012.07.005. <http://www.ncbi.nlm.nih.gov/pmc/articles/PMC3448860/>.
  
13. Bulte JWM, Zhang SC, Gelderen P van, Herynek V, Jordan EK, Duncan ID, Frank JA (1999) Neurotransplantation of magnetically labeled oligodendrocyte progenitors: Magnetic resonance tracking of cell migration and myelination. *Proc. Natl. Acad. Sci.* 96: 15256–15261. doi:10.1073/pnas.96.26.15256. <http://www.pnas.org/content/96/26/15256>.
  
14. Campelj S, Makovec D, Drogenik M (2008) Preparation and properties of water-based magnetic fluids. *J. Phys. Condens. Matter* 20: 204101. doi:10.1088/0953-8984/20/20/204101. <http://stacks.iop.org/0953-8984/20/i=20/a=204101>.

15. Cao Guozhong, Wang Ying (2011) Nanostructures and Nanomaterials: Synthesis, Properties, and Applications. World Scientific.
16. Carlos Martinez-Boubeta Konstantinos Simeonidis (2013) Learning from Nature to Improve the Heat Generation of Iron-Oxide Nanoparticles for Magnetic Hyperthermia Applications. *Sci. Rep.* 3: 1652. doi:10.1038/srep01652.
17. Carta D, Casula MF, Falqui A, Loche D, Mountjoy G, Sangregorio C, Corrias A (2009) A Structural and Magnetic Investigation of the Inversion Degree in Ferrite Nanocrystals  $MFe_2O_4$  ( $M = Mn, Co, Ni$ ). *J. Phys. Chem. C* 113: 8606–8615. doi:10.1021/jp901077c. <http://dx.doi.org/10.1021/jp901077c>.
18. Carta D, Casula MF, Floris P, Falqui A, Mountjoy G, Boni A, Sangregorio C, Corrias A (2010) Synthesis and microstructure of manganese ferrite colloidal nanocrystals. *Phys. Chem. Chem. Phys.* 12: 5074–5083. doi:10.1039/B922646J. <http://pubs.rsc.org/en/content/articlelanding/2010/cp/b922646j>.
19. Chavhan Govind B, Babyn Paul S, Thomas Bejoy, Shroff Manohar M, Haacke E Mark (2009) Principles, Techniques, and Applications of T2\*-based MR Imaging and Its Special Applications. *Radiographics* 29: 1433–1449. doi:10.1148/rg.295095034. <http://www.ncbi.nlm.nih.gov/pmc/articles/PMC2799958/>.
20. Chen Feng, Bu Wenbo, Lu Chunhua, Chen Gaoxiang, Chen Moying, Shen Xincheng, Liu Rui, Shi Jianlin (2011) Hydrothermal Synthesis of a Highly Sensitive T2-Weighted MRI Contrast Agent: Zinc-Doped Superparamagnetic Iron Oxide Nanocrystals. *J. Nanosci. Nanotechnol.* 11: 10438–10443. doi:10.1166/jnn.2011.3934.
21. Cheng Gong, Wang Zhi-Gang, Liu Yan-Lin, Zhang Ji-Lin, Sun De-Hui, Ni Jia-Zuan (2013) Magnetic Affinity Microspheres with Meso-/Macroporous Shells for Selective Enrichment and Fast Separation of Phosphorylated Biomolecules. *ACS Appl. Mater. Interfaces* 5: 3182–3190. doi:10.1021/am400191u. <http://dx.doi.org/10.1021/am400191u>.

22. Chen Jialong, Huang Nan, Ma Baolong, Maitz Manfred F, Wang Juan, Li Jingan, Li Quanli, Zhao Yuancong, Xiong Kaiqin, Liu Xin (2013) Guidance of Stem Cells to a Target Destination in Vivo by Magnetic Nanoparticles in a Magnetic Field. *ACS Appl. Mater. Interfaces* 5: 5976–5985. doi:10.1021/am400249n. <http://dx.doi.org/10.1021/am400249n>.
23. Chen Liu (2003) Atomic force microscopy of soil inorganic colloids. <http://www.tandfonline.com/doi/pdf/10.1080/00380768.2003.10409974>.
24. Chris Binns (2014) Nanomagnetism: Fundamentals and Applications, 1st Edition | Chris Binns | ISBN 9780080983530. <http://store.elsevier.com/Nanomagnetism-Fundamentals-and-Applications/isbn-9780080983530/>.
25. Chu Katrina F, Dupuy Damian E (2014) Thermal ablation of tumours: biological mechanisms and advances in therapy. *Nat. Rev. Cancer* 14: 199–208. doi:10.1038/nrc3672. <http://www.nature.com/nrc/journal/v14/n3/full/nrc3672.html>.
26. Coey JMD (2010) Magnetism and Magnetic Materials. Cambridge University Press, March 25.
27. Daou TJ, Grenèche JM, Pourroy G, Buathong S, Derory A, Ulhaq-Bouillet C, Donnio B, Guillon D, Begin-Colin S (2008) Coupling Agent Effect on Magnetic Properties of Functionalized Magnetite-Based Nanoparticles. *Chem. Mater.* 20: 5869–5875. doi:10.1021/cm801405n. <http://dx.doi.org/10.1021/cm801405n>.
28. Deatsch Alison E, Evans Benjamin A (2014) Heating efficiency in magnetic nanoparticle hyperthermia. *J. Magn. Magn. Mater.* 354: 163–172. doi:10.1016/j.jmmm.2013.11.006. <http://www.sciencedirect.com/science/article/pii/S0304885313007981>.
29. Demiroglu H (1997) The importance of erythrocyte aggregation in blood rheology: considerations on the pathophysiology of thrombotic disorders. *Blood* 89: 4236.

30. D'Souza Ajit Joseph M, Schowen Richard L, Topp Elizabeth M (2004) Polyvinylpyrrolidone-drug conjugate: synthesis and release mechanism. *J. Control. Release Off. J. Control. Release Soc.* 94: 91–100.
31. Dubois E, Cabuil V, Boué F, Perzynski R (1999) Structural analogy between aqueous and oily magnetic fluids. *J. Chem. Phys.* 111: 7147–7160. <http://scitation.aip.org/content/aip/journal/jcp/111/15/10.1063/1.480007>.
32. Edmundson Matthew, Thanh Nguyen Tk, Song Bing (2013) Nanoparticles based stem cell tracking in regenerative medicine. *Theranostics* 3: 573–582. doi:10.7150/thno.5477.
33. Fang Chen, Bhattarai Narayan, Sun Conroy, Zhang Miqin (2009) Functionalized Nanoparticles with Long-Term Stability in Biological Media. *Small Weinh. Bergstr. Ger.* 5: 1637–1641. doi:10.1002/sml.200801647. <http://www.ncbi.nlm.nih.gov/pmc/articles/PMC2883049/>.
34. Feynman Richard P (1960) There's Plenty of Room at the Bottom. *Eng. Sci.* 23: 22–36. <http://resolver.caltech.edu/CaltechES:23.5.1960Bottom>.
35. Fleige Gerrit, Seeberger Florian, Laux Daniela, Kresse Mayk, Taupitz Matthias, Pilgrimm Herbert, Zimmer Claus (2002) In vitro characterization of two different ultrasmall iron oxide particles for magnetic resonance cell tracking. *Invest. Radiol.* 37: 482–488. doi:10.1097/01.RLI.0000023571.21359.B4.
36. Fornaguera Cristina, Calderó Gabriela, Mitjans Montserrat, Vinardell Maria Pilar, Solans Conxita, Vauthier Christine (2015) Interactions of PLGA nanoparticles with blood components: protein adsorption, coagulation, activation of the complement system and hemolysis studies. *Nanoscale* 7: 6045–6058. doi:10.1039/C5NR00733J. <http://pubs.rsc.org/en/content/articlelanding/2015/nr/c5nr00733j>.
37. Fuente Jesus M de la, Grazu V (2012) Nanobiotechnology: Inorganic Nanoparticles Vs Organic Nanoparticles. Elsevier.

38. Fu Peter P, Xia Qingsu, Hwang Huey-Min, Ray Paresh C, Yu Hongtao (2014) Mechanisms of nanotoxicity: Generation of reactive oxygen species. *J. Food Drug Anal.* 22. Nanomaterials - Toxicology and Medical Applications: 64–75. doi:10.1016/j.jfda.2014.01.005. <http://www.sciencedirect.com/science/article/pii/S1021949814000064>.
39. Gaipa G, Dassi M, Perseghin P, Venturi N, Corti P, Bonanomi S, Balduzzi A, Longoni D, Uderzo C, Biondi A, Masera G, Parini R, Bertagnolio B, Uziel G, Peters C, Rovelli A (2003) Allogeneic bone marrow stem cell transplantation following CD34+ immunomagnetic enrichment in patients with inherited metabolic storage diseases. *Bone Marrow Transplant.* 31: 857–860. doi:10.1038/sj.bmt.1704024. <http://www.nature.com/bmt/journal/v31/n10/full/1704024a.html>.
40. Van Gelderen P, Ramsey NF, Liu G, Duyn JH, Frank JA, Weinberger DR, Moonen CT (1995) Three-dimensional functional magnetic resonance imaging of human brain on a clinical 1.5-T scanner. *Proc. Natl. Acad. Sci. U. S. A.* 92: 6906–6910. <http://www.ncbi.nlm.nih.gov/pmc/articles/PMC41439/>.
41. Getzlaff Mathias (2007) Fundamentals of Magnetism. Springer Science & Business Media, September 20.
42. Giustini Andrew J, Petryk Alicia A, Cassim Shiraz M, Tate Jennifer A, Baker Ian, Hoopes P Jack (2010) MAGNETIC NANOPARTICLE HYPERTHERMIA IN CANCER TREATMENT. *Nano LIFE* 1. doi:10.1142/S1793984410000067. <http://www.ncbi.nlm.nih.gov/pmc/articles/PMC3859910/>.
43. Gobbo Oliviero L, Sjaastad Kristine, Radomski Marek W, Volkov Yuri, Prina-Mello Adriele (2015) Magnetic Nanoparticles in Cancer Theranostics. *Theranostics* 5: 1249–1263. doi:10.7150/thno.11544. <http://www.ncbi.nlm.nih.gov/pmc/articles/PMC4568452/>.
44. Gossuin Yves, Gillis Pierre, Hocq Aline, Vuong Quoc L, Roch Alain (2009) Magnetic resonance relaxation properties of superparamagnetic particles. *Wiley Interdiscip. Rev. Nanomed. Nanobiotechnol.* 1: 299–310. doi:10.1002/wnan.36.

45. Grobner Thomas (2006) Gadolinium--a specific trigger for the development of nephrogenic fibrosing dermopathy and nephrogenic systemic fibrosis? *Nephrol. Dial. Transplant. Off. Publ. Eur. Dial. Transpl. Assoc. - Eur. Ren. Assoc.* 21: 1104–1108. doi:10.1093/ndt/gfk062.
46. Gupta Ajay Kumar, Gupta Mona (2005) Synthesis and surface engineering of iron oxide nanoparticles for biomedical applications. *Biomaterials* 26: 3995–4021. doi:10.1016/j.biomaterials.2004.10.012.
47. Haisler William L, Timm David M, Gage Jacob A, Tseng Hubert, Killian TC, Souza Glauco R (2013) Three-dimensional cell culturing by magnetic levitation. *Nat. Protoc.* 8: 1940–1949. doi:10.1038/nprot.2013.125.
48. Hamley IW (2003) Nanotechnology with Soft Materials. *Angew. Chem. Int. Ed.* 42: 1692–1712. doi:10.1002/anie.200200546. <http://onlinelibrary.wiley.com/doi/10.1002/anie.200200546/abstract>.
49. Harmon BV, Corder AM, Collins RJ, Gobé GC, Allen J, Allan DJ, Kerr JFR (1990) Cell Death Induced in a Murine Mastocytoma by 42–47°C Heating in Vitro: Evidence that the Form of Death Changes from Apoptosis to Necrosis Above a Critical Heat Load. *Int. J. Radiat. Biol.* 58: 845–858. doi:10.1080/09553009014552221. <http://www.tandfonline.com/doi/abs/10.1080/09553009014552221>.
50. Ho Don, Sun Xiaolian, Sun Shouheng (2011) Monodisperse Magnetic Nanoparticles for Theranostic Applications. *Acc. Chem. Res.* 44: 875–882. doi:10.1021/ar200090c. <http://dx.doi.org/10.1021/ar200090c>.
51. Horev-Azaria Limor, Baldi Giovanni, Beno Delila, Bonacchi Daniel, Golla-Schindler Ute, Kirkpatrick James C, Kolle Susanne, Landsiedel Robert, Maimon Oded, Marche Patrice N, Ponti Jessica, Romano Roni, Rossi François, Sommer Dieter, Uboldi Chiara, Unger Ronald E, Villiers Christian, Korenstein Rafi (2013) Predictive toxicology of cobalt ferrite nanoparticles: comparative in-vitro study of different cellular models using methods of knowledge discovery from data. *Part. Fibre Toxicol.* 10: 32. doi:10.1186/1743-8977-10-32.

52. Hou Chun-han, Chen Ching-wei, Hou Sheng-mou, Li Yu-ting, Lin Feng-huei (2009) The fabrication and characterization of dicalcium phosphate dihydrate-modified magnetic nanoparticles and their performance in hyperthermia processes in vitro. *Biomaterials* 30: 4700–4707. doi:10.1016/j.biomaterials.2009.05.018.
53. Huang Zheyong, Pei Ning, Wang Yanyan, Xie Xinxing, Sun Aijun, Shen Li, Zhang Shuning, Liu Xuebo, Zou Yunzeng, Qian Juying, Ge Junbo (2010) Deep magnetic capture of magnetically loaded cells for spatially targeted therapeutics. *Biomaterials* 31: 2130–2140. doi:10.1016/j.biomaterials.2009.11.062. <http://www.sciencedirect.com/science/article/pii/S0142961209013064>.
54. Hu Anming, Apblett Allen (2014) *Nanotechnology for Water Treatment and Purification*. Springer, July 4.
55. Jang Jung-tak, Nah Hyunsoo, Lee Jae-Hyun, Moon Seung Ho, Kim Min Gyu, Cheon Jinwoo (2009) Critical Enhancements of MRI Contrast and Hyperthermic Effects by Dopant-Controlled Magnetic Nanoparticles. *Angew. Chem. Int. Ed.* 48: 1234–1238. doi:10.1002/anie.200805149. <http://onlinelibrary.wiley.com/doi/10.1002/anie.200805149/abstract>.
56. Jiang Weiting, Ding Guoliang, Peng Hao, Hu Haitao (2010) Modeling of nanoparticles' aggregation and sedimentation in nanofluid. *Curr. Appl. Phys.* 10: 934–941. doi:10.1016/j.cap.2009.11.076. <http://www.sciencedirect.com/science/article/pii/S1567173909005781>.
57. Jiles David C (1998) *Introduction to Magnetism and Magnetic Materials*, Second Edition. CRC Press, June 16.
58. Jordan Andreas, Scholz Regina, Wust Peter, Fähling Horst, Felix Roland (1999) Magnetic fluid hyperthermia (MFH): Cancer treatment with AC magnetic field induced excitation of biocompatible superparamagnetic nanoparticles. *J. Magn. Magn. Mater.* 201: 413–419. doi:10.1016/S0304-8853(99)00088-8. <http://www.sciencedirect.com/science/article/pii/S0304885399000888>.

59. Kamaly Nazila, Xiao Zeyu, Valencia Pedro M, Radovic-Moreno Aleksandar F, Farokhzad Omid C (2012) Targeted polymeric therapeutic nanoparticles: design, development and clinical translation. *Chem. Soc. Rev.* 41: 2971–3010. doi:10.1039/c2cs15344k. <http://www.ncbi.nlm.nih.gov/pmc/articles/PMC3684255/>.
60. Kester Mark, Heakal Yasser, Fox Todd, Sharma Arati, Robertson Gavin P, Morgan Thomas T, Altinoğlu Erhan I, Tabaković Amra, Parette Mylisa R, Rouse Sarah M, Ruiz-Velasco Victor, Adair James H (2008) Calcium phosphate nanocomposite particles for in vitro imaging and encapsulated chemotherapeutic drug delivery to cancer cells. *Nano Lett.* 8: 4116–4121. doi:10.1021/nl802098g.
61. Khademhosseini Ali, Rajalingam Bimal, Jinno Satoshi, Langer Robert (2010) Nanoengineered Systems for Tissue Engineering and Regeneration. In *Nanotechnology*. Wiley-VCH Verlag GmbH & Co. KGaA. <http://onlinelibrary.wiley.com/doi/10.1002/9783527628155.nanotech061/abstract>.
62. Khandhar Amit P, Ferguson R Matthew, Arami Hamed, Kemp Scott J, Krishnan Kannan M (2015) Tuning surface coatings of optimized magnetite nanoparticle tracers for in vivo Magnetic Particle Imaging. *IEEE Trans. Magn.* 51. doi:10.1109/TMAG.2014.2321096. <http://www.ncbi.nlm.nih.gov/pmc/articles/PMC4403869/>.
63. Khlebtsov Nikolai, Dykman Lev (2011) Biodistribution and toxicity of engineered gold nanoparticles: a review of in vitro and in vivo studies. *Chem. Soc. Rev.* 40: 1647–1671. doi:10.1039/c0cs00018c.
64. Kim Byung Hyo, Lee Nohyun, Kim Hyongsu, An Kwangjin, Park Yong Il, Choi Yoonseok, Shin Kwangsoo, Lee Youjin, Kwon Soon Gu, Na Hyon Bin, Park Je-Geun, Ahn Tae-Young, Kim Young-Woon, Moon Woo Kyung, Choi Seung Hong, Hyeon Taeghwan (2011) Large-Scale Synthesis of Uniform and Extremely Small-Sized Iron Oxide Nanoparticles for High-Resolution T1 Magnetic Resonance Imaging Contrast Agents. *J. Am. Chem. Soc.* 133: 12624–12631. doi:10.1021/ja203340u. <http://dx.doi.org/10.1021/ja203340u>.

65. Kobayashi Takeshi (2011) Cancer hyperthermia using magnetic nanoparticles. *Biotechnol. J.* 6: 1342–1347. doi:10.1002/biot.201100045.
66. Kohler Nathan, Sun Conroy, Wang Jassy, Zhang Miqin (2005) Methotrexate-modified superparamagnetic nanoparticles and their intracellular uptake into human cancer cells. *Langmuir ACS J. Surf. Colloids* 21: 8858–8864. doi:10.1021/la0503451.
67. Kolhatkar Arati G, Jamison Andrew C, Litvinov Dmitri, Willson Richard C, Lee T Randall (2013) Tuning the Magnetic Properties of Nanoparticles. *Int. J. Mol. Sci.* 14: 15977–16009. doi:10.3390/ijms140815977. <http://www.ncbi.nlm.nih.gov/pmc/articles/PMC3759896/>.
68. Kolosnjaj-Tabi Jelena, Wilhelm Claire, Clément Olivier, Gazeau Florence (2013) Cell labeling with magnetic nanoparticles: Opportunity for magnetic cell imaging and cell manipulation. *J. Nanobiotechnology* 11: S7. doi:10.1186/1477-3155-11-S1-S7. <http://www.jnanobiotechnology.com/content/11/S1/S7/abstract>.
69. Kou Longfa, Sun Jin, Zhai Yinglei, He Zhonggui (2013) The endocytosis and intracellular fate of nanomedicines: Implication for rational design. *Asian J. Pharm. Sci.* 8: 1–10. doi:10.1016/j.ajps.2013.07.001. <http://www.sciencedirect.com/science/article/pii/S1818087613000020>.
70. Kubinová Sárka, Syková Eva (2010) Nanotechnology for treatment of stroke and spinal cord injury. *Nanomed.* 5: 99–108. doi:10.2217/nnm.09.93.
71. Kyle Terri (2008) *Essentials of Pediatric Nursing*. Lippincott Williams & Wilkins.
72. Kyrtatos Panagiotis G, Lehtolainen Pauliina, Junemann-Ramirez Manfred, Garcia-Prieto Ana, Price Anthony N, Martin John F, Gadian David G, Pankhurst Quentin A, Lythgoe Mark F (2009) Magnetic tagging increases delivery of circulating progenitors in vascular injury. *JACC Cardiovasc. Interv.* 2: 794–802. doi:10.1016/j.jcin.2009.05.014.
73. Labhasetwar Vinod, Leslie-Pelecky Diandra L (2007) *Biomedical Applications of Nanotechnology*. John Wiley & Sons, September 28.

74. Lao LL, Ramanujan RV (2004) Magnetic and hydrogel composite materials for hyperthermia applications. *J. Mater. Sci. Mater. Med.* 15: 1061–1064. doi:10.1023/B:JMSM.0000046386.78633.e5. <http://link.springer.com/article/10.1023/B%3AJMSM.0000046386.78633.e5>.
75. Laurent Sophie, Bridot Jean-Luc, Elst Luce Vander, Muller Robert N (2010) Magnetic iron oxide nanoparticles for biomedical applications. *Future Med. Chem.* 2: 427–449. doi:10.4155/fmc.09.164.
76. Laurent Sophie, Forge Delphine, Port Marc, Roch Alain, Robic Caroline, Vander Elst Luce, Muller Robert N (2008) Magnetic iron oxide nanoparticles: synthesis, stabilization, vectorization, physicochemical characterizations, and biological applications. *Chem. Rev.* 108: 2064–2110. doi:10.1021/cr068445e.
77. Laurent Sophie, Mahmoudi Morteza (2011) Superparamagnetic iron oxide nanoparticles: promises for diagnosis and treatment of cancer. *Int. J. Mol. Epidemiol. Genet.* 2: 367–390. <http://www.ncbi.nlm.nih.gov/pmc/articles/PMC3243452/>.
78. Lee Haerim, Lee Eunhye, Kim Do Kyung, Jang Nam Kyu, Jeong Yong Yeon, Jon Sangyong (2006) Antibiofouling Polymer-Coated Superparamagnetic Iron Oxide Nanoparticles as Potential Magnetic Resonance Contrast Agents for in Vivo Cancer Imaging. *J. Am. Chem. Soc.* 128: 7383–7389. doi:10.1021/ja061529k. [http:// dx.doi.org /10.1021/ja061529k](http://dx.doi.org/10.1021/ja061529k).
79. Lee Jae-Hyun, Huh Yong-Min, Jun Young-wook, Seo Jung-wook, Jang Jung-tak, Song Ho-Taek, Kim Sungjun, Cho Eun-Jin, Yoon Ho-Geun, Suh Jin-Suck, Cheon Jinwoo (2007) Artificially engineered magnetic nanoparticles for ultra-sensitive molecular imaging. *Nat. Med.* 13: 95–99. doi:10.1038/nm1467. <http://www.nature.com/nm/journal/v13/n1/abs/nm1467.html>.
80. Lei Kin Fong, Wu Min-Hsien, Hsu Che-Wei, Chen Yi-Dao (2014) Real-time and non-invasive impedimetric monitoring of cell proliferation and chemosensitivity in a perfusion 3D cell culture microfluidic chip. *Biosens.*

*Bioelectron.* 51: 16–21. doi:10.1016/j.bios.2013.07.031.  
<http://www.sciencedirect.com/science/article/pii/S0956566313005034>.

81. Leventouri Th, Kis AC, Thompson JR, Anderson IM (2005) Structure, microstructure, and magnetism in ferrimagnetic bioceramics. *Biomaterials* 26: 4924–4931. doi:10.1016/j.biomaterials.2005.01.017.
82. Liao Susan, Murugan Ramalingam, Chan Casey K, Ramakrishna Seeram (2008) Processing nanoengineered scaffolds through electrospinning and mineralization suitable for biomimetic bone tissue engineering. *J. Mech. Behav. Biomed. Mater.* 1: 252–260. doi:10.1016/j.jmbbm.2008.01.007.
83. Li Li, Jiang Wen, Luo Kui, Song Hongmei, Lan Fang, Wu Yao, Gu Zhongwei (2013) Superparamagnetic Iron Oxide Nanoparticles as MRI contrast agents for Non-invasive Stem Cell Labeling and Tracking. *Theranostics* 3: 595–615. doi:10.7150/thno.5366.  
<http://www.ncbi.nlm.nih.gov/pmc/articles/PMC3741608/>.
84. Li Shu-Hong, Lai Teresa YY, Sun Zhuo, Han Mihan, Moriyama Eduardo, Wilson Brian, Fazel Shafie, Weisel Richard D, Yau Terrence, Wu Joseph C, Li Ren-Ke (2009) Tracking cardiac engraftment and distribution of implanted bone marrow cells: Comparing intra-aortic, intravenous, and intramyocardial delivery. *J. Thorac. Cardiovasc. Surg.* 137: 1225–1233.e1. doi:10.1016/j.jtcvs.2008.11.001.  
<http://www.jtcvsonline.org/article/S0022522308019442/abstract>.
85. Liu Hon-Man, Wu Si-Han, Lu Chen-Wen, Yao Ming, Hsiao Jong-Kai, Hung Yann, Lin Yu-Shen, Mou Chung-Yuan, Yang Chung-Shi, Huang Dong-Ming, Chen Yao-Chang (2008) Mesoporous silica nanoparticles improve magnetic labeling efficiency in human stem cells. *Small Weinh. Bergstr. Ger.* 4: 619–626. doi:10.1002/sml.200700493.
86. Liu Jia, Sun Zhenkun, Deng Yonghui, Zou Ying, Li Chunyuan, Guo Xiaohui, Xiong Liqin, Gao Yuan, Li Fuyou, Zhao Dongyuan (2009) Highly Water-Dispersible Biocompatible Magnetite Particles with Low Cytotoxicity Stabilized by Citrate Groups. *Angew. Chem. Int. Ed.* 48: 5875–5879.

doi:10.1002/anie.200901566.  
<http://onlinelibrary.wiley.com/doi/10.1002/anie.200901566/abstract>.

87. Li Zhen, Tan Bien, Allix Mathieu, Cooper Andrew I, Rosseinsky Matthew J (2008) Direct Coprecipitation Route to Monodisperse Dual-Functionalized Magnetic Iron Oxide Nanocrystals Without Size Selection. *Small* 4: 231–239. doi:10.1002/sml.200700575. <http://onlinelibrary.wiley.com/doi/10.1002/sml.200700575/abstract>.
88. Li Zhen, Yi Pei Wei, Sun Qiao, Lei Hao, Li Zhao Hong, Zhu Zhong Hua, Smith Sean C, Lan Min Bo, Lu Gao Qing (Max) (2012) Ultrasmall Water-Soluble and Biocompatible Magnetic Iron Oxide Nanoparticles as Positive and Negative Dual Contrast Agents. *Adv. Funct. Mater.* 22: 2387–2393. doi:10.1002/adfm.201103123. <http://onlinelibrary.wiley.com/doi/10.1002/adfm.201103123/abstract>.
89. Longmire Michelle, Choyke Peter L, Kobayashi Hisataka (2008) Clearance Properties of Nano-sized Particles and Molecules as Imaging Agents: Considerations and Caveats. *Nanomed.* 3: 703–717. doi:10.2217/17435889.3.5.703. <http://www.ncbi.nlm.nih.gov/pmc/articles/PMC3407669/>.
90. Lu An-Hui, Salabas EL, Schüth Ferdi (2007) Magnetic nanoparticles: synthesis, protection, functionalization, and application. *Angew. Chem. Int. Ed Engl.* 46: 1222–1244. doi:10.1002/anie.200602866.
91. Lu Jian, Ma Shuli, Sun Jiayu, Xia Chunchao, Liu Chen, Wang Zhiyong, Zhao Xuna, Gao Fabao, Gong Qiyong, Song Bin, Shuai Xintao, Ai Hua, Gu Zhongwei (2009) Manganese ferrite nanoparticle micellar nanocomposites as MRI contrast agent for liver imaging. *Biomaterials* 30: 2919–2928. doi:10.1016/j.biomaterials.2009.02.001.
92. Lv Qing, Deng Meng, Ulery Bret D, Nair Lakshmi S, Laurencin Cato T (2013) Nano-ceramic composite scaffolds for bioreactor-based bone engineering. *Clin. Orthop.* 471: 2422–2433. doi:10.1007/s11999-013-2859-0.

93. Mahmoudi Morteza, Hofmann Heinrich, Rothen-Rutishauser Barbara, Petri-Fink Alke (2012) Assessing the In Vitro and In Vivo Toxicity of Superparamagnetic Iron Oxide Nanoparticles. *Chem. Rev.* 112: 2323–2338. doi:10.1021/cr2002596. <http://dx.doi.org/10.1021/cr2002596>.
94. Marcos-Campos I, Asín L, Torres TE, Marquina C, Tres A, Ibarra MR, Goya GF (2011) Cell death induced by the application of alternating magnetic fields to nanoparticle-loaded dendritic cells. *Nanotechnology* 22: 205101. doi:10.1088/0957-4484/22/20/205101.
95. Matuszewski Lars, Persigehl Thorsten, Wall Alexander, Schwindt Wolfram, Tombach Bernd, Fobker Manfred, Poremba Christopher, Ebert Wolfgang, Heindel Walter, Bremer Christoph (2005) Cell Tagging with Clinically Approved Iron Oxides: Feasibility and Effect of Lipofection, Particle Size, and Surface Coating on Labeling Efficiency. *Radiology* 235: 155–161. doi:10.1148/radiol.2351040094. <http://pubs.rsna.org/doi/abs/10.1148/radiol.2351040094>.
96. McCurrie RA (1994) *Ferromagnetic Materials: Structure and Properties*. Academic, January 1.
97. Ming Ma Yu Zhang (2003) Preparation and Characterization of Magnetite Nanoparticles Coated by Amino Silane. *Colloids Surf. Physicochem. Eng. Asp.* 212: 219–226. doi:10.1016/S0927-7757(02)00305-9.
98. Min Younjin, Akbulut Mustafa, Kristiansen Kai, Golan Yuval, Israelachvili Jacob (2008) The role of interparticle and external forces in nanoparticle assembly. *Nat. Mater.* 7: 527–538. doi:10.1038/nmat2206. <http://www.nature.com/nmat/journal/v7/n7/full/nmat2206.html>.
99. Moghimi SM, Hunter AC, Murray JC (2001) Long-circulating and target-specific nanoparticles: theory to practice. *Pharmacol. Rev.* 53: 283–318.
100. Mohamed Bououdina (2014) *Handbook of Research on Nanoscience, Nanotechnology, and Advanced Materials*. IGI Global, March 31.
101. Mooney David J, Vandenberg Herman (2008) Cell delivery mechanisms for tissue repair. *Cell Stem Cell* 2: 205–213. doi:10.1016/j.stem.2008.02.005.

102. Moreno EM, Zayat M, Morales MP, Serna CJ, Roig A, Levy D (2002) Preparation of Narrow Size Distribution Superparamagnetic  $\gamma$ -Fe<sub>2</sub>O<sub>3</sub> Nanoparticles in a Sol–Gel Transparent SiO<sub>2</sub> Matrix. *Langmuir* 18: 4972–4978. doi:10.1021/la020037s. <http://dx.doi.org/10.1021/la020037s>.
103. Mosmann T (1983) Rapid colorimetric assay for cellular growth and survival: application to proliferation and cytotoxicity assays. *J. Immunol. Methods* 65: 55–63.
104. Muruganandham Manickavachagam, Amutha Ramakrishnan, Ahmmad Bashir, Repo Eveliina, Sillanpää Mika (2010) Self-Assembled Fabrication of Superparamagnetic Highly Stable Mesoporous Amorphous Iron Oxides. *J. Phys. Chem. C* 114: 22493–22501. doi:10.1021/jp110326m. <http://dx.doi.org/10.1021/jp110326m>.
105. Na Hyon Bin, Song In Chan, Hyeon Taeghwan (2009) Inorganic Nanoparticles for MRI Contrast Agents. *Adv. Mater.* 21: 2133–2148. doi:10.1002/adma.200802366. <http://onlinelibrary.wiley.com/doi/10.1002/adma.200802366/abstract>.
106. Nemala Humeshkar Bhaskar (2015) Investigation of Temperature Dependent Magnetic Hyperthermia in Fe<sub>3</sub>O<sub>4</sub> Ferrofluids. Springer International Publishing, September 22.
107. Neoh Koon Gee, Kang En Tang (2011) Functionalization of inorganic nanoparticles with polymers for stealth biomedical applications. *Polym. Chem.* 2: 747–759. doi:10.1039/C0PY00266F. <http://pubs.rsc.org/en/content/articlelanding/2011/py/c0py00266f>.
108. Nogi Kiyoshi, Naito Makio, Yokoyama Toyokazu (2012) Nanoparticle Technology Handbook. Elsevier.
109. Nune Satish K, Gunda Padmaja, Thallapally Praveen K, Lin Ying-Ying, Forrest M Laird, Berkland Cory J (2009) Nanoparticles for biomedical imaging. *Expert Opin. Drug Deliv.* 6: 1175–1194. doi:10.1517/17425240903229031. <http://www.ncbi.nlm.nih.gov/pmc/articles/PMC3097035/>.

110. O’Handley Robert C (1999) *Modern Magnetic Materials: Principles and Applications*. Wiley, November 26.
111. O’Neill KL, Fairbairn DW, Smith MJ, Poe BS (1998) Critical parameters influencing hyperthermia-induced apoptosis in human lymphoid cell lines. *Apoptosis Int. J. Program. Cell Death* 3: 369–375.
112. Pampaloni Francesco, Reynaud Emmanuel G, Stelzer Ernst HK (2007) The third dimension bridges the gap between cell culture and live tissue. *Nat. Rev. Mol. Cell Biol.* 8: 839–845. doi:10.1038/nrm2236. <http://www.nature.com/nrm/journal/v8/n10/full/nrm2236.html>.
113. Pareta Rajesh A, Taylor Erik, Webster Thomas J (2008) Increased osteoblast density in the presence of novel calcium phosphate coated magnetic nanoparticles. *Nanotechnology* 19: 265101. doi:10.1088/0957-4484/19/26/265101.
114. Park Jeong-Hui, Pérez Román A, Jin Guang-Zhen, Choi Seung-Jun, Kim Hae-Won, Wall Ivan B (2013) Microcarriers designed for cell culture and tissue engineering of bone. *Tissue Eng. Part B Rev.* 19: 172–190. doi:10.1089/ten.TEB.2012.0432.
115. Parsa Hamed, Shamsasenjan Karim, Movassaghpour Aliakbar, Akbarzadeh Parvin, Amoghli Tabrizi Bahram, Dehdilani Nima, Lotfinegad Parisa, Soleimanloo Farzaneh (2015) Effect of Superparamagnetic Iron Oxide Nanoparticles-Labeling on Mouse Embryonic Stem Cells. *Cell J. Yakhteh* 17: 221–230. <http://www.ncbi.nlm.nih.gov/pmc/articles/PMC4503836/>.
116. Pati SS, Gopinath S, Panneerselvam G, Antony MP, Philip John (2012) High temperature phase transformation studies in magnetite nanoparticles doped with Co<sup>2+</sup> ion. *J. Appl. Phys.* 112: 054320. doi:10.1063/1.4748318. <http://scitation.aip.org/content/aip/journal/jap/112/5/10.1063/1.4748318>.
117. Pearce John, Giustini Andrew, Stigliano Robert, Jack Hoopes P (2013) *Magnetic Heating of Nanoparticles: The Importance of Particle Clustering to*

- Achieve Therapeutic Temperatures. *J. Nanotechnol. Eng. Med.* 4: 0110071–01100714. doi:10.1115/1.4024904. <http://www.ncbi.nlm.nih.gov/pmc/articles/PMC3732028/>.
118. Peng Xiang-Hong, Qian Ximei, Mao Hui, Wang Andrew Y, Chen Zhuo (Georgia), Nie Shuming, Shin Dong M (2008) Targeted magnetic iron oxide nanoparticles for tumor imaging and therapy. *Int. J. Nanomedicine* 3: 311–321. <http://www.ncbi.nlm.nih.gov/pmc/articles/PMC2626938/>.
119. Pereira Clara, Pereira André M, Fernandes Carlos, Rocha Mariana, Mendes Ricardo, Fernández-García María Paz, Guedes Alexandra, Tavares Pedro B, Grenèche Jean-Marc, Araújo João P, Freire Cristina (2012) Superparamagnetic MFe<sub>2</sub>O<sub>4</sub> (M = Fe, Co, Mn) Nanoparticles: Tuning the Particle Size and Magnetic Properties through a Novel One-Step Coprecipitation Route. *Chem. Mater.* 24: 1496–1504. doi:10.1021/cm300301c. <http://dx.doi.org/10.1021/cm300301c>.
120. Pham Hoai Linh Pham Van Thach (2009) Magnetic fluid based on Fe<sub>3</sub>O<sub>4</sub> nanoparticles: Preparation and hyperthermia application. *J. Phys. Conf. Ser.* 187. doi:10.1088/1742-6596/187/1/012069.
121. Piñeiro-Redondo Yolanda, Bañobre-López Manuel, Pardiñas-Blanco Iván, Goya Gerardo, López-Quintela M Arturo, Rivas José (2011) The influence of colloidal parameters on the specific power absorption of PAA-coated magnetite nanoparticles. *Nanoscale Res. Lett.* 6: 383. doi:10.1186/1556-276X-6-383. <http://www.nanoscalereslett.com/content/6/1/383/abstract>.
122. Pinho Sonia LC, Pereira Giovannia A, Voisin Pierre, Kassem Jinane, Bouchaud Véronique, Etienne Laetitia, Peters Joop A, Carlos Luis, Mornet Stéphane, Geraldés Carlos FGC, Rocha João, Delville Marie-Hélène (2010) Fine Tuning of the Relaxometry of  $\gamma$ -Fe<sub>2</sub>O<sub>3</sub>@SiO<sub>2</sub> Nanoparticles by Tweaking the Silica Coating Thickness. *ACS Nano* 4: 5339–5349. doi:10.1021/nn101129r. <http://dx.doi.org/10.1021/nn101129r>.
123. P.M. Huang (1991) influence of citrate on the kinetics of fe(ii) oxidation and the formation of iron oxyhydroxides. <http://www.clays.org/journal/archive/volume%2039/39-1-28.pdf>.

124. Polyak Boris, Fishbein Ilia, Chorny Michael, Alferiev Ivan, Williams Darryl, Yellen Ben, Friedman Gary, Levy Robert J (2008) High field gradient targeting of magnetic nanoparticle-loaded endothelial cells to the surfaces of steel stents. *Proc. Natl. Acad. Sci. U. S. A.* 105: 698–703. doi:10.1073/pnas.0708338105.
125. Rebolledo Aldo F, Laurent Sophie, Calero Macarena, Villanueva Angeles, Knobel Marcelo, Marco Jose F, Tartaj Pedro (2010) Iron Oxide Nanosized Clusters Embedded in Porous Nanorods: A New Colloidal Design to Enhance Capabilities of MRI Contrast Agents. *ACS Nano* 4: 2095–2103. doi:10.1021/nn9013388. <http://dx.doi.org/10.1021/nn9013388>.
126. Riegler Johannes, Wells Jack A, Kyrtatos Panagiotis G, Price Anthony N, Pankhurst Quentin A, Lythgoe Mark F (2010) Targeted magnetic delivery and tracking of cells using a magnetic resonance imaging system. *Biomaterials* 31: 5366–5371. doi:10.1016/j.biomaterials.2010.03.032.
127. Rondinone Adam J, Liu Chao, Zhang Z John (2001) Determination of Magnetic Anisotropy Distribution and Anisotropy Constant of Manganese Spinel Ferrite Nanoparticles. *J. Phys. Chem. B* 105: 7967–7971. doi:10.1021/jp011183u. <http://dx.doi.org/10.1021/jp011183u>.
128. Rosensweig RE (2002) Heating magnetic fluid with alternating magnetic field. *J. Magn. Magn. Mater.* 252. Proceedings of the 9th International Conference on Magnetic Fluids: 370–374. doi:10.1016/S0304-8853(02)00706-0. <http://www.sciencedirect.com/science/article/pii/S0304885302007060>.
129. Rotello Vincent (2012a) Nanoparticles: Building Blocks for Nanotechnology. Springer Science & Business Media, December 6.
130. Rotello Vincent (2012b) Nanoparticles: Building Blocks for Nanotechnology. Springer Science & Business Media, December 6.

131. Saraswathy Ariya, Nazeer Shaiju S, Jeevan Madhumol, Nimi Nirmala, Arumugam Sabareeswaran, Harikrishnan Vijayakumar S, Varma PR Harikrishna, Jayasree Ramapurath S (2014) Citrate coated iron oxide nanoparticles with enhanced relaxivity for in vivo magnetic resonance imaging of liver fibrosis. *Colloids Surf. B Biointerfaces* 117: 216–224. doi:10.1016/j.colsurfb.2014.02.034.
132. Schoepf U, Marecos EM, Melder RJ, Jain RK, Weissleder R (1998) Intracellular magnetic labeling of lymphocytes for in vivo trafficking studies. *BioTechniques* 24: 642–646, 648–651.
133. Shi Kam Nadine Wong, Jessop Theodore C, Wender Paul A, Dai Hongjie (2004) Nanotube Molecular Transporters: Internalization of Carbon Nanotube–Protein Conjugates into Mammalian Cells. *J. Am. Chem. Soc.* 126: 6850–6851. doi:10.1021/ja0486059. <http://dx.doi.org/10.1021/ja0486059>.
134. Sigmund Wolfgang, El-Shall Hassan, Shah Dinesh O, Moudgil Brij M (2008) Particulate Systems in Nano- and Biotechnologies. CRC Press, December 22.
135. Silva CC, Filho FP, Graça MFP, Valente MA, Sombra ASB (2008) Dielectrical and structural characterization of iron oxide added to hydroxyapatite. *Bull. Mater. Sci.* 31: 635–638. doi:10.1007/s12034-008-0101-6. <http://link.springer.com/article/10.1007/s12034-008-0101-6>.
136. Singh Jai Pal (2009) Enabling Technologies for Homing and Engraftment of Cells for Therapeutic Applications. *JACC Cardiovasc. Interv.* 2: 803–804. doi:10.1016/j.jcin.2009.06.009. <http://dx.doi.org/10.1016/j.jcin.2009.06.009>.
137. Singh Neenu, Jenkins Gareth JS, Asadi Romisa, Doak Shareen H (2010) Potential toxicity of superparamagnetic iron oxide nanoparticles (SPION). *Nano Rev.* 1. doi:10.3402/nano.v1i0.5358. <http://www.ncbi.nlm.nih.gov/pmc/articles/PMC3215220/>.
138. Singh Rajesh, Lillard Jr. James W (2009) Nanoparticle-based targeted drug delivery. *Exp. Mol. Pathol.* 86. Special Issue: Structural Biology: 215–

223.doi:10.1016/j.yexmp.2008.12.004. <http://www.sciencedirect.com/science/article/pii/S001448000800141X>.

139. Sokolova Viktoriya, Kozlova Diana, Knuschke Torben, Buer Jan, Westendorf Astrid M, Epple Matthias (2013) Mechanism of the uptake of cationic and anionic calcium phosphate nanoparticles by cells. *Acta Biomater.* 9: 7527–7535. doi:10.1016/j.actbio.2013.02.034.
140. Sperling RA, Parak WJ (2010) Surface modification, functionalization and bioconjugation of colloidal inorganic nanoparticles. *Philos. Transact. A Math. Phys. Eng. Sci.* 368: 1333–1383. doi:10.1098/rsta.2009.0273.
141. Srivastava A, Gunjekar VG, Sinha APB (1987) Thermoanalytical studies of zinc citrate, bismuth citrate and calcium citrate. *Thermochim. Acta* 117: 201–217. doi:10.1016/0040-6031(87)88115-7. <http://www.sciencedirect.com/science/article/pii/0040603187881157>.
142. Srivastava S, Awasthi Rishi, Gajbhiye Namdeo S, Agarwal Vikas, Singh Amit, Yadav Abhishek, Gupta Rakesh K (2011) Innovative synthesis of citrate-coated superparamagnetic Fe<sub>3</sub>O<sub>4</sub> nanoparticles and its preliminary applications. *J. Colloid Interface Sci.* 359: 104–111. doi:10.1016/j.jcis.2011.03.059.
143. Storm FK, Harrison WH, Elliott RS, Morton DL (1979) Normal tissue and solid tumor effects of hyperthermia in animal models and clinical trials. *Cancer Res.* 39: 2245–2251.
144. Street Anita, Sustich Richard, Duncan Jeremiah, Savage Nora (2014) Nanotechnology Applications for Clean Water: Solutions for Improving Water Quality. William Andrew, May 15.
145. Stuber Matthias, Gilson Wesley D, Schär Michael, Kedziorek Dorota A, Hofmann Lawrence V, Shah Saurabh, Vonken Evert-Jan, Bulte Jeff WM, Kraitchman Dara L (2007) Positive contrast visualization of iron oxide-labeled stem cells using inversion-recovery with ON-resonant water suppression (IRON). *Magn. Reson. Med.* 58: 1072–1077.

doi:10.1002/mrm.21399.

<http://onlinelibrary.wiley.com/doi/10.1002/mrm.21399/abstract>.

146. Sunil Dehipalawage, Dong Jinqun, Gafney Harry D (2009) Influence of Amorphous Silica Matrices on the Formation, Structure, and Chemistry of Iron and Iron Oxide Nanoparticles. *J. Am. Chem. Soc.* 131: 14768–14777. doi:10.1021/ja9031874. <http://dx.doi.org/10.1021/ja9031874>.
147. Sun Shouheng, Zeng Hao, Robinson David B, Raoux Simone, Rice Philip M, Wang Shan X, Li Guanxiong (2004) Monodisperse MFe<sub>2</sub>O<sub>4</sub> (M = Fe, Co, Mn) Nanoparticles. *J. Am. Chem. Soc.* 126: 273–279. doi:10.1021/ja0380852. <http://dx.doi.org/10.1021/ja0380852>.
148. Terrovitis John V, Smith Rachel Ruckdeschel, Marbán Eduardo (2010) Assessment and optimization of cell engraftment after transplantation into the heart. *Circ. Res.* 106: 479–494. doi:10.1161/CIRCRESAHA.109.208991.
149. Treuel Lennart, Jiang Xiue, Nienhaus Gerd Ulrich (2013) New views on cellular uptake and trafficking of manufactured nanoparticles. *J. R. Soc. Interface* 10. doi:10.1098/rsif.2012.0939. <http://www.ncbi.nlm.nih.gov/pmc/articles/PMC3627074/>.
150. Tseng Hubert, Gage Jacob A, Raphael Robert M, Moore Robert H, Killian Thomas C, Grande-Allen K Jane, Souza Glauco R (2013) Assembly of a three-dimensional multitype bronchiole coculture model using magnetic levitation. *Tissue Eng. Part C Methods* 19: 665–675. doi:10.1089/ten.TEC.2012.0157.
151. Tsunehiro Masaya, Meki Yuma, Matsuoka Kanako, Kinoshita-Kikuta Emiko, Kinoshita Eiji, Koike Tohru (2013) A Phos-tag-based magnetic-bead method for rapid and selective separation of phosphorylated biomolecules. *J. Chromatogr. B Analyt. Technol. Biomed. Life. Sci.* 925: 86–94. doi:10.1016/j.jchromb.2013.02.039.
152. Tukmachev Dmitry, Lunov Oleg, Zablotskii Vitalii, Dejneka Alexandr, Babic Michal, Syková Eva, Kubinová Šárka (2015) An effective strategy of magnetic stem cell delivery for spinal cord injury therapy. *Nanoscale* 7:

3954–3958.doi:10.1039/C4NR05791K.  
<http://pubs.rsc.org/en/content/articlelanding/2015/nr/c4nr05791k>.

153. Tzur Amit, Moore Jodene K, Jorgensen Paul, Shapiro Howard M, Kirschner Marc W (2011) Optimizing Optical Flow Cytometry for Cell Volume-Based Sorting and Analysis. *PLoS ONE* 6: e16053. doi:10.1371/journal.pone.0016053.  
<http://dx.doi.org/10.1371/journal.pone.0016053>.
154. Ugelstad J, Stenstad P, Kilaas L, Prestvik WS, Herje R, Berge A, Hornes E (1993) Monodisperse magnetic polymer particles. New biochemical and biomedical applications. *Blood Purif.* 11: 349–369.
155. Urtizberea Ainhoa, Natividad Eva, Arizaga Ana, Castro Miguel, Mediano Arturo (2010) Specific Absorption Rates and Magnetic Properties of Ferrofluids with Interaction Effects at Low Concentrations. *J. Phys. Chem. C* 114: 4916–4922. doi:10.1021/jp912076f.  
<http://dx.doi.org/10.1021/jp912076f>.
156. Vamvakidis K, Katsikini M, Sakellari D, Paloura EC, Kalogirou O, Dendrinou-Samara C (2014) Reducing the inversion degree of MnFe<sub>2</sub>O<sub>4</sub> nanoparticles through synthesis to enhance magnetization: evaluation of their <sup>1</sup>H NMR relaxation and heating efficiency. *Dalton Trans.* 43: 12754–12765. doi:10.1039/C4DT00162A.  
<http://pubs.rsc.org/en/content/articlelanding/2014/dt/c4dt00162a>.
157. Varadan VK (2010) Nanoscience and Nanotechnology in Engineering. World Scientific.
158. Veranth John M, Kaser Erin G, Veranth Martha M, Koch Michael, Yost Garold S (2007) Cytokine responses of human lung cells (BEAS-2B) treated with micron-sized and nanoparticles of metal oxides compared to soil dusts. *Part. Fibre Toxicol.* 4: 2. doi:10.1186/1743-8977-4-2.  
<http://www.ncbi.nlm.nih.gov/pmc/articles/PMC1821039/>.
159. Vertrees Roger A, Das Gokul C, Coscio Angela M, Xie Jingwu, Zwischenberger Joseph B, Boor Paul J (2005) A mechanism of hyperthermia-

- induced apoptosis in ras-transformed lung cells. *Mol. Carcinog.* 44: 111–121. doi:10.1002/mc.20124.
160. Wadajkar Aniket S, Menon Jyothi U, Kadapure Tejaswi, Tran Richard T, Yang Jian, Nguyen Kytai T (2013) Design and Application of Magnetic-based Theranostic Nanoparticle Systems. *Recent Pat. Biomed. Eng.* 6: 47–57. doi:10.2174/1874764711306010007. <http://www.ncbi.nlm.nih.gov/pmc/articles/PMC3686518/>.
161. Wang Tiantian, Bai Jing, Jiang Xiue, Nienhaus G Ulrich (2012) Cellular Uptake of Nanoparticles by Membrane Penetration: A Study Combining Confocal Microscopy with FTIR Spectroelectrochemistry. *ACS Nano* 6: 1251–1259. doi:10.1021/nn203892h. <http://dx.doi.org/10.1021/nn203892h>.
162. Wang Yaqi, Xu Chenjie, Ow Hooisweng (2013) Commercial Nanoparticles for Stem Cell Labeling and Tracking. *Theranostics* 3: 544–560. doi:10.7150/thno.5634. <http://www.thno.org/v03p0544.htm>.
163. Wang Yi-Xiang J (2011) Superparamagnetic iron oxide based MRI contrast agents: Current status of clinical application. *Quant. Imaging Med. Surg.* 1: 35–40. doi:10.3978/j.issn.2223-4292.2011.08.03. <http://www.ncbi.nlm.nih.gov/pmc/articles/PMC3496483/>.
164. Wang Yi-Xiang J, Hussain Shahid M, Krestin Gabriel P (2001) Superparamagnetic iron oxide contrast agents: physicochemical characteristics and applications in MR imaging. *Eur. Radiol.* 11: 2319–2331. doi:10.1007/s003300100908. <http://link.springer.com/article/10.1007/s003300100908>.
165. Westbrook Catherine (2014) Handbook of MRI Technique. John Wiley & Sons, August 7.
166. Wilhelm C, Billotey C, Roger J, Pons JN, Bacri JC, Gazeau F (2003) Intracellular uptake of anionic superparamagnetic nanoparticles as a function of their surface coating. *Biomaterials* 24: 1001–1011. doi:10.1016/S0142-9612(02)00440-4. <http://www.sciencedirect.com/science/article/pii/S0142961202004404>.

167. Wu Wei, He Quanguo, Jiang Changzhong (2008) Magnetic Iron Oxide Nanoparticles: Synthesis and Surface Functionalization Strategies. *Nanoscale Res. Lett.* 3: 397. doi:10.1007/s11671-008-9174-9. <http://www.nanoscalereslett.com/content/3/11/397>.
168. Xu Chenjie, Mu Luye, Roes Isaac, Miranda-Nieves David, Nahrendorf Matthias, Ankrum James A, Zhao Weian, Karp Jeffrey M (2011) Nanoparticle-based monitoring of cell therapy. *Nanotechnology* 22: 494001. doi:10.1088/0957-4484/22/49/494001. <http://www.ncbi.nlm.nih.gov/pmc/articles/PMC3334527/>.
169. Yang Hung-Wei, Hua Mu-Yi, Liu Hao-Li, Huang Chiung-Yin, Wei Kuo-Chen (2012) Potential of magnetic nanoparticles for targeted drug delivery. *Nanotechnol. Sci. Appl.* 5: 73–86. doi:10.2147/NSA.S35506. <http://www.ncbi.nlm.nih.gov/pmc/articles/PMC3781723/>.
170. Yathindranath Vinith, Rebbouh Leila, Moore David F, Miller Donald W, van Lierop Johan, Hegmann Torsten (2011) A Versatile Method for the Reductive, One-Pot Synthesis of Bare, Hydrophilic and Hydrophobic Magnetite Nanoparticles. *Adv. Funct. Mater.* 21: 1457–1464. doi:10.1002/adfm.201002111. <http://onlinelibrary.wiley.com/doi/10.1002/adfm.201002111/abstract>.
171. Yoo Dongwon, Jeong Heeyeong, Preihs Christian, Choi Jin-sil, Shin Tae-Hyun, Sessler Jonathan L, Cheon Jinwoo (2012) Double-Effector Nanoparticles: A Synergistic Approach to Apoptotic Hyperthermia. *Angew. Chem. Int. Ed.* 51: 12482–12485. doi:10.1002/anie.201206400. <http://onlinelibrary.wiley.com/doi/10.1002/anie.201206400/abstract>.
172. Yoo Dongwon, Lee Jae-Hyun, Shin Tae-Hyun, Cheon Jinwoo (2011) Theranostic Magnetic Nanoparticles. *Acc. Chem. Res.* 44: 863–874. doi:10.1021/ar200085c. <http://dx.doi.org/10.1021/ar200085c>.
173. Zhang Yong, Kohler Nathan, Zhang Miqin (2002) Surface modification of superparamagnetic magnetite nanoparticles and their intracellular uptake. *Biomaterials* 23: 1553–1561.

174. Zucker RM, Massaro EJ, Sanders KM, Degn LL, Boyes WK (2010) Detection of TiO<sub>2</sub> nanoparticles in cells by flow cytometry. *Cytometry A* 77A: 677–685. doi:10.1002/cyto.a.20927. <http://onlinelibrary.wiley.com/doi/10.1002/cyto.a.20927/abstract>.

## List of Publications

- [1] **E.B. Ansar**, M. Ajeesh, Y. Yokogawa, W. Wunderlich, H. Varma, Synthesis and Characterization of Iron Oxide Embedded Hydroxyapatite Bioceramics, *J. Am. Ceram. Soc.* 95 (2012) 2695–2699. doi:10.1111/j.1551-2916.2011.05033.x.
- [2] **A.E. Beeran**, S.S. Nazeer, F.B. Fernandez, K.S. Muvvala, W. Wunderlich, S. Anil, et al., An aqueous method for the controlled manganese (Mn<sup>2+</sup>) substitution in superparamagnetic iron oxide nanoparticles for contrast enhancement in MRI, *Phys. Chem. Chem. Phys.* 17 (2015) 4609–4619. doi:10.1039/C4CP05122J.
- [3] **A.E. Beeran**, F.B. Fernandez, A. John, Self-assembled superparamagnetic nanocomposite-labelled cells for noninvasive, controlled, targeted delivery and therapy, *RSC Adv.* 5 (2015) 36742–36752. <http://pubs.rsc.org/en/content/articlehtml/2015/ra/c4ra16185h> (accessed December 20, 2015).
- [4] **A.E. Beeran**, F.B. Fernandez, S.S. Nazeer, R.S. Jayasree, A. John, S. Anil, et al., Multifunctional nano manganese ferrite ferrofluid for efficient theranostic application, *Colloids Surf. B Biointerfaces.* 136 (2015) 1089–1097. doi:10.1016/j.colsurfb.2015.11.010.
- [5] M.K. Surendra, S. Annapoorani, **E.B. Ansar**, P.R.H. Varma, M.S.R. Rao, Magnetic hyperthermia studies on water-soluble polyacrylic acid-coated cobalt ferrite nanoparticles, *J. Nanoparticle Res.* 16 (2014) 1–14. doi:10.1007/s11051-014-2773-8.
- [6] M.S. Shyma, **E.B. Ansar**, V. Gayathri, H.K. Varma, P.V. Mohanan, Attenuation of Cisplatin Induced Toxicity by Melatonin, Loaded on a Dextran Modified Iron Oxide Nanoparticles: An In Vitro Study, (2015). <http://dspace.sctimst.ac.in/xmlui/handle/123456789/2644> (accessed December 20, 2015).

[7] S. Anil, A.F. Al-Sulaimani, **A.E. Beeran**, E.P. Chalisserry, H.P. Varma, M.D. Al Amri, Drug Delivery Systems in Bone Regeneration and Implant Dentistry, (2015). <http://cdn.intechopen.com/pdfs-wm/48155.pdf> (accessed December 20, 2015).

[8] Sabareeswaran A, **Ansar E.B.**, Mohanan PV, Varma HK, Kumari TV “Mast cell infiltration and antioxidant induction of dextran and polyethylene glycol coated SPIONs: An in-vivo study.” Nanomedicine: Nanotechnology, Biology and Medicine 12 (2016) 1523-1533.

[9] Vineeth M. V, Ansar E B, Sachin J Shenoy , Sunita P. Victor and Jayabalalan Muthu “PEGylated Super paramagnetic near 1 R emitting fluorescent iron oxide nanogel for potential theranostic applications” Journal of Materials Chemistry B (Submitted)

[10] **ANSAR E.B.**, SEKHARAPILLAI VIJAYAN, HARIKRISHNA VARMA PR “Ceramic Moiety Modified Magnetic Nanoparticle – Biomedical Applications in Cell Separation & Hyperthermia Therapy”, Patent Ref Number IPBCL 055.Y14.

### **Selected Conference Presentations**

1) **Ansar E.B.**, Yoshiyuki Yokogawa, Harikrishna Varma PR “Preparation of Iron Oxide Embedded Hydroxyapatite for Biomedical Applications”, - International Conference on Biomaterials and Implants: Prospects and Possibilities in the New Millennium (BIO 2011) at CGCRI, Kolkata 21-23 July, 2011.

2) **Ansar E.B.**, Manoj Komath, Harikrishna Varma P R “Iron Oxide Embedded Hydroxyapatite – A New Generation Magnetic Bioceramic” - nanobio, 2<sup>nd</sup> International Conference on Nanotechnology at the Bio-Medical Interface at Amrita Centre for Nanosciences & Molecular Medicine- AIMS, Kochi 21- 23, 2012 February, 2012.

3) **Ansar.E.B.**, Fernandez.F.B, Annie John, Harikrishna Varma P R “The ceramic moiety modified superparamagnetic nanoparticles for efficient cell separation” - TERMIS-AP 2013 October 23-26 in Shanghai and Wuzhen, PR China.

- 4) **Ansar.E.B**, Fernandez.F.B, Krishna Surendra.M, Annie John, M.S. Ramachandra Rao, Harikrishna Varma P R “The evaluation of hyperthermia effect to cancerous cells by biocompatible inorganic matrix modified magnetic nanocrystals in the presence of RF induction alternating magnetic field” - IUMRS-ICA 2013: 16th – 20th December 2013, at Indian Institute of Science, Bangalore, India.
- 5) **Ansar.E.B**, Fernandez.F.B, Shaiju. S.N, R.S. Jayasree, Annie John, Harikrishna Varma P R “Manganese ferrite superparamagnetic nanoparticles for theranostic application” - International Symposium on Photonics Applications and Nanomaterials, ISPAN-2015; 28-30 October 2015.
- 6) Francis B Fernandez, **Ansar E B**, H K Varma, and Annie John "Microspheroid Assemblies : Levitating PCL –IO Spheroids in Biomedical Applications"- International Symposium on Photonics Applications and Nanomaterials, ISPAN-2015; 28-30 October 2015.
- 7) R. Sreekumar, **Ansar E.B** and Harikrishna Varma P R “Iron Oxide embedded Hydroxyapatite crystallites-A new bioceramic composite” - The XXXIII Annual Meet of Electron Microscope Society of India, Indian institute of science and south zone chapter of EMSI at Bangalore 2-4 July 2012.
- 8) Ansar.E.B, Harikrishna Varma P R “Theranostic Approaches Using Superparamagnetic Nanoparticles” (MRSI) Thiruvananthapuram Chapter at IIST-trivandrum 2<sup>nd</sup>, April 2016 (Best Presentation award)

## **Curriculum vitae**

### **Education**

- PhD (2011 till date)** Enrolled in January 2011 at SCTIMST, Kerala, India. Advisor  
Dr. Harikrishna Varma P R
- M.Sc (2007-2009)** Chemistry (Inorganic Chemistry specialization) with 71.3%. 2007-2009 School of chemical science, M G University, Kerala, India.
- B.Sc (2003-2007)** Chemistry with 84.2% and first class 2003-2007, M G University, Kerala, India

### **Professional Experience**

- 4<sup>th</sup> March 2015 to 24<sup>th</sup> March 2015** Research Scholar, Osaka City University, 3-3-138 Sugimoto, Sumiyoshi-ku, Osaka 558-8585, Japan
- 2013 till date** Senior Research fellow (SCTIMST)

### **Home address**

Ereath House

Mudickal (PO)

Perumbavoor

Ernalkulam-683547

Email: ansareb@gmail.com